Dissertation

submitted to the

Combined Faculties of the Natural Sciences and Mathematics

of the Ruperto-Carola-University of Heidelberg, Germany

for the degree of

Doctor of Natural Sciences

Put forward by

Alessandra Edda Baas

born in Cologne

Oral examination on July 26th, 2017

$WW\gamma$ and $WZ\gamma$ Production at the ATLAS Experiment

Referees: Prof. Dr. Hans-Christian Schultz-Coulon
Prof. Dr. Stephanie Hansmann-Menzemer

Abstract

The study of three electroweak gauge bosons is not only a precise test of the electroweak structure of the Standard Model, but it is also sensitive to new physics. In this thesis, the measurement of $WW\gamma$ and $WZ\gamma$ production in proton−proton collisions is presented, in which events are analysed where the W boson decays leptonically and the other heavy gauge boson decays hadronically. Two decay channels differing in the flavour of the final state lepton are studied: the electron and the muon channel. The analysed proton−proton collisions are recorded in 2012 with the ATLAS experiment at a centre-of-mass energy of $\sqrt{s} = 8\,\text{TeV}$ and correspond to an integrated luminosity of $20.2\,\text{fb}^{-1}$. Exclusion limits on the production cross section are derived at 95 % confidence level (CL) in two different phase space regions: one is optimised for the Standard Model production and one for the search of new physics beyond the Standard Model. The best upper limits on the $WW\gamma$ and $WZ\gamma$ production, determined in this analysis, exclude cross sections above 2.5 times the Standard Model expectation. In addition, Frequentist limits at 95 % CL are derived on fourteen different anomalous quartic gauge couplings of mass dimension eight, using the framework of an effective field theory. The exclusion limits are presented with and without unitarisation.

Zusammenfassung

Die Messung der gleichzeitigen Produktion von drei elektroschwachen Eichbosonen ist nicht nur ein präziser Test des Standardmodells der Teilchenphysik, sondern auch sensitiv auf neue Physik. Die vorliegende Arbeit präsentiert die Messung der $WW\gamma$- und $WZ\gamma$-Produktion in Proton−Proton Kollisionen, bei der Endzustände untersucht werden, in denen das W-Boson leptonisch und das andere schwere Eichboson hadronisch zerfällt. Abhängig von dem Leptonflavour werden zwei verschiedene Kanäle analysiert: der Elektron- und der Muonkanal. Dafür werden Proton−Proton Kollisionen untersucht, die im Jahr 2012 mit dem ATLAS Detektor, bei einer Schwerpunktsenergie von $\sqrt{s} = 8\,\text{TeV}$ aufgenommen wurden und einer integrierten Luminosität von $20.2\,\text{fb}^{-1}$ entsprechen. In zwei verschiedenen Phasenraumbereichen werden obere Ausschlussgrenzen auf den Produktionswirkungsquerschnitt mit Hilfe der CL_S Methode gesetzt. Der eine Phasenraumbereich ist optimiert für Standardmodellmessungen und der andere für die Suche nach neuer Physik jenseits des Standardmodells. Die besten Limits, die in dieser Arbeit präsentiert werden, schließen Wirkungsquerschnitte der $WW\gamma$ und $WZ\gamma$ Produktion aus, welche um einen Faktor 2.5 größer sind als die Standardmodellerwartung. Zusätzlich werden Ausschlussgrenzen auf vierzehn verschiedene anormale quartische Eichkopplungen mit der Massendimension acht gesetzt, die mit einer effektiven Feldtheorie parametrisiert werden. Die Ergebnisse auf die Ausschlussgrenzen werden mit und ohne Unitarisierung präsentiert.

Contents

1. Introduction

The quest for answers to the open questions in physics, elucidate the laws of nature and understand the origin of matter or the evolution of the universe, is tightly interwoven with our knowledge of the elementary particles and their interactions. The *Standard Model of Particle Physics*, which has been developed over several decades starting in the 1960s, describes the fundamental particles and their interactions with each other. This overwhelmingly suggestive theory explains the data of nearly all particle physics experiments. In 2012, the last missing particle of the Standard Model, the Higgs boson [1–6] has been discovered by the ATLAS and the CMS Collaborations [7, 8]. Despite the enormous success of the Standard Model, there are many observations that cannot be explained with this theory. One of the most prominent examples is the content of the universe: only 5 % of the universe is made up of matter, which consists of the fundamental particles of the Standard Model [9]; the rest of the universe is made up of dark matter (26 %) [9] and dark energy (69 %) [9], neither of which has an explanation from the Standard Model. Other open questions involve the precise fine tuning of the Higgs mass, the observed matter-antimatter asymmetry in the universe, the weakness of gravity compared to the other forces and the feasibility to unify gravity with the Standard Model into one universal theory. Collider experiments using large particle accelerators can help answering some of these questions. The production of three electroweak gauge bosons via one quartic vertex, is precisely predicted by the Standard Model. Therefore, the measurement of triboson final states is a unique test of the Standard Model and at the same time it is a probe for physics beyond the Standard Model, as any deviation would hint to new phenomena.

In this thesis, triboson production of $WW\gamma$ and $WZ\gamma$ events are studied, with the semi-leptonic decay of the heavy gauge bosons, using proton−proton data, provided by the Large Hadron Collider and collected with the ATLAS detector at a centre-of-mass energy of $\sqrt{s} = 8\,\text{TeV}$, corresponding to an integrated luminosity of $20.2\,\text{fb}^{-1}$. A visualisation of a $WV\gamma$ candidate event in the electron channel with $e\nu\text{jj}\gamma$ final states is shown in Figure 1.1. In the upper left corner, the final state products of the event are represented by the coloured bars in the $\eta - \phi$ plane[1]: the electron in green, the jets in white, the photon in yellow and the missing transverse energy in red. The height of the bars corresponds to the energy of the final state objects. The figure shows in addition two different cross sections of the ATLAS detector and an enlargement of the calorimeter and the inner detector. Tracks, arising from the interaction point in the middle of the detector are illustrated as well as energy depositions in the electromagnetic and hadronic calorimeter. See Appendix A.1 for an event display in the muon channel.

The CMS Collaboration has studied $WW\gamma$ and $WZ\gamma$ production, using a dataset at the same centre-of-mass energy and with comparable integrated luminosity, as in this thesis [11]. At LEP, the predecessor of the Large Hadron Collider, triboson production was also studied at a centre-of-mass energy between 183 GeV and 207 GeV. Since LEP collided electrons and positrons, only neutral final states could be produced. Therefore, only $WW\gamma$ production was studied in several different fully and semi-leptonic decay modes [12]. Other triboson

[1]The azimuthal angle ϕ and the pseudorapidity η are introduced in Chapter 3.

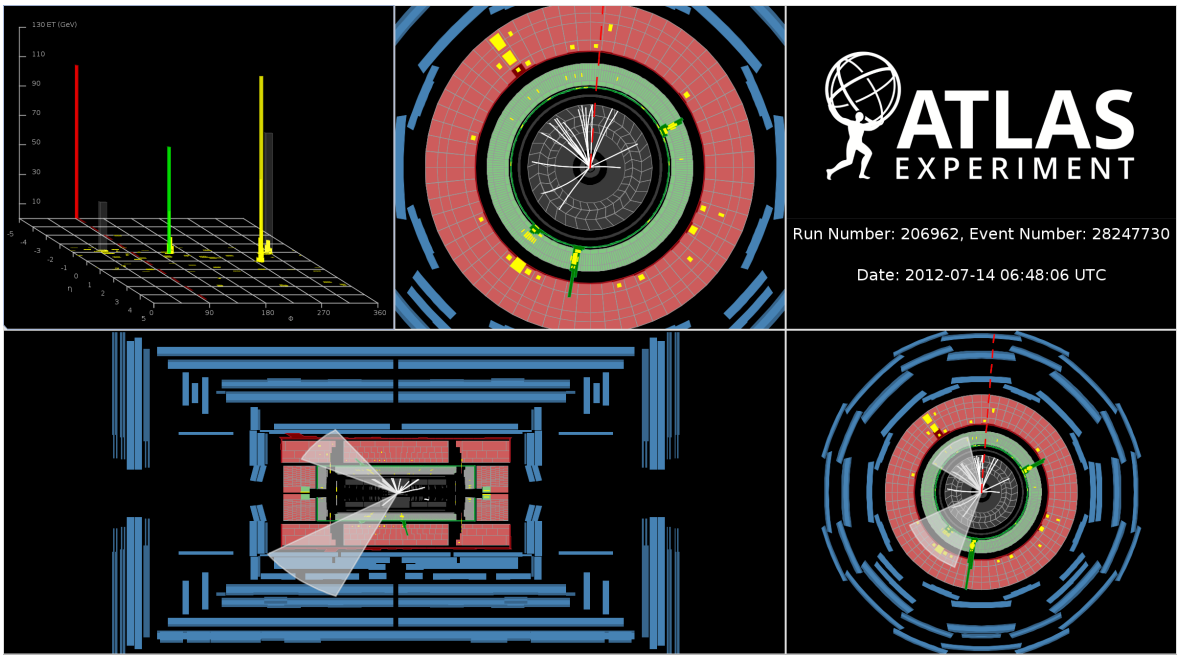

Figure 1.1.: Visualisation of a $WV\gamma$ candidate event with the decay into $e\nu jj\gamma$ final states, recorded with ATLAS detector at a centre-of-mass energy of $\sqrt{s} = 8\,\text{TeV}$ on July, 14^{th} 2012. [10]

measurement, which are sensitive to quartic gauge couplings, are published by the ATLAS and CMS Collaborations [13–16]. Furthermore, the ATLAS and CMS Collaborations studied quartic gauge couplings in diboson final states [17–24].

The thesis is organised as follows. In Chapter 2, the Standard Model is introduced as theoretical foundation and triboson production within the Standard Model is discussed, with an emphasis on $WW\gamma$ and $WZ\gamma$ production. Furthermore, this chapter describes anomalous quartic gauge couplings in the framework of an effective field theory, as one possible parametrisation in the search for physics beyond the Standard Model. The experimental setup, including the LHC machine and the ATLAS detector are presented in Chapter 3. In Chapter 4 the simulation of proton−proton collisions is discussed, with details about the production of the $WW\gamma$ and $WZ\gamma$ signal simulation samples. In addition, all simulation samples used in the analysis are presented. The reconstruction, identification and calibration in the ATLAS detector of the physics objects used in this thesis, are described in Chapter 5. In Chapter 6, the event selection is motivated and presented. The estimation of the backgrounds is described in Chapter 7 and the results including systematic uncertainties is discussed. Chapter 8 is dedicated to the determination of the exclusion limits on the production cross section. The interpretation of the results in the context of a search for new physics beyond the Standard Model is given in Chapter 9. Finally, in Chapter 10 the results of the thesis are summarised.

Author's Contribution The author conducted this work as a member of the ATLAS Collaboration. Within the collaboration, the data taking is a common effort and the author used the provided infrastructure for the reconstruction, identification and calibration of the physics objects. The study of $WW\gamma$ and $WZ\gamma$ production has been carried out by the author as the sole analyser. The author was in charge for all parts of the analysis and for both lepton channels. This included the production of the signal Monte Carlo samples with SHERPA and MADGRAPH, as well as the next-to-leading order normalisation of the cross section using the VBFNLO generator. The optimisation of the selection criteria and the strategy for the background estimation method have been developed, implemented and performed by the author including systematic studies. Furthermore, the author determined the correction factors and derived the exclusion limits on the production cross section. The final interpretation in the framework of anomalous quartic gauge coupling has also been carried out by the author. All figures in the thesis that are related to the analysis have been produced by the author. Figures that are not produced by the author are referenced.

As main analyser, the author has reported regularly to the different ATLAS expert groups, ensuring completeness and integrity. In the near future, the results of the study will be published by the ATLAS Collaboration together with the study of $WW\gamma \to e\nu\mu\nu\gamma$ final states. The respective paper draft is in the final review of the ATLAS Collaboration and preliminary figures are already available [10]. Here, the author is responsible to determine exclusion limits using the CL_S method for all final states as well as to derive the final limits on the anomalous quartic gauge couplings for the combination of all channels. Furthermore, the author is one of the two contact editors within the ATLAS Collaboration for the paper.

The author contributed to additional studies, which are not reported here. These include a performance study for the Run 2 trigger menu, studying a dedicated triobject trigger to select events with one muon and two electromagnetic objects. Furthermore, the author was involved in upgrade studies of the Level-1 calorimeter trigger, in particular a new calibration, applied to hadronic objects and its performance with respect to the jet energy response. In addition, the author contributed to the η-intercalibration of jets, studying a method, where various triggers are combined, which are not necessarily fully efficient. This work is documented in an ATLAS internal report [25].

2. Theoretical Concepts

The Standard Model of particle physics is the theoretical foundation of our current knowledge about the fundamental particles and their interaction. Therefore, Section 2.1 introduces the Standard Model with a focus on the electroweak sector. It is based on References [26–28] and follows their notations. Theoretical aspects of $WW\gamma$ and $WZ\gamma$ production are discussed in Section 2.2. In Section 2.3, anomalous quartic gauge couplings are introduced as one possible parametrisation in the search of physics beyond the Standard Model.

2.1. The Standard Model of Particle Physics

The Standard Model of particle physics is a Lorentz invariant quantum field theory, describing the elementary particles and their interactions. It obeys local gauge invariance under the symmetries of the $\mathrm{SU}(3)_C \times \mathrm{SU}(2)_L \times \mathrm{U}(1)_Y$ gauge group. The Standard Model combines the electroweak theory, formulated by S.Glashow, A.Salam and S.Weinberg [29–31] and the theory of the strong interaction [32, 33], also called *Quantum Chromodynamics* (QCD). The electroweak theory describes the electromagnetic and weak interactions between the fundamental particles. Its symmetry group is the $\mathrm{SU}(2)_L \times \mathrm{U}(1)_Y$ with the third component of the weak isospin I_3 and the weak hypercharge $Y = 2\,(Q - I_3)$, where Q is the electric charge, being the respective quantum numbers. Quantum Chromodynamics describes the strong interaction between the fundamental particles and is based on the $\mathrm{SU}(3)_C$ symmetry group, with the three colour charges red, green and blue being the quantum numbers. In this framework, all elementary particles and all gauge bosons are massless and thus an additional piece is necessary to generate the masses of the fermions and some of the gauge bosons, as observed in nature. The masses can be generated through the Higgs mechanism [1–6] in the Standard Model, which spontaneously breaks the electroweak $\mathrm{SU}(2)_L \times \mathrm{U}(1)_Y$ gauge symmetry to the electromagnetic $\mathrm{U}(1)_{EM}$ symmetry. This is done by introducing an additional $\mathrm{SU}(2)_L$ scalar doublet field, the Higgs field, with a non-vanishing vacuum expectation value. Interactions with the Higgs field generate the different masses of the fermions and some of the gauge bosons. The last degree of freedom, which does not take part in the generation of the masses, manifests itself as a scalar particle, the physical Higgs boson, discovered by the ATLAS and the CMS Collaborations [7, 8] in 2012. As the electroweak sector with the Higgs mechanism is the basis for the description of weak vector bosons and photons, measured in this thesis, this part is reviewed in more detail.

In the Standard Model, the fundamental particles, the fermions, are spin $1/2$ matter fields. The fermion fields along with some of their quantum numbers are given in Table 2.1. They are introduced as left-handed chiral doublets ($I_3 = \pm 1/2$) and right-handed chiral singlets ($I_3 = 0$) under the third component of the weak isospin. The fermions are divided into quarks and leptons, depending on their interactions. Quarks carry colour charge and thus can interact via the strong force, in contrast to leptons. There are six types of quarks in the Standard Model, three so-called *up-type* quarks, the up (u), the charm (c) and the top (t) quark and three

Fermion	Generation I	Generation II	Generation III	$SU(3)_C$ Colour Charge	$SU(2)_L$ I_3	$U(1)_Y$ Weak Hypercharge Y
Quarks	$\begin{pmatrix} u_L \\ d_L \end{pmatrix}$	$\begin{pmatrix} c_L \\ s_L \end{pmatrix}$	$\begin{pmatrix} t_L \\ b_L \end{pmatrix}$	yes	$^1/_2$ $-^1/_2$	$^1/_3$
	u_R	c_R	t_R	yes	0	$^4/_3$
	d_R	s_R	b_R	yes	0	$-^2/_3$
Leptons	$\begin{pmatrix} e_L \\ \nu_{e,L} \end{pmatrix}$	$\begin{pmatrix} \mu_L \\ \nu_{\mu,L} \end{pmatrix}$	$\begin{pmatrix} \tau_L \\ \nu_{\tau,L} \end{pmatrix}$	no	$-^1/_2$ $^1/_2$	-1
	e_R	μ_R	τ_R	no	0	-2

Table 2.1.: The fermions of the Standard Model with a selection of their quantum numbers [35]. The sub-script L (R) represent left (right) handed chiral lepton fields. The right-handed singlets have a zero component of the third isospin, $I_3 = 0$, whereas the left-handed doubles have $I_3 = \pm^1/_2$.

so-called *down-type* quarks, the down (d), the strange (s) and the bottom (b) quark. Quarks are grouped into three generations, as illustrated in Table 2.1. In contrast, leptons carry no colour charge and cannot interact via the strong force. There are three lepton flavours, appearing as electrically charged leptons: the electron (e), the muon (μ) and the tau (τ) and as electrically neutral neutrino with the same flavours: the electron neutrino (ν_e), the muon neutrino (ν_μ) and the tau neutrino (ν_τ). The leptons are also grouped into generations, as indicated in Table 2.1. To date, right-handed neutrinos have not been observed [34], and are therefore not included in the Standard Model.

The interactions are mediated by spin one gauge fields. The generator of the $U(1)_Y$ symmetry group is the B_μ field, the generators of the $SU(2)_L$ symmetry group are the three W^a_μ fields, with $a \in [1, 2, 3]$ and the generators of the $SU(3)_C$ symmetry group are the eight gluon fields G^b_μ, with $b \in [1, ..., 8]$. In addition, the Higgs field, a complex scalar doublet Φ under the $SU(2)_L$ with four degrees of freedoms, is introduced. The boson fields of the Standard Model are listed in Table 2.2. The $U(1)_Y$ symmetry group is commutative, also called *abelian*, and the B_μ field cannot interact with itself. In contrast, the $SU(2)_L$ symmetry group is non-commutative, a property also referred to as *non-abelian*, and allows the W^a_μ fields to interact with themself. The $SU(3)_C$ symmetry group, describing Quantum Chromodynamics, is also non-abelian and thus the gluons can interact with themself. The coupling of the strong interaction, α_s, is the strongest of all fundamental forces, but its range is limited to a few femtometer due to the self-interaction of the gluons. Two important characteristics of Quantum Chromodynamics are the *asymptotic freedom* and the *colour confinement*. Asymptotic freedom refers to the strong coupling α_s, which depends on the energy scale: for high energies, corresponding to small distances, the strong coupling decreases asymptotically, allowing the particles to behave freely. Colour confinement refers to the experimental observation that colour charged particles cannot be observed as individual particles, but only in colour-neutral states, so-called *hadrons*. The potential of the strong force increases linearly with larger distances, leading to an increase of the energy in the colour field between two particles interacting via the strong force, that is for example, a quark-antiquark pair. When enough energy is provided by the colour field, a new quark-antiquark pair is produced and colour-neutral states are formed with the initial quark-antiquark pair.

Gauge Field	$SU(3)_C$ Colour Charge	$SU(2)_L$ I_3	$U(1)_Y$ Weak Hypercharge Y
G^b_μ	yes	no	0
W^a_μ	no	yes	0
B^μ	no	no	0
Φ	no	yes	1

Table 2.2.: The gauge boson fields of the Standard Model before the electroweak symmetry breaking.

The electroweak interactions between the gauge fields and the left- and right-handed matter fields, $\Psi_{R/L}$, as well as between the scalar Higgs doublet Φ are described by covariant derivatives:

$$D_\mu \Psi_L = \left(\partial_\mu - i\frac{g}{2} W^a_\mu \sigma^a - i\frac{g'}{2} B_\mu\right) \Psi_L \tag{2.1}$$

$$D_\mu \Psi_R = \left(\partial_\mu - i\frac{g'}{2} B_\mu\right) \Psi_R \tag{2.2}$$

$$D_\mu \Phi \;\; = \left(\partial_\mu - i\frac{g}{2} W^a_\mu \sigma^a - i\frac{g'}{2} B_\mu\right) \Phi \tag{2.3}$$

where g and g' are the coupling constants of the $SU(2)_L$ and the $U(1)_Y$, respectively and σ^a are the Pauli matrices. The interactions between the gauge fields and the left- and right-handed fermion fields are different, as the W^a_μ fields couple solely to left-handed fields. The Lagrange density for the electroweak sector, including interactions with the Higgs field, is given by:

$$\mathcal{L} = -\frac{1}{4} W^a_{\mu\nu} W^{\mu\nu}_a - \frac{1}{4} B_{\mu\nu} B^{\mu\nu} \tag{2.4a}$$

$$+ \sum_{\text{fermions}} \left(i\bar{\Psi}_L D_\mu \gamma^\mu \Psi_L + i\bar{\Psi}_R D_\mu \gamma^\mu \Psi_R\right) \tag{2.4b}$$

$$+ \left(D^\mu \Phi\right)^\dagger \left(D_\mu \Phi\right) - V(\Phi) \tag{2.4c}$$

$$- \sum_{\text{fermions}} \lambda_f \left(\bar{\Psi}_L \Phi \Psi_R + \bar{\Psi}_R \bar{\Phi} \Psi_L\right). \tag{2.4d}$$

The kinetic terms and the self-interactions of the gauge fields are described by the first term of the Equation 2.4a. It is based on the the field strength tensors $W^a_{\mu\nu} = \partial_\mu W^a_\nu - \partial_\nu W^a_\mu + g\epsilon^{ajk} W^j_\mu W^k_\nu$ and $B_{\mu\nu} = \partial_\mu B_\nu - \partial_\nu B_\mu$ of the respective gauge fields, using the totally antisymmetric Levi-Civita tensor ϵ_{ajk} and the Dirac matrices γ^μ. The second term of the Equation 2.4b describes the dynamics of the matter fields as well as the interaction between the fermion and the gauge fields. In the third term of the Equation 2.4c, the interactions between the gauge and the Higgs fields are described as well as the self-coupling of the Higgs via its potential, $V(\Phi)$. The fourth term of the Equation 2.4d, describes the interaction between the fermions and the Higgs field, where the Yukawa coupling, λ_f, for each fermion, f, is introduced.

The minimum of the Higgs potential $V(\Phi)$ has a non-vanishing vacuum expectation value, v, which breaks the $SU(2)_L \times U(1)_Y$ symmetry, as the Lagrange density is no longer invariant

under this gauge group. The W_μ^a and B_μ fields are combined to the new fields:

$$W_\mu^\pm = \frac{1}{\sqrt{2}}\left(W_\mu^1 \mp iW_\mu^2\right) \tag{2.5}$$

$$Z_\mu = \frac{1}{\sqrt{g^2+g'^2}}\left(gW_\mu^3 - g'B_\mu\right) \tag{2.6}$$

$$A_\mu = \frac{1}{\sqrt{g^2+g'^2}}\left(gW_\mu^3 + g'B_\mu\right) \tag{2.7}$$

leading to the physical $W^\pm$ and Z bosons as well as the photon A. The longitudinal polarisations and the masses of the $W^\pm$ and Z bosons are obtained by absorbing three of the four degrees of freedom of the Higgs field Φ. The remaining degree of freedom manifests itself as the massive Higgs boson H, with spin zero. The masses generated with the Higgs mechanism are:

$$m_W = \frac{gv}{2} \qquad m_Z = \frac{v}{2}\sqrt{g^2+g'^2} \qquad m_A = 0 \tag{2.8}$$

$$m_H = 2\lambda v^2 \tag{2.9}$$

$$m_f = \frac{\lambda_f v}{\sqrt{2}} \tag{2.10}$$

where λ is the self coupling of the Higgs boson.

The photon (γ) is the mediator of electromagnetic interactions between charged particles. It is massless, electrically neutral and cannot couple to itself. Therefore, the range of the electromagnetic force is infinite. The $W^\pm$ and the Z bosons are the mediators of the weak interactions. The W bosons have either an electric charge of $Q = -1$ (W^-) or $Q = +1$ (W^+) and are mediating the so-called *charged currents*. In the following, the charge information of the $W^\pm$ bosons is omitted when not explicitly necessary. The Z boson has no electric charge and thus mediates the so-called *neutral currents*. As the W and Z bosons are massive, the weak interaction has only a limited range and has the weakest strength of the three fundamental forces.

2.2. $WW\gamma$ and $WZ\gamma$ Phenomenology

As described in the precious section, the $\mathrm{SU}(2)_L$ symmetry group is non-abelian, allowing the weak gauge bosons to couple to themselves. Therefore, the Standard Model predicts interactions of three and four gauge bosons at one vertex. The interaction of three gauge bosons at one vertex is called *Triple Gauge Coupling* (TGC). In the Standard Model two triple gauge couplings are described: $W^+W^-\gamma$ and W^+W^-Z. The interaction of four gauge bosons at one vertex is called *Quartic Gauge Coupling* (QGC) and the Standard Model describes four different quartic gauge couplings: $W^+W^-\gamma\gamma$, $W^+W^-Z\gamma$, W^+W^-ZZ and $W^+W^-W^+W^-$. The Standard Model

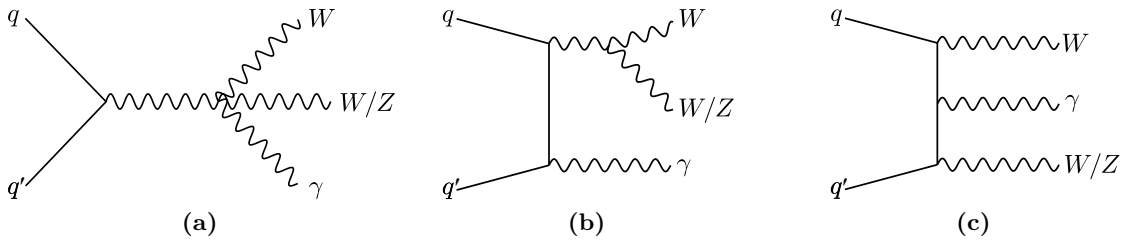

Figure 2.1.: Three examples of Feynman diagrams for $WW\gamma$ and $WZ\gamma$ production at the LHC. The processes are produced via (a) quartic gauge boson vertex, via (b) triple gauge boson coupling in association with a radiated photon and via (c) radiation processes only. [10]

Lagrangian describing the quartic interactions is given by [28]:

$$\mathcal{L}_{\text{QGC}} = -e^2 \left(W_\mu^- W^{+\mu} A_\nu A^\nu - W_\mu^- A^\mu W_\nu^+ A^\nu\right) \tag{2.11a}$$

$$-e^2 \cot\theta_W \left(2W_\mu^- W^{+\mu} Z_\nu A^\nu - W_\mu^- Z^\mu W_\nu^+ A^\nu - W_\mu^- A^\mu W_\nu^+ Z^\nu\right) \tag{2.11b}$$

$$-e^2 \cot^2\theta_W \left(W_\mu^- W^{+\mu} Z_\nu Z^\nu - W_\mu^- Z^\mu W_\nu^+ Z_\nu\right) \tag{2.11c}$$

$$-e^2 \frac{1}{\sin^2\theta_W} \left((W_\mu^- W^{+\mu})^2 - W_\mu^- W^{-\mu} W_\nu^+ W^{+\nu}\right) \tag{2.11d}$$

where $e = gg'/\sqrt{g^2+g'^2}$ is the electromagnetic coupling constant and θ_W is the so-called *Weinberg angle*. The $WW\gamma$ and $WZ\gamma$ processes studied in this thesis are described by the terms 2.11a and 2.11b of the Lagrangian and their measurement provide an excellent opportunity to test the gauge structure of the Standard Model as well as the symmetry breaking of the electroweak sector. Typical Feynman diagrams for the production of the $WW\gamma$ and $WZ\gamma$ processes are depicted in Figure 2.1. The analysed processes are produced via the quartic gauge boson vertex, shown in Figure 2.1(a), as well as via triple gauge boson coupling in association with a radiated photon, shown in Figure 2.1(b), and via radiation processes only, shown in Figure 2.1(c).

In this thesis, the *semi-leptonic* decay channel is analysed, where one W boson decays into a lepton-neutrino pair and the other W or Z boson decays hadronically into a pair of quarks. Due to the colour confinement of the quarks, the decay products of the hadronically decaying W or Z bosons produce collimated sprays of particles, which are reconstructed as so-called *jets* (j). Jet definitions are discussed in more detail in Section 5.1. The semi-leptonic decay channel is chosen over the *fully-leptonic* one, where both heavy gauge bosons decay leptonically, since the branching ratio of the W and Z bosons into hadrons is about a factor of 2.3 higher than the branching ratio into leptons [35]. Through this thesis, the sum of the two final states $WW\gamma$ and $WZ\gamma$ is referred to as $WV\gamma$, where the V denotes one hadronically decaying W or Z boson. The production cross section of the $WV\gamma$ production is $\sigma_{WV\gamma} = (2.29 \pm 0.06)$ fb in the analysed phase space and derived using the VBFNLO generator [36–39]. A detailed explanation how this cross section is derived is given in Section 8.3. In Figure 2.2, several cross section measurements of the ATLAS Collaboration are shown, for different centre-of-mass energies with different corresponding integrated luminosities. The production cross section of the $WV\gamma$ process would be located at the bottom right corner of the figure and is more than fourteen order of magnitude smaller than the total pp cross section. The cross section for the $WW\gamma$

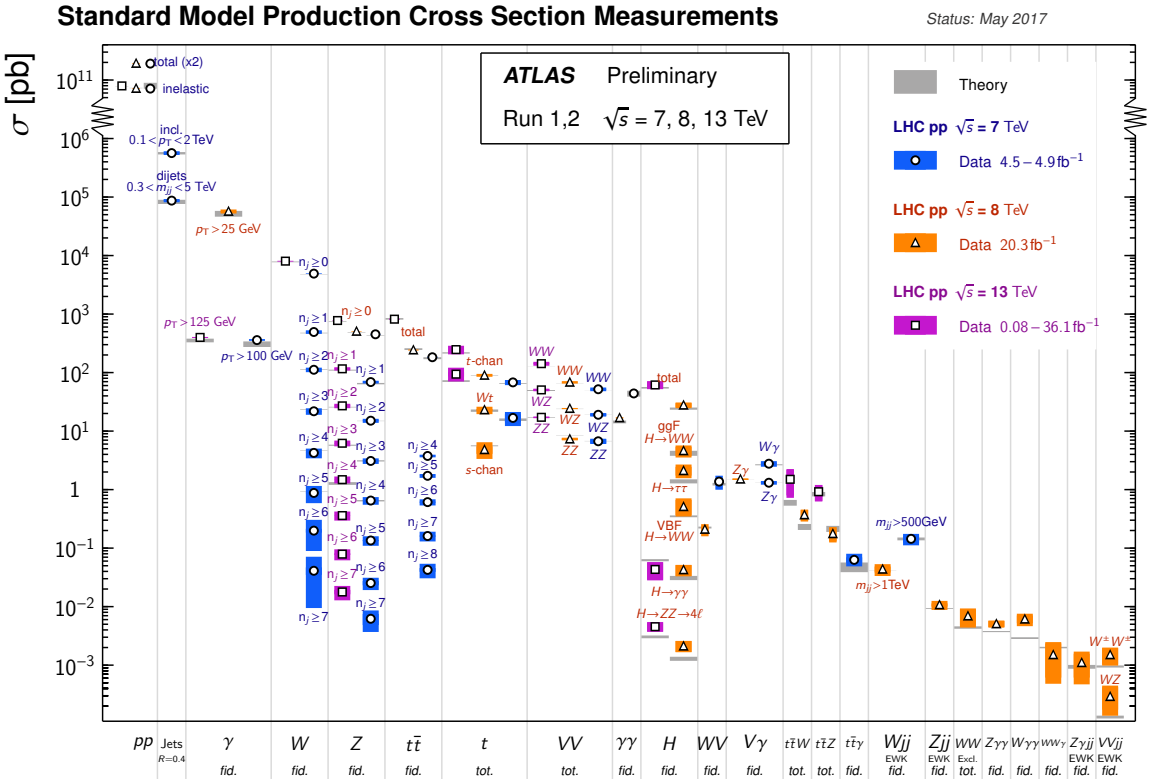

Figure 2.2.: Overview of several Standard Model cross section measurements by the ATLAS Collaboration at different centre-of-mass energies and corresponding integrated luminosities, indicated by different colours. The cross sections are corrected for leptonic branching fractions and compared to theoretical predictions. The uncertainties on the theoretical predictions are illustrated as grey bands. Taken from Reference [40].

process shown in the figure is determined using the fully-leptonic decay channel $WW\gamma \to e\nu\mu\nu\gamma$. The experimental challenges of the semi-leptonic decay channel are the small signal production cross section and large background contributions.

As described above, final states containing two heavy gauge bosons and a photon are generated via different production modes, for example via the quartic vertex, via WV production in association with a photon or via radiation processes only. A quantification of the contribution of the production mode via the quartic vertex to the total cross section expectation is not gauge invariant and therefore meaningless. The behaviour of the photon radiation is studied using the invariant mass distribution of the lepton, neutrino and photon system, $m_{\ell\nu\gamma}$, and the invariant mass distribution of the two jets and the photon, $m_{\mathrm{jj}\gamma}$. These two distributions are shown in Figure 2.3 at next-to-leading order accuracy using VBFNLO, in the analysed fiducial phase space defined in Section 8.1. The $m_{\ell\nu\gamma}$ distribution in Figure 2.3(a) has a sharp peak at the W boson mass $m_W = 80\,\mathrm{GeV}$ arising from events where the lepton radiates a photon, which carries away a part of the transverse momentum of the W boson. In the continuum above the W boson mass the photons originate from other sources. The fraction of events where the photon arises from radiation off the lepton from the W boson decay compared to the total number of events is about 11 %.

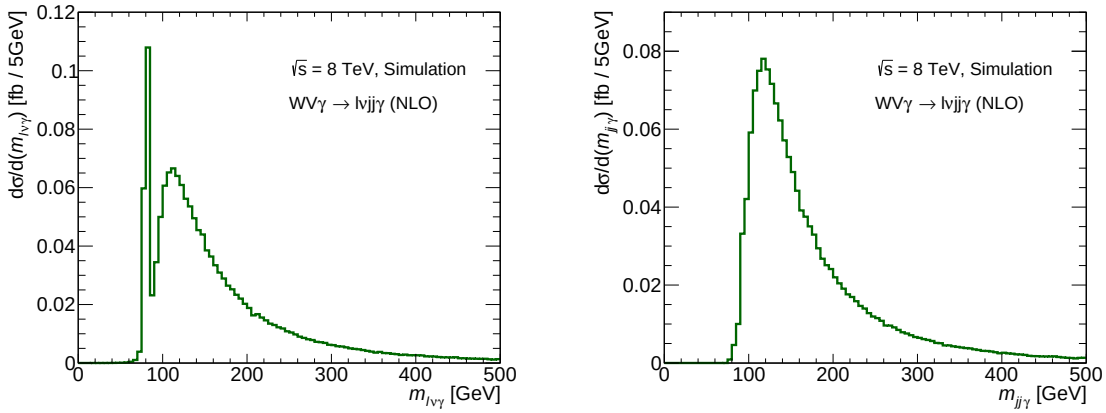

(a) **(b)**

Figure 2.3.: Invariant mass of (a) the lepton, neutrino and photon $m_{\ell\nu\gamma}$ and (b) the two jets and the photon $m_{\mathrm{jj}\gamma}$.

To estimate the number of events where the photon is radiated off a quark from the V boson decay, the $m_{\mathrm{jj}\gamma}$ distribution is used, shown in Figure 2.3(b). No peak is visible at the mass resonances of the W and Z bosons and only about 1 % of the events fall within this mass window. This is due to the lower electric charge of the quarks ($\pm 1/3$ or $\pm 2/3$) in comparison to the electric charge of the leptons (± 1), which leads to a lower probability to radiate a photon. In addition, stringent selection criteria are required for the fiducial region, leading to a significant reduction of the phase space region where an additional photon can be radiated off quarks from the V boson decay. One of these selection criteria is the requirement on the invariant dijet mass of $70\,\mathrm{GeV} < m_{\mathrm{jj}} < 100\,\mathrm{GeV}$. Removing this requirement leads to an increase of the number of events where a photon is radiated off a quark from the V boson decay by more than a factor of four. The number of events, where the photon is radiated off the lepton from the W boson decay is not influenced by the criterion on the invariant dijet mass. In summary, in about 11 % of the events the photon is radiated off the lepton arising from the W boson decay and in only 1 % of the events the photon is radiated off one of the quarks arising from the V boson decay.

2.3. Anomalous Quartic Gauge Couplings

The non-abelian $\mathrm{SU}(2)_L \times \mathrm{U}(1)_Y$ gauge structure of the Standard Model allows triple and quartic self-interactions of the electroweak gauge bosons. The strength of the interaction is determined by the electromagnetic coupling constant and the Weinberg angle, as shown in Equation 2.11. New physics phenomena, not described in the Standard Model, can modify the coupling, for example by introducing a new heavy boson, which modifies the Standard Model gauge boson couplings. This modified triple and quartic self-interactions are called *anomalous Triple Gauge Couplings* (aTGC) and *anomalous Quartic Gauge Couplings* (aQGC), respectively and are a unique way to search for new physics Beyond the Standard Model (BSM). Anomalous gauge couplings are an indirect way to search for new physics, as potentially new particles would modify the coupling via virtual corrections. Since potentially new particles are not produced on their mass-shell, higher energy regimes can be tested with this approach in contrast to direct searches, where potentially new particles are produced on their mass resonances.

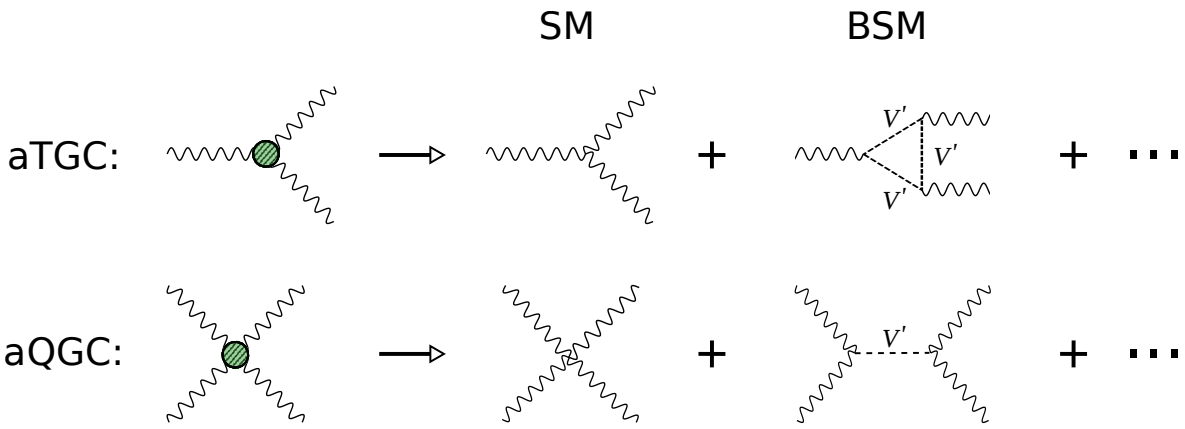

Figure 2.4.: Feynman diagrams involving a new heavy boson, V', in a physics scenario beyond the Standard Model. The effective field theory describes a contact interaction (left side) depicted by the green circle. Once the energy is high enough, the underlying structure of the new physics scenario can be resolved (right side): in addition to the Standard Model coupling, the new heavy boson V' could appear at loop level in aTGCs (top) and at tree level in aQGCs (bottom).

Probing anomalous quartic gauge couplings provides a search for new physics, which is complementary to the search of anomalous triple gauge couplings. The production cross section of triboson processes is in general lower than the production of diboson processes but nevertheless, new physics effects could have a greater impact on aQGCs than on aTGCs. If, for example a new heavy boson appears as new physics and modifies the triple and quartic gauge boson couplings. The triple gauge boson couplings would be modified only at loop level, in contrast to quartic gauge boson couplings, which would be modified at tree level. Therefore, the effect is suppressed for aTGCs and even though the production cross section is larger for diboson processes, equal or even more sensitivity to this type of new physics can be achieved with triboson measurements [41]. This is illustrated in Figure 2.4 with examples of Feynman diagrams. The effective field theory describes a contact interaction on the left side and is illustrated by the green circle. Once the energies are high enough to resolve the vertex, leading order contributions in the quartic gauge coupling are visible (bottom) but only next-to-leading order contributions in the triple gauge coupling (top), in addition to the Standard Model contribution.

In this thesis, the $WV\gamma$ measurement is also used to search for anomalous quartic gauge couplings or constrain them, in case no deviation from the Standard Model is observed. The anomalous quartic gauge couplings are introduced in the framework of an *Effective Field Theory* (EFT), which is a model independent approach without any assumptions on explicit theories or underlying physics. The concept of the effective field theory approach is discussed briefly, following the descriptions in References [42, 43].

The effective Lagrangian, $\mathcal{L}_{\text{EFT}}$, describes the new interactions, caused by the anomalous quartic gauge couplings, and is required to restore the Standard Model in the low energy limit. Thus, it is the sum of the Standard Model Lagrangian, $\mathcal{L}_{\text{SM}}$ and the Lagrangian for the anomalous quartic gauge couplings $\mathcal{L}_{\text{aQGC}}$, using operators of higher mass dimensions, $\mathcal{O}$:

$$\begin{aligned} \mathcal{L}_{\text{EFT}} &= \mathcal{L}_{\text{SM}} + \mathcal{L}_{\text{aQGC}} \\ &= \mathcal{L}_{\text{SM}} + \sum_{d>4} \sum_{i} \frac{f_i}{\Lambda^{d-4}} \mathcal{O}_i^{(d)} \end{aligned} \tag{2.12}$$

where d is the mass dimension, Λ is the scale of new physics and f_i is the effective coupling for the operator $\mathcal{O}_i^{(d)}$ at a given mass dimension. The new physics scale, for example the mass of the new particle, can be between a few TeV and the Planck scale. The lower dimensional operators dominate the effective interaction, since higher mass dimensions are suppressed by increasing powers of the new physics scale Λ, when Λ is below the tested energy scale. Operators with odd mass dimensions are excluded in order to conserve lepton and baryon numbers [42]. Thus, the largest new physics contributions are expected to arise from dimension six operators, which modify the quartic gauge boson couplings as well as the triple gauge boson couplings. Since diboson processes have typically a higher production cross sections than triboson final states, they are more sensitive to the dimension six operators and can set more stringent limits. In addition, the dimension six operators cannot generate all possible quartic gauge couplings: neutral vertices, for example, are not described. The lowest mass dimension, which generates all quartic gauge couplings and modifies only couplings including four or more electroweak gauge bosons, is dimension eight. Therefore, the $WV\gamma$ analysis uses dimension eight operators to search for new physics.

The dimension eight operators are constructed from the covariant derivative of the Higgs field $D_\mu\Phi$ and the field strength tensors $W^a_{\mu\nu}$ and $B_{\mu\nu}$ of the $\mathrm{SU}(2)_L$ and $\mathrm{U}(1)_Y$, respectively. Operators constructed from the covariant derivative of the Higgs field and the field strength tensors are called $\mathcal{O}_M$ and operators constructed only from the field strength tensors are referred to as $\mathcal{O}_T$. This yields 18 genuine dimension eight operators [42] of which the $WV\gamma$ process is sensitive to 14. The effective Lagrangian used for the analysis of final states containing $WV\gamma$ is given by:

$$\mathcal{L}^{\mathrm{EFT}} = \mathcal{L}^{\mathrm{SM}} + \sum_j \frac{f_{M,j}}{\Lambda^4}\mathcal{O}_{M,j} + \sum_k \frac{f_{T,k}}{\Lambda^4}\mathcal{O}_{T,k} \tag{2.13}$$

where $j \in [0, ..., 7]$ and $k \in [0, 1, 2, 5, 6, 7]$. The complete list of all 14 operators considered in the analysis is given in Appendix A.2.

Unitarisation

One of the most famous examples of an effective theory is Fermi's interaction, a theory to explain the beta decay [44] in 1933. In this theory, the beta decay is described as a point-like interaction of four particles $n \to pe^-\bar{\nu}_e$ and at that time, it successfully described the observations. However, in this theory the cross section depends quadratically on the interaction energy, leading to very large cross sections with increasing energies. This behaviour violates perturbative unitarity, as the probability to produce a particle becomes larger than one at tree level. Today it is known from the electroweak sector of the Standard Model that the W boson, as the force carrier of the weak interaction, is responsible for the beta decay. With this knowledge, the four-point interaction in Fermi's theory transforms into two three-point interactions with the W boson as mediator. Fermi's theory describes the observations at energies below the W boson mass well, but when the centre-of-mass energy approaches the W boson mass, the results become meaningless, as the effective field theory is not valid any more.

This example shows that effective field theories are powerful tools, but only as long as the tested energy scale, $\hat{s}$, is far below the new physics scale, Λ. When the tested energy scale approaches Λ, the higher order operators cannot be neglected any more, as their contributions become large, leading to unitarity violations. To remove kinematic regions where the effective field theory is

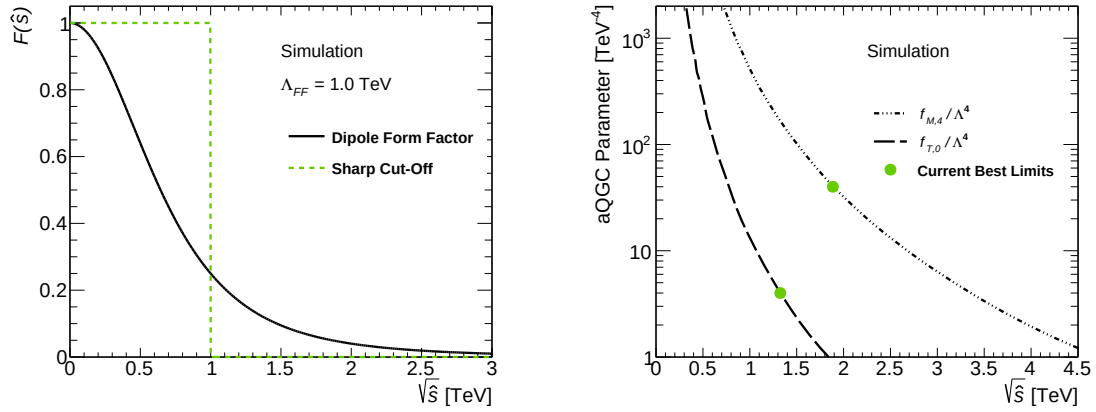

(a) (b)

Figure 2.5.: Comparison of a sharp cut-off and a dipole form factor with $\Lambda_{FF} = 1.0\,\text{TeV}$ in (a) and the unitarity bounds in (b) for the $f_{M,4}$ and the $f_{T,0}$ parameters and the current best limits [17, 18].

not valid any more, a so-called *form factor*, $\mathcal{F}(\hat{s})$, which depends on the energy scale of the interaction, $\hat{s}$, is introduced. The coupling f_i is modified via:

$$f_i \to \mathcal{F}(\hat{s}) \cdot f_i \tag{2.14}$$

and enforces a damping of the coupling strength. The simplest choice for a form factor is a sharp cut-off such that no contributions are allowed above a specific energy scale. This can be described using the Heaviside function and the so-called *form factor scale*, Λ_{FF}, which defines the cut-off:

$$\mathcal{F}(\hat{s}) = \Theta(\Lambda_{FF}^2 - \hat{s}). \tag{2.15}$$

Another theoretically equally well motivated choice, which is often employed, is the so-called *dipole form factor*:

$$\mathcal{F}(\hat{s}) = \left(1 + \frac{\hat{s}}{\Lambda_{FF}^2}\right)^{-2}. \tag{2.16}$$

Figure 2.5(a) illustrates the sharp cut-off and the dipole form factor for $\Lambda_{FF} = 1.0\,\text{TeV}$. Compared to the sharp cut-off, the dipole form factor allows for a smoother damping and a larger reach of the interaction energy scale $\sqrt{\hat{s}}$. Nevertheless, the choice of the form factor is arbitrary and none of the options is intrinsically preferred. The main disadvantage with using form factors is the dependence on the form factor scale Λ_{FF}, which introduces a model dependence into the otherwise model independent effective field theory approach.

To test if unitarity is violated at the energies obtained at the LHC, the form factor tool provided by the VBFNLO authors is used, which has a dipole form factor implemented. This tool calculates the maximal value of Λ_{FF} that still conserves unitarity for all energies up to $\sqrt{\hat{s}} = 8\,\text{TeV}$, by performing a partial wave decomposition of the scattering matrix from on-shell vector boson scattering, $VV \to VV$ where $V \in \{\gamma, W, Z\}$. Unitarity is conserved when the absolute value of the real part of the zeroth partial wave of the amplitude is below 0.5 [45]. For the calculations, the VBFNLO tool uses two-to-two processes, but it is not ensured that values obtained with this method are also correct for triboson production, which are one-to-three processes. Since no algorithms are available to determine the form factor scale for triboson processes, the tool is

used nevertheless. Therefore, the results obtained with the VBFNLO form factor tool shown in this thesis, are no precise evaluations of the unitarity bounds but rather provide an estimate of the scales.

The unitarity bounds for two different aQGC parameters, $f_{M,4}/\Lambda^4$ and $f_{T,0}/\Lambda^4$, are depicted in Figure 2.5(b), as a function of the effective energy transfer of the hard interaction $\sqrt{\hat{s}}$. The current best limits on the aQGC parameters are indicated by the green markers. Coupling values above these limits are excluded by experimental constraints. The regions towards higher values of $\sqrt{\hat{s}}$ and above the curves, violate unitarity. The resulting unitarity bound for the current best limits is at 1.9 TeV for the $f_{M,4}$ parameter and at 1.3 TeV for the $f_{T,0}$ parameter. As the effective field theories might not be valid any more at interactions energies below 8 TeV, unitarisation can be an issue at energies accessible at the LHC. Therefore, unitarisation is considered in the limit setting of the $WV\gamma$ analysis.

In summary, the effective field theory is used to parametrise new physics in a model independent way. It provides a framework to probe new physics by setting limits on the ratio of the anomalous quartic coupling parameters and the energy scale f_i/Λ^4. However, this yields only meaningful results as long as the tested energy scale is below the new physics scale and the effective field theory does not violate perturbative unitarity. As unitarity violation can occur at energies accessible at the LHC, both unitarised limits, using a dipole form factor, and non-unitarised limits are derived in this thesis. Since no tool is available to provide strictly valid values for one-to-three processes, three different form factor scales Λ_{FF} have been chosen arbitrarily for this analysis, namely 0.5 TeV, 1 TeV and ∞, where the latter one corresponds to the non-unitarised case.

3. LHC and ATLAS Detector

This thesis analyses data from proton−proton collisions, produced by the Large Hadron Collider (LHC) at CERN in Geneva, Switzerland, and recorded with the ATLAS detector in 2012. This chapter discusses the experimental setup, which was used to collect the data. In Section 3.1, the accelerator complex is introduced, and the LHC is described in greater detail. The layout of the ATLAS detector is discussed in Section 3.2, along with detailed descriptions of the inner detector, the calorimeters and the muon spectrometer, as well as the trigger system and the luminosity measurement.

3.1. Large Hadron Collider

The *Large Hadron Collider* (LHC) [46], hosted at CERN[2], is the most powerful particle accelerator in the world. It is located in a tunnel with a circumference of 27 km around 100 m underground, re-using the existing tunnel from LEP[3], the predecessor of the LHC at CERN. The LHC accelerates protons and heavy ions, such as lead ions. Since the proton−proton operation mode is relevant for this analysis it is discussed in the following. Two proton beams, one clockwise and the other counter-clockwise, are made to circulate in the tunnel in separate beam pipes, sharing the same mechanical structure with a common cooling system and return yoke of the magnets. The LHC has been running since 2009 and has delivered pp data at centre-of-mass energies of $\sqrt{s} = 7\,\text{TeV}$, $\sqrt{s} = 8\,\text{TeV}$ and $\sqrt{s} = 13\,\text{TeV}$. Its design centre-of-mass energy of $\sqrt{s} = 14\,\text{TeV}$ is planned to be reached in the coming years.

The LHC has four locations at which the two beams intersect and these define the interaction points of the four main experiments: ATLAS[4], ALICE[5], CMS[6] and LHCb[7]. ATLAS and CMS are multi-purpose detectors, designed to not only accurately measure Standard Model processes but also search for new physics scenarios beyond the Standard Model. The ALICE detector is dedicated to heavy ion physics and the study of quark gluon plasma, a new state of matter where quarks and gluons are deconfined. LHCb is a forward spectrometer, specialised to study the decay of rare hadrons including bottom or charm quarks, for high precision measurements of CP violation.

The protons for the LHC are produced from hydrogen gas, where the electrons are stripped off the nucleus with an electric field. Afterwards, the protons are accelerated to the collision energy in steps using several pre-accelerators, as illustrated in Figure 3.1. The accelerator complex includes the linear accelerator LINAC2, the booster, the Proton Synchrotron (PS) and the Super

[2] *European organisation for nuclear research*, Geneva Switzerland.
[3] *Large electron-positron collider.*
[4] *A toroidal LHC Apparatus.*
[5] *A large ion collider experiment.*
[6] *Compact muon solenoid.*
[7] *Large hadron collider beauty.*

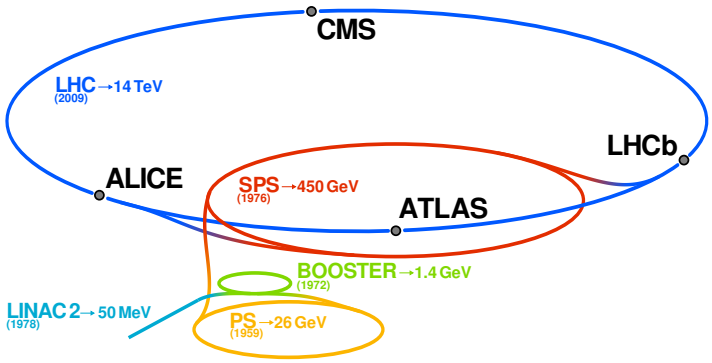

Figure 3.1.: The LHC and its four main experiments ATLAS, ALICE, CMS and LHCb. Also shown is the pre-accelerator complex along with the year of first operation and the final beam energies reached at each stage. Taken from Reference [47].

Proton Synchrotron (SPS), before the protons are finally injected into the LHC and accelerated to collision energy. One complete turnaround time from the production of the protons to the final collision energy takes about two hours.

To accelerate the protons, the LHC uses superconducting radio frequency (RF) cavities with an electric field of 2 MV and an oscillation frequency of 400 MHz. As a consequence, the proton beam is not continuous but structured into bunches, each containing about 10^{11} protons. In order to keep the protons on the ring-trajectory, 1232 superconducting dipole magnets are used providing a magnetic field of 8.3 T. Their operation temperature is 1.9 K, obtained via liquid helium cooling. To focus the beam in vertical and horizontal direction, 858 superconducting quadrupole magnets are installed at the LHC. Before the ATLAS interaction point, the beams are focussed to 16 µm in the vertical and horizontal direction. This increases the *instantaneous luminosity*, which quantifies how many particle interactions occur per area and time:

$$L_{\text{inst}} = \frac{n_b \cdot f_r \cdot n_1 \cdot n_2}{A} \tag{3.1}$$

where n_b is the number of colliding bunch pairs, f_r is the revolution frequency, $n_{1/2}$ is the number of protons in the two beams and A is the cross-section area of the beams. During a run, the instantaneous luminosity decreases over time, as the number of particles in the beams decreases due to the collisions. The design instantaneous luminosity of the LHC of $10^{34}\,\text{cm}^{-2}\,\text{s}^{-1}$ was reached in 2016 and even exceeded by 50 %. High luminosities are advantageous for processes with small cross sections, such as Higgs production, as many collisions are necessary in order to collect a statistically significant sample. However, high luminosities also provoke several proton−proton collisions in one bunch crossing, an effect called *pileup*, and one of the major challenges for the experiments at the LHC. The luminosity collected over a specific time interval, is referred to as *integrated luminosity*:

$$L_{\text{int}} = \int L_{\text{inst}}\, dt. \tag{3.2}$$

The proton−proton collisions at a centre-of-mass energy of $\sqrt{s} = 8\,\text{TeV}$ corresponding to an integrated luminosity of $20.2\,\text{fb}^{-1}$ analysed in this thesis, were recorded in the year 2012 with the ATLAS detector. On average, about 21 interactions per bunch crossing were observed with the 2012 run conditions.

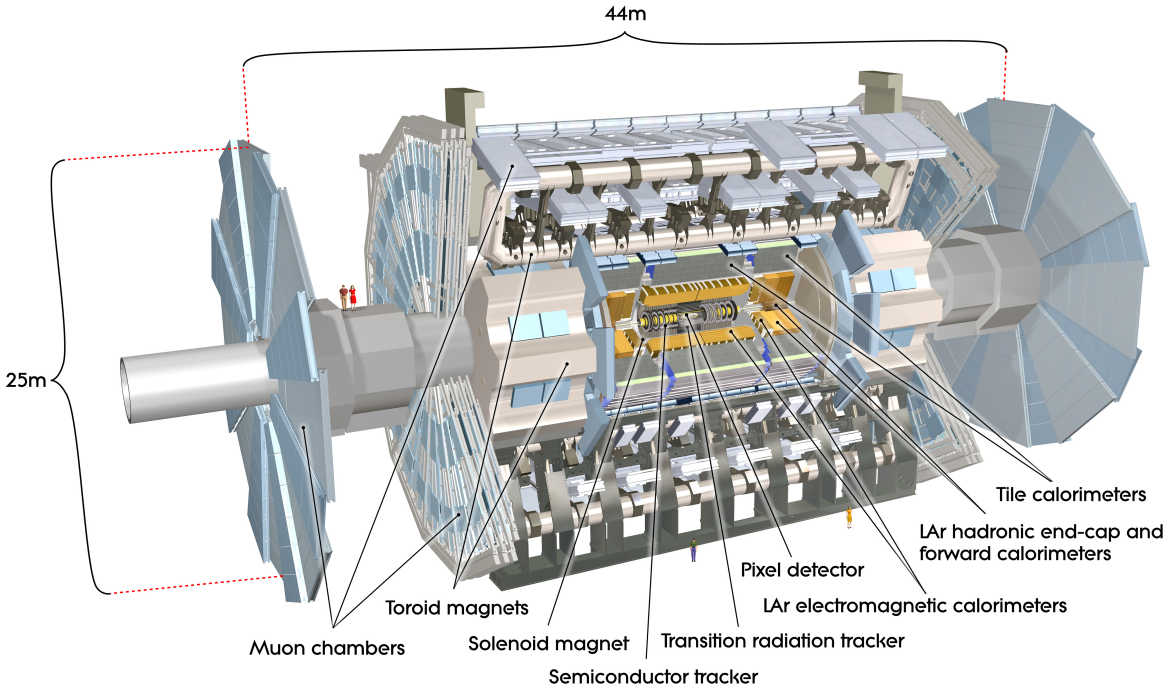

Figure 3.2.: Overview of the ATLAS detector and its sub-systems. The total length and the diameter are indicated as well as two persons for proportion. Taken from Reference [48].

3.2. ATLAS Detector

The design of the ATLAS detector is driven by a set of benchmark processes, which define the needed performances of the sub-systems. One of the benchmark processes is the search for the Higgs boson, which was finally discovered in 2012 by the ATLAS and the CMS Collaborations [7, 8]. In addition, many other benchmark processes are defined, covering a broad spectrum of the ATLAS physics program, such as searches for new, heavy gauge bosons, for supersymmetric particles or for extra dimensions. These benchmark processes, define several requirements on the detector: a precise tracking system with a high momentum resolution for charged particles and the ability to reconstruct secondary vertices, good electromagnetic and hadronic calorimeters with large coverage and fine granularity for energy measurements and particle identification as well as a system to efficiently reconstruct and identify muons. In addition, technical demands influence the detector design: The unprecedented high energies, particle multiplicities and interaction rates, provided by the LHC, required radiation-hard sensors and electronics, as well as a highly efficient and fast trigger system, to select the most interesting processes while rejecting uninteresting ones. Following these prerequisites, the ATLAS collaboration, consisting of more than 3000 physicists from 38 countries, designed and constructed the ATLAS detector [48].

The reference coordinate system of the ATLAS detector is a right-handed, orthogonal coordinate system with its origin at the interaction point. The x-axis points to the centre of the LHC ring, the y-axis points upwards and the z-axis along the beam line. The azimuthal angle ϕ is defined as the angle in the plane orthogonal to the beam line and the polar angle θ as the

angle from the beam line. The pseudorapidity η is defined as $\eta = -\ln\tan(\frac{\theta}{2})$ and the rapidity as $y = \frac{1}{2}\ln\frac{E+p_z}{E-p_z}$, which is often employed for jets. The distance between two objects in η-ϕ is defined as $\Delta R = \sqrt{(\eta_1-\eta_2)^2+(\phi_1-\phi 2)^2}$. Transverse variables, such as the transverse momentum p_{T}, the transverse energy E_{T} or the transverse missing energy $E_{\mathrm{T}}^{\mathrm{miss}}$, are defined as the projections into the x-y plane.

An overview of the ATLAS detector is shown in Figure 3.2. It consists of three major subsystems, arranged from inside out concentrically around the beam axis: the inner detector, the calorimeters and the muon spectrometer. The layout is completed with a magnet system comprising a solenoid magnet, immersing the inner detector in a magnetic field and three toroid magnets, providing a magnetic field for the muon system. Eight large toroid magnets in the barrel region dominate the appearance of the ATLAS detector. In total the ALTAS detector has a weight of 7 000 tons, a length of 44 m and a height of 25 m. After the first data taking campaign from 2009 to the end of 2012, the ATLAS detector underwent a series of upgrades in the years 2013 and 2014. This thesis presents a study, which is carried out using data collected in the year 2012 and therefore, the design and layout of the ATLAS detector, described in the following, refers to its status in 2012.

3.2.1. Magnets

Two different magnet systems are incorporated into ATLAS: a superconducting solenoid provides a magnetic field in the inner detector to deflect charged particles, and a superconducting toroidal magnet system, deflects muons in the muon spectrometer. The curvature of the trajectory, induced by the magnetic field, is used for the momentum measurement of the particles. Both magnet systems operate at a temperature of about 4.5 K and are illustrated in Figure 3.3, along with the hadronic calorimeter. The solenoid surrounds the inner detector and is located in front of the calorimeters. To minimise the energy loss before the calorimeters, the solenoid is designed to be thin, corresponding to a radiation length of $0.6\,\mathrm{X}_0$. The radiation length X_0 is defined as the average distance an electron traverses in a medium, until it has lost all but $1/e$ of its initial energy. The solenoid immerses the inner detector in a magnetic field of 2 T, parallel to the beam axis. The air-cored toroid magnets consist of one barrel and two end-caps, surrounding the calorimeters. The barrel consists of eight coils, which are arranged symmetrically around the beam axis and provide a magnetic field of about 0.5 T in a region of $|\eta| < 1.4$, bending the muons in the R-ϕ plane. The end-caps are interleaved at either end with the barrel magnets and provide a magnetic field of about 1 T in the region $1.6 < |\eta| < 2.7$. In the overlap region $1.4 < |\eta| < 1.6$, the magnetic field is a superposition of the magnetic fields produced by the barrel and the end-caps.

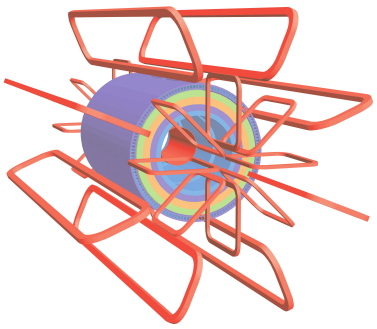

Figure 3.3.: The magnet system of the ATLAS detector is illustrated in red, along with the tile calorimeter, which provides the return yoke at the outermost layer. Taken from Reference [48].

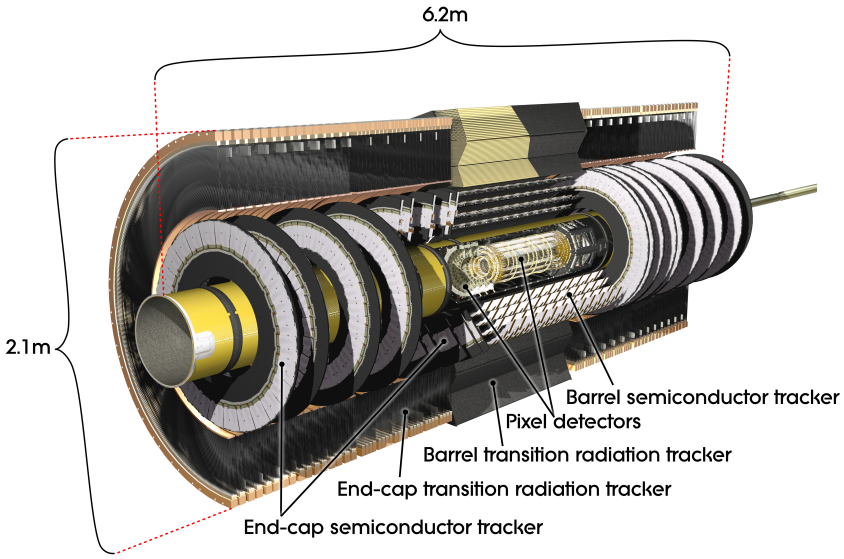

Figure 3.4.: The inner detector of the ATLAS experiment with the three main components the Silicon Pixel Detector, the Silicon Microstrip Tracker (called Semiconductor Tracker in the figure) and the Transition Radiation Tracker. Taken from Reference [48].

3.2.2. Inner Detector

The inner detector (ID) is used for precise track measurements of charged particles and covers a range of $|\eta| < 2.5$. As it is immersed in the 2 T magnetic field of the solenoid, the trajectories are curved, allowing the determination of the momentum of the particles. The inner detector can resolve secondary vertices, arising from the decay of long lived particles, such as B-mesons, and it provides electron identification for electrons with a transverse momentum between 500 MeV and 150 GeV within $|\eta| < 2.0$. Three individual components are part of the inner detector, starting from inside out: the *Silicon Pixel Detector*, the *Silicon Microstrip Tracker* and the *Transition Radiation Tracker* (TRT). Each of the three sub-systems consists of a central barrel with a cylindrical geometry arranged concentric around the beam axis and end-caps, realised as wheels, which are arranged orthogonal to the beam axis to cover the forward region. Figure 3.4 shows the layout of the inner detector and its three sub-components. The total length of the inner detector is about 6.2 m and a diameter of 2.1 m. For noise suppression, the silicon detectors are operated at temperatures between −5 °C and −10 °C.

The pixel detector comprises three layers in the barrel and three discs as end-caps on either side. The first pixel layer is closest to the interaction point with a minimal distance of 5 cm. In order to allow the reconstruction of secondary vertices, a high granularity is needed close to the interaction point. Thus, the pixel sensors have an area of $50 \times 400\,\mu\text{m}^2$ with an intrinsic accuracy of 10 µm in $R - \phi$ and 115 µm in z-direction (R-direction) in the barrel (end-cap) region. More than 80 million channels are needed for the readout of the pixel detector.

The silicon microstrip detector comprises four stereo layers of silicon microstrips in the barrel and nine discs as end-caps in forward direction on either side. Each stereo layer has silicon microstrips with a size of 80 µm×64 mm, on both sides, arranged back-to-back and with an angle of 40 mrad between them. Due to the angle between the silicon microstrips in each layer, the two coordinates ϕ and z (ϕ and R) can be measured in the barrel (end-cap). The provided intrinsic

accuracy is 17 µm in $R-\phi$ and 580 µm in z-direction (R-direction) in the barrel (end-cap) region. More than 6 million channels are needed to read out the silicon microstrip detector.

The transition radiation tracker only covers the region of $|\eta| < 2.0$ and provides additional hits for the track measurement. It is made up of straw tubes with a diameter of 4 mm and a length of 144 cm (37 cm) in the barrel (end-cap), filled with a gas mixture of xenon, carbon dioxide and oxygen. In the middle of the tube a gold-plated tungsten wire with a diameter of 31 µm is used as an anode. In the barrel region, the straws are arranged parallel to the beam axis and in the end-caps radially to it, providing around 36 additional hits per track. Only coordinates in the R-ϕ are measured with an intrinsic accuracy of 130 µm. In total, the transition radiation tracker has about 351000 readout channels. Besides its functionality to measure the tracks of charged particles, the transition radiation tracker can also identify electrons. The area between the straw tubes is filled with polypropylene, a material which causes particles to emit low energy *transition radiation* photons. These transition radiation photons are absorbed by the xenon gas mixture in the straw tubes and thus also produce a signal in the detector. The amount of transition radiation produced by a particle is proportional to $1/m$, where m is the mass of the particle. Hence lighter particles, such as electrons, generate more transition radiation than heavier particles, such as hadrons. In this way electrons can be separately identified. Signals arising from transition radiation are typically higher than tracking signals and are distinguished on a straw-by-straw basis, using a high and a low threshold criteria.

The momentum resolution of the inner detector is measured in 7.6 million cosmic ray events and found to be $\frac{\sigma_{p_\mathrm{T}}}{p_\mathrm{T}} = (4.83 \pm 0.16) \times 10^{-4}\,\mathrm{GeV}^{-1} \times p_\mathrm{T}$ [49]. In the same study, the resolutions of the longitudinal and transversal impact parameters are measured to be (22.1 ± 0.9) μm and (112 ± 4) μm, respectively [49].

3.2.3. Calorimeter

The calorimeters are used to provide a measurement of the energy of charged and neutral particles as well as their direction. Also, the determination of the transverse energy strongly relies on the energy measurements of the calorimeters. In addition, the information from the calorimeters is used for particle identification, as different particles exhibit different shower characteristics. Two different calorimeter types are employed: the electromagnetic (EM) and the hadronic (HAD) calorimeter, where the first one is optimised for showers induced by electrons and photons and the latter one for showers induced by hadronic objects. To provide a good spacial resolution, both calorimeter types are segmented in longitudinal and transverse directions. The electromagnetic calorimeter is surrounded by the hadronic calorimeter and both calorimeters are divided into a central barrel region and two end-cap regions. These regions overlap to ensure a good coverage over the pseudorapidity range. However, for the very forward region $|\eta| > 3.1$, a dedicated *Forward Calorimeter* (FCal) is used. The electromagnetic, hadronic and forward calorimeters of the ATLAS detector are shown in Figure 3.5.

For the precise energy measurement of particles, the full shower of the incident particle must be contained within the calorimeter. In order to build a relatively small and compact detector, ATLAS uses *sampling calorimeters*, where layers of active and absorber material alternate. The absorber material induces showering when particles interact with it, a process during which additional particles are produced. These additional particles are measured in the active material layers. The electromagnetic calorimeter uses liquid argon (LAr) as active material and lead as absorber, in the barrel and the end-cap regions. In contrast, the hadronic barrel uses scintillating

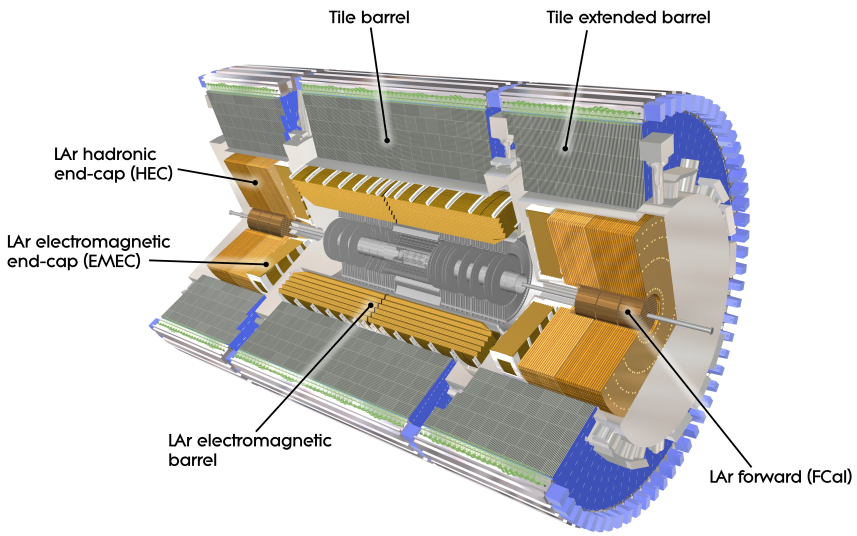

Figure 3.5.: Overview over the ATLAS calorimeters including the electromagnetic, hadronic and forward calorimeter. Areas coloured in gold are calorimeter components using liquid argon (LAr) as active material and in grey the calorimeter components using tiles. Taken from Reference [48].

tiles as active material and steel as absorber whereas the hadronic end-cap regions also use liquid argon as active and copper as absorber material. The electromagnetic calorimeter has a thickness of more than $22\,X_0$ in the barrel and more than $24\,X_0$ in the end-cap regions. The hadronic calorimeter has a total thickness of 9.7 interaction lengths λ, defined as the average distance of a high energy hadron in a medium, until it lost all but $1/e$ of its initial energy. The calorimeter system has in total more than 192 000 readout channels.

The calorimeter resolution is generically parametrised using:

$$\frac{\sigma_E}{E} = \frac{N}{E} \oplus \frac{S}{\sqrt{E}} \oplus C \tag{3.3}$$

where N accounts for detector and electronics noise, S for statistical fluctuations in the shower development and C for energy losses in non-instrumented regions. Typically, the noise term is dominant at low energies, the statistical term at intermediate energies and the constant term at high energies.

Electromagnetic Calorimeter

The barrel of the electromagnetic calorimeter covers the pseudorapidity range up to $|\eta| < 1.475$ and the two end-caps the region $1.375 < |\eta| < 3.2$. The electromagnetic calorimeter use liquid argon as active material, as it is radiation-hard and exhibits a stable response over time as well as a linear behaviour. The absorber material is lead, as it induces bremsstrahlung and pair production. It is arranged in an accordion geometry, which allows the full coverage over the azimuthal angle ϕ, without any gaps. Kapton electrodes are installed in the middle of the two absorber plates, also following the accordion geometry. The liquid argon is filled in the gap between two absorber plates. In the central region $|\eta| < 2.5$, the electromagnetic barrel is divided

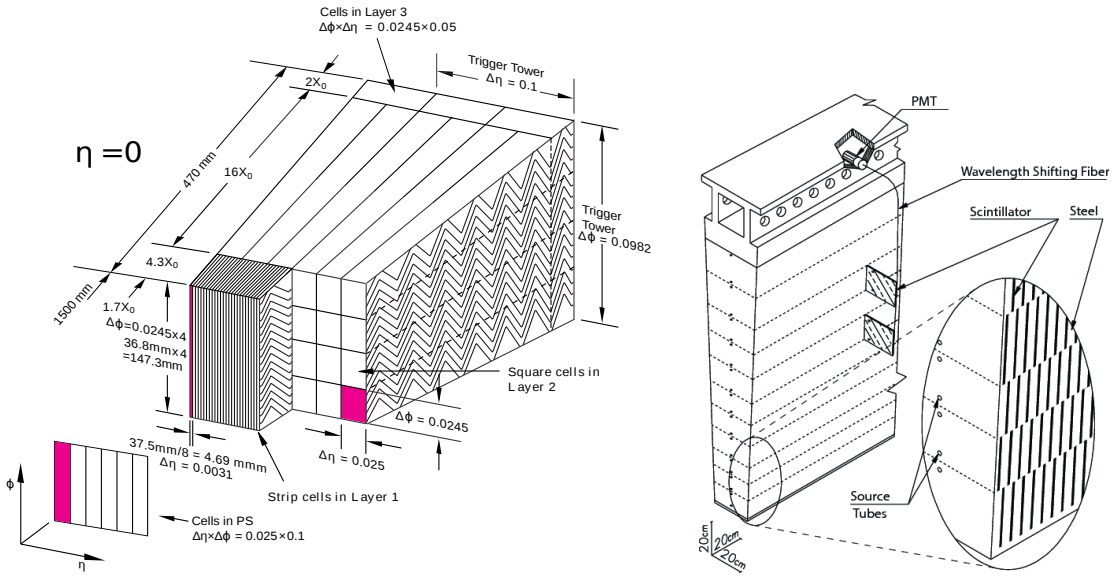

Figure 3.6.: ATLAS electromagnetic calorimeter is illustrated in (a) with its segmentation into strip (Layer 1), middle (Layer 2) and back layer (Layer 3). The accordion shape of the three layers ensures full azimuthal coverage and is indicated in the figure. Also, the presampler (PS) is shown. Typical sizes of a cell in the presampler, strip and middle layer are coloured in pink. Taken from Reference [51]. A module from the ATLAS hadronic calorimeter is shown in (b), using scintillating tiles as active material and steel as absorber. Also shown are the wavelength shifting fibres and the readout via the photomultiplier tubes (PMT). Taken from Reference [48].

longitudinally into the *strip layer*, the *middle layer* and the *back layer*. An overview of the three layers and the accordion structure of the electromagnetic calorimeter is given in Figure 3.6(a). The strip layer is designed with the finest segmentation in $\Delta\eta \times \Delta\phi$ with $0.025/8 \times 0.1$ and has a thickness of 4.3 radiation lengths X_0. Due to the high granularity, this layer can distinguish between isolated photons and π^0, which decay into two photons, due to the slightly different shower shapes. The middle layer is the longest of the three, corresponding to 16 radiation lengths. In general the maximum of the electromagnetic shower is in the middle layer. The segmentation of the middle layer in $\Delta\eta \times \Delta\phi$ is 0.025×0.025 and thus larger than the strip layer. The back layer has the coarsest segmentation of the three layers with 0.05×0.025 $\Delta\eta \times \Delta\phi$ and has a thickness of $2\,X_0$. The end-caps are divided into two segments in the longitudinal direction and have a coarser lateral segmentation than the barrel region. In order to estimate the energy loss of the electrons and photons in the upstream material of the calorimeter, a *Presampler* (PS) is installed in the region $|\eta| < 1.8$, consisting of a thin active liquid argon layer.

The design energy resolution of the electromagnetic calorimeter is $\frac{\sigma_E}{E} = \frac{10\,\%}{\sqrt{E}} \oplus 0.7\,\%$ [48] and was achieved in test beam measurements [50].

Hadronic Calorimeter

The hadronic calorimeter is placed around the electromagnetic calorimeter and comprises a central barrel region $|\eta| < 1.0$ and two extended barrels on each side at $0.8 < |\eta| < 1.7$. In the barrel region, scintillating tiles are used as active material and steel as absorber with a ratio of

the material volumes of 1 : 4.7. In the longitudinal direction it is segmented in three layers with interaction lengths of 1.5 λ, 4.1 λ and 1.8 λ (1.5 λ, 2.6 λ and 3.3 λ) in the barrel (extended barrel), respectively. The scintillating tiles are read out using photomultiplier tubes (PMTs), which are connected to the tiles via wavelength shifting fibres. An approximate projective granularity of 0.1×0.1 in $\Delta\eta \times \Delta\phi$ is achieved, by grouping the fibres accordingly before they are read out by the PMT. Figure 3.6(b) illustrates a tile module with its optical readout.

The hadronic end-cap calorimeters (HEC) cover the region in $1.5 < |\eta| < 3.2$ and each comprises two separate wheels: the front and the rear wheel. Both wheels use liquid argon as active material and copper as absorber, but the volume ratios of active to absorber material differs. In the region of $1.5 < |\eta| < 2.5$, the segmentation in $\Delta\eta \times \Delta\phi$ is 0.1×0.1 and in the region $2.5 < |\eta| < 3.2$ it is slightly larger with 0.2×0.2.

The design resolution of the hadronic barrel and end-cap calorimeter is $\frac{\sigma_E}{E} = \frac{50\,\%}{\sqrt{E}} \oplus 3\,\%$ [48]. Measurements at a test beam are found to be in reasonable agreement with this specifications [52, 53].

Forward Calorimeter

The forward calorimeter is located in the very forward region, covering the range from $3.1 < |\eta| < 4.9$. It is segmented into three layers, where the first one uses copper as absorber and the other two tungsten. In all layers liquid argon is used as active material. The forward calorimeter has a thickness of about 10 interaction lengths. Its design resolution is $\frac{\sigma_E}{E} = \frac{100\,\%}{\sqrt{E}} \oplus 10\,\%$ [48] and was confirmed in test beam measurements [54].

3.2.4. Muon System

The outermost part of the ATLAS detector is covered by the muon spectrometer to measure the momentum of charged particles, which completely traverse the calorimeter system. The muon spectrometer measures the trajectories of charged particles using high-precision tracking chambers: the *Monitored Drift Tubes* (MDT) and the *Cathode Strip Chambers* (CSC) in the region $|\eta| < 2.7$. Additionally, it provides fast triggering on these particles in the region $|\eta| < 2.4$ using the *Resistive-Plate Chambers* (RPC) and *Thin-Gap Chambers* (TGC). In the barrel, the high-precision tracking chambers are mounted in three concentric layers surrounding the calorimeter and placed between and above the eight coils of the toroid magnet. The end-caps consist of three wheels, that are perpendicular to the beam line, placed before and behind the toroid end-cap magnets. The material budget of the air-cored toroidal magnets is minimised to limit multiple scattering of the particles with the magnet material. The first layer of the end-cap, which is closest to the interaction point, within $2.0 < |\eta| < 2.7$, uses cathode strip chambers to cope with the high particle flux. The coverage of the tracking chambers has a small gap in the central barrel region at $\eta \approx 0$, needed for service structures of the inner detector, the calorimeter and the magnets. For the triggering, resistive-plate chambers are used in the barrel region and thin-gap chambers in the end-caps. In addition, they provide measurements of the coordinates in η and a ϕ direction. Figure 3.7 illustrates the geometry of the muon spectrometer.

Each monitored drift chamber contains between three and eight layers of drift tubes. The drift tubes are made of aluminium and have a diameter of 30 mm. They are filled with a gas mixture of argon-carbon dioxide and the anode is a tungsten-rhenium wire with a diameter of 50 µm. These allow for an intrinsic resolution of the monitored drift chambers of 35 µm in the

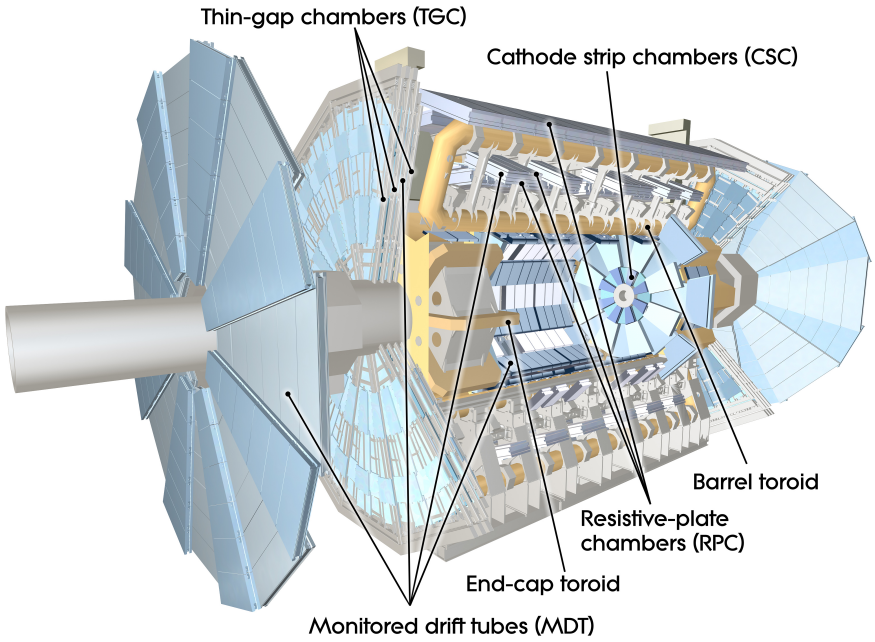

Figure 3.7.: Overview of the ATLAS muon spectrometer. The monitored drift tubes and the cathode strip chambers are used for high-precision measurements of the trajectories of charged particles. Fast triggering on charged particles in the muon spectrometer is provided by the resistive-plate chambers and the thin-gap chambers. Taken from Reference [48].

z-direction. The cathode strip chambers are multiwire proportional chambers, also filled with an argon-carbon dioxide gas mixture, using wires with a diameter of 30 µm serving as anodes. The cathodes are segmented in such a way that the coordinate in R and ϕ can be measured, with accuracies of 40 µm and 5 mm respectively.

The trigger chambers, consisting of the resistive-plate chambers and the thin-gap chambers, provide the tracking information within a few tens of nanoseconds, allowing an efficient triggering on charged particles and the identification of the bunch crossing. The resistive-plate chambers are made of parallel electrode-plates, with an electric field of 4.9 kV/mm in the gap, which is about 2 mm. Charged particles traversing the resistive-plate chambers, ionise the gas between the plates and due to the high electric field, avalanches of secondary particles are created. This setup allows an intrinsic resolution of the resistive-plate chambers of 10 mm in z- and ϕ-direction and an intrinsic time resolution of 1.5 ns. The end-cap region is equipped with thin-gap chambers, which are multiwire proportional chambers filled with highly quenching gas mixture. As the wire-to-wire distance is larger than the wire-to-cathode distance, the chambers can be operated in a quasi-saturated mode. The resolution of the thin-gap chambers is between 2 mm and 6 mm in R and slightly larger in ϕ. The intrinsic time resolution of the thin-gap chambers is about 4 ns.

3.2.5. Trigger System

At design energy and luminosity, the LHC will deliver proton−proton collisions at a rate of 40 MHz with up to several dozen of interactions per bunch crossing. The permanent storage however is limited to an output rate of 200 Hz, which requires a reduction of a factor of 10^6. In

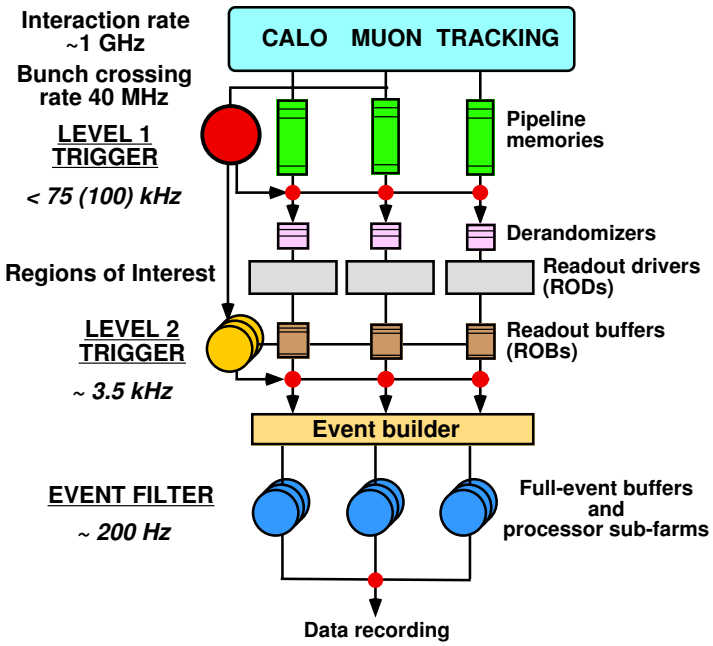

Figure 3.8.: The ATLAS trigger system consisting of Level-1 trigger, Level-2 trigger and Event Filter. At design luminosity, the LHC provides collisions at a rate of 40 MHz, corresponding to an interaction rate of about 1 GHz. The trigger system reduces the rate by more than six orders of magnitude to about 200 Hz. Taken from Reference [55].

addition, many of the interesting physics processes have low production cross sections, placing additional requirements on the trigger system to efficiently select these interesting events while rejecting the uninteresting ones. The ATLAS trigger system consists of three levels that each execute a trigger decision on events passed by the previous level. These are, starting from the first filter: the *Level-1* (L1) trigger, the *Level-2* (L2) trigger and the *Event Filter* (EF). The L1 trigger provides very fast trigger decisions, which is facilitated by the implementation in custom-made hardware and the usage of a coarse detector granularity. The L2 and the Event Filter are software based triggers, running on software farms and employing the full detector granularity. All three levels of the ATLAS trigger system are illustrated in Figure 3.8.

The L1 trigger decision is based on information from the calorimeters as well as from the trigger chambers of the muon spectrometers. It is divided into two sub-components: the L1 calorimeter trigger (L1Calo) and the L1 muon trigger (L1Muon). Events with high energy depositions arising from electromagnetic objects, τ leptons and jets as well as events with high missing transverse energy are identified by the L1 calorimeter trigger and events containing muons with large transverse momenta are identified by the L1 muon trigger. To achieve the timing restrictions, the L1 calorimeter trigger uses a coarser granularity of the calorimeters, provided by so-called *Trigger Towers*, which are the analogue sum of the cell energies in 0.1×0.1 ($\Delta\eta \times \Delta\phi$), indicated in Figure 3.6(a). The L1 calorimeter trigger uses a sliding-window algorithm on these trigger-towers, to search for energy deposits above predefined thresholds, thereby locating so-called *Regions-of-Interests* (ROIs). The L1 trigger decision is based on energy and multiplicity of the objects and is taken within 2.5 µs, reducing the output rate to about 75 kHz. The full event information is hold in buffers until the L1 trigger accepts or rejects the event. At the next trigger level, the L2 trigger, only regions that have been identified as a region-of-interest by the L1 trigger are evaluated. In these regions, the L2 trigger employs the full detector granularity.

The L2 trigger uses advanced algorithms to reconstruct and identify particles, also including tracking information from the inner detector with an average processing time of about 40 ms per event. In total, the L2 trigger reduces the output rate to 3.5 kHz. The final trigger level, the Event Filter, reconstructs the complete event exploiting the full detector granularity using algorithms, which are similar to the algorithms used for the final offline reconstruction of the objects. For the processing of one event, the Event Filter needs on average about 4 s and reduces the final output rate to the required 200 Hz. The total size of an event that is accepted by the trigger system and stored on disc is about 1.3 MByte.

Triggers with low energy thresholds and low multiplicity requirements have the highest acceptance rates, due to the exponentially falling energy spectrum. To ensure that these triggers do not fill up the available disc space, either the threshold criteria are raised, or so-called *prescales* are introduced. Prescales are constant factors defined for and applied to individual triggers, to only select a fraction of the events fulfilling the specialised criteria. The prescale factors vary in order to adapt to changing running conditions, such as the decreasing instantaneous luminosity. However, the prescale factors are constant over a *luminosity block*, a short time interval of about 2 min during which the run conditions are approximately constant. The total luminosity a prescaled trigger collects during a given number of luminosity blocks is:

$$L_{\text{int}} = \sum_{i}^{\text{lumi. blocks}} \frac{L_i}{p_i} \tag{3.4}$$

where L_i is the integrated luminosity and p_i is the prescale in luminosity block i.

3.2.6. Luminosity Measurement

For most physics analyses, the precise measurement of the luminosity is a crucial part of the analysis, as it directly influences cross section measurements, background estimations and sensitivity studies. The luminosity determination in ATLAS is based on the *Beam Conditions Monitor* (BCM) [56] and LUCID[1] [48], both providing a bunch-wise measurement of the instantaneous luminosity. The Beam Conditions Monitor consists of two modules located about 2 m away from the interaction point, on either side along the z-axis and 5.5 cm from the beam line corresponding to $|\eta| = 4.2$. Each module is made up of four radiation-hard diamond sensors with a size of $8{\times}8\,\text{mm}^2$, arranged in a cross pattern. Besides the luminosity measurement, the Beam Condition Monitor is used to detect beam conditions, which could lead to serious damages in the detector. LUCID is based on the detection of Cherenkov light produced by the particles traversing the detector. Two identical detectors are located about 17 m away from the interaction point at each side in the z direction and a radial distance of 10 cm, corresponding to $|\eta| = 5.8$. Each detector consists of sixteen Cherenkov tubes, with a length of 1.5 m and a diameter of 15 mm. They are arranged concentrically around the beam line and are aligned parallel to the beam axis. The Cherenkov tubes are read out via photomultiplier tubes.

Both detectors provide only relative luminosity measurements and thus a calibration is needed to obtain the absolute luminosity. This is achieved in dedicated runs with special beam conditions using the so-called *van-der-Meer* method [57]. With this method, the beam profiles in $x(y)$-direction are obtained, by scanning low intensity beams through each other. The instantaneous

[1] *Luminosity measurement using a Cherenkov Integrating Detector.*

luminosity is determined from:

$$L_{\text{inst}} = \frac{n_b \cdot f_r \cdot n_1 \cdot n_2}{2\pi\, \Sigma_x \Sigma_y} \tag{3.5}$$

where n_b is the number of colliding bunch pairs at the interaction point per revolution, f_r is the revolution frequency, n_1 and n_2 are the number of protons in the colliding bunches for each beam and Σ_x and Σ_y are the convoluted beam profiles in the horizontal (x) and vertical (y) direction. The total luminosity delivered to ATLAS by the LHC in 2012 with a centre-of-mass energy of $\sqrt{s} = 8\,\text{TeV}$ is measured to be $22.7\,\text{fb}^{-1}$ with an uncertainty of $\pm 1.9\,\%$ [58].

4. Monte Carlo Simulations

Proton−proton collisions are governed by the strong interaction. They consist of phases which are described with perturbative Quantum Chromodynamics (QCD), and phases which are not. Due to non-perturbative QCD processes, the outcome of the collisions cannot be calculated precisely from first principles. Therefore, Monte Carlo simulators, which are tuned to empirical data, are commonly used to model high energy collisions. To describe a proton−proton collisions in a high energy physics experiment, *event generators* are used to simulate the particles of the event, including the hard interaction and the evolution of the collision, and *detector simulation* frameworks, specialised on modelling the interaction between the produced particles and the detector material as well as the detector response.

Section 4.1 describes a typical proton−proton collision and the different phases of its evolution, based on the descriptions of References [47, 59, 60]. In addition, the different Monte Carlo generators, used in this thesis, are presented. In Section 4.2 the $WV\gamma$ signal simulation samples are discussed along with their next-to-leading order normalisation. The simulation samples used for the background estimation are presented in Section 4.3.

4.1. Simulation of Proton−Proton Collisions

The structure of a proton−proton collision is complex, as the proton is not a point-like particle but rather has a structure, consisting of quarks and gluons, which are called *partons*. The proton consists of three *valence quarks* (uud) determining its quantum numbers. In addition, it contains so-called *sea quarks*, virtual quarks and antiquarks arising from gluon splitting into quark-antiquark pairs. Gluons are also part of the proton content, as they are the mediators of the strong force, which bounds the constituents of the protons. Gluon splitting and quark-antiquark annihilation processes set the average composition of the sea in the proton.

In a proton−proton collision, the partons interact with each other, causing the proton to break up. The evolution of the interaction can be divided into several different phases and a detailed picture of a collision is illustrated in Figure 4.1. The collision starts with two incoming protons, A and B, at the left side of the figure. Two of their partons a and b, carrying the momentum fractions x_a and x_b of the incoming protons A and B respectively, scatter at a high energy scale and produce the final state partons. The probability that the parton a (b) carries the momentum fraction $x_{a(b)}$ is described by the *parton density function*, $f_{a(b)}$. In the final state, all known Standard Model particles can be produced as well as potentially new particles, which have not yet been observed. The production of the process $pp \to X$, where X represents the final state particles, is described by the partonic cross section $\hat{\sigma}_X$, which corresponds to the probability how likely this process is. For the following discussion, the production of a quark-antiquark pair is considered. When gluons and photons are radiated off the incoming partons, this is called *initial state radiation* (ISR), while radiation off the outgoing partons is called *final state radiation* (FSR). On short time scales, the final state partons are close to each other and, due

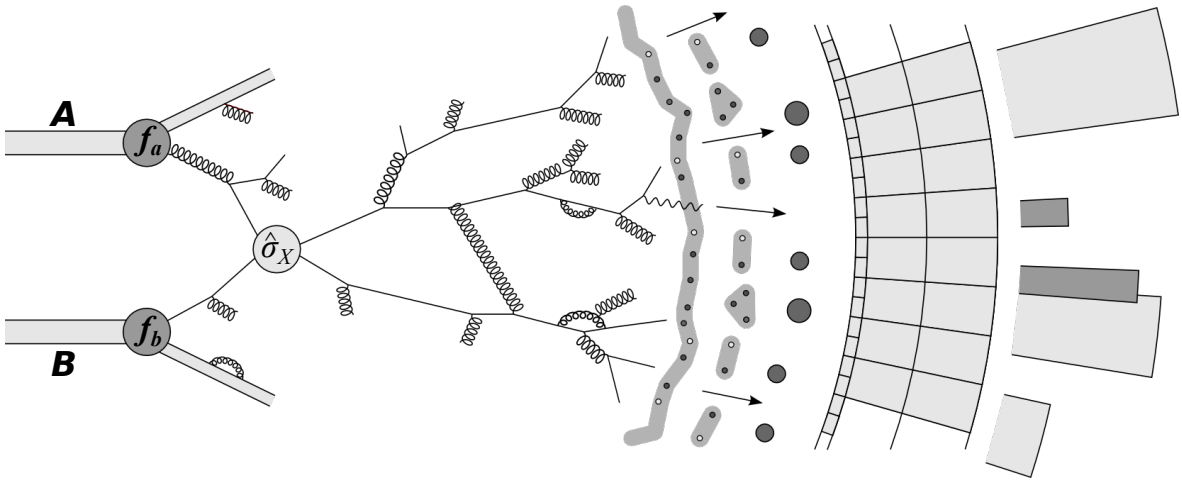

Figure 4.1.: Detailed picture of a proton−proton collision. The colliding partons, a and b, originate from the protons A and B, with the respective parton distribution functions f_a and f_b. The hard interaction for the process $pp \to X$ is described by the partonic cross section $\hat{\sigma}_X$. The outgoing final state particles undergo parton showering, where gluons and photons can be radiated off, or gluons split into quark-antiquark or gluon-gluon pairs. During the hadronisation phase the particles from the parton shower form hadrons, illustrated by the groups of either two or three quarks, corresponding to mesons and baryons and marked as grey tubes or triangles. As many of these hadrons are not stable, they further decay and when the particles interact with the detector material, they generate a signal in the detector, illustrated as energy depositions. Modified from Reference [47]

to the asymptotic freedom of the strong force, the partons are freely moving. However, in the further evolution of the parton showering, the partons drift apart from each other, increasing the strong colour field between them. When the colour field has enough energy, new quark-antiquark pairs are produced. The parton shower continues until the hadronisation phase starts, where the produced quarks and gluons form hadrons, colourless states of either two quarks, called *mesons*, or three quarks, called *baryons*. As many of these hadrons are not stable, they further decay and their decay products are measured in the detector. The measurement of the interaction in the detector is illustrated at the right side of Figure 4.1 as energy depositions in the detector. Other particles and energy depositions observed in the proton−proton collision, not originating from the hard interaction are referred to as *underlying event*. All of the above steps need to be included in the simulation of proton−proton collisions and are discussed in the following in more detail.

Partonic Cross Section The hard process of an interaction is calculated using perturbative Quantum Chromodynamics and can include radiation processes. In general, the partonic cross section for a specific process $\hat{\sigma}_X$ is proportional to the matrix element squared $|\mathcal{M}_{if}^X|^2$ for the respective process. The matrix element contains all the physical information of the transition, from an initial state i to the final state f, including couplings and spins. It is determined from the Lagrangian of the process using Feynman rules. To obtain the probability, or cross section, for the production of a specific process in a proton−proton collision, the partonic cross section and the parton distribution functions of the incoming protons are convoluted:

$$\sigma_{pp\to X} = \int dx_a dx_b \, f_a(x_a, Q^2) f_b(x_b, Q^2) \, \hat{\sigma}_X \tag{4.1}$$

where a and b denote the two incoming partons and f_a and f_b the respective parton distribution

functions. Due to the *factorisation theorem* [61] the perturbative and non-perturbative contributions can be treated separately. The parton distribution functions describe the probability to find a specific parton carrying the momentum fraction x of the proton at the hard interaction scale Q^2. The Q^2 evolution of the parton density functions is described by the DGLAP equations [62–65], but the dependence on the momentum fraction x cannot be calculated perturbatively and is therefore determined experimentally. Several groups provide sets of parton distribution functions, which are obtained from global fits considering deep inelastic scattering data, multijet and Drell-Yan production as well as electroweak production of W and Z bosons. In this thesis the CT10 [66], CT14 [67] and the CTEQ6L1 [68] sets are used for the simulation of the $WV\gamma$ signal samples.

The perturbative expansion of Equation 4.1 in the strong coupling α_s, up to a given order N, yields:

$$\sigma_{pp\to X} = \int dx_a dx_b \, f_a(x_a, \mu_F^2) f_b(x_b, \mu_F^2) \cdot [\hat{\sigma}_0 + \alpha_S(\mu_R^2)\hat{\sigma}_1 + ... + \alpha_S^N(\mu_R^2)\hat{\sigma}_N]_X \tag{4.2}$$

where μ_R and μ_F are the renormalisation and factorisation scales respectively and $\hat{\sigma}_i$ the parton cross section at a specific order i of the perturbation theory. The ultraviolet divergences are absorbed into the strong coupling α_s, which thus becomes dependent on the interaction scale, referred to as *running coupling*, and the renormalisation scale μ_R defines the scale at which the non-physical divergences cancel. The factorisation scale μ_F is introduced to treat the collinear divergences and defines the scale at which the hard and soft parts of the collision are separated. The more orders of perturbation theory are included in the calculation, the less depends the result on the choice of the scales. In the limit when all orders are included in the calculation, the result is independent of the scale choice. However, typically numerical calculations only consider the first few orders of the perturbative expansion and therefore the cross section expectations depend on the choice of the scales. This scale dependency is accounted for by considering it as one source of uncertainty in the simulation process. A common choice for the scales is $\mu_R = \mu_F$ and is often set to the scale of the hard interaction, such as the invariant mass of the final state particles, for example. In case the process of interest contains the resonant production of particles which are not stable, such as the W or the Z boson, the subsequent decay of these particles can also be accounted for in the cross section calculation by including the respective branching ratios in the partonic cross section.

Parton Shower The strongly interacting particles produced in the final state are connected via a colour fields. As the particles are moving away from each other, the energy in the colour field increases, leading to additional radiation and parton splitting, producing many gluons and quark-antiquarks pairs. This process is called *fragmentation*. The fragmentation process is described using the parton distribution functions and the Altarelli-Parisi splitting functions $\mathcal{P}_{q\to qg}$, $\mathcal{P}_{g\to q\bar{q}}$ and $\mathcal{P}_{g\to gg}$ [62] and is calculated in perturbative expansions of the strong coupling α_s. The additional parton emissions and splitting correspond to the real terms of the higher-order corrections. Considering solely the real correction terms lead to divergences, which are cancelled when virtual corrections, originating from quantum loop effects, are also included. These virtual corrections are incorporated via Sudakov form factors [69], which determine the probability for one parton i to evolve without additional fragmentation from a scale Q to another scale Q'. In the Monte Carlo generators, parton splitting and emissions are simulated to a cut off scale Q_0, which is usually about 1 GeV. In order to simulate final state radiation, the parton shower evolves from the scale of the hard interaction $\hat{Q}$ to the cutoff scale Q_0, with $\hat{Q} > Q_0$. In contrast, for initial state radiation the additional branching occurs for partons before the hard

interaction. In this case, the parton shower is often simulated using a *backward evolution* [70] of the event, where it evolves from the scale of the hard interaction $\hat{Q}$ back to an initial energy, which must be below or equal to the maximal centre-of-mass energy of the collision.

In addition, the emission of a photon from a quark can also appear during the parton shower process. This process can be calculated using the fragmentation function $\mathcal{P}_{q\to q\gamma}$, analogue to the parton emissions and splitting of quarks and gluons. However, they are not always implemented in Monte Carlo generators, which can lead to divergent cross sections for certain phase spaces. In order to restore a finite cross section, the *Frixione isolation* [71] is commonly used, where events are only accepted when the photon fulfils:

$$\sum_i E_{\mathrm{T}}^i \, \theta(\delta - \Delta R_{i\gamma}) \leq \epsilon^{\mathrm{iso}} \, E_{\mathrm{T}}^{\gamma} \Big(\frac{1-\cos\delta}{1-\cos\delta_0} \Big), \text{ for all } \delta < \delta_0 \tag{4.3}$$

where E_{T}^i is the transverse energy of hadron i, $\Delta R_{i\gamma}$ is the radial separation between the hadron i and the photon with transverse energy E_{T}^{γ}, δ_0 is a predefined minimum separation and ϵ^{iso} is the efficiency of the photon isolation requirement. The sum on the left side of the equation, considers only hadrons which have an angular separation to the photon of less than δ, due to the Heavyside function $\theta(\delta - \Delta R_{i\gamma})$. In this definition, hadrons are allowed to be arbitrary close to the photons, but must have vanishing energy in case they are strictly collinear. The VBFNLO generator [36–39], which is used to determine the cross section expectations for the $WV\gamma$ signal at next-to-leading order in the strong coupling α_{s}, has the Frixione isolation implemented and the minimum separation is set to $\delta_0 = 0.4$ and the efficiency of the photon isolation to $\epsilon^{\mathrm{iso}} = 0.5$.

Hadronisation After the parton showering, the process enters the *hadronisation* phase, when quarks and antiquarks form colourless states. Due to the colour confinement, the partons which are produced during the parton shower cannot exist freely and thus they combine into hadrons. The hadronisation process can only be described using phenomenological models and two models which are often employed are the *Lund-string model* [72] and the *cluster model* [73].

Underlying Event The underlying event refers to the features of a proton−proton collision not originating from the hard scattering and comprises several different effects. This includes *multiple interactions*, when more than one parton pair of the protons interact with each other as well as the evolution of the proton remnants, after it breaks up in the hard interaction. Typically, these interactions are soft, but also hard scatterings might occur and need to be considered during the generation. These effects need to be taken into account when simulating proton−proton collisions, in order to obtain reliable predictions.

Detector simulation The interaction of the produced particles with the detector material is simulated using special simulation frameworks, such as GEANT4 [74]. These frameworks allow to model the full detector with its special geometry, sub components and different responses. It is an important tool to predict how particles interact with the different detector materials and how their signatures look like in the detector. This information is also used to optimise the reconstruction and identification algorithms of the objects.

Throughout this thesis, particles are defined on different levels of the evolution of the collision. Therefore, in the following *parton level* refers to particles produced in the hard scattering and before the parton showering, *particle level* refers to particles after the hadronisation process and *detector* or *reconstruction level* refers to objects reconstructed in the detector.

4.1.1. Monte Carlo Generators

In order to simulate a proton−proton collision, all of the above steps need to be considered. As these are complex processes, the event generation is split into separate steps which are performed sequentially. In order to connect the results of the hard scattering with the subsequent parton shower, special care has to be taken in order to not double count particles or to produce gaps in the phase space. Double counting occurs, if the matrix element includes the real emission of a parton, which could also originate during the parton shower. As this emission should only be counted once, dedicated schemes have been developed to match the matrix element calculations to the parton showering models, called *ME-PS matching*. Typical examples for matching schemes at leading-order are the CKKW [75] or MLM [76] schemes, which resolve the ambiguity on an event-by-event basis.

Many different Monte Carlo generators are available, some are *multi-purpose* generators, which comprise several of the above steps, and other are more specialised, for example on the hard matrix element of specific processes or the evolution of parton showers. The more specialised generators therefore need to be interfaced to other generators in order to simulate the full proton−proton collision. In general, the hard matrix element is calculated at a fixed order in perturbation theory, but so-called *multi-leg* generators allow additional partons in the final state. Thus, their predictions are not at a fixed order in α_s and often the descriptions of the differential distributions improve with respect to the fixed (lower) order description. In this thesis, several different Monte Carlo generators are used to model the signal and different background processes. If not stated otherwise, the presented generators determine the matrix element at leading-order in the strong coupling α_s.

Sherpa [77–80] The Sherpa generator is a multi-leg and multi-purpose generator. It simulates the hard matrix element, the parton showering, the hadronisation and the underlying event. For the ME-PS matching the CKKW scheme is employed and the hadronisation is implemented using the cluster model.

VbfNlo [36–39] The VbfNlo generator is specialised on the simulation of the matrix elements for several processes with vector boson fusion and vector boson scattering topologies as well as with diboson and triboson final states. It provides predictions at leading and at next-to-leading order in α_s. In this thesis, VbfNlo is only used to derive the $WV\gamma$ signal cross section expectation at next-to-leading order in the strong coupling α_s. It is also used to determine the cross section expectations for anomalous quartic gauge couplings, implemented as dimension eight operators in the framework of an effective field theory.

Pythia [81, 82] The Pythia generator is a multi-purpose generator, simulating the hard matrix element, the parton shower, the hadronisation and the underlying event. For the ME-PS matching several options are provided, such as the MLM or a modified CKKW scheme. For the hadronisation the Lund-string model is implemented.

MadGraph5_aMC@NLO [83, 84] In the following referred to as MadGraph, is a generator specialised on the simulation of the matrix element at leading and next-to-leading order in α_s as well as of the parton showering process. For the ME-PS matching several options, such as the CKKW and the MLM schemes, are implemented. In this thesis, it is interfaced to Pythia for the hadronisation and underlying event simulation.

Powheg [85, 86] The Powheg generator is specialised on the simulation of the hard matrix element at next-to-leading order in α_s and the parton showering. For the ME-PS matching a

special scheme is implemented, the so-called POWHEG method. In this thesis, the simulations obtained with the POWHEG generator are interfaced to PYTHIA for the full event simulation.

ALPGEN [87] The ALPGEN generator is a multi-leg generator specialised on the simulation of the hard matrix element. In this thesis, it is interfaced to HERWIG [88] for the parton showering and to JIMMY [89] for the underlying event. For the ME-PS matching the MLM scheme is used.

4.1.2. ATLAS Simulation Infrastructure

The simulation procedure of the ATLAS collaboration is described in detail in Reference [90] and summarised in the following. The complete simulation process is a multi-step procedure integrated in the ATLAS software framework ATHENA [91]. In the first step, the events for a specific physics process are simulated using event generators, as described in the previous section. The output are lists of stable particles, originating from the hard scattering as well as from the parton shower and the hadronisation. Typically, a particle is defined as stable, if $c\tau \geq 10\,\text{mm}$, with τ the mean lifetime of the particle. The stable particles are then interfaced to a detailed simulation of the ATLAS detector implemented using GEANT4 in order to emulate their interactions with the detector material. The energy deposits in the active detector parts are registered as *hits*, which are converted into voltages and currents during the *digitisation*. After this step, the simulated events are provided in the same format as the recorded data. This allows the usage of the same reconstruction algorithms for data and simulated events, ensuring an equal treatment. During the event generation and the detector simulation, so-called *truth information* of the simulated events are stored. These contain information about the original hard scattering process as well as the origin of each particle and are used for performance studies.

During the digitisation, each event is overlaid with *pileup* and detector noise. Pileup refers to additional particles in the final state originating either from multiple proton−proton interactions in the same bunch-crossing, called *in-time pileup*, or from multiple proton−proton interactions from other bunch-crossings, called *out-of-time pileup*. The average number of inelastic interactions per bunch crossings $\langle\mu\rangle$ is used to quantify pileup events. Since $\langle\mu\rangle$ depends on the instantaneous luminosity, its value changes constantly during the data taking. In simulation, each generated event is overlaid with a specific number of pileup events, which is drawn from a Poission distribution. To minimise the differences of the $\langle\mu\rangle$ distribution in data and simulation, correction factors are applied to the simulation on an event-by-event basis, to reproduce the $\langle\mu\rangle$ distribution observed in data. Similarly, differences in the vertex distribution along the z-axis are observed between data and simulation. These differences are also minimised by applying dedicated correction factors to the simulation, to obtain the distribution measured in data.

4.2. Signal Simulation

The nominal $WV\gamma$ signal Monte Carlo samples are generated with SHERPA 2.1.1 with up to one additional parton in the hard matrix element and the CT10 [66] parton distribution function set. It is normalised to the next-to-leading order cross section, computed with VBFNLO 2.7.1, employing the CT14 (NLO) [67] parton distribution function set and a dynamical choice for the renormalisation and factorisation scales, set equal to the invariant mass of the triboson

system. The SHERPA signal sample is the nominal signal sample used for performance studies. An alternative $WV\gamma$ signal sample is generated with MADGRAPH 2.2.2 at leading order, interfaced to PYTHIA 6.427 for the parton shower and the hadronisation, with the CTEQ6L1 parton distribution function set. The renormalisation and factorisation scales are also set dynamically [92] and the samples are also normalised to the next-to-leading cross section, determined with VBFNLO. The MADGRAPH samples are used to cross check the predictions obtained with the SHERPA samples. In addition, five simulation samples with different anomalous quartic gauge couplings are generated with MADGRAPH, using the same production chain and parameters as for the Standard Model MADGRAPH samples. As before, the samples are normalised to the next-to-leading cross section, computed with the VBFNLO generator. Those samples are used for performance studies in the search for new physics.

Signal Cross Section

The $WV\gamma$ signal samples are normalised to the cross section predictions computed with VBFNLO in the fiducial region of this analysis, which is defined in Section 8.1. Example input files steering the VBFNLO generator with the explicit parameters used, are given in Appendix A.3. To obtain the cross section prediction for the combined $WV\gamma$ process, four different processes are considered: $WW\gamma \to l^+\nu\mathrm{jj}\gamma$, $WW\gamma \to l^-\bar{\nu}\mathrm{jj}\gamma$, $WZ\gamma \to l^+\nu\mathrm{jj}\gamma$ and $WZ\gamma \to l^-\bar{\nu}\mathrm{jj}\gamma$, with l being either an electron or a muon. Naively, it is expected that higher-order corrections should be small in comparison to the leading-order calculation, as the contributions of higher orders are suppressed by a factor of α_s^2. However, for $WW\gamma$ and $WZ\gamma$ production, next-to-leading order corrections originate not only from loop corrections to leading-order diagrams, but also from completely new production channels. This makes the next-to-leading order correction for the $WW\gamma$ and $WZ\gamma$ final states not negligible. One example for such a production topology at next-to-leading order is depicted in Figure 4.2 and includes a gluon in the initial state.

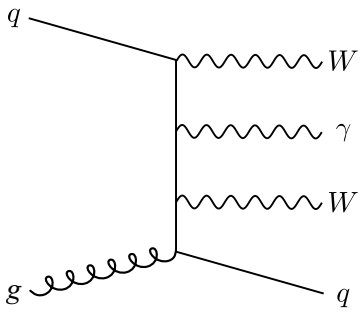

Figure 4.2.: Exemplary Feynman diagram for a NLO production topology of $WW\gamma$ final states including a gluon in the initial state.

Table 4.1 gives the next-to-leading order parton level cross sections for the four processes that account for the $WV\gamma$ process in the fiducial phase space region, analysed in this thesis and defined in Section 8.1. The cross section for the combined process $WV\gamma$ is also given in the table and corresponds to the sum over the four separate processes since no interferences between the four processes are present as they have distinguishable final states. In addition, Table 4.1 lists the *k-factor*, which quantifies the impact of the next-to-leading order with respect to the leading-order prediction. It is defined as $k = \sigma_{NLO}/\sigma_{LO}$. The $WW\gamma$ cross section increases by 30 % at the next-to-leading order and the $WZ\gamma$ cross section by 48 %. Thus, it is important to include higher order corrections for the $WV\gamma$ cross section predictions, as otherwise a potential access might be misinterpreted as new physics effects. The k-factors are given with the statistical uncertainty of the Monte Carlo generation only.

	NLO Fiducial Cross Section [fb]	k-Factor
$WW\gamma \to l^+\nu jj\gamma$	1.66 ± 0.08	1.300 ± 0.002
$WW\gamma \to l^-\bar{\nu}jj\gamma$	1.58 ± 0.07	
$WZ\gamma \to l^+\nu jj\gamma$	0.34 ± 0.02	1.484 ± 0.006
$WZ\gamma \to l^-\bar{\nu}jj\gamma$	0.20 ± 0.01	
$WV\gamma \to l\nu jj\gamma$	3.78 ± 0.11	1.323 ± 0.002

Table 4.1.: Cross section expectations on parton level at next-to-leading order in the fiducial phase space region along with the k-factor. The values are given for the four separate processes, implemented in VBFNLO that account for the combined $WV\gamma$ process studied in this thesis. The uncertainties on the cross sections include statistical and systematic uncertainties. For the k-factor, only the statistical uncertainties of the Monte Carlo simulation are shown. All numbers are given per lepton flavour.

The cross section predictions for the two $WW\gamma$ processes, shown in Table 4.1, are very similar and agree within their uncertainties in contrast to the cross section predictions for the two $WZ\gamma$ processes, which are significantly different from each other. This difference is directly related to the parton distribution functions of the proton. To produce the $W^+Z\gamma$ process at leading-order, the dominant initial state is $u\bar{d}$ and at next-to-leading order ug or $\bar{d}g$. The dominant initial state of the $W^-Z\gamma$ production is $d\bar{u}$ at leading-order and dg or $\bar{u}g$ at next-to-leading order. For large momentum fraction values x of the colliding partons, the probability to produce the $WZ\gamma$ process is higher than for low values of the momentum fraction. Figure 4.3 shows the CT14 parton distribution functions of the proton for the scale of the hard interaction $Q = 100\,\text{GeV}$. The probability to find an up quark at large x values is larger than the probability to find a down quark, as the valence quarks of the proton are two up quarks and only one down quark (uud). Since the LHC is a proton−proton collider, this is true for both incoming partons, leading to an increased probability for $W^+Z\gamma$ production with respect to the $W^-Z\gamma$ production. Therefore, the asymmetry in the production cross section is a special characteristic of proton−proton collisions and is not expected in neutral initial states, such as proton−antiproton collisions.

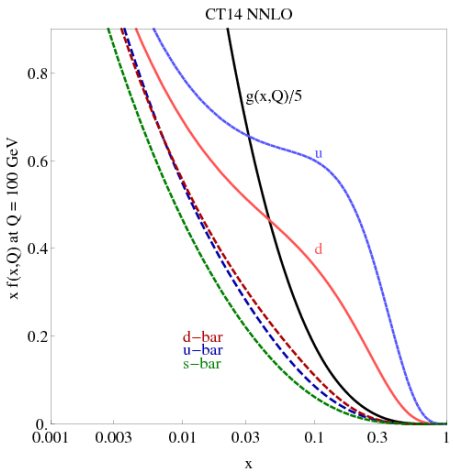

Figure 4.3.: The CT14 parton distribution functions of the proton at $Q = 100\,\text{GeV}$ for the valence quarks u and d, the gluon g (scaled by $1/5$) and the sea quarks $\bar{u}$, $\bar{d}$ and $\bar{s}$. Taken from [67].

The theoretical uncertainties on the cross sections, shown in Table 4.1 include the statistical uncertainty of the Monte Carlo generation as well as systematic uncertainties. These include uncertainties arising from the variation of the renormalisation and factorisation scales, from the uncertainty of the parton distribution functions, from the choice of the value of the strong coupling as well as uncertainties arising from photon fragmentation. The size of the relative uncertainties of the separate components are listed in Table 4.2 for all four VBFNLO processes. The total uncertainty on the expected cross sections is the quadratic sum over all considered components. The dominant contributions to the systematic uncertainties arise from the parton distribution functions and the scale dependencies.

	$WW\gamma$		$WZ\gamma$	
	$l^+\bar{\nu}\mathrm{jj}\gamma$	$l^-\nu\mathrm{jj}\gamma$	$l^+\bar{\nu}\mathrm{jj}\gamma$	$l^-\nu\mathrm{jj}\gamma$
Source	Theory Uncertainty [%]			
Numerical Accuracy	0.9	0.6	0.4	0.2
Scale Dependence	2.3	2.0	3.8	4.5
PDF	3.8	3.9	4.7	4.4
α_s	0.2	0.5	0.5	0.6
γ Fragmentation	0.9	0.9	1.0	1.2
Total Uncertainty	4.6	4.5	6.2	6.5

Table 4.2.: Uncertainties considered on the theoretical predictions of the cross sections for the four processes as implemented in VBFNLO, to obtain the predictions for the combined $WV\gamma$ processes studied in this thesis.

For the nominal determination of the theory predictions, the renormalisation and factorisation scales are both set to the invariant mass of the electroweak system. In order to evaluate the uncertainties due to these scale choices, they are varied independently by a factor of two. Out of the eight possible combinations, only six are considered, as the two extreme cases, $\mu_R = 4\mu_F$ and $\mu_F = 4\mu_R$, are excluded as commonly chosen. The envelope of the variations is taken as uncertainty and ranges between 2.0 % - 4.5 % for the different processes.

The nominal choice of the parton distribution functions (PDF) for the derivation of the theoretical predictions of the signal cross section is the CT14 [67] set. The CT14 set is obtained from a global fit with 28 free parameters to several datasets from various experiments. The uncertainties on the parton distribution function are quantified by the 56 *error PDF* sets, obtained from individual up and down variations by one standard deviation of the 28 orthogonal eigenvectors. To determine the uncertainty arising from the uncertainties on the parton distribution functio, the cross section expectation is evaluated for each error PDF set. The uncertainty of each parameter is taken as half the difference between the cross sections evaluated with the up and the down variation, since the full difference corresponds to twice the uncertainty. The total uncertainty due to the parton distribution functions is obtained by adding the uncertainty of each parameter in quadrature:

$$\Delta\sigma_{PDF} = \frac{1}{2}\sqrt{\sum_{i}^{28}\left(\sigma_i^{\mathrm{up}} - \sigma_i^{\mathrm{down}}\right)^2} \tag{4.4}$$

providing symmetric uncertainties on the cross section. The relative uncertainty on the production cross section due to the parton distribution functions is found to be between 3.8 % - 4.7 % for the different processes. In order to validate that the uncertainty obtained with this strategy predicts reliable results, the cross section expectation is also derived with the CT10 and the MSTW2008 [93] parton distribution functions. The cross section expectations determined with the two alternative parton distribution functions and the nominal one are found to agree well within the quoted PDF uncertainties.

The strong coupling α_s in the nominal parton distribution function is set to $\alpha_s = 0.118$ at the Z boson mass scale. It is obtained from measurements and therefore exhibits experimental uncertainties. To evaluate the impact of these uncertainties on the $WV\gamma$ cross section prediction, the value of α_s is varied up and down by 0.0015, following the recommendations from Reference [94]. Since the CT14 parton distribution functions are not available with these variations of the strong coupling, the theory predictions are evaluated with the values closest to the recommended variations, namely $\alpha_s = 0.120$ and $\alpha_s = 0.116$. The uncertainty is calculated as the difference between the cross section predictions of the up and the down variations:

$$\Delta\sigma_{\alpha_s} = f_{\alpha_s} \frac{1}{2}\left(\sigma^{\text{up}} - \sigma^{\text{down}}\right) \tag{4.5}$$

where $f_{\alpha_s} = \frac{0.0015}{0.0020}$, a scale factor to derive the uncertainty in the recommended step size. As before, the factor $\frac{1}{2}$ is introduced, as the difference between the up and down variation corresponds to twice the uncertainty. The relative uncertainty due to the strong coupling, is determined to be between 0.2 % - 0.6 % depending on the process.

Uncertainties due to the photon fragmentation are evaluated by varying the isolation energy of the photons. In VBFNLO the Frixione isolation, defined in Section 4.1, is implemented, ensuring the calculations to be collinear and infrared safe. For the nominal determination of the theory predictions, the efficiency of the photon isolation is set to $\epsilon^{\text{iso}} = 0.5$. To estimate the influence of this choice on the cross section expectation, the efficiency is varied up and down by 0.25. The envelope is taken as uncertainty and found to be about 1.0 %.

Phase Space Dependence

The kinematic distributions are dependent on the higher-order corrections. To illustrate this effect, Figure 4.4 shows the $WW\gamma$, $WZ\gamma$ and $WV\gamma$ cross section expectations at leading-order and at next-to-leading order as a function of the transverse momentum of the photon, p_T^γ in the upper panel and the k-factor in the lower panel. The uncertainties are the statistical uncertainties of the Monte Carlo generation. Figure 4.4(a) illustrates the $WW\gamma$ expectations, Figure 4.4(b) the $WZ\gamma$ expectations and Figure 4.4(c) the combined $WV\gamma$ expectations. The k-factor of the $WW\gamma$ process exhibits only a small dependence on the transverse momentum of the photon and is relatively constant at a value of around 1.3. For the $WZ\gamma$ process, the k-factor has larger fluctuations over the studied phase space, but also the uncertainties are significantly larger. The k-factor for the combined $WV\gamma$ process has a similar behaviour as the $WW\gamma$ process, since the $WW\gamma$ cross section is about a factor of ten higher than the $WZ\gamma$ production and the k-factor of the $WV\gamma$ process is also dominated by the $WW\gamma$ contribution.

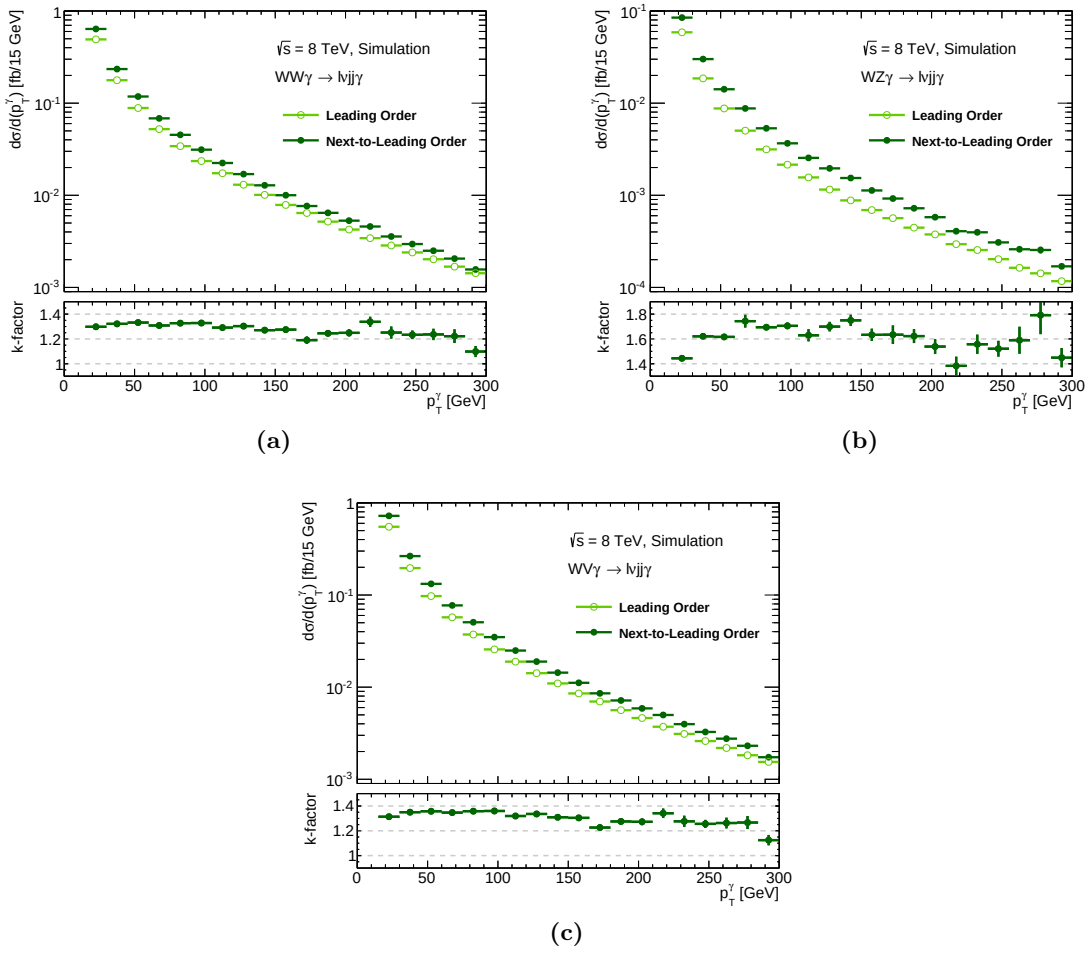

Figure 4.4.: Cross section expectations at leading order and at next-to-leading order as a function of the transverse momentum of the photon for (a) the $WW\gamma$ process, (b) the $WZ\gamma$ process and (c) the $WV\gamma$ process.

4.3. Samples Used in the Analysis

For the $WV\gamma$ analysis, several background processes are considered, which are discussed in Section 6.2. The background estimation is explained in detail in Chapter 7 and relies partially on Monte Carlo simulation. Therefore, all Monte Carlo samples used in this analysis for the background estimation are presented briefly in the following.

The production of a W boson in association with a photon ($W\gamma$ + jets) is generated with ALPGEN, interfaced to HERWIG for the parton showering and the hadronisation and to JIMMY for the underlying event. The CTEQ6L1 parton distribution function set is used. The production of a Z boson in association with a photon ($Z\gamma$ + jets) and up to three additional partons in the event is generated with SHERPA, employing the CT10 parton distribution function set. This simulation sample is generated with a requirement on the dilepton invariant mass of $m_{ll} > 40\,\text{GeV}$. As the signal selection, discussed in Section 6.1, allows only one lepton in the final state, this requirement cannot be accounted for in the event selection, however it influences the expected event yield of this background in the signal region. The impact of the m_{ll}

requirement on the event yield is estimated to be about 10 % using Z + jets simulation samples, as these samples are available with lower m_{ll} criteria. Therefore, a conservative theoretical uncertainty of 20 % is assumed. The production of top pairs in association with a photon ($t\bar{t}\gamma$) is generated with MadGraph and interfaced to Pythia for the hadronisation and the underlying event, using the CTEQ6L1 parton distribution function set. The cross section is normalised to next-to-leading order accuracy with a theoretical uncertainty of 22 % [95, 96]. The production of a Z boson with additional jets (Z + jets) is also generated with AlpGen and interfaced to Herwig for the parton shower and hadronisation and to Jimmy for the underlying event, using the CTEQ6L1 parton distribution function set. The production of top quarks pairs ($t\bar{t}$) is simulated with Powheg at next-to-leading order in α_s, employing the CT10 parton distribution function set. It is interfaced to Pythia, using the CTEQ6L1 parton distribution function set for the hadronisation and the underlying event. The samples for Z + jets and $t\bar{t}$ production are used to determine the background contribution of events containing electrons which are misidentified as photons and a theoretical uncertainty of 5 % is taken on both samples.

5. Object Reconstruction

The particles produced in the proton collision leave signals in various detector parts. From these signatures, the different object types are reconstructed and identified. The algorithms for the reconstruction and identification must be very efficient in identifying the type of an object, while rejecting objects which originate from different sources but have similar detector signatures. Reconstructed and identified objects have ideally the same properties as the original particle, but due to detector effects, like noise and resolution, the properties are usually altered. Therefore, dedicated calibrations and corrections are applied to each reconstructed object to obtain kinematic properties close to the properties of the original particle.

The algorithms for the reconstruction and identification are implemented in ATHENA, the software framework of ATLAS. For data and Monte Carlo simulation, the same algorithms are used, to ensure equal treatment. In this chapter, the reconstruction, identification and calibration of all objects used in the $WV\gamma$ analysis are discussed in the following order: jets in Section 5.1, electrons and photons in Section 5.2, muons in Section 5.3 and missing transverse energy in Section 5.4. In addition, objects considered for the analysis are required to fulfil a dedicated baseline selections, which is presented in Section 5.5.

5.1. Jets

5.1.1. Jet Reconstruction

Quarks and gluons, produced in the collisions, cannot exist freely due to the colour confinement of Quantum Chromodynamics. Thus, they form colour neural hadrons, which are either stable or unstable and decay further. The stable hadrons and the decay products of the unstable hadrons are measured in the detector as collimated and localised sprays of particles. The sprays of particles are grouped into *jets* using dedicated *jet algorithms*, which connect the tracks and energy deposits in the detector to the original partons. Thus, jets are not fundamental particles, but objects defined with a specific jet algorithm.

The $WV\gamma$ analysis uses jets defined with the anti-k_t [97] algorithm, implemented in the ATHENA framework using FASTJET [98, 99]. It is a *sequential recombination algorithm*, which combines two input objects at a time, until a predefined condition is fulfilled and the recombination is stopped. The inputs to the anti-k_t algorithm can be defined on parton, particle or detector level. The input objects, which are supposed to be clustered by the anti-k_t algorithm, are stored in the input list and arranged according to their transverse momenta, from the highest to the lowest. In order to identify the next object to be combined with the reference object, i, the distances d_{ij} between the object i and all other objects, j, are determined using:

$$d_{ij} = \min\left(\frac{1}{p_{\mathrm{T},i}^2}, \frac{1}{p_{\mathrm{T},j}^2}\right) \frac{\Delta R_{ij}^2}{R^2} \tag{5.1}$$

where $p_{\mathrm{T},i/j}$ is the transverse momentum of the two objects i and j, R is a radius parameter, fixed to a predefined value, and ΔR_{ij}^2 is the geometrical distance between the two objects defined as $\Delta R_{ij}^2 = (y_i^2 - y_j^2)^2 + (\phi_i^2 - \phi_j^2)^2$, where y is the rapidity and ϕ is the azimuthal angle. In addition, the distance between the object i and the beam axis is evaluated, using:

$$d_{iB} = \frac{1}{p_{\mathrm{T},i}^2}. \tag{5.2}$$

When the difference between the two objects is smaller than the distance to the beam axis ($d_{ij} < d_{iB}$), the four-momenta of the objects i and j are added into a new object k. The objects i and j are removed from the input list and the distances are recomputed for the object k as new reference object. When the distance to the beam axis is smaller ($d_{iB} < d_{ij}$), the recombination is stopped and the object i is declared a stable jet and removed from the input list. This procedure is sequentially repeated until no input objects are left and all objects are clustered into stable jets. Since soft objects are combined with nearby hard objects, the algorithm is *infrared* and *collinear safe*. This ensures that the same jets are obtained even if a soft particle is radiated off a parton or if a particle splits into two collinear particles during the showering and fragmentation process. Also, jets clustered with the anti-k_t algorithm, have a cone-like shape in the $y - \phi$ plane. Due to these advantages, the anti-k_t algorithm is the standard jet algorithm used by the ALTAS and CMS Collaborations.

This thesis uses anti-k_t jets with a radius parameter $R = 0.4$ and reconstructed from *topological calorimeter clusters* [100]. The topological clusters are obtained by clustering calorimeter cells together, with no constraints on the cluster shape or the number of constituent cells. In order to form the topological clusters the signal-to-noise ratio, S/N, is employed. The noise in the calorimeter cell is defined as the quadratic sum of the root mean square (RMS) of the energy distribution in the calorimeter cell obtained from random bunch crossings and the cell noise arising from readout electronics. The algorithms starts with a *seed cell*, which has a signal-to-noise ratio of $S/N > 4$. Neighbouring cells are added to the seed cell, when their signal-to-noise ratio is $S/N \geq 2$. The *proto-cluster* is completed by adding all additional perimeter cells around the hitherto cluster which have a positive signal-to-noise ratio, $S/N \geq 0$. Proto-clusters with multiple maxima, originating from separate particles that are close to each other, are split: if the proto-cluster contains several energy maxima above 500 MeV, it is split up into smaller, individual clusters. After the splitting procedure, remaining clusters are the topological clusters. Due to the signal-to-noise ratio thresholds, this clustering algorithm is also referred to as the *4-2-0 scheme* and effectively suppresses both, pileup and calorimeter noise. The energy of the topological cluster is the total energy deposited in its constituent cells and the direction is determined as weighted average over the individual pseudorapidities and azimuthal angles.

The calorimeters are calibrated to correctly measure the energy of electromagnetic particles, such as electrons and photons. Jets however, have electromagnetic constituents, predominantly arising from the decay of neutral pions, as well as hadronic constituents, which have different detector responses. The topological clusters, used in this analysis as inputs for the anti-k_t algorithm, are calibrated using the *local cluster calibration* (LCW) [101]. In this calibration, the clusters are classified as either electromagnetic or hadronic, depending on their shower shape variables. Calibration factors for the two cluster types are derived using Monte Carlo simulation of single pion events and correct for nuclear energy losses, for energy losses in inactive material and energy losses outside the topological cluster, arising from noise threshold effects. These corrections are applied to the respective cluster type.

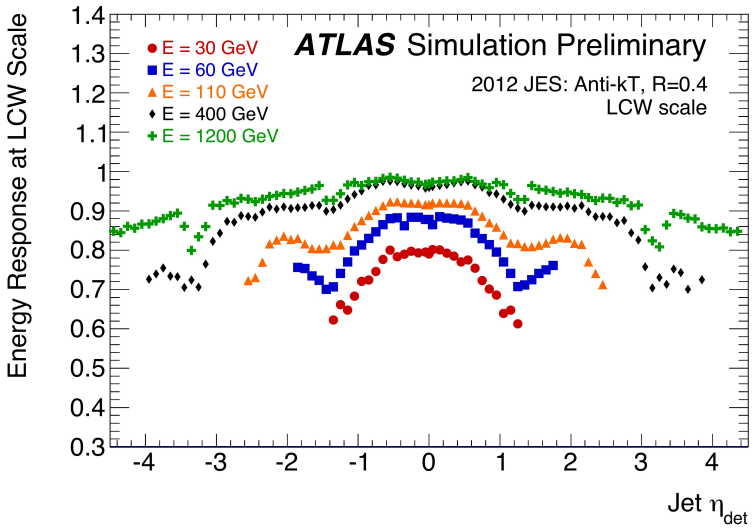

Figure 5.1.: Average calorimeter response for simulated jets calibrated to the LCW scale for different particle jet energies, illustrated in different colours, and as a function of the detector jet pseudorapidity. The inverse of the jet response are the calibration factors to obtain jets at the LCW+JES scale. Taken from Reference [102].

5.1.2. Jet Calibration and Uncertainty

Jet algorithms that use calibrated topological clusters as inputs, yield calorimeter jets at the LCW scale. However, additional corrections are necessary to obtain the jets at the jet energy scale (JES), which corresponds to the true jet energy scale at particle level. The determination of the jet energy scale and its uncertainty using data collected at a centre-of-mass energy of $\sqrt{s} = 8\,\text{TeV}$ is described in detail in References [102–105]. The complete calibration scheme to obtain jets at the jet energy scale consists of multi steps and is summarised in the following.

In the first step an *origin correction* is applied, which corrects the jets to point back to the primary vertex[1]. The topological clusters used for the jet clustering, and therefore also the reconstructed jets themselves, point to the centre of the ATLAS detector. However, when the full event is reconstructed, the primary vertex is a better assumption of the jet origin. The correction only modifies the direction of the jets and leads to a significant improvement of the η resolution, due to the luminous beamspot size of about 40 to 55 mm along the beam axis in 2012. The next step is the *pileup correction*, where the jet is corrected for pileup effects by subtracting the pileup energy density of the event, scaled to the area of the jet[2]. Residual pileup dependencies are removed with an additional correction, depending on the number of reconstructed vertices in the event and on the average number of interactions per bunch crossing. The next calibration step is the jet energy scale correction, which corrects the four-momenta of the jets to particle level. The calibration is provided as a function of the transverse momenta and the pseudorapidities of the jets and determined using an inclusive jet Monte Carlo sample. Figure 5.1 shows the average jet response for simulated jets, defined as $\mathcal{R} = E_{\text{jet}}^{\text{LCW}}/E_{\text{jet}}^{\text{truth}}$ where $E_{\text{jet}}^{\text{LCW}}$ is the measured jet energy at the LCW scale, including origin and pileup corrections, and $E_{\text{jet}}^{\text{truth}}$ is the truth jet energy at particle level. The inverse of the response, $1/\mathcal{R}$, are the

[1] The primary vertex is defined as the vertex with the highest $\sum p_{\text{T}}^2$ of all associated tracks with a transverse momentum above 400 GeV.

[2] The area of the jet is obtained by using a ghost association.

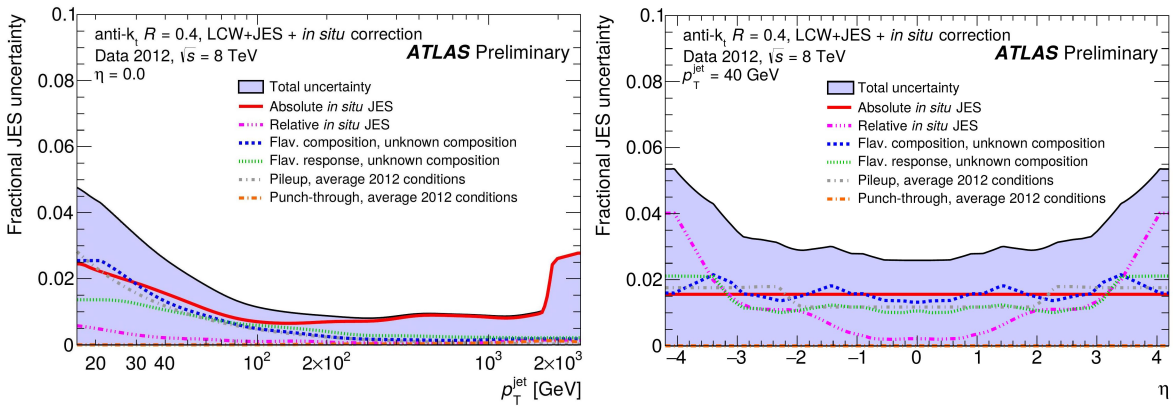

(a) **(b)**

Figure 5.2.: Jet energy scale uncertainty as a function of (a) the transverse momentum p_T and (b) the pseudorapidity η of the jet. The total uncertainty is the quadratic sum of the individual components. Uncertainties arising from the $Z+$ jet, $\gamma+$ jet and multijet balance measurements are labelled as *Absolute in-situ JES* and uncertainties from the η-intercalibration are labelled as *Relative in-situ JES*. The flavour uncertainties with the label *unknown composition* indicates that the flavour composition of the jet is assumed to consist of 50 % quarks and 50 % gluons with an additional uncertainty of 100 %. Taken from Reference [102].

calibration factors. After this step the jets are calibrated to the LCW+JES scale. The calibrated jets are further corrected with the *global sequential correction* (GSC), to account for different jet responses, arising from different flavour compositions of gluon and quark initiated jets as well as for *punch through jets*. Punch-through jets are high energetic jets, which are not fully contained within the calorimeter and thus generate a signal in the muon spectrometer. For jets calibrated at the LCW scale, the GSC correction depends on the track information of the inner detector and the muon spectrometer. The GSC correction does not modify the mean jet energy response. A final *residual in-situ* calibration is determined from several measurements and applied to data only. All measurements are based on momentum balance, where the jet being calibrated is recoiling against a well measured reference object. The correction is then derived from the double ratio:

$$\frac{\mathcal{R}_{\text{data}}}{\mathcal{R}_{\text{MC}}} = \frac{\langle p_{\text{T}}^{\text{jet}} / p_{\text{T}}^{\text{ref}} \rangle_{\text{data}}}{\langle p_{\text{T}}^{\text{jet}} / p_{\text{T}}^{\text{ref}} \rangle_{\text{MC}}} \tag{5.3}$$

where $p_{\text{T}}^{\text{jet}}$ is the transverse momentum of the jet being calibrated and $p_{\text{T}}^{\text{ref}}$ is the transverse momentum of the well measured reference object. First, the jet response over the full pseudorapidity range is unified in the η-intercalibration using dijet events. Further corrections are derived from a combination of measurements using events where a jet is recoiling against a Z boson or photon ($Z+$ jet or $\gamma+$ jet) and events where a high p_T jet is recoiling against a system of several low p_T jets (multijet).

The uncertainty of the jet energy scale is shown in Figure 5.2 and accounts for uncertainties arising from the in-situ measurements, from the flavour composition and response, from the pileup correction and from the punch-through corrections. The uncertainty ranges from 1 % for central jets with transverse momenta between 100 GeV and 1.5 TeV up to 5.5 % for forward jets with $|\eta| \approx 4.0$ and low transverse momenta around 40 GeV. The jet energy resolution is also measured with in-situ methods based on momentum balance using dijet and $Z/\gamma+$ jets

events. Good agreement between the jet energy resolutions measured in data and simulation is observed within the maximal uncertainty of 10 % [104] and therefore, no additional correction to the simulation is applied.

5.1.3. Jet Vertex Fraction

In order to suppress jets produced in pileup events, a requirement on the *jet vertex fraction* [106] (JVF) is introduced for jets with transverse momenta below 50 GeV and $|\eta| < 2.4$. The jet vertex fraction is defined as the ratio of the sum of the p_{T} of the tracks matched to the jet originating from the primary vertex and the sum of the p_{T} of all tracks matched to the jet, without restrictions on the origin. Therefore, the jet vertex fraction is at unity for jets, where all associated tracks originate from the primary vertex. Opposite, the jet vertex fraction is at zero for jets, where none of the associated tracks originate from the primary vertex. Values of the jet vertex fraction between zero and unity indicate that the jet contains tracks, which are likely to originate from the primary vertex as well as tracks from different origins. The modelling of the jet vertex fraction is studied in data and simulation using $Z \to \mu\mu$ events, produced in association with jets. The systematic uncertainty on the jet vertex fraction is determined to be between 2 % and 6 %, depending on the pseudorapidity and the transverse momentum of the jet [106].

5.1.4. Jets Originating from b-Hadrons

Jets originating from the decay of a hadron including bottom quarks, in the following referred to as *b-jets*, have special features, that are employed for their identification. For example, the lifetime of a b-hadron with a transverse momentum of about 50 GeV is of the order of 1.5 ps ($c\tau \approx 450\,\mu$m), corresponding to a mean flight path length of about 3 mm [107]. The inner detector can resolve the displacement of such a secondary decay vertex. In this analysis, the MV1 algorithm [107] is used to identify b-jets, with an efficiency of 85 % and a probability to misidentify a light flavour jet as a b-jet of 10 % [107]. The MV1 algorithm is based on an artificial neural network, using information about the impact parameters of charged particles as well as about the secondary vertex. As the identification of b-jets depends on the inner detector information, it is only available for central jets with $|\eta| < 2.5$.

The performance of the MV1 algorithm is studied using di-leptonic $t\bar{t}$ events, events with jets containing D^{*+} mesons and multijet events. Three different types of efficiencies are determined: the efficiency to correctly identify a jet originating from a b-hadron (b-jet efficiency) [108], the efficiency to identify a jet originating from a c-hadron as b-jet (c-jet efficiency) [109], and the efficiency to misidentify a light-flavour jet as b-jet (misidentification rate) [109]. The modelling of these efficiencies in simulation is found to be slightly different from the efficiencies measured in data. Thus, correction factors are determined and applied to the simulation in order to match the efficiencies measured in data. The uncertainty on the b-jet efficiencies are between 2 % and 8 % depending on the transverse momentum of the jet [108]. For the c-jet efficiencies, the correction factors are consistent with unity within their uncertainty of 8 % to 15 %, depending on the transverse momentum of the jet [109]. The corrections factors for the light jet misidentification are found to be slightly larger than unity with uncertainties between 15 % and 43 %, also depending on the transverse momentum of the jet [109].

5.2. Photons and Electrons

Electrons and photons both induce electromagnetic showers in the calorimeters and therefore, they have similar detector signatures. Thus, large parts of their reconstruction algorithms are the same, as described in detail in References [51, 110–113]. More details on the electromagnetic energy calibration is given in Reference [111], on the electron and photon identification in References [51, 110, 114] and on the isolation definitions in Reference [51, 110, 111, 113]. The strategies for the reconstruction and identification for photons and electrons is summarised in the following section.

5.2.1. Photon and Electron Reconstruction

The reconstruction of photons and electrons is based on energy deposits in the electromagnetic calorimeters and on tracks from the inner detector. The calorimeter cells are combined into *towers* with a fixed size of 0.025×0.025 in $\Delta\eta \times \Delta\phi$, which correspond to the granularity of the middle layer of the electromagnetic calorimeter, see Figure 3.6(a) in Section 3.2.3. The tower energy is the sum over the energies deposited in all cells in longitudinal direction, spanning over the strip, middle and back layer. In case a cell contributes to several towers, the energy of the cell is split uniformly among the participating towers. A sliding window algorithm [112] with a window size of 3×5 towers in $\eta \times \phi$, scans the complete volume of the calorimeter, to locate *seed-clusters*, with a transverse energy of at least 2.5 GeV.

Track reconstruction in the inner detector is based on pattern recognition and track fitting. The pattern recognition tests two different hypotheses: the pion hypothesis and a specific electron hypothesis, which accounts for bremsstrahlung by allowing an energy loss of up to 30 % at each material surface. A global χ^2-fit is performed for each track candidate using the pion hypothesis. In case the pion hypothesis fails, the track candidate is refitted using the electron hypothesis. Only track candidates which are fitted with one of the two hypothesis, are considered as tracks. To ensure the tracks are well measured, special quality criteria are required, such as a minimum transverse momentum of $p_{\mathrm{T}} > 400$ GeV or on the number of hits in the silicon detectors.

Electron candidates must have at least one well measured track matched to the seed-cluster. In case several tracks can be associated, the best-matched one is chosen as the primary track. The final electron clusters are rebuilt in the barrel (end-cap) region using 3×7 (5×5) cells in $\eta \times \phi$, adjusting the cluster position for each layer, in order to reflect the shower development of the object [110].

If no track can be associated to the electromagnetic seed-cluster, it is classified as an *unconverted photon*. When a photon interacts with the inner detector material, it can produce an electron-positron pair, which is measured as two tracks originating from one common conversion vertex. Thus, electromagnetic seed-clusters, matched to two tracks and consistent with the photon conversion hypothesis, are classified as *double-track conversion* photons. In some cases, only one track is reconstructed, if, for example, an asymmetric conversion occurs, where one of the two electrons is very soft and its track is not reconstructed, or when the two tracks are too close together and cannot be resolved. Therefore, electromagnetic seed-clusters, which are matched to one track are classified as *single-track conversion* photons, if the track has no hit in the first silicon pixel layer. This additional requirement is necessary to distinguish single-track converted photons from electrons. The final photon cluster is rebuild using 3×5 (3×7) cells in $\eta \times \phi$ for

unconverted (converted) photons. The larger cluster sizes for converted photon and electron candidates account for the larger extension of the electromagnetic shower in ϕ-direction, caused by the magnetic field of the solenoid.

The electron reconstruction efficiency is measured using a tag-and-probe method analysing $Z \to ee$ and J/Ψ events. Electrons with transverse energies above 15 GeV have reconstruction efficiencies between 95 % to 99 %, depending on the pseudorapidity range [110]. The reconstruction efficiencies measured in Monte Carlo simulation are corrected on an event-by-event basis, in order to reproduce the efficiencies observed in data. The uncertainties on the electron reconstruction range from below 0.5 % to 2.0 %, depending on the transverse energy of the electron [110]. The reconstruction efficiencies for unconverted and converted photons are derived for prompt photons using simulated $H \to \gamma\gamma$ events, with $m_H = 120\,\text{GeV}$, and found to be about (99.83 ± 0.01) % and (94.33 ± 0.09) %, respectively [113]. This corresponds to an overall photon reconstruction efficiency of (97.82 ± 0.03) % [113].

5.2.2. Photon and Electron Calibration

The energy of the electron and photon candidates are determined from the final cluster energy, which needs to be calibrated to the electromagnetic scale at particle level. The calibration of the electromagnetic objects is determined in several steps [111]. The first step of the calibration is an intercalibration of the longitudinal layers of the calorimeter to ensure equal scales over all layers. In data, the scale in each layer is corrected with respect to the scales found in simulation. The intercalibration is an important step, performed before the actual energy scale determination, to assure the energy response is extrapolated correctly in the full energy range. In the next step, correction factors are applied to the reconstructed photon and electron clusters, in order to obtain the true object energy on particle level. The correction factors are determined using simulated single electron events and employing multivariate algorithms. They are optimised for electrons, converted and unconverted photons individually, as they have different shower characteristics. The correction accounts for energy losses in inactive material in front of the calorimeters, for energy deposited in neighbouring cells and energy deposited in the hadronic calorimeters. The final energy scale is derived selecting $Z \to ee$ events, close to the Z boson mass $80\,\text{GeV} < m_{ee} < 100\,\text{GeV}$, as this resonance is known with high precision. The correction factors are defined as $E^{\text{data}} = E^{\text{MC}}(1 - \alpha_i)$, with the electron energies E^{data} and E^{MC} measured in data and Monte Carlo simulation, respectively and the energy scale correction α_i for the pseudorapidity bin i. In Figure 5.3(a), the energy scale corrections are shown, as a function of the pseudorapidity. For electrons with a transverse energy above 40 GeV, the energy scale uncertainty is about 0.04 % for most of the pseudorapidity range and rises up to 0.2 % in the transition region of the calorimeter barrel to the end-cap, $1.37 < |\eta| < 1.82$ [111]. For electrons with low transverse momenta of about 11 GeV, the uncertainty ranges from 0.4 % to 1.1 %, depending on the pseudorapidity range [111]. The photon energy scale uncertainty for unconverted photons is between 0.2 % and 0.9 % and for converted photons between 0.2 % and 0.4 %, both depending on the pseudorapidity region [111].

The electromagnetic energy resolution is determined using the invariant dielectron mass m_{ee} selected from $Z \to ee$ events. In data, the resolution is found to be slightly larger than the resolution obtained in simulation. Therefore, a momentum smearing is applied to the simulation in order to reproduce the energy resolution observed in data. The invariant dielectron mass is shown in Figure 5.3(b), for the calibrated data as well as for the uncorrected Monte Carlo

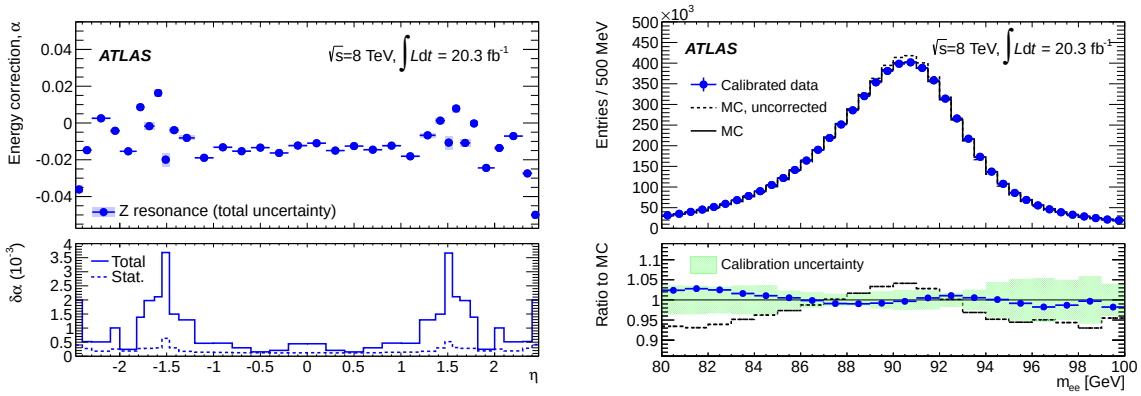

(a) **(b)**

Figure 5.3.: The energy scale corrections α is shown in (a) as a function of the pseudorapidity η, determined in the invariant dielectron mass range $80\,\text{GeV} < m_{ee} < 100\,\text{GeV}$. The lower panel shows the statistical and the total uncertainties of the energy calibration. The invariant dielectron mass distribution of $Z \to ee$ events is shown in (b), for data in blue dots, for uncorrected simulation as black dashed line and for corrected simulation as solid black line. The lower panel shows the ratio of the distributions in data and simulation, along with the calibration uncertainty as green band. Taken from Reference [111].

simulation and the corrected Monte Carlo simulation. The agreement between the data and the corrected simulation in the interval $80\,\text{GeV} < m_{ee} < 100\,\text{GeV}$ is about 1 % in the central region of the interval and slightly larger at the boarders [111]. For objects with an transverse energies above 50 GeV, the uncertainty of the energy resolution is below 10 % and increases to 40 % at high object energies [111]. The calibration of photons and electrons is validated using J/Ψ events as well as Z boson production in association with a radiated photon, $Z \to ll\gamma$.

5.2.3. Photon and Electron Identification

Photon

Not all reconstructed photon candidates are prompt photons from the hard interaction; many of the photon candidates originate from hadron decays. Therefore, additional identification criteria on the photon candidates are introduced to predominantly select prompt photons and reject photons from different sources. The additional criteria are mainly based on calorimeter variables in the middle and strip layer. For photons, two different identification selections are defined: `loose` and `tight` [113]. In the $WV\gamma$ analysis, the signal photons are required to fulfil the `tight` identification. A complete overview of the variables used for the photon identification are listed in Appendix A.4.

`Loose` The `loose` identification is based on longitudinal and transversal shower shape variables, defined using the middle layer of the electromagnetic calorimeter. In addition, it relies on the ratio of the energy measured in the first layer of the hadronic calorimeter close to the photon candidate and the energy of the photon cluster in the middle layer of electromagnetic calorimeter.

`Tight` The `tight` identification selects a sub-set of the `loose` identified photons. It includes all criteria used for the `loose` identification, but with stricter requirements on the variables. In addition, information from the strip layer of the electromagnetic calorimeter are included. This is especially important to separate prompt photons and photons originating from the decay of a neutral pion, $\pi^0 \to \gamma\gamma$. The fine granularity of the strip layer allows to resolve the slightly different shower shapes of prompt photons and two photons from the π^0 decay. Therefore, the `tight` identification requires the photon candidates to be reconstructed in regions where the strip layer provides good coverage: within $|\eta| < 2.37$, excluding the region of transition between the electromagnetic calorimeter barrel and the end-cap $1.37 < |\eta| < 1.52$. The `tight` photon identification is optimised as a function of the photon conversion type and the pseudorapidity.

Another set of identification criteria, called the `non-tight` identification, is introduced. The identification criteria are optimised to select *fake photons*, objects originating from different sources, such as jets. The `non-tight` identification is needed to estimate the background arising from events containing jets which are misidentified as photons, described in Section 6.2.

`Non-tight` The `non-tight` identification requires the same criteria as the `tight` identification, but at least one of the strip layer requirements must be failed. This definition provides a minimal bias on the isolation energy of the photons (defined in the next section) as the strip layer variables exhibit only low correlations with the isolation energy. The `non-tight` identification has been used in other analyses published by the ATLAS collaboration [13, 115]

The photon identification efficiency is evaluated using three different data-driven methods, each providing results in different energy regimes [51]. For the low energy region, events containing a leptonically decaying Z boson in association with an isolated radiated photon, $Z \to ll\gamma$ are used. For the intermediate energy region a tag-and-probe method is used analysing $Z \to ee$ events. The results are extrapolated for photons, based on the similarity of the electron and photon showers. For the high energy region a matrix-method is used. This method uses an inclusive sample of isolated photons and employs information about the photon object and its isolation from tracks. Figure 5.4 shows the identification efficiencies measured in data collected at a centre-of-mass energy of $\sqrt{s} = 8\,\text{TeV}$ and of $\sqrt{s} = 7\,\text{TeV}$ as a function of the transverse energy and for converted and unconverted photons in different pseudorapidity regions. For unconverted photons, the `tight` identification efficiency rises from 50 % for low E_T photons to about 95 % for high E_T photons [51]. The behaviour of the identification efficiency for unconverted photons is similar, starting from 45 % for low E_T photons and rises up to almost 100 % for high E_T photons [51]. The identification efficiencies, obtained from simulation are found to be different from the efficiencies measured in data. Thus, correction factors are derived and applied to simulation to account for the mismodelling and reproduce the efficiencies observed in data. The uncertainty is largest at low values of the photon E_T with about 4.5 % (5.6 %) and drops to 0.2 % (0.2 %) for unconverted (converted) photons at high values of the photon E_T [51].

Electron

Reconstructed electron candidates contain prompt electrons of the hard interaction and objects originating from misidentified jets, from photon conversions or from hadronic decays. To select mainly prompt electrons, while rejecting most of the electrons arising from other sources, additional selection requirements are imposed on the electron candidates, based on calorimeter and track information. Three different cut-based identification criteria are defined for the

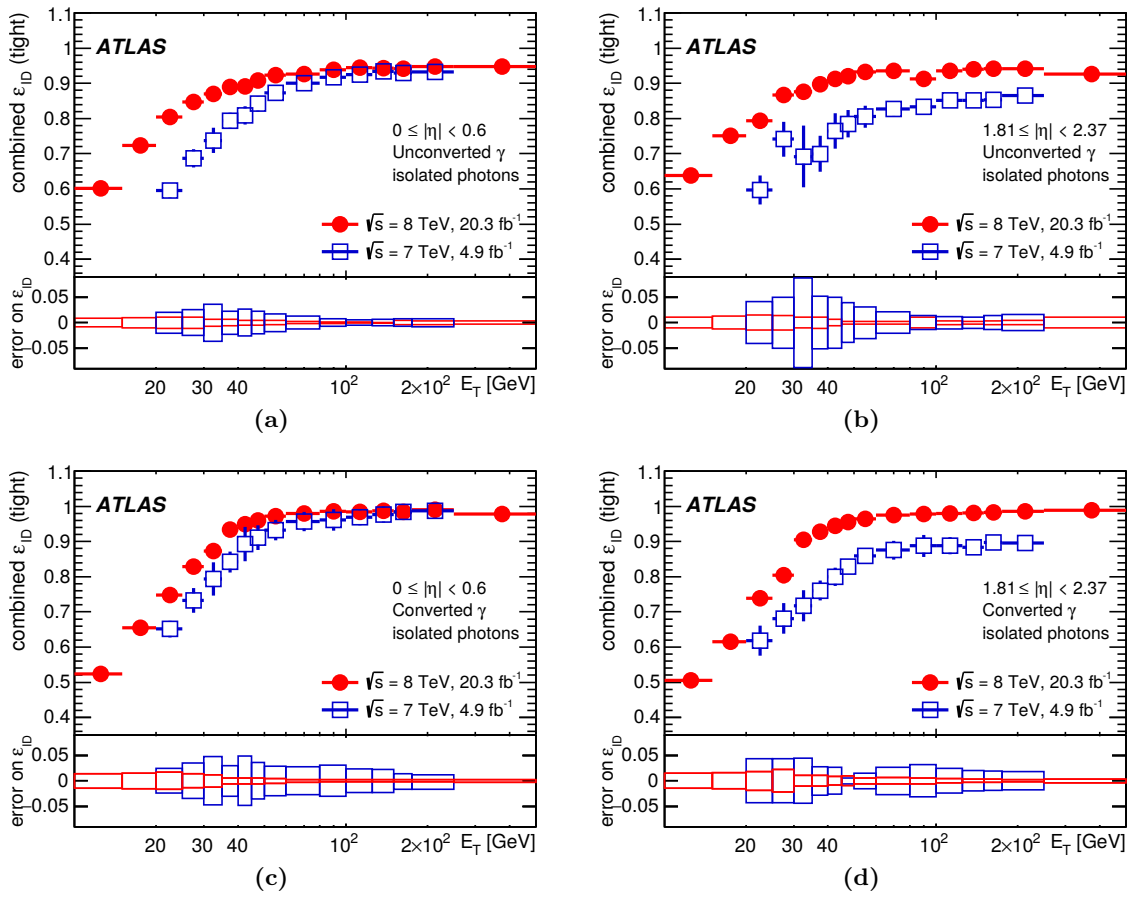

Figure 5.4.: Identification efficiency for the `tight` photon identification as a function of the transverse energy of the photon, for data collected at a centre-of-mass energies of $\sqrt{s} = 8\,\text{TeV}$, shown as red dots and of $\sqrt{s} = 7\,\text{TeV}$, shown as blue, open squares. The upper figures, (a) and (b), illustrate the identification efficiencies for unconverted photons and the lower figures, (c) and (d) for converted photons. Shown are two different pseudorapidity regions $|\eta| < 0.6$ (left) and $1.81 \leq |\eta| < 2.37$ (right). The lower panel depicts the relative uncertainty on the identification efficiencies. Taken from Reference [51].

electrons: `loose`, `medium` and `tight`, imposing stricter selection criteria in a hierarchical order [110]. In the $WV\gamma$ analysis, signal electrons are required to fulfil the `tight` identification criteria and events containing an additional electron, identified with the `medium` criteria are rejected. The three identification criteria are build on one another and are thus presented briefly. A complete overview of the variables used for the electron identification are listed in Appendix A.4.

`Loose` The `loose` identification is based on longitudinal and transversal shower shape variables in the strip and middle layer of the accordion calorimeter. In addition, dedicated track quality criteria are required, as well as requirements on the track-cluster matching and on the ratio of the energy deposited in the first layer of the hadronic calorimeter close to the electrons candidate and the energy of the electromagnetic cluster.

`Medium` The `medium` identification selects a sub-set of the `loose` identified electrons. It is thus based on the same variables, but with stricter selection criteria. To suppress electrons arising from photon conversions, the electron track is required to have a hit in the first layer of the silicon detector. Furthermore, requirements on the absolute value of the transverse impact parameter are imposed, as well as on TRT variables, in case the track extends into the TRT. The rejection power of non-prompt electrons is about an order of magnitude higher for the `medium` identification, compared to the `loose` identification criteria.

`Tight` The `tight` identification is a sub-set of the `medium` criteria, and the common variables have tighter selection requirements applied. Additional requirements on the ratio of the calorimeter cluster energy of the electron and the momentum of the associated track are imposed. Also, electron candidates that are consistent with originating from a photon conversion are rejected. With respect to the `medium` identification, the rejection power of non-prompt electrons or the `tight` identification is increased by a factor of two.

The electron identification efficiencies are determined using a tag-and-probe method at the resonances of $Z \to ee$ and $J/\Psi \to ee$ events [110]. The identification efficiencies are derived in data as well as in simulation. Correction factors are determined and applied to simulation on an event-by-event basis, to match the efficiencies measured in data. Figure 5.5, shows the identification efficiencies for the different identification criteria as a function of the electron transverse momentum and the pseudorapidity. A clear dependence of the identification efficiency on the transverse energy is visible: at low E_{T} values of the electron the identification efficiency is also low and with increasing E_{T} the electron identification efficiency rises. This originates from a better discrimination between prompt electrons and electrons from other sources at high energies in several variables. Also, the `tight` identification efficiency exhibits a strong dependence on the pseudorapidity, arising from the detector geometry. The `tight` electron identification efficiency is about 76 % for prompt electrons, averaged over the pseudorapidity and the transverse energy [110]. Its uncertainty ranges from 1 % for electrons with $E_{\mathrm{T}} > 25\,\mathrm{GeV}$ and rises up to 6 % for lower transverse energies [110].

5.2.4. Photon and Electron Isolation

The photon and electron identification criteria are quite stringent and provide good discrimination between prompt objects and objects originating from other sources. However, many hadronic objects still pass the identification criteria and lead to a misidentification. Prompt photons and electrons are expected to be isolated with only low energy flow around them. In contrast, jets are expected to have many associated tracks and broader showers in the calorimeter. This characteristic can be used, by introducing dedicated isolation criteria for futher rejection of non-prompt objects. Two different types of isolation criteria are defined, either based on calorimeter or track information [51, 110, 111, 113].

The *calorimeter based isolation* is the sum of all energy deposits in the electromagnetic cells around the object within a cone of radius ΔR and referred to as $E_{\mathrm{T}}^{\mathrm{cone}\Delta R \cdot 100}$. For example, if the radius of the cone is $\Delta R = 0.3$, the corresponding variable is referred to as $E_{\mathrm{T}}^{\mathrm{cone30}}$. The energy deposited in the 5×7 cells in $\eta \times \phi$ around the barycentre of the electromagnetic object, is excluded. Energy deposits from the original electromagnetic objects can be contained in the isolation energy $E_{\mathrm{T}}^{\mathrm{cone}\Delta R \cdot 100}$, if the shower is not fully contained within the central cluster. The isolation energy is corrected for this energy leakage, which is depended on the transverse energy

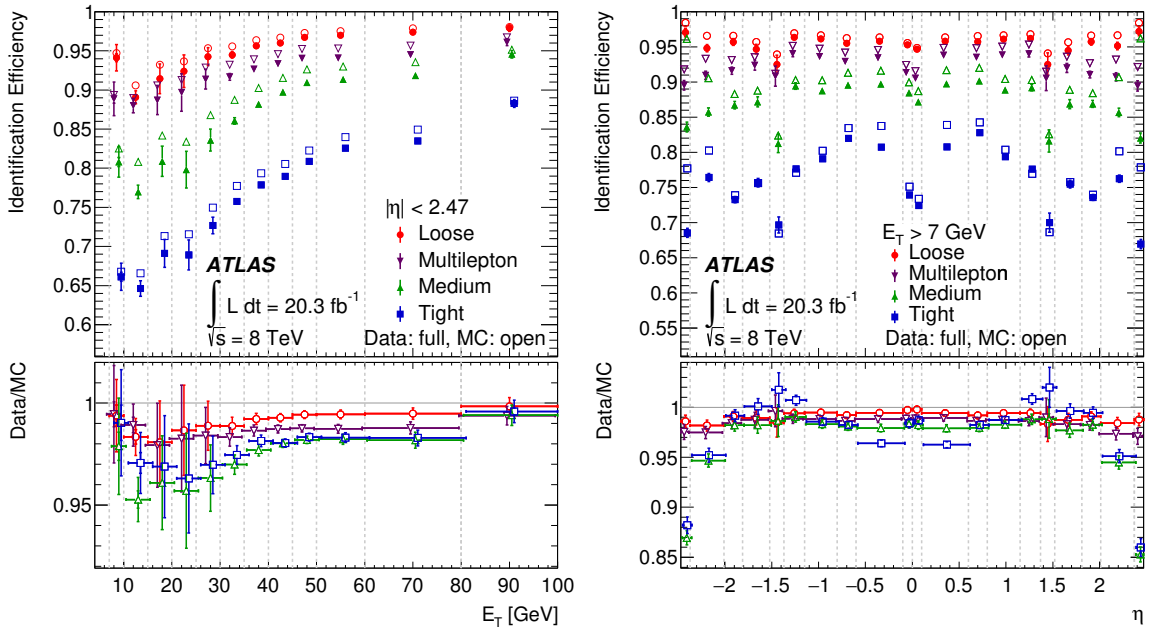

(a) (b)

Figure 5.5.: Electron identification efficiencies for different identification types, represented by different colours, as a function of (a) the electron p_{T} and (b) the electron η. The $WV\gamma$ analysis requires the `tight` identification for signal electrons and rejects events with additional electrons identified with the `medium` criteria. The efficiencies are shown for data as full markers and for Monte Carlo simulation as open markers. The uncertainties represent the statistical (inner error bars) as well as the statistic and systematic uncertainties added in quadrature (outer error bars). The lower panel shows the ratio of the efficiencies measured in data and in Monte Carlo simulation. Taken from Reference [110].

of the electromagnetic object and amounts to a few percent of the E_{T} of the electromagnetic object [115]. In addition, the isolation energy is corrected for pileup and underlying event effects. This correction is determined from the median transverse energy density of the jets, which is scaled to the area of the isolation cone. The obtained corrections fluctuate significantly, reflecting the varying pileup and underlying event conditions in each event [115]. For events with exactly one reconstructed primary vertex, the mean correction is found to be about 540 MeV and increases by about 170 MeV for every additional reconstructed vertex [115]. The distribution of the isolation energy after subtracting the leakage and the pileup corrections is centred around zero and has a root mean square width of 1.5 GeV [115]. Negative values of the isolation energy can occur due to the applied corrections.

The *track based isolation*, $p_{\mathrm{T}}^{\mathrm{cone}\Delta R\cdot 100}$, is only used for electrons and similarly defined as the calorimeter based isolation: it is the scalar sum of all transverse momenta of tracks around the electron within a cone of radius ΔR. The electron track itself is excluded. All tracks considered for the track isolation are required to have a minimum $p_{\mathrm{T}} > 0.4\,\mathrm{GeV}$, to originate from the primary vertex and fulfil special quality requirements, such as a minimum number of silicon hits. This definition is more robust against pileup than the pileup-corrected calorimeter based isolation.

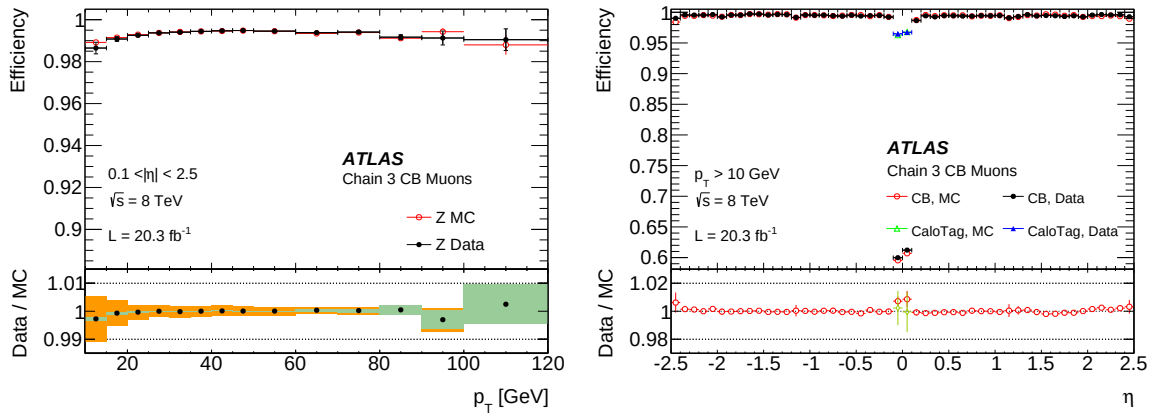

Figure 5.6.: Muon reconstruction efficiency for the Chain3 muons as a function of the (a) muon p_{T} and (b) muon η for different reconstruction types. The $WV\gamma$ analysis uses the combined muons (CB). The efficiencies are shown for data and for Monte Carlo simulation. In the ratio of the left figure, the green areas illustrate the statistical uncertainty and the orange areas illustrate the statistical and systematic uncertainty added in quadrature. The uncertainty in the ratio of the right figure comprises the statistical and systematic uncertainty added in quadrature. Taken from Reference [116].

5.3. Muons

5.3.1. Muon Reconstruction and Identification

The muon reconstruction algorithms are mainly based on tracks in the inner detector and in the muon spectrometer. Tracks in the inner detector are reconstructed as explained in Section 5.2. In the muon spectrometer, the tracks are reconstructed in two steps. In the first step, *regions of activity* (ROA) of the size 0.4×0.4 in $\eta \times \phi$ are localised using information from the trigger chambers and within each ROA, small track segments are reconstructed. In the second step, the separate track segments are combined into the muon track, by fitting the individual hits of the track segments in the different muon chambers. The reconstruction of muons is based on the successful matching of a track in the muon spectrometer to a track in the inner detector, taking the impact of the magnetic field on the trajectory and the energy loss in the calorimeters into account. In this thesis, so-called *Chain3* [116] muons are used, where the tracks of the different sub-detectors are matched using a combination of two methods: either the tracks are matched with a statistical combination or by performing a global refit to the individual hits in the inner detector and the muon spectrometer. The reconstruction efficiency is studied with a tag-and-probe method using $Z \to \mu\mu$ and $J/\psi \to \mu\mu$ events [116]. For muons with $p_{\mathrm{T}} > 10\,\mathrm{GeV}$ and $|\eta| < 2.5$, it is above 99 % with a per mille precision [116]. It is uniform over the transverse momentum, as shown in Figure 5.6(a) as well as over the pseudorapidity range, apart from the region $\eta \approx 0$, as shown in Figure 5.6(b). The efficiency loss at the very central region is due to the only partially equipped muon chambers in this region, since space is needed for service structures of the calorimeters, the inner detector and the magnet system. The reconstruction efficiency of muons is also studied in Monte Carlo simulation and in general, good agreement, within 1 %, is observed with the efficiencies measured in data [116]. However, in order to minimise the difference, correction factors are derived and applied to the simulation to reproduce

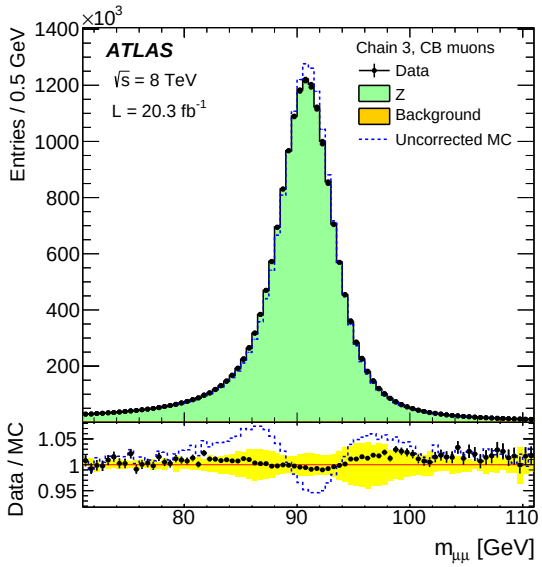

Figure 5.7.: Invariant dimuon mass distribution of $Z \to \mu\mu$ events, for the data, represented as black dots, the uncorrected Monte Carlo prediction, represented as dashed blue line and the corrected Monte Carlo predictions, represented as the filled histogram. The lower panel shows the ratio of the data and the corrected Monte Carlo as black dots, as well as the ratio of the data and the uncorrected Monte Carlo as the dashed blue lines. The yellow band in the lower panel illustrates the systematic uncertainties. Taken from Reference [116].

the efficiency distribution measured in data. The precision of the correction factors are also at the per mille level [116]. In addition, the $WV\gamma$ analysis applies a `medium` identification criteria, imposing requirements on the pseudorapidity range of the muons of $|\eta| < 2.5$ and the number of hits in the muon spectrometer layers.

The muon momentum scale and resolution is measured with $Z \to \mu\mu$, $J/\psi \to \mu\mu$ and $\Upsilon \to \mu\mu$ events in data and in Monte Carlo [116]. Differences observed for the muon momentum scale in data and simulation are corrected in simulation. The momentum scale of the muons and its corresponding correction have an uncertainty between 0.05 % and 0.2 %, depending on the pseudorapidity of the muons [116].

The muon momentum resolution is determined by fitting the invariant dimuon mass $m_{\mu\mu}$, shown in Figure 5.7. In simulation, the invariant dimuon mass distribution is found to be shifted towards larger values and to have a smaller width, with respect to distribution measured in data, as can be seen in the figure. Thus, the simulation applies smearing factors to the momentum measurement of the muon, to reproduce the resolutions observed in data. In Figure 5.7, the improvement of the corrections is clearly visible in the data over Monte Carlo ratio, shown in the lower panel. For the resolution, separate smearing corrections are derived for the inner detector and the muon spectrometer and the uncertainties are between 3 % and 10 %, depending on the pseudorapidities and the transverse momenta of the muons [116].

5.3.2. Muon Isolation

In order to distinguish prompt muons from the hard interaction and muons produced in jets, an isolation criterion is introduced, similar to the one defined for electrons in Section 5.2.4.

Muons, produced by hadron decays within a jet, are in general surrounded by many particles, in contrast to prompt muons that are expected to be isolated. As muons are mainly reconstructed from tracks of the inner detector and the muon spectrometer, a track based isolation p_T^{cone20} is used, defined as the sum over the transverse momenta of all tracks, which are within a cone of radius $\Delta R = 0.2$ of the muon candidate and carry a minimum transverse momentum of 1 GeV. The momentum of the track originating from the muon candidate is excluded. In addition, the tracks are required to originate from the primary vertex and therefore the track based isolation exhibits only a low dependence on the pileup activity.

5.4. Missing Transverse Energy

Momentum imbalances in the plane orthogonal to the beam axis can arise from neutrinos, which do not leave any signature in the detector, as their interaction cross section with matter is very low. Therefore, the reconstruction and calibration of the missing transverse momentum, $\vec{E}_{\mathrm{T}}$, is crucial for processes that contain neutrinos. However, not only neutrinos can induce the momentum imbalance in an event, but also mismeasurements of the reconstructed objects, pileup effects or new particles, not included in the Standard Model. Therefore, robust algorithms are needed to correctly reconstruct the missing transverse momentum in an event. More details about the reconstruction and performance of the missing transverse momentum for the data collected at an centre-of-mass energy of $\sqrt{s} = 8$ TeV in 2012 with the ATLAS detector, is given in Reference [117] and summarised in the following.

The magnitude of the missing transverse momentum is denoted with $E_{\mathrm{T}}^{\mathrm{miss}}$ and referred to as missing transverse energy in the following. It is determined from the sum of the missing transverse energy projections in x- and y-direction:

$$E_{x(y)}^{\mathrm{miss}} = E_{x(y)}^{\mathrm{miss},e} + E_{x(y)}^{\mathrm{miss},\gamma} + E_{x(y)}^{\mathrm{miss},\tau} + E_{x(y)}^{\mathrm{miss,jet}} + E_{x(y)}^{\mathrm{miss},\mu} + E_{x(y)}^{\mathrm{miss,soft}} \tag{5.4}$$

including contributions from electrons (e), photons (γ), visible parts of the hadronically decaying τ leptons (τ), jets and muons (μ). The contributions from electrons, photons, hadronically decaying τ leptons and jets are determined from the calorimeter cells using [118]:

$$E_x^{\mathrm{miss},k} = -\sum_i^{N_{\mathrm{cell}}^k} E_i \sin\theta_i \cos\phi_i \tag{5.5}$$

$$E_y^{\mathrm{miss},k} = -\sum_i^{N_{\mathrm{cell}}^k} E_i \sin\theta_i \sin\phi_i \tag{5.6}$$

with the energy E_i, the azimuthal angle ϕ_i and the polar angle θ_i, for the cell i associated to the reconstructed object k. The contribution arising from muons is derived using the track momenta:

$$E_{x(y)}^{\mathrm{miss},\mu} = -\sum_{\mathrm{muons}} p_{x(y)}^{\mu}. \tag{5.7}$$

It is corrected for energy depositions in the calorimeter, that are associated with reconstructed muons. The terms in Equation 5.4, that are associated with the reconstructed physics objects, are called *hard terms*. Remaining signals in the detector, which are not matched to any of the objects are considered in the so-called *soft term*, $E_{x(y)}^{\mathrm{miss,soft}}$. The soft term is the most challenging

part of the missing transverse energy reconstruction as it involves residual contributions from the hard interaction, which should be considered in the calculation, as well as contributions from pileup or underlying event activity, which should not be considered in the calculation.

In the $WV\gamma$ analysis, the soft term is determined using tracks from the inner detector and called *Track Soft Term*. The Track Soft Term is reconstructed from tracks not associated to any physics object considered in the hard terms, which have $p_{\mathrm{T}} > 0.5\,\mathrm{GeV}$ and are matched to the primary vertex. However, neutral particles are not accounted for, as they do not leave tracks in the inner detector. This leads to a response of the Track Soft Term, which is not as good as the response of a soft term, calculated solely from calorimeter information. Nevertheless, due to the vertex matching, the Track Soft Term is almost independent of the pileup and underlying event activity, in contrast to a soft term, calculated solely from calorimeter information, and is therefore chosen for the $WV\gamma$ analysis. The total systematic uncertainty of the Track Soft Term ranges from 0.3 % to 1.4 % depending on the total transverse momentum of the hard terms.

The final missing transverse energy and its azimuthal angle are determined using:

$$E_{\mathrm{T}}^{\mathrm{miss}} = \sqrt{(E_x^{\mathrm{miss}})^2 + (E_y^{\mathrm{miss}})^2} \tag{5.8}$$

$$\phi^{\mathrm{miss}} = \arctan\Big(\frac{E_y^{\mathrm{miss}}}{E_x^{\mathrm{miss}}}\Big). \tag{5.9}$$

The physics objects used for the determination of the missing transverse energy are calibrated according to their respective calibration schemes. Electron and photon candidates are calibrated to the electromagnetic scale and considered in the calculation when their transverse momentum is above 10 GeV. In addition, electrons are required to fulfil the `medium` identification criteria and photons the `tight` criteria. Muon candidates are considered in the calculation when their transverse momentum is above 5 GeV. The hadronically decaying τ leptons and the jets are calibrated to the hadronic scale using the LCW+JES scheme and considered in the calculation when their transverse momentum is above 20 GeV.

5.5. Baseline Selection

The reconstructed objects must fulfil a dedicated baseline selection to be further considered in the $WV\gamma$ analysis. The baseline selection criteria are given below, for the individual objects considered in this study.

Jets Jets are required to have $p_{\mathrm{T}} > 25\,\mathrm{GeV}$ and to be reconstructed within the rapidity $|y| < 4.4$. To suppress jets arising from pileup, the jet vertex fraction of jets with transverse momenta below 50 GeV in the pseudorapidity range of $|\eta| < 2.4$ is required to be above 0.5. In addition, jets originating from cosmic rays or noise bursts in the calorimeter are rejected and not considered for the analysis.

Photons Photons are required to have a transverse energy of $E_{\mathrm{T}} > 15\,\mathrm{GeV}$ and to fulfil the `tight` identification criteria. Therefore, they must be reconstructed within the central detector region $|\eta| < 2.37$, excluding the transition region of the calorimeter barrel to the end cap $1.37 < |\eta| < 1.52$. In addition, the calorimeter based isolation energy of the photon is required to fulfil $E_{\mathrm{T}}^{\mathrm{iso},\gamma} < 4\,\mathrm{GeV}$, within a cone of $\Delta R = 0.4$ around the photon object.

Leptons Electrons must have a transverse momentum above 7 GeV and be reconstructed within the central detector region with $|\eta| < 2.47$, again excluding the transition region of the calorimeter barrel to the end cap $1.37 < |\eta| < 1.52$. The `medium` isolation criteria are imposed. The calorimeter based isolation E_{T}^{cone30} is required to be below 14 % of the transverse energy of the electron: $E_{\mathrm{T}}^{cone30}\ E_{\mathrm{T}} < 0.14$ and the track based isolation p_{T}^{cone30} below 7 % of the transverse momentum of the electron: $p_{\mathrm{T}}^{cone30}/p_{\mathrm{T}} < 0.07$. Furthermore, the electron track is required to originate from the primary vertex by imposing selection criteria on the longitudinal impact parameter[1] $|z_0 \cdot \sin\theta| < 0.5\,\mathrm{mm}$, as well as the transverse impact parameter[2] $|d_0/\sigma(d_0)| < 5.0$, with its uncertainty $\sigma(d_0)$, determined from the fit to the lepton track.

Muons are required to have a transverse momentum above 7 GeV, to be reconstructed within $|\eta| < 2.4$ and fulfil the `medium` identification criteria. The track based isolation p_{T}^{cone20} is required to be below 10 % of the transverse momentum of the muon: $p_{\mathrm{T}}^{cone20}/p_{\mathrm{T}} < 0.1$. In addition, the transverse impact parameter must fulfil $|d_0/\sigma(d_0)| < 3.0$, to ensure the track stems from the primary vertex.

5.5.1. Overlap Removal

All objects that deposit energy in the calorimeters, are reconstructed as jets, as the jet algorithm runs independently of the electron, photon and muon reconstruction. Therefore, electrons, photons and muons are reconstructed as jets. In order to avoid double counting of the objects, an *overlap removal* (OLR) is applied, which removes any ambiguity of the reconstructed objects. The overlap removal is applied to the objects passing the baseline selection and is executed strictly consecutively in the following order:

1. Electron candidates are discarded, if they are closer than $\Delta R < 0.1$ to a muon or another electron. In the latter case, the electron with the lower transverse momentum is discarded.
2. Photon candidates are discarded, if they are closer than $\Delta R < 0.5$ to a muon or any selected electron.
3. Jets are discarded, if they are closer than $\Delta R < 0.3$ to any selected electron or closer than $\Delta R < 0.5$ to any selected photon.
4. Muon candidates are discarded, if they are closer than $\Delta R < 0.3$ to any selected jet.

The electron-jet and jet-muon overlap removal is not identical, as in the first case the jet is discarded if it is close to an electron and in the latter case, the muon is discarded if a jet is close by. A stricter overlap removal for muons is necessary, to suppress muons that originate from heavy flavour decays within jets. The strict requirements on the photon candidates of $\Delta R > 0.5$ to any other reconstructed object, reduces final state radiation of photons in the $WV\gamma$ production. Objects, fulfilling the baseline selection, are used in the following for the $WV\gamma$ analysis.

[1] The longitudinal impact parameter, z_0, is defined as the shortest distance between a track and the primary vertex, measured in the $y - z$ plane.

[2] The transverse impact parameter, d_0, is defined as the shortest distance between a track and the primary vertex, measured in the $x - y$ plane.

6. Event Selection

In order to study $WV\gamma$ production, the analysed dataset must be enriched with signal events while events arising from background processes are suppressed. This is obtained by defining dedicated selection criteria, which include requirements on the detector status, as any malfunctioning can lead to mismeasurements of the objects, as well as requirements on the properties of the reconstructed physics objects. Defining efficient selection criteria is one of the main challenges in the $WV\gamma$ analysis, since the signal production cross section is very low and many background processes have production cross sections, which are several orders of magnitude larger. Therefore, the chapter starts with the definition of the $WV\gamma$ signature in the detector in Section 6.1 and is followed by a discussion of the backgrounds and their characteristics in Section 6.2. In Section 6.3 the analysed dataset is defined and special event quality criteria are discussed. The complete criteria to select final states containing $WV\gamma$, defining the signal region, are discussed in detail in Section 6.4.

6.1. $WV\gamma$ Signal Definition

The signature of the $WW\gamma$ and $WZ\gamma$ production in the detector depends on the decay of the heavy gauge bosons. In this thesis, the semi-leptonic decay of the two heavy gauge bosons is studied, searching for the signature in the detector of $pp \to l\nu\mathrm{jj}\gamma$, comprising one lepton (l) and missing transverse energy (ν), both arising from the leptonically decaying W boson, at least two jets (jj) originating from the other heavy gauge boson and at least one photon (γ). The $WV\gamma$ production via the quartic coupling with the subsequent semi-leptonic decay is shown in Figure 6.1. Two exclusive channels are analysed, depending on the lepton flavour of the leptonically decaying W boson: the electron and the muon channel ($l = e$ or μ). Decays into τ leptons are not considered as signal. The experimental signature of τ leptons differs from that of electrons or muons, as they decay within the inner detector volume either into light leptons (35 %) or into hadrons (65 %) [35]. This leads to larger reconstruction and identification uncertainties of τ leptons. Therefore, the fraction of events originating from the leptonic decay of τ leptons are not included in the signal definition. This choice has the additional benefit that the theoretical cross section predictions do not need to be corrected for different lepton flavours and their branching ratios.

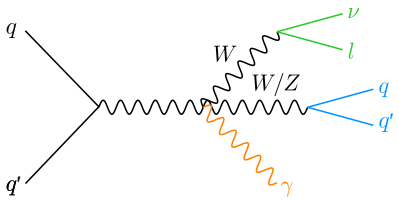

Figure 6.1.: Feynman diagram of the semi-leptonic $WV\gamma$ process, produced via the quartic vertex. The lepton and the neutrino are shown in green, the two jets in blue and the photon in orange.

The signatures of the two processes $WW\gamma$ from the $WZ\gamma$ cannot be separated, as the detector resolution is not high enough. This is illustrated in Figure 6.2, where the distribution of the invariant dijet mass, m_{jj}, is shown for both lepton channels using the Sherpa signal Monte

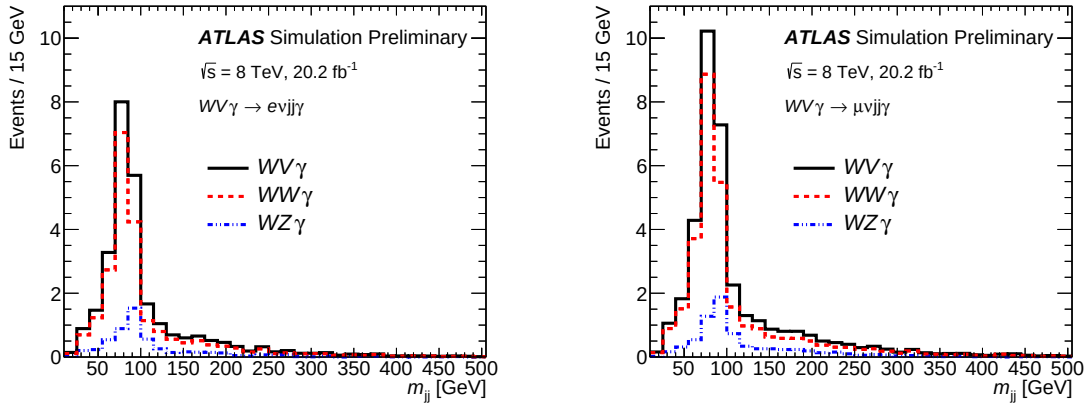

(a) (b)

Figure 6.2.: Invariant dijet mass distribution for the $WW\gamma$ (red) and $WZ\gamma$ (blue) processes as well as for the sum of the two, the $WV\gamma$ process (black) for the (a) electron and (b) muon channel. The expectations are normalised to $20.2\,\mathrm{fb}^{-1}$. [10]

Carlo simulation samples, normalised to NLO. The distributions of the two individual $WW\gamma$ and $WZ\gamma$ processes show a resonance at the respective masses but nevertheless, they have a large overlap and cannot be distinguished clearly. In addition, the $WZ\gamma$ process has a significantly lower cross section than the $WW\gamma$ process, making it even more difficult to distinguish the two processes. Therefore, the sum of the two processes is studied and referred to as $WV\gamma$ process. The dominant contribution to the $WV\gamma$ cross section arises from $WW\gamma$ production with about 86 %; the $WZ\gamma$ process contributes only with 14 %.

6.2. Background Processes

Many processes have similar signatures as the $WV\gamma$ process in the detector and pass the selection criteria. These processes are considered as backgrounds to the $WV\gamma$ analysis. Two main background categories are defined: *irreducible* and *reducible* backgrounds. The irreducible backgrounds refer to processes, where the physics objects are reconstructed and identified correctly in the detector and the reducible backgrounds refer to processes, where at least one physics object is either not reconstructed or misidentified. Thus, in case of a perfect detector, irreducible backgrounds remain backgrounds while the reducible backgrounds would vanish. The choice of the selection criteria, which are defining the signal region, are a trade-off between a high signal efficiency and a good background rejection. In order to optimise the event selection, all backgrounds considered in the $WV\gamma$ analysis are discussed, along with characteristic properties of each.

6.2.1. Irreducible Backgrounds

As irreducible backgrounds to the $WV\gamma$ analysis are considered $W\gamma$ + jets production, $t\bar{t}\gamma$ production and $WV\gamma \to \tau\nu\mathrm{jj}\gamma$ production. Examples of Feynman diagrams for the first two processes are shown in Figure 6.3.

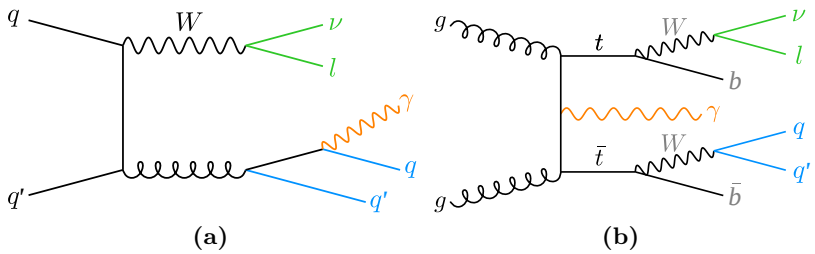

Figure 6.3.: Examples of Feynman diagrams for the irreducible background processes (a) $W\gamma$ + jets production and (b) $t\bar{t}\gamma$ production. The lepton and the neutrino are shown in green, the two jets in blue and the photon in orange.

$W\gamma$ + jets production When the W boson decays leptonically in association with a photon and at least two jets, this final state mimics the signal signature in the detector, as shown in Figure 6.3(a). It is the dominant background and its production cross section is about three orders of magnitude higher [119] than the one of the $WV\gamma$ signal process. Hence, understanding this background component is a crucial part of the analysis. This is especially challenging, as the signal and background signature differ mainly in the properties of the two jets. For the $WV\gamma$ signal, the invariant dijet mass is expected to have a resonance around the masses of the W and Z bosons. In contrast, the invariant dijet mass distribution of the $W\gamma$ + jets process is expected to fall exponentially, as the jets solely originate from QCD processes. Thus, the invariant dijet mass as well as angular information between the two jets are excellent candidates to separate this background process from the $WV\gamma$ signal.

$t\bar{t}\gamma$ production Top quarks are the heaviest of the known elementary particles and decay almost exclusively into a W boson and a bottom quark. The $t\bar{t}\gamma$ process mimics the signal signature when one of the W bosons decays leptonically and the other one hadronically, as depicted in Figure 6.3(b). By identifying jets that are likely to originate from a bottom quark, as described in Section 5.1, events containing top quarks can be effectively selected. The $t\bar{t}\gamma$ production cross section is more than an order of magnitude [120] above the $WV\gamma$ signal production cross section and therefore this process is not negligible in the $WV\gamma$ analysis.

$WV\gamma$ ($\rightarrow \tau\nu$jjγ) production When the τ lepton, originating from the leptonic W boson decay, further decays into an electron or a muon, this process has the same signature in the detector. As discussed in the previous section, $WV\gamma$ production with the subsequent decay of the W boson into a τ lepton is not considered as signal. This is only a minor contribution to the total background composition.

6.2.2. Reducible Backgrounds

Besides the backgrounds arising from irreducible processes, there are also several backgrounds originating from processes where objects are not reconstructed at all or misidentified. The reducible backgrounds considered in this thesis are $Z\gamma$ + jets production, events containing jets which are misidentified as photons, events containing jets which are misidentified as leptons and events containing electrons which are misidentified as photons. Examples of Feynman diagrams for all four processes are illustrated in Figure 6.4.

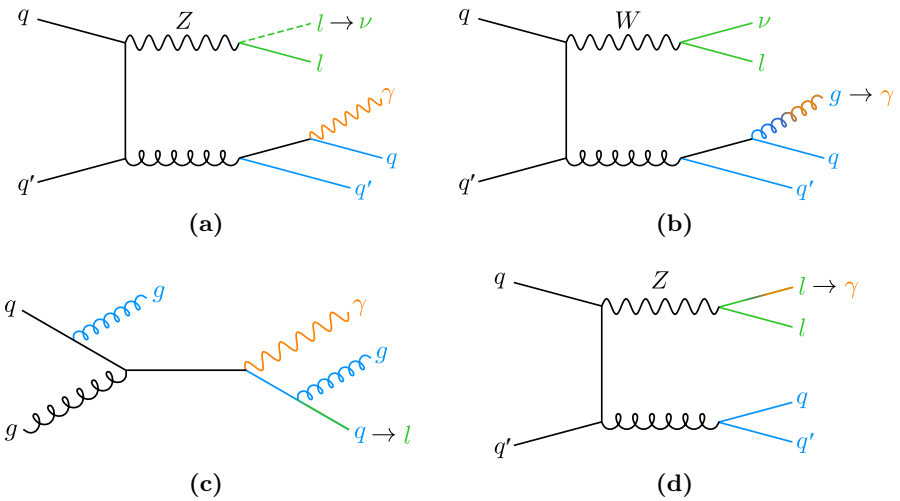

Figure 6.4.: Examples of Feynman diagrams for the reducible background processes: in (a) $Z\gamma$ + jets production, in (b) W + jets production, representing a process where a jet is misidentified as photon, in (c) γ + jets production, representing a process where a jet is misidentified as lepton and in (d) Z + jets production, representing a process where an electron is misidentified as photon. The same colours as before are used. Lines with two colours indicate the original object as well as the object it is misidentified as. The dotted lepton line indicates that the lepton is not reconstructed in the detector and therefore identified as missing transverse energy.

$Z\gamma$ + jets production When the Z boson decays into a pair of leptons in association with a photon and jets, the process mimics the $WV\gamma$ signal signature in case one of the leptons is not reconstructed in the detector, as shown in Figure 6.4(a). This happens mainly due to two different effects: either due to inefficiencies in the reconstruction and identification of the leptons or due to the geometrical acceptance of the detector. In general, the reconstruction and identification efficiencies for electrons and muons ranges from 50 % to 99 %, depending on the lepton flavour, the pseudorapidity and the energy of the lepton, as explained in Chapter 5. The geometrical acceptance of the detector for leptons is restricted to the central region for the $WV\gamma$ analysis. Leptons which fall outside this region, for example in forward direction, are not considered. In addition, lepton flavour specific restrictions on the geometrical acceptance are imposed, for example electron candidates are not allowed to fall in the transition region of the calorimeter barrel and the end-cap, due to large uncertainties in this region. The $Z\gamma$ + jets production cross section is also more than three orders of magnitude larger [14] than the $WV\gamma$ signal process. Even though the rate to miss one lepton in the detector is low, the large production cross section of the $Z\gamma$ + jets process makes it a considerable background component.

Jets misidentified as photons This background is referred to as *fake photons (γ) from jets* background in the following. When a jet is misidentified as photon, events originating from processes such as W + jets, $t\bar{t}\gamma$, WV + jets or single top production can fulfil the signal selection criteria. The W + 3 jets production is the dominant background process in this category and shown as example in Figure 6.4(b). A jet can be misidentified as a photon, if the shower shape of the jet in the calorimeter is similar to a shower shape expected for photons. However, jets which are misidentified as photons typically have broader energy depositions in the calorimeter in contrast to prompt photons. Thus, the calorimeter based isolation energy, as defined in

Section 5.2.4, is expected to be larger for jets and provides a good candidate to separate prompt photons and fake photons from jets. The probability that a jet is misidentified as a photon is very small, but due to the abundant jet production at the LHC, this is the second largest background for the $WV\gamma$ analysis.

Jets misidentified as leptons This background is referred to as *fake leptons (l) from jets* background in the following. When a jet is misidentified as lepton, γ + jets production mimics the signal signature, as illustrated in Figure 6.4(c). This background is expected to have no or only low genuine missing transverse energy, $E_{\mathrm{T}}^{\mathrm{miss}}$, as no neutrinos are produced in the process. Since the $WV\gamma$ signal is expected to have real missing transverse energy, the $E_{\mathrm{T}}^{\mathrm{miss}}$ is a viable observable to separate this background from the $WV\gamma$ signal.

Different mechanisms leads to the misidentification of jets as electrons or muons. Therefore, the contribution from this background is not expected to be of the same magnitude in the two channels. In the muon channel, there are two main processes for the misidentification: punch-through jets or muons which originate from heavy flavour decays. Punch-through jets, defined in Section 5.1, are jets which are not fully contained within the calorimeter volume and thus generate a signal in the muon spectrometer. In general, punch-trough jets are rare, as the calorimeters are designed to stop the entire jet within the calorimeter volume. Muons arising from heavy flavour decays are real muons, but since they are not part of the original hard interaction, they are not considered as signal muons. Typically, fake muons arising from either mechanism are surrounded by substantial activity in the inner detector and an isolation requirement on the objects helps to discriminate between prompt muons and fake muons from jets. The misidentification of a jet as an electron happens when the jet fulfils the identification criteria of the electron, as described in Section 5.2. The misidentification rate is lower in the muon channel, due to the low rates of punch-through jets and because of the jet-muon overlap removal, defined in Section 5.5.1, which rejects very efficiently muons, originating from heavy flavour decays.

Misidentified photons from electrons This background is referred to as *fake photons (γ) from electrons (e)* background in the following. When an electron is misidentified as photon, $Z \to ee$ events can fulfil the signal selection requirements, as shown in Figure 6.4(d). This is the dominant contribution to this background in the electron channel. $Z \to \tau\tau$ events with the subsequent decay into two electrons or an electron and a muon is found to be negligible for both lepton channels. The production of $t\bar{t}$ events contributes to this background when one of the two W bosons from the top quark decay, decays into an electron, which is misidentified as a photon and the other W boson, decays either into an electron or a muon and is correctly identified. The contribution of $t\bar{t}$ production is about a factor of ten smaller than the contribution from $Z \to ee$ events. As the latter one is absent in the muon channel, this background is expected to be significantly smaller in the muon channel. The misidentification of an electron as photon can happen, as the two objects have very similar detector signatures. Electrons can be misidentified as unconverted, single- or double-track converted, as defined in Section 5.2.

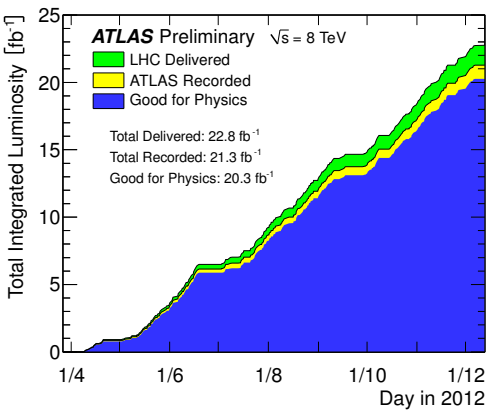

Figure 6.5.: The total integrated luminosity delivered by the LHC in green, recorded by the ATLAS detector in yellow and passing good data quality requirements, the baseline for physics analyses in blue. Taken from Reference [121].

6.3. Dataset and Event Quality

The dataset used for the analysis was recorded in 2012 with the ATLAS detector at a centre-of-mass energy of $\sqrt{s} = 8\,\text{TeV}$. Figure 6.5 shows the total integrated luminosity delivered by the LHC, the fraction recorded by the ATLAS detector and the amount of luminosity identified as good quality data[1], called *good for physics* in the figure. The total luminosity, delivered by the LHC refers to the amount of data, which is provided by the LHC once stable beam conditions are declared until the request of the LHC to bring the ATLAS detector into a safe standby mode. The ATLAS detector records slightly less luminosity than delivered by the LHC, about 93 %, due to inefficiencies of the data acquisition system and due to the time the ATLAS detector needs to be ramped up to be fully operational after the LHC declared stable beam conditions. The good quality criteria require all subsystems to be up and running, to ensure a high quality of the reconstructed physics objects. About 95 % of the events recorded by the ATLAS detector fulfil these criteria. Since the $WV\gamma$ analysis studies final state objects that rely on all detector components, the data identified to be of good quality is used, corresponding to an integrated luminosity of $20.2\,\text{fb}^{-1}$ [58].

Further event quality criteria are defined on an event-by-event level and require the exclusion of corrupted or incomplete events, which occur in rare cases after restarting one or more subsystems, or the exclusion of events with noise bursts or misbehaving cells in the calorimeters. To assure at least one proton-proton collision per event, the presence of at least one well-measured vertex [122, 123] is required. A vertex is well-measured when at least three tracks with transverse momenta larger than 400 MeV are associated to it. In addition, jet quality requirements are imposed, to ensure the correct calculation of the missing transverse energy. Events are discarded if they contain jets that are likely to originate from beam induced backgrounds or cosmic rays. Also events containing jets with a significant amount of energy measured in misbehaving detector regions are rejected. Thus, dedicated quality criteria, based on calorimeter variables, are applied on an event-by-event basis, since jets arising or affected from any of these defects have slightly distorted shower shapes in the calorimeter.

[1]The figure was released before the final luminosity determination in August 2016 [58], leading to slightly different numbers in the Figure with respect to the integrated luminosity given in other figures.

Trigger Selection The $l\nu jj\gamma$ final states are selected by single lepton triggers. Events in the electrons channel must either pass the `EF_e24vhi_medium1` or the `EF_e60_medium1` trigger criteria [124]. These triggers are defined on event filter (`EF`) level, as described in Section 3.2.5. The `EF_e24vhi_medium1` trigger requires one electron with transverse momentum larger than 24 GeV (`e24`). The trigger is not prescaled and to keep the rate of this trigger at a reasonable level and meet the bandwidth limitations of the detector readout, the electron candidate is required to be isolated (`i`). The threshold criteria on the energy of the electron is varying (`v`) depending on the geometrical region, accounting for inactive material in front of the calorimeters. Furthermore, a hadronic veto is applied, requiring that the shower does not extend into the hadronic calorimeter (`h`). The isolation criteria, the varying threshold criteria and the hadronic veto requirement, lead to inefficiencies of the trigger at high electron transverse momenta. Therefore, the higher threshold trigger, `EF_e60_medium1`, requiring one electron with a transverse momentum above 60 GeV, ensures that the efficiency remains high with increasing electron p_{T}. Both triggers have the `medium1` identification criteria applied to the electron, which is less stringent than the identification criteria required for the reconstructed electron in the analysis.

In the muon channel, the event is either selected by passing the `EF_mu24i_tight` or the `EF_mu36_tight` [125] trigger criteria. The triggers are defined similarly to the electron triggers. Either one isolated muon with a transverse momentum above 24 GeV is required in the event or one muon with transverse momentum larger than 36 GeV without any additional requirements on the isolation. The muon candidates must fulfil `tight` identification criteria, however they are less stringent than the identification criteria required for the reconstructed muons in the analysis.

For both lepton channels, the efficiency of the combination of the two triggers reaches its plateau at transverse momenta of about 25 GeV. The signal selection efficiency of the two triggers is about 96 % in the electron channel and about 77 % in the muon channel. Furthermore, it is required that the reconstructed lepton is identical to the lepton passing the trigger requirements by matching the two objects within a cone of radius $\Delta R < 0.1$. This is done to obtain theoretically well defined trigger efficiencies.

6.4. $WV\gamma$ Event Selection

In order to efficiently select the $WV\gamma$ signal while rejecting as much background events as possible, special selection criteria are developed. The requirements are optimised with respect to the signal efficiency $\epsilon_{sig} = \frac{S}{\sqrt{S+B}}$ where S is the number of signal events and B is the number of background events. The signal selection criteria are discussed in the following section and are applied to objects, fulfilling the baseline selection, defined in Section 5.5. A tabular overview of the requirements imposed on the reconstructed objects is given in Appendix A.5.

Photon At least one photon, as defined in the baseline selection. These require the photon to be identified as `tight`, to have a transverse energy above 15 GeV and to be central $|\eta| < 2.37$, excluding the transition region of the calorimeter barrel to the end cap $1.37 < |\eta| < 1.52$. In addition, the calorimeter based isolation $E_{\mathrm{T}}^{\mathrm{iso},\gamma}$ is required to be smaller than 4 GeV, to suppress fake photons from jets. If more than one photon satisfy these criteria in an event, the photon with the highest E_{T} is used.

Criteria	Electron Candidate	Muon Candidate
Calorimeter Based Isolation	$E_{\mathrm{T}}^{cone30}/E_{\mathrm{T}} < 0.14$	-
Track Based Isolation	$p_{\mathrm{T}}^{cone30}/p_{\mathrm{T}} < 0.07$	$p_{\mathrm{T}}^{cone20}/p_{\mathrm{T}} < 0.1$
Vertex	$\lvert d_0/\sigma(d_0)\rvert < 5.0$	$\lvert d_0/\sigma(d_0)\rvert < 3.0$
	$\lvert z_0 \cdot \sin\theta\rvert < 0.5\,\mathrm{mm}$	-

Table 6.1.: Isolation and vertex requirements on the lepton candidates for the electron (left) and the muon channel (right). The polar angle θ is defined as the angle between the lepton track and the beam line.

***W* boson** Exactly one `tight` electron or one `medium` muon must be present in the event. The transverse momentum of the signal lepton is required to be larger than 25 GeV to ensure the triggers are fully efficient. Events are discarded if a second lepton with $p_{\mathrm{T}}^{l} > 7\,\mathrm{GeV}$ is reconstructed[1]. The lepton candidate is required to be within the acceptance of the inner detector, with $|\eta^e| < 2.47$ and excluding the transition region $1.37 < |\eta^e| < 1.52$ for electron candidates, and with $|\eta^\mu| < 2.4$ for muon candidates. In order to reduce fake leptons, stringent isolation criteria on the calorimeter based isolation as well as on the track based isolation, are imposed on the lepton objects. For further suppression of fake leptons from jets, the tracks of the objects are required to be close to the primary vertex, by imposing selection criteria on the longitudinal impact parameter, z_0, as well as on the transverse impact parameter, d_0 and its uncertainty $\sigma(d_0)$. The uncertainty on the transverse impact parameter is determined from the fit to the lepton track. The precise isolation and vertex criteria are listed in Table 6.1.

To account for the neutrino in the signal process, the missing transverse energy of the event must satisfy $E_{\mathrm{T}}^{\mathrm{miss}} > 30\,\mathrm{GeV}$. The transverse mass of the lepton-neutrino system is defined as:

$$m_{\mathrm{T}}^{l\nu} = \sqrt{2\,p_{\mathrm{T}}^{l} E_{\mathrm{T}}^{\mathrm{miss}}\,(1 - \cos\Delta\phi)}. \tag{6.1}$$

where $\Delta\phi$ is the azimuthal angle between the lepton; the transverse mass $m_{\mathrm{T}}^{l\nu}$ must also exceed 30 GeV. Both, the $E_{\mathrm{T}}^{\mathrm{miss}}$ as well as the $m_{\mathrm{T}}^{l\nu}$ requirements effectively suppress backgrounds arising from fake leptons from jets. In addition, the invariant mass of the electron-photon pair is required to not coincide with the Z boson mass peak, $|m_{e\gamma} - m_Z| > 10\,\mathrm{GeV}$, in the electron channel. This requirement reduces backgrounds originating from Z boson production, such as the fake photons from electrons background, which arises predominantly from $Z \to ee$ events.

***V* boson** For the reconstruction of the hadronically decaying V boson, at least two central jets with $|\eta| < 2.5$ and a transverse momentum of $p_T > 25\,\mathrm{GeV}$ are required in the event. If more than two jets fulfil the selection criteria, the two jets with the highest transverse momenta are chosen. Jets exceeding the requirement on the pseudorapidity are not considered, as these jets have larger jet energy scale uncertainties, as shown in Figure 5.2(b) in Section 5.1.2. To suppress jets arising from pileup, the jet vertex fraction, defined in Section 5.1.3, is required to exceed 0.5 and is applied to jets with transverse momenta below 50 GeV in the pseudorapidity range of the inner detector of $|\eta| < 2.4$. In addition, events containing the production of top quarks are

[1] In the electron channel a looser identification criteria (`medium`) is required for additional electrons in the events, leading to stricter veto conditions.

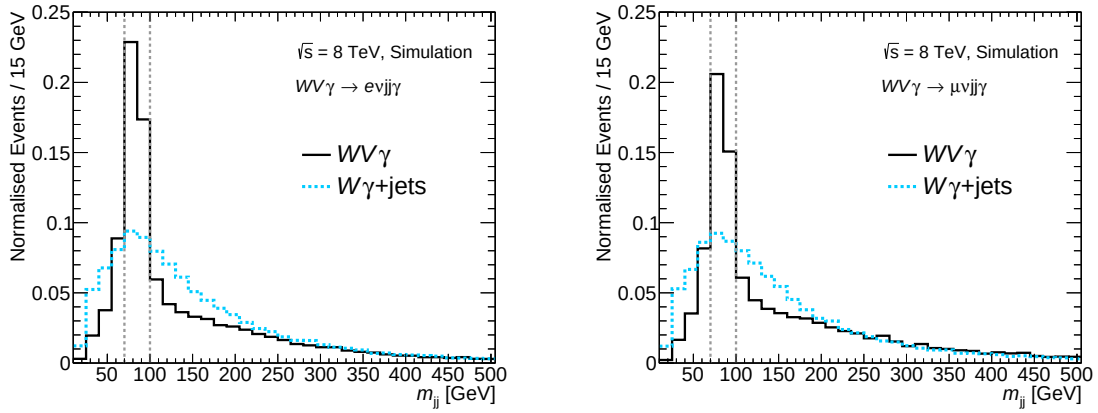

(a) **(b)**

Figure 6.6.: Shape comparison of the invariant dijet mass distribution m_{jj} for the $WV\gamma$ signal (solid black line) and $W\gamma$ + jets (dashed blue line) processes in the (a) electron and (b) muon channel. Both distributions are obtained from simulation.

suppressed, by allowing no b-tagged jets in the event (b-jet veto). Since the algorithm to identify jets originating from b-hadrons utilises tracking information, as described in Section 5.1.4, the choice of the pseudorapidity requirement on jets to be within the acceptance of the inner detector is additionally motivated.

The $W\gamma$ + jets production is the dominant background in the analysis and its suppression crucial for the $WV\gamma$ analysis. The main difference between the $W\gamma$ + jets background and the $WV\gamma$ signal is the origin of the two jets. For the signal, the two jets are produced from the hadronically decaying heavy gauge boson, leading to a resonance in the invariant dijet mass distribution m_{jj}. For the $W\gamma$ + jets process, the jets are produced from QCD processes and the m_{jj} distribution is expected to fall exponentially. The invariant dijet mass distribution for the $WV\gamma$ signal and the $W\gamma$ + jets background is shown in Figure 6.6 for both lepton channels. The $W\gamma$ + jets distribution exhibits an increase at low m_{jj} values, which solely arises from the jet selection criteria. The signal region is defined to be on the W and Z boson mass resonance, $70\,\mathrm{GeV} < m_{\mathrm{jj}} < 100\,\mathrm{GeV}$ and indicated by the grey, dotted line in the figure. This requirement reduces the signal by 50 % in both lepton channels, but reduces the $W\gamma$ + jets background by more than 71 %, improving the signal significance. Additional requirements on the angular separation between the two jets decrease the $W\gamma$ + jets contribution in the signal region further. Jets, originating from the hadronically decaying heavy gauge boson, are in general closer to each other than jets produced in QCD processes. Therefore, requirements on the difference between the pseudorapidities of the two jets, $|\Delta\eta(\mathrm{jet}_1,\mathrm{jet}_2)| < 1.2$ and their spacial separation, $\Delta R(\mathrm{jet}_1,\mathrm{jet}_2) < 3.0$, are imposed. In the following, the two variables are referred to as $|\Delta\eta_{\mathrm{jj}}|$ and ΔR_{jj}, respectively. These two additional selection criteria are correlated and the chosen combination is optimised with respect to the signal significance. The comparison of the $|\Delta\eta_{\mathrm{jj}}|$ and the ΔR_{jj} distributions for the $WV\gamma$ signal and $W\gamma$ + jets background process are shown in Figure 6.7(a) and Figure 6.7(b), respectively. In both figures, the combination of the two lepton channels is shown, as the distributions are similar for the individual lepton channels. The grey, dotted line indicates the value of the selection requirement and lower values are allowed in the signal region. The requirement on the $|\Delta\eta_{\mathrm{jj}}|$ is the more stringent criteria of the two.

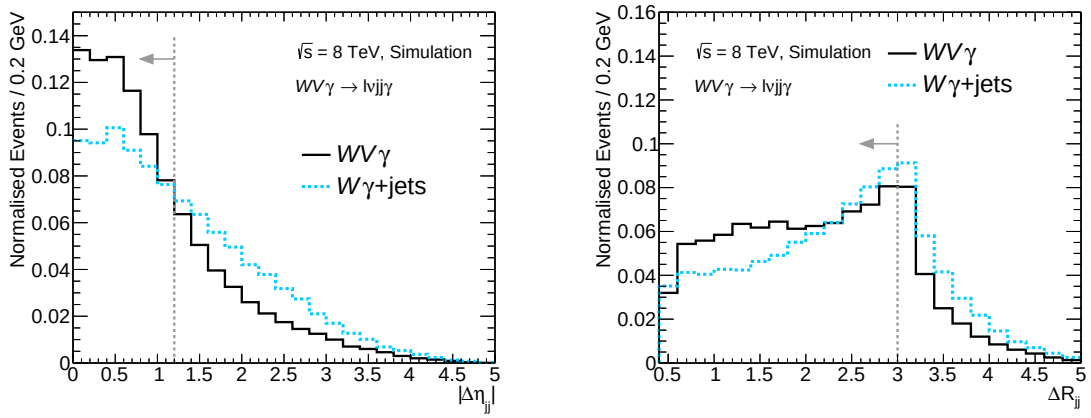

(a) **(b)**

Figure 6.7.: Shape comparison in (a) of the $|\Delta\eta_{jj}|$ distribution and in (b) of the ΔR_{jj} distribution for the $WV\gamma$ signal (solid black) and $W\gamma$ + jets (dashed blue) processes. The combination $l\nu jj\gamma$ of the two lepton channels are shown. Both distributions are obtained from simulation.

6.4.1. Selection Stability

Applying the defined selection criteria to the data, yields 490 events in the electron and 599 events in the muon channel. The lower event yield in the electron channel is due to the additional requirement on the invariant mass of the electron-photon pair $m_{e\gamma}$. The stability of the event yields are studied as a function of time and the pileup activity. Data periods are time intervals of the order of a few weeks, where the detector and run conditions were very similar during the data taking. In 2012, the data taking was divided into eleven periods out of which ten are used for this analysis. Figure 6.8 shows the event yield per data taking period for both lepton channels, normalised to one fb^{-1}. The normalisation to one fb^{-1} is necessary, since different integrated luminosities were collected in the periods. To test the stable behaviour, a constant function is fitted to the data. The fit predicts on average (23.6 ± 1.1) events per one fb^{-1} in the electron channel, and (28.9 ± 1.2) events in the muon channel. The obtained χ^2 value divided by the degrees of freedom of the distribution (NDF) provides a quantification of the quality of the fit, as it is expected to be unity in case the fit describes the data well. The χ^2 test yields a $\chi^2/\text{NDF} = 12.4/9.0$ for the electron channel and $\chi^2/NDF = 12.8/9.0$ for the muon channel, validating a stable behaviour in time for both lepton selections. In addition, the pileup dependence of the selection is studied as a function of the average number of interactions per bunch crossing $\langle\mu\rangle$. The event yield, normalised to one fb^{-1}, is depicted in Figure 6.9 separately for both lepton channels. The bins for low and high $\langle\mu\rangle$ values of the distribution have large uncertainties arising from low statistics and large normalisation factors. For central $\langle\mu\rangle$ values the distribution exhibits a relatively flat behaviour. As before, a constant function is fitted to the data and a χ^2 test is used to quantify how well the fit describes the data, yielding $\chi^2/\text{NDF} = 7.7/6.0$ for the electron and $\chi^2/\text{NDF} = 13.2/7.0$ for the muon channel. The results from the χ^2 test show reasonable agreement between the fit and the data and therefore verify the selection can be assumed independent of the pileup conditions.

In summary, the selection criteria defined in this section, are found to be sound and well founded. The selected events are used for the background estimation of the $WV\gamma$ analysis, which is presented in the next chapter.

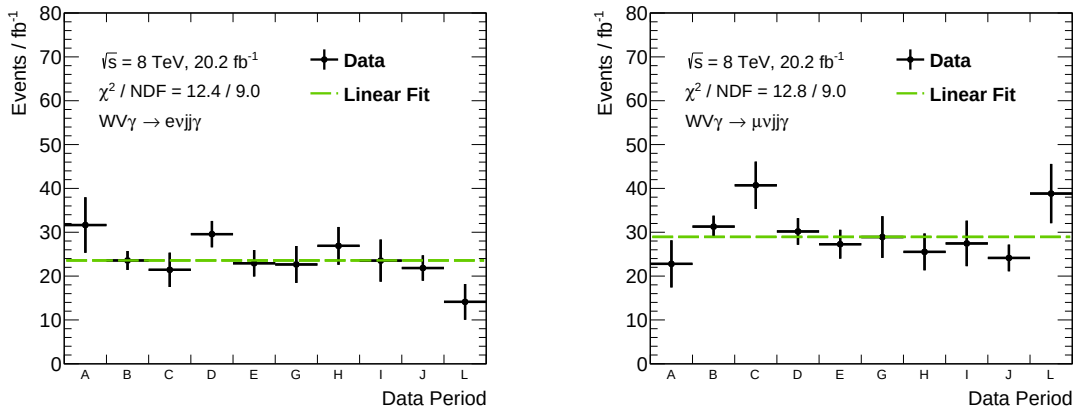

(a) **(b)**

Figure 6.8.: Event yield in data as a function of the data taking periods normalised to one fb^{-1} for the (a) electron and (b) muon channel. A constant function is fitted to the data validating the time-independence of the selection.

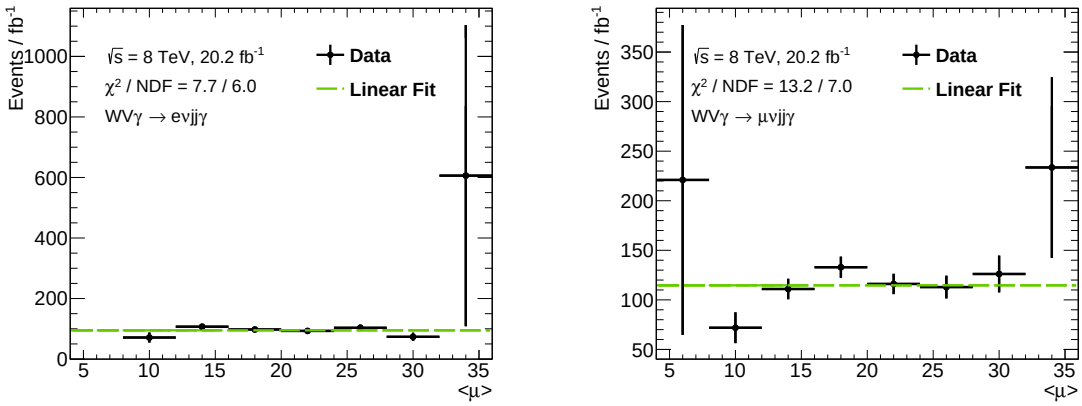

(a) **(b)**

Figure 6.9.: Event yield in data as a function of the average number of interactions per bunch crossing $\langle\mu\rangle$ normalised one fb^{-1} for the (a) electron and (b) muon channel. A constant function is fitted to the data to validate the pileup independence of the selection.

7. Background Estimation

The dataset obtained with the selection criteria defined in the previous chapter is enriched with signal events. However, it also contains events arising from the background processes and their event yields in the signal region needs to be determined. The background estimation is the essential part of the $WV\gamma$ analysis due to the small signal cross section and the large background contributions.

This chapter starts with an overview of the background estimation method in Section 7.1. Three background components are determined using three individual data driven methods. Two of the data driven methods, are based on the concept of binned extended likelihood fitting, which is introduced in Section 7.2. Backgrounds originating from $W\gamma$ + jets are constrained using a maximum likelihood fit to the m_{jj} distribution, discussed in Section 7.3 and backgrounds originating from fake leptons from jets are constrained using a maximum likelihood fit to the $E_{\mathrm{T}}^{\mathrm{miss}}$ distribution, discussed in Section 7.4. The template shapes for the maximum likelihood fits are presented in Section 7.5. The third data driven method is a two-dimensional sideband method, used to constrain backgrounds originating from fake photons from jets, and is explained in Section 7.6. Additional backgrounds considered in the $WV\gamma$ analysis are discussed in Section 7.7. Since the three data driven methods are interdependent, they are performed simultaneously, which is explained in Section 7.8. In Section 7.9, the final background estimation in the signal region is presented along with the discussion of the systematic uncertainties.

7.1. Method Overview

The backgrounds of the $WV\gamma$ analysis are split into two categories: backgrounds estimated with data-driven methods, such as $W\gamma$ + jets, fake photons from jets and fake leptons from jets and backgrounds estimated with Monte Carlo simulation, such as $t\bar{t}\gamma$, $Z\gamma$ + jets, fake photons from electrons and $WV\gamma$ ($\rightarrow \tau\nu\mathrm{jj}\gamma$). The $W\gamma$ + jets background ist constrained using a fit to the m_{jj} distributions, the fake leptons from jets background is constrained using a fit to the $E_{\mathrm{T}}^{\mathrm{miss}}$ distribution and the fake photons from jets background is constrained using a *two-dimensional sideband* method. As each of the methods relies on the results of the other two, they are interdependent and thus performed simultaneously. The three data-driven methods are combined into one *simultaneous fit*, illustrated in Figure 7.1.

The dominant background to $WV\gamma$, arises from $W\gamma$ + jets production and has very similar kinematic properties as the signal; the only difference is the origin of the jets. A data-driven method minimises the dependence on theoretical models and reduces the experimental uncertainties. To constrain this background, the invariant dijet mass distribution, m_{jj}, is used as it allows to separate the $W\gamma$ +jets background from the $WV\gamma$ signal, as shown in Figure 6.6 in Section 6.4. A control region, $\mathrm{CR}_{m_{\mathrm{jj}}}$, is defined in the region of the invariant dijet mass $m_{\mathrm{jj}} < 70\,\mathrm{GeV}$ or $m_{\mathrm{jj}} > 100\,\mathrm{GeV}$. This corresponds to the inverted selection criteria on the invariant dijet mass and it thus independent of it. In the control region the $WV\gamma$ signal

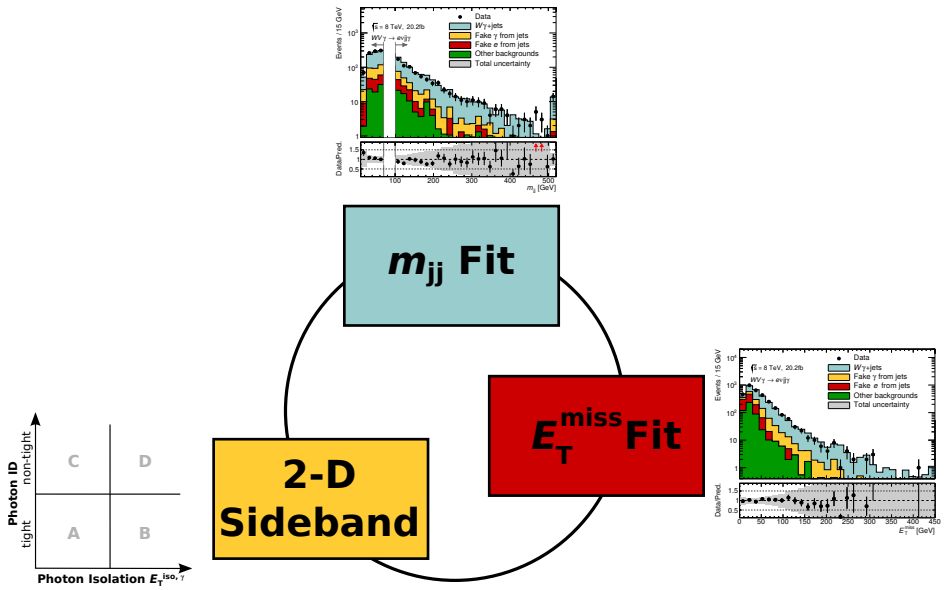

Figure 7.1.: Overview of the simultaneous background estimation method. The three data-driven methods, a binned extended likelihood fit to the m_{jj} distribution, a binned extended likelihood fit to the $E_{\mathrm{T}}^{\mathrm{miss}}$ distribution and a two-dimensional sideband method are performed simultaneously to estimate the $W\gamma$ + jets, the fake l from jets and the fake γ from jets backgrounds.

contamination is about 0.7 % (0.8 %) in the electron (muon) channel. In the following, the $WV\gamma$ signal contribution is neglected in the control region $\mathrm{CR}_{m_{\mathrm{jj}}}$, which has the advantage that the background estimation is independent of the signal modelling and in addition provides more conservative cross sections limits, presented in Chapter 8. More details are given in Appendix A.7. The invariant dijet mass distribution in the control region $\mathrm{CR}_{m_{\mathrm{jj}}}$ is fit using a binned extended maximum likelihood method.

In the $WV\gamma$ analysis, the fake leptons from jets background arises predominantly from γ + jets production. Backgrounds originating from misidentified objects are in general not well modelled in simulation. Therefore, a data-driven method is employed to estimate the contribution of the fake lepton from jets background. This background has a similar shape in the m_{jj} distribution as the dominant $W\gamma$ + jets background, since in both the jets originate from QCD processes. Thus, a fit using the m_{jj} distribution cannot distinguish these two background components. Genuine missing transverse energy is expected in $W\gamma$ + jets production due to the neutrino in the event in contrast to γ + jets production, where no or only low genuine missing transverse energy is expected. Therefore, the $E_{\mathrm{T}}^{\mathrm{miss}}$ distributions allows to distinguish the fake lepton from jets from the $W\gamma$ + jets background. A second control region, $\mathrm{CR}_{E_{\mathrm{T}}^{\mathrm{miss}}}$, is introduced which has an increased fake lepton from jets contribution. This control region is also defined with an inverted invariant dijet mass requirement, $m_{\mathrm{jj}} < 70\,\mathrm{GeV}$ or $m_{\mathrm{jj}} > 100\,\mathrm{GeV}$, and no selection criteria on the missing transverse energy[1]. Figure 7.2 depicts the missing transverse energy distributions in the control region $\mathrm{CR}_{E_{\mathrm{T}}^{\mathrm{miss}}}$ for the $W\gamma$ + jets and the fake leptons from jets background, normalised to unity for comparability. The missing transverse energy distribution is also fit using a binned extended maximum likelihood method in the control region $\mathrm{CR}_{E_{\mathrm{T}}^{\mathrm{miss}}}$. Since the control region also applies the inverted invariant dijet mass selection criterion, the signal contribution is again neglected in the fit.

[1]The nominal selection criteria on the missing transverse energy is $E_{\mathrm{T}}^{\mathrm{miss}} > 30\,\mathrm{GeV}$.

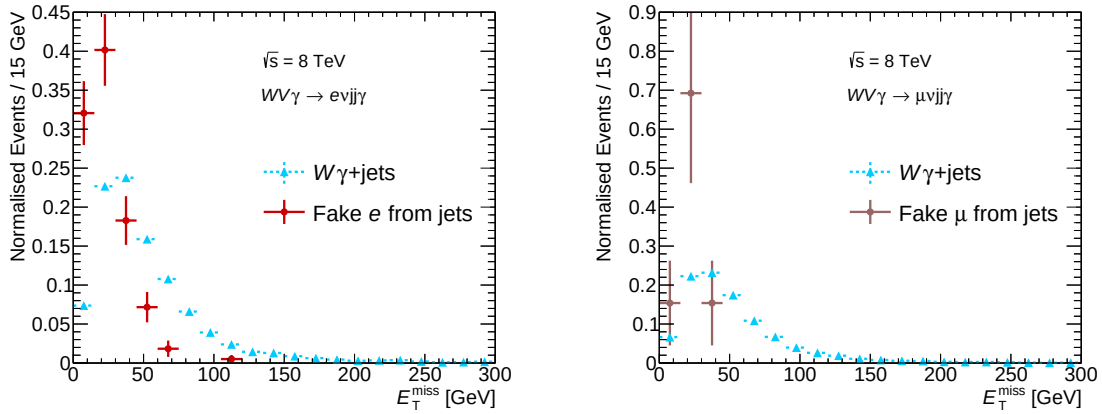

Figure 7.2.: The $E_{\mathrm{T}}^{\mathrm{miss}}$ distributions in the control region $\mathrm{CR}_{E_{\mathrm{T}}^{\mathrm{miss}}}$ for the $W\gamma$ + jets process in red and for events containing fake leptons from jets in blue, normalised to unity in the (a) electron and (b) muon channel. The $W\gamma$ + jets distribution is obtained using simulation and the the fake leptons from jets distribution using data with dedicated selection criteria, explained in Section 7.5.

For the $WV\gamma$ analysis, background events containing jets, which are misidentified as photons, arise predominantly from W + 3 jets production, but also from WV + jets, $t\bar{t}$ or single top production. The m_{jj} and $E_{\mathrm{T}}^{\mathrm{miss}}$ distributions for the fake photon from jets background are very similar to the distributions for the $W\gamma$ + jets background, as both processes contain a leptonically decaying W boson and predominantly jets, arising from QCD processes. Therefore, the fake photons from jets background cannot be determined using either of the above described maximum likelihood fits. To constrain the fake photon from jets background, a two-dimensional sideband method [115] is used. In this method, four orthogonal regions, A, B, C and D, are defined using two sets of non-correlated variables: the photon isolation and the photon identification criteria, both defined in Section 5.2. Region A is the same as control region $\mathrm{CR}_{m_{\mathrm{jj}}}$ and regions B, C and D are defined to be enriched with events where a jet is misidentified as a photon. The number of fake photons from jets in region A is determined by relating the event counts in the four regions.

The three data-driven methods are interdependent as each method relies on the results from the other two as input. Therefore, they are performed simultaneously and the obtained result is extrapolated into the signal region. The event yields of the $W\gamma$ + jets, fake photons from jets and fake leptons from jets backgrounds are the free parameters in the simultaneous fit while all other backgrounds, estimated using Monte Carlo simulation, are fixed in the fit procedure.

7.2. Binned Extended Maximum Likelihood Fit

The $W\gamma$ + jets and fake lepton from jets backgrounds are constrained by using separate maximum likelihood methods. The maximum likelihood method is a statistical concept to determine the values of unknown parameters, which describe the measured data best. This section reviews the main ideas of the method, following the description of reference [126].

A given variable x is distributed according to its probability density function (p.d.f.), $f(\boldsymbol{\theta}_{\mathbf{true}})$, which is a function of the true parameters, $\boldsymbol{\theta}_{\mathbf{true}} = (\theta_{\text{true},1}, ..., \theta_{\text{true},p})$. The probability to measure the value x_a given the parameters $\boldsymbol{\theta}_{\mathbf{true}}$, is $f(x_a|\boldsymbol{\theta}_{\mathbf{true}})$. Therefore, the probability to obtain several values $x_1, ..., x_z$, is given by the joint probability function, f_{joint}, which multiplies the individual probabilities:

$$f_{\text{joint}} = \prod_{a=1}^{z} f(x_a|\boldsymbol{\theta}_{\mathbf{true}}) \tag{7.1}$$

However, usually in an experiment the true values of the parameters $\boldsymbol{\theta}_{\mathbf{true}}$ are not known. An experiment, which measures the given variable x, obtains the values $x_1, ..., x_z$, when it is repeated z times. The parameters $\boldsymbol{\theta}_{\mathbf{true}} = (\theta_1, ..., \theta_p)$ are unknown. The *likelihood function*:

$$L(\boldsymbol{\theta}) = \prod_{a=1}^{z} f(x_a|\boldsymbol{\theta}) \tag{7.2}$$

quantifies how likely the values of the parameters $\boldsymbol{\theta}$ are, given the measurement $x_1, ..., x_z$. Thus, the likelihood function is equivalent to the joint probability function f_{joint}, but dependents on the unknown parameters $\boldsymbol{\theta}$. Maximising the likelihood for the parameters $\boldsymbol{\theta}$ by solving $\frac{dL(\boldsymbol{\theta})}{d\boldsymbol{\theta}} = 0$, yields the parameter values $\hat{\boldsymbol{\theta}} = (\hat{\theta}_1, ..., \hat{\theta}_p)$. For these values $\hat{\boldsymbol{\theta}}$, the probability to obtain the measured data is maximal and thus they are called the *maximum likelihood estimators*.

When the data sample becomes very large, it is inconvenient to determine the likelihood function for every single event. Therefore, the measured values of the variable x are filled into a histogram with m bins. The total number of events in the histogram, N, is the sum over all bin entries $\boldsymbol{n} = (n_1, ..., n_m)$:

$$N = \sum_{i=1}^{m} n_i \tag{7.3}$$

where n_i is the measured event yield in bin i. Since the given variable x is distributed according to a continuous probability density function $f(x|\boldsymbol{\theta})$, the probability, p_i, that an event is filled in bin i is given by the integral:

$$p_i(\boldsymbol{\theta}) = \int_{x_i^{min}}^{x_i^{max}} f(x|\boldsymbol{\theta})dx \tag{7.4}$$

$$\equiv f_i(x|\boldsymbol{\theta}) \tag{7.5}$$

with x_i^{min} (x_i^{max}) being the lower (upper) edge of bin i. The continuous probability density function fulfils per definition $\int_{-\infty}^{\infty} f(x|\boldsymbol{\theta})dx = 1$. The joint probability density function of the histogram is a multinomial distribution:

$$f_{\text{joint}} = \frac{N!}{n_1! \cdots n_m!} p_1^{n_1} \cdots p_m^{n_m} \tag{7.6}$$

describing the probability that n_1 entries end up in the first bin, n_2 entries in the second and so on. The expectation values $\boldsymbol{\nu} = (\nu_1, ..., \nu_m)$ for each bin is derived using:

$$\nu_i = N \cdot p_i(\boldsymbol{\theta}). \tag{7.7}$$

Applying this to the joint probability function, the *binned likelihood* is given by:

$$L(\boldsymbol{\theta}) = \prod_{i=1}^{m} \left(\frac{\nu_i(\boldsymbol{\theta})}{N} \right)^{n_i} \tag{7.8}$$

with n_i the measured event yield in each bin and where all terms independent of the parameters $\boldsymbol{\theta}$ are dropped, as they are only a fixed offset in the likelihood function and have no impact on the minimisation. In the limit where the number of bins approaches infinity and the bin size converges to zero, the binned maximum likelihood function becomes the same as the unbinned likelihood function.

In the previous considerations, the total number of events in the histogram, N, is fixed. However, for many experimental setups, including the one of this thesis, this is not a good assumption, as another measurement is likely to obtain a different total event yield. Therefore, the total number of events N is considered as a random value from a Poisson distribution with expectation value ν. Similar to Equation 7.3, the expectation value for the histogram is given by the sum over the expectation values for each bin:

$$\nu = \sum_{i=1}^{m} \nu_i. \tag{7.9}$$

The joint probability density function is the product of a Poisson distribution, describing the probability to measure N events when ν are expected, and the multinomial distribution, described in Equation 7.6:

$$f_{\text{joint}} = \frac{\nu^N e^{-\nu}}{N!} \frac{N!}{n_1! \cdots n_m!} \left(\frac{\nu_1}{\nu} \right)^{n_1} \cdots \left(\frac{\nu_m}{\nu} \right)^{n_m} = \prod_{i=1}^{m} \frac{\nu_i^{n_i}}{n_i!} e^{-\nu_i}. \tag{7.10}$$

Comparing the two expressions shows that the joint probability density function can be interpreted as the product of one global Poisson distribution with a multinomial distribution, but also as the product of several Poisson distributions, one for each bin of the histogram. Therefore, the so-called *extended binned likelihood* is given by:

$$L(\boldsymbol{\theta}) = \prod_{i=1}^{m} \left(\nu_i(\boldsymbol{\theta}) \right)^{n_i} e^{-\nu_i(\boldsymbol{\theta})} \tag{7.11}$$

where ν_i is the expectation value in each bin and dependent on the parameter $\boldsymbol{\theta}$ as well as the expectation value ν via:

$$\nu_i(\nu, \boldsymbol{\theta}) = \nu \, f_i(x|\boldsymbol{\theta}). \tag{7.12}$$

Instead of maximising the likelihood, it is often computationally more convenient to minimise the negative logarithm of the likelihood ($-\log L$), as the product in the likelihood function is converted into a sum. The result of the maximisation is not changed, since the logarithm is monotonically increasing and the parameters minimising $-\log L$ are also maximising L. Therefore, Equation 7.11 becomes [126]:

$$-\log L(\boldsymbol{\theta}) = \sum_{i=1}^{m} \nu_i(\nu, \boldsymbol{\theta}) - \sum_{i=1}^{m} n_i \log(\nu_i(\nu, \boldsymbol{\theta})). \tag{7.13}$$

Applying this formalism to the analysis in this thesis, the parameters of interest $\boldsymbol{\theta}$, are the event

yields of the background components. This allows to rewrite the probability density function as sum over all parameters $\boldsymbol{\theta}$:

$$f_i(x|\boldsymbol{\theta}) = \sum_{j=1}^{p} \theta_j \, f_{ij}(x) \tag{7.14}$$

where $f_{ij}(x)$ is the probability density function of background component j in bin i. The θ_j is the relative contribution of the background component j and therefore holds $\sum_{j=1}^{p} \theta_j = 1$. Using Equations 7.12 and 7.18, the first term of Equation 7.13, simplifies to [127]:

$$\sum_{i=1}^{m} \nu_i(\nu, \boldsymbol{\theta}) = \sum_{i=1}^{m} \nu \sum_{j=1}^{p} \theta_j f_{ij}(x) \tag{7.15}$$

$$= \sum_{j=1}^{p} \nu\theta_j \sum_{i=1}^{m} f_{ij}(x) \tag{7.16}$$

$$= \sum_{j=1}^{p} \nu\theta_j \;\equiv\; \sum_{j=1}^{p} N_j. \tag{7.17}$$

In Equation 7.16 it is used, that $\sum_{i=1}^{m} f_{ij}(x)$ is the probability density function for the background component j of variable x , which is normalised to unity per definition. The expected number of events for background component j is defined as $N_j \equiv \nu\theta_j$, in Equation 7.17. Applying a similar transformation to the second term, Equation 7.13 ca be re-written to [127]:

$$-\log L(\boldsymbol{\theta}) = \sum_{j=1}^{p} N_j - \sum_{i=1}^{m} n_i \log\Big(\sum_{j=1}^{p} N_j f_{ij}(x)\Big) \tag{7.18}$$

where N_j is the expected event yield of the background component j, n_i are the measured event yields per bin and $f_{ij}(x)$ the probability density function of background component j in bin i. The probability density functions used in this thesis are obtained from distributions of a specific variable normalised to unity and in the following referred to as *template shapes*. The template shapes are determined separately for each background component and are described in Section 7.5.

7.3. $W\gamma$ + Jets Background: m_{jj} Fit

The $W\gamma$ + jets background is constrained by performing a binned extended maximum likelihood fit[1] to the m_{jj} distribution in the control region $\mathrm{CR}_{m_{\mathrm{jj}}}$, with the inverted requirement on the invariant dijet mass, $m_{\mathrm{jj}} < 70\,\mathrm{GeV}$ or $m_{\mathrm{jj}} > 100\,\mathrm{GeV}$. This definition of the control region allows to select a sample enriched with events originating from $W\gamma$ + jets and the $WV\gamma$ signal contribution is neglected. The maximum likelihood fit range extends from $10\,\mathrm{GeV} < m_{\mathrm{jj}} < 70\,\mathrm{GeV}$ to $100\,\mathrm{GeV} < m_{\mathrm{jj}} < 505\,\mathrm{GeV}$. For the definition of the likelihood, the following definitions are used:

1. $N^{W\gamma}$, the expected event yield of the $W\gamma$ + jets background and $f^{W\gamma}$, its probability density function.

[1] For ease of simplicity, the binned extended likelihood fit is in the following referred to as maximum likelihood fit.

2. $N^{\text{fake }\gamma}$, the expected event yield of the fake photons from jets background and $f^{\text{fake }\gamma}$, its probability density function.

3. $N^{\text{fake }l}$, the expected event yield of the fake leptons from jets background and $f^{\text{fake }l}$, its probability density function.

4. The expected event yields for the $t\bar{t}\gamma$, electron misidentified as photons ($e \to \gamma$), $Z\gamma$ + jets as well as the $WV\gamma$ (τ) backgrounds are fixed in the minimisation procedure and collectively defined as:
$N^{\text{fixed}} f^{\text{fixed}} = N^{t\bar{t}\gamma} f^{t\bar{t}\gamma} + N^{e\to\gamma} f^{e\to\gamma} + N^{Z\gamma} f^{Z\gamma} + N^{WV\gamma(\tau)} f^{WV\gamma(\tau)}$.

The determination of the template shapes, used as the probability density functions, is discussed in Section 7.5.

Using the definitions, the negative logarithm of the binned extended likelihood function for the variable m_{jj} and the free parameters $\boldsymbol{N} = (N^{W\gamma},\ N^{\text{fake }\gamma},\ N^{\text{fake }l})$, is given by:

$$\begin{aligned} -\log L(m_{\mathrm{jj}}|\boldsymbol{N}) =& \left(N^{W\gamma} + N^{\text{fake }\gamma} + N^{\text{fake }l} + N^{\text{fixed}}\right) \\ & - \sum_{i=0}^{m} n_i \log\left(N^{W\gamma} f^{W\gamma} + N^{\text{fake }\gamma} f^{\text{fake }\gamma} + N^{\text{fake }l} f^{\text{fake }l} + N^{\text{fixed}} f^{\text{fixed}}\right). \end{aligned} \tag{7.19}$$

The total number of expected background events in the control region $\mathrm{CR}_{m_{\mathrm{jj}}}$ is the sum over all components $N^{\text{bkd}} = (N^{W\gamma} + N^{\text{fake }\gamma} + N^{\text{fake }l} + N^{\text{fixed}})$.

7.4. Fake Lepton from Jets Background: $E_{\mathrm{T}}^{\mathrm{miss}}$ Fit

The fake lepton from jets background is constrained using a maximum likelihood fit to the $E_{\mathrm{T}}^{\mathrm{miss}}$ distribution. The maximum likelihood fit is performed in the control region $\mathrm{CR}_{E_{\mathrm{T}}^{\mathrm{miss}}}$ to increase the amount of events containing fake leptons from jets. The fit range is defined as $0\,\mathrm{GeV} < E_{\mathrm{T}}^{\mathrm{miss}} < 300\,\mathrm{GeV}$. In the control region $\mathrm{CR}_{E_{\mathrm{T}}^{\mathrm{miss}}}$, the $WV\gamma$ signal contribution is also neglected due to the inverted selection criteria on m_{jj}. For the definition of the likelihood, the following definitions are used:

1. $\widetilde{N}^{W\gamma}$, the expected event yield of the $W\gamma$ + jets background and $\widetilde{f}^{W\gamma}$, its probability density function.

2. $\widetilde{N}^{\text{fake }\gamma}$, the expected event yield of the fake photons from jets background and $\widetilde{f}^{\text{fake }\gamma}$, its probability density function.

3. $\widetilde{N}^{\text{fake }l}$, the expected event yield of the fake leptons from jets background and $\widetilde{f}^{\text{fake }l}$, its probability density function.

4. The expected event yields for the $t\bar{t}\gamma$, electrons misidentified as photons, $Z\gamma$ + jets as well as the $WV\gamma$ (τ) backgrounds are fixed in the minimisation procedure and collectively defined as:
$\widetilde{N}^{\text{fixed}} \widetilde{f}^{\text{fixed}} = \widetilde{N}^{t\bar{t}\gamma} \widetilde{f}^{t\bar{t}\gamma} + \widetilde{N}^{e\to\gamma} \widetilde{f}^{e\to\gamma} + \widetilde{N}^{Z\gamma} \widetilde{f}^{Z\gamma} + \widetilde{N}^{WV\gamma(\tau)} \widetilde{f}^{WV\gamma(\tau)}$.

The tilde indicates the difference of the variables with respect to the variables defined in the control region $\mathrm{CR}_{m_{\mathrm{jj}}}$. The negative logarithm of the likelihood for the binned extended

likelihood fit with the missing transverse energy as random variable and the free parameters $\widetilde{\boldsymbol{N}} = (\widetilde{N}^{W\gamma},\ \widetilde{N}^{\text{fake }\gamma},\ \widetilde{N}^{\text{fake }l})$ is given by:

$$-\log L(E_{\text{T}}^{\text{miss}}|\widetilde{\boldsymbol{N}}) = \left(\widetilde{N}^{W\gamma} + \widetilde{N}^{\text{fake }\gamma} + \widetilde{N}^{\text{fake }l} + \widetilde{N}^{\text{fixed}}\right) - \sum_{i=0}^{m} n_i \log\left(\widetilde{N}^{W\gamma}\widetilde{f}^{W\gamma} + \widetilde{N}^{\text{fake }\gamma}\widetilde{f}^{\text{fake }\gamma} + \widetilde{N}^{\text{fake }l}\widetilde{f}^{\text{fake }l} + \widetilde{N}^{\text{fixed}}\widetilde{f}^{\text{fixed}}\right). \tag{7.20}$$

The total number of expected background events in the control region $\text{CR}_{E_{\text{T}}^{\text{miss}}}$ is the sum over all components $\widetilde{N}^{\text{bkd}} = (\widetilde{N}^{W\gamma} + \widetilde{N}^{\text{fake }\gamma} + \widetilde{N}^{\text{fake }l} + \widetilde{N}^{\text{fixed}})$. The event yields in the two control regions $\text{CR}_{E_{\text{T}}^{\text{miss}}}$ and $\text{CR}_{m_{\text{jj}}}$ are related via scale factors and is explained in detail in Section 7.8.

7.5. Templates Shapes

The probability density functions, used in the maximum likelihood fits and referred to as *template shapes* in the following, are obtained from the distribution of the respective background, normalised to unity. Different strategies are used to determine the template shapes for the individual background components. For the $W\gamma$ + jets background, the template shapes ($f^{W\gamma}/\widetilde{f}^{W\gamma}$) are taken from simulation in the respective control regions ($\text{CR}_{m_{\text{jj}}}$ / $\text{CR}_{E_{\text{T}}^{\text{miss}}}$), as good agreement between data and theory has been observed by the ATLAS collaboration [119]. The template shapes for the $t\bar{t}\gamma$ ($f^{t\bar{t}\gamma}/\widetilde{f}^{t\bar{t}\gamma}$), $Z\gamma$ + jets ($f^{Z\gamma}/\widetilde{f}^{Z\gamma}$) and $WV\gamma$ (τ) ($f^{WV\gamma(\tau)}/\widetilde{f}^{WV\gamma(\tau)}$), as well as the fake photons from electrons ($f^{e\to\gamma}/\widetilde{f}^{e\to\gamma}$) backgrounds, are also obtained from simulation in the respective control regions.

For the fake leptons from jets background, the template shapes $f^{\text{fake }l}/\widetilde{f}^{\text{fake }l}$ are obtained from data using dedicated criteria to enrich the selection with events containing fake leptons from jets. This is done, as the misidentification of jets is not well modelled in simulation. Due to the low fake rate and the high cross section of the γ + jets process, several million simulated events are necessary to achieve reasonably small statistical uncertainties of the template shapes. The available simulation samples of this process do not have the required event yields and thus yield inconclusive results, due to huge statistical uncertainties. Therefore, the template shapes are selected using data.

The mechanisms to misidentify a jet as an electron are different from the mechanisms to misidentify a jet as a muon and thus, the requirements to select the template shapes are optimised separately for the two lepton channels. The requirements to obtain the dedicated template selection are optimised for high statistics while keeping the contamination from correctly identified leptons small. The selection criteria are based on different trigger selections and special requirements on the isolation variables, the impact parameters as well as the identification criteria of the leptons. A complete list of the modified requirements is given in Table 7.1. All other selection criteria, on the m_{jj}, $\Delta\eta_{jj}$, ΔR_{jj} and the b-jet veto, are also applied.

In both lepton channels, the trigger used for the dedicated template selections, is different than the nominal trigger. The alternative triggers[1] have the same minimum threshold criteria on

[1] The full name of the alternative trigger items are `EF_e24vh_medium1` (`EF_mu24_tight`) in the electron (muon) channel.

	Electron Channel	Muon Channel
Trigger	`EF_e24vh_medium1`	`EF_mu24_tight`
Track Based Isolation	$p_{\mathrm{T}}^{cone30}/p_{\mathrm{T}} > 0.07$	p_{T}^{cone20} / $p_{\mathrm{T}} > 0.1$
Calorimeter Bases Isolation	none	none (nominal)
Object ID	`medium` && `!tight`	`medium` (nominal)
$\lvert z_0 \cdot \sin\theta \rvert$	none	none (nominal)
$\lvert d_0/\sigma(d_0) \rvert$	none	> 3
$E_{\mathrm{T}}^{\mathrm{miss}}$	none	

Table 7.1.: Modified selection criteria to obtain the template shapes for the fake lepton from jets background. All other selection criteria required for the control region $\mathrm{CR}_{m_{\mathrm{jj}}}$ are applied in addition.

the energy of the lepton as the nominal triggers, but the isolation criteria on the objects is dropped, leading to a significant increase of the trigger rates. To cope with the bandwidth requirements of the readout, both alternative triggers are prescaled. The integrated luminosities of the alternative triggers are evaluated using the ATLAS Luminosity Calculator [128] and found to be $2.7\,\mathrm{fb}^{-1}$ for both. Due to the specific choice of the alternative triggers, the isolation requirement of the leptons can be modified, without introducing a bias to the selection.

In the electron channel, the track based isolation is inverted to require more transverse momentum around the electron track in the inner detector and the calorimeter based isolation is dropped, to allow more energy depositions around the electron cluster. Both criteria enhance the selection of events, which contain jets misidentified as electrons. The identification criteria is chosen to be less strict, but orthogonal to the nominal selection by requiring the electron candidate to pass the `medium` identification but to fail at least one criterion of the `tight` selection. The requirements on the transverse and longitudinal impact parameters are also dropped.

In the muon channel, the selection requirements are similarly defined. The muon candidate has to fulfil the nominal identification criteria, but the selection on the track based isolation is inverted, to allow more tracks around the muon in the inner detector. The requirement on the transverse impact parameter is inverted, in order to enhance events containing muons originating from heavy flavour decays, as they are expected to be displaced from the primary vertex. No requirements on the calorimeter isolation or on the longitudinal impact parameter are imposed, as for the nominal selection.

In Figure 7.3 the $E_{\mathrm{T}}^{\mathrm{miss}}$ distribution is shown for the data enriched with fake leptons from jets selected with the specified criteria. The contamination of events containing true leptons in this region is determined using the truth information of the simulated events and is also depicted in the figure. For both lepton channels the contamination is found to be below 2 % and the template shapes are corrected for it.

The template shapes for the background containing events where a jet misidentified as a photon, $f^{\mathrm{fake}\,\gamma}/\widetilde{f}^{\mathrm{fake}\,\gamma}$, are also taken from data. The criteria are optimised to enhance the selection with events where a jet is misidentified as a photon. Since jets are expected to have more energy depositions in the calorimeter cells around the object, the photon isolation requirement is dropped. Furthermore, the photon candidates are required to be identified as `non-tight`, where the photon must fail at least one criterion of the strip layer criteria of the calorimeter, as defined in Section 5.2. In addition to the modified photon identification criteria, the inverted m_{jj}

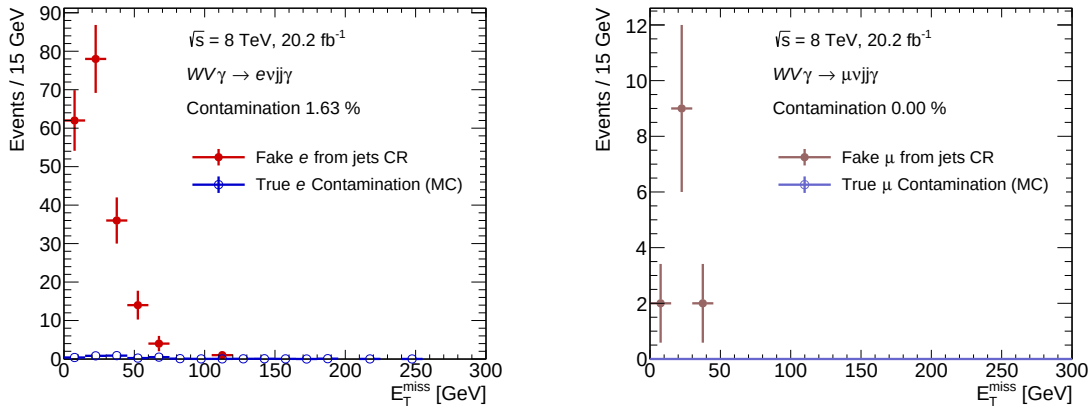

Figure 7.3.: Data selected with the dedicated selection criteria to obtain the template shapes for the fake photons from jets background is shown in red and the contamination of events containing true leptons with this selection is shown in blue for the (a) electron and (b) muon channel.

criterion is required for the template shapes used in the $\mathrm{CR}_{m_{\mathrm{jj}}}$. This data sample coincides with region C+D of the two-dimensional sideband method, discussed in the following section. For the template shapes used in the $\mathrm{CR}_{E_{\mathrm{T}}^{\mathrm{miss}}}$, the m_{jj} criteria is inverted and the $E_{\mathrm{T}}^{\mathrm{miss}}$ requirement is dropped.

In Figure 7.4 the template shapes for the fake photon from jets background obtained from data are compared to the template shapes obtained from simulation, normalised to unity for better comparability. The template shapes obtained from data have significantly smaller statistical uncertainties. Good agreement between the template shapes obtained from simulation and from data is observed within the statistical uncertainties for both lepton channels and both distributions. This indicates that the distributions are not biased by the dedicated selection and it is justified to use the template shapes selected from data.

The contamination of events containing real photons in the template selection for the fake photons from jets is estimated to be below 20 %. As this is a relatively high contamination, a second data selection is defined by requiring the `non-tight` identification and inverting the nominal criterion on the isolation energy of the photon candidate, $E_{\mathrm{T}}^{\mathrm{iso}} > 4\,\mathrm{GeV}$, corresponding to region D in the two-dimensional sideband method. This second template selection has a smaller contamination from events containing real photons of only a few percent. The template shapes are found to be in good agreement between the two template selections and therefore region C+D is chosen to obtain the template shapes for the maximum likelihood fits, as these template shapes have higher statistics and thus lower statistical uncertainties.

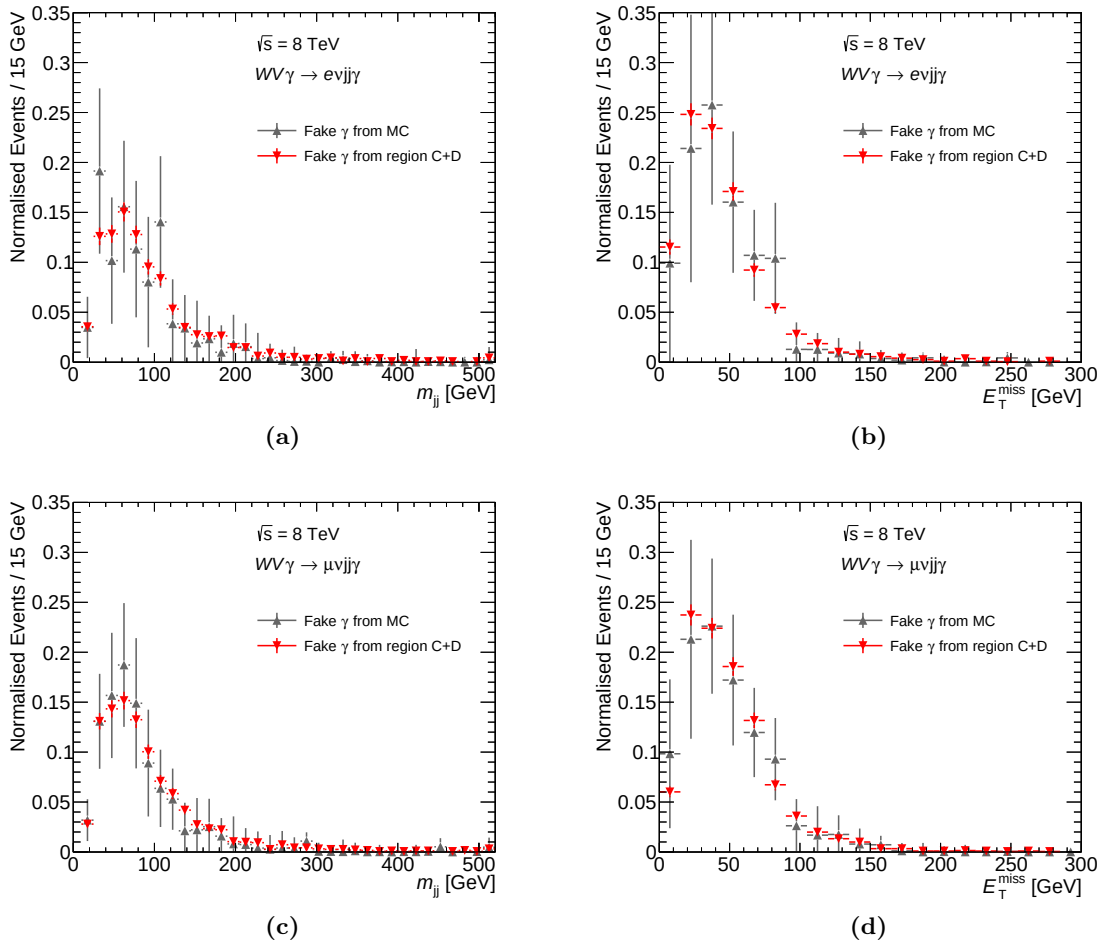

Figure 7.4.: Comparison of the template shapes obtained from simulation in grey and from data in red. The template shapes are compared in (a) and (c) for the m_{jj} distributions and in (b) and (d) for the $E_{\mathrm{T}}^{\mathrm{miss}}$ distribution. The upper figures show the electron channel and lower figures the muon channel.

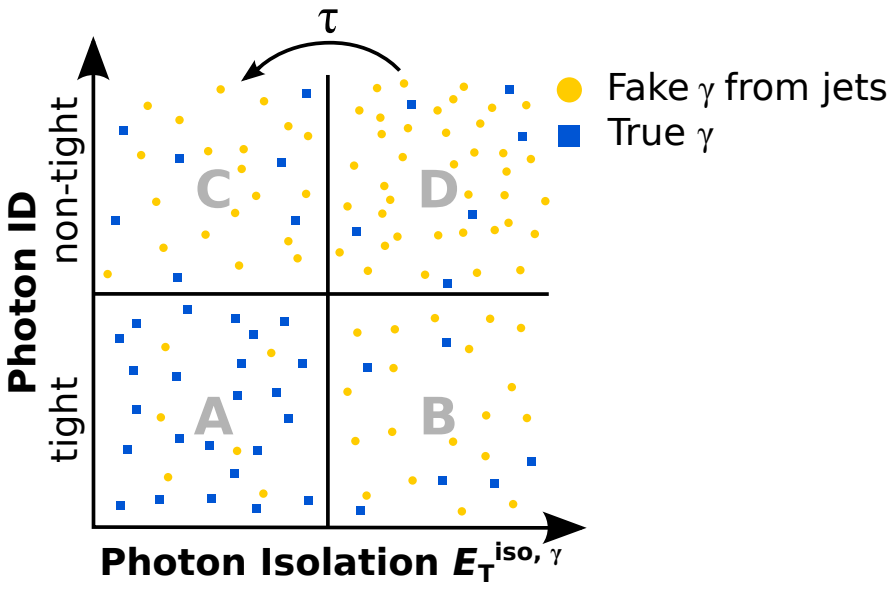

Figure 7.5.: Illustration of the two-dimensional sideband method with its four disjoint phase space regions A, B, C and D defined by the photon isolation energy $E_{\mathrm{T}}^{\mathrm{iso},\gamma}$ and the photon identification criteria. Region A coincides with the control region $\mathrm{CR}_{m_{\mathrm{jj}}}$ and the $WV\gamma$ signal is neglected in this region. Background events containing jets misidentified as photons are shown as yellow dots and other backgrounds containing real photons as blue squares. The number of events where a jet is misidentified as photon in region A (C) is related to the number of events where a jet is misidentified as photon in region B (D) by the transfer factor τ.

7.6. Fake Photons from Jets Background: Two-Dimensional Sideband Method

As described above, the maximum likelihood fits of the m_{jj} and the $E_{\mathrm{T}}^{\mathrm{miss}}$ distribution cannot distinguish the $W\gamma$ + jets and the fake photons from jets backgrounds, as their shapes are too similar. Therefore, a two-dimensional sideband method is used to constrain the background arising from jets that are misidentified as photons. This method was used in other data analyses [115] and only a few modifications are made here. For the two-dimensional sideband method, four orthogonal regions are defined: region A, B, C and D. In the $WV\gamma$ analysis, the method is used to determine the number of events originating from fake photons from jets in region A. Region A is the same as the control region $\mathrm{CR}_{m_{\mathrm{jj}}}$ and region B, C and D are defined with the inverted selection criteria on the invariant dijet mass, $m_{\mathrm{jj}} < 70\,\mathrm{GeV}$ or $m_{\mathrm{jj}} > 100\,\mathrm{GeV}$. Therefore, the $WV\gamma$ signal is neglected in all four regions.

The four phase space regions are defined by two independent sets of variables, the isolation energy of the photon, $E_{\mathrm{T}}^{\mathrm{iso},\gamma}$, and the identification criteria of the photon. Region A coincides with the control region $\mathrm{CR}_{m_{\mathrm{jj}}}$ imposing the `tight` identification criteria on photons as well as the requirement to be isolated $E_{\mathrm{T}}^{\mathrm{iso},\gamma} < 4\,\mathrm{GeV}$. Region B is defined by inverting the requirement on the photon isolation energy while keeping the `tight` identification criteria. Regions C and D are obtained by requiring the `non-tight` identification criteria, and are also separated via the photon isolation energy criteria. The definitions of the four regions are illustrated in Figure 7.5. Region A is dominated by events containing real photons, predominantly arising from $W\gamma$ + jets production. In contrast, regions B, C and D are dominated by events containing fake photons

	Electron Channel	Muon Channel
$N_{\mathrm{A}}^{\mathrm{obs.}}$	1705	1989
$N_{\mathrm{B}}^{\mathrm{obs.}}$	869	1022
$N_{\mathrm{C}}^{\mathrm{obs.}}$	500	559
$N_{\mathrm{D}}^{\mathrm{obs.}}$	770	924

Table 7.2.: Observed event yield in the four phase space regions A, B, C and D of the two-dimensional sideband method in the electron and the muon channel.

from jets. The observed event yields in each of the four regions and for both lepton channels are given in Table 7.2.

The isolation energy distributions of events containing correctly identified photons and events containing misidentified photons are depicted in Figure 7.6(a) and Figure 7.6(c), for the electron and the muon channel, respectively. For events containing real photons, the photon isolation energy $E_{\mathrm{T}}^{\mathrm{iso},\gamma}$ has a pronounced peak at around 0 GeV and only few events at higher values. In contrast, the photon isolation energy for events which contain fake photons from jets is much broader, as jets have in general a broader signature in the calorimeters. The isolation energy distributions for events containing fake photons from jets in region A & B and in region C & D are compared in Figures 7.6(b) and 7.6(d) for the electron and the muon channel, respectively. In both lepton channels, the two distributions agree well, as indicated by the ratio in the lower panel. Therefore, the photon identification criteria do not bias the selection of events containing fake photons from jets. As the isolation energy distribution for events containing fake photons from jets is independent of the photon identification criteria, the ratio, τ, is introduced, relating the event yields containing fake photons from jets in the four regions:

$$\tau \equiv \rho \cdot \frac{N_{\mathrm{B}}^{\text{fake }\gamma}}{N_{\mathrm{A}}^{\text{fake }\gamma}} = \frac{N_{\mathrm{D}}^{\text{fake }\gamma}}{N_{\mathrm{C}}^{\text{fake }\gamma}} \tag{7.21}$$

where ρ accounts for any remaining correlation between the four regions. Solving the equation for the correlation factor gives:

$$\rho = \frac{N_{\mathrm{A}}^{\text{fake }\gamma} \cdot N_{\mathrm{D}}^{\text{fake }\gamma}}{N_{\mathrm{B}}^{\text{fake }\gamma} \cdot N_{\mathrm{C}}^{\text{fake }\gamma}}. \tag{7.22}$$

When no correlation is present, ρ is expected to be equal unity. The expected number of events in each region i is given by the sum of the number of events containing real photons $N_i^{\text{true }\gamma}$ and the number of events containing fake photons from jets $N_i^{\text{fake }\gamma}$:

$$N_i^{\mathrm{exp}} = N_i^{\text{true }\gamma} + N_i^{\text{fake }\gamma} \tag{7.23}$$

where $i \in$ [A, B, C, D]. The number of background events containing real photons can be split into individual contributions from $W\gamma$ + jets, $N_i^{W\gamma}$, fake leptons from jets, $N_i^{\text{fake }l}$, and other backgrounds, N_i^{other}, which are estimated using simulation:

$$N_i^{\mathrm{exp}} = N_i^{W\gamma} + N_i^{\text{fake }l} + N_i^{\mathrm{other}} + N_i^{\text{fake }\gamma}. \tag{7.24}$$

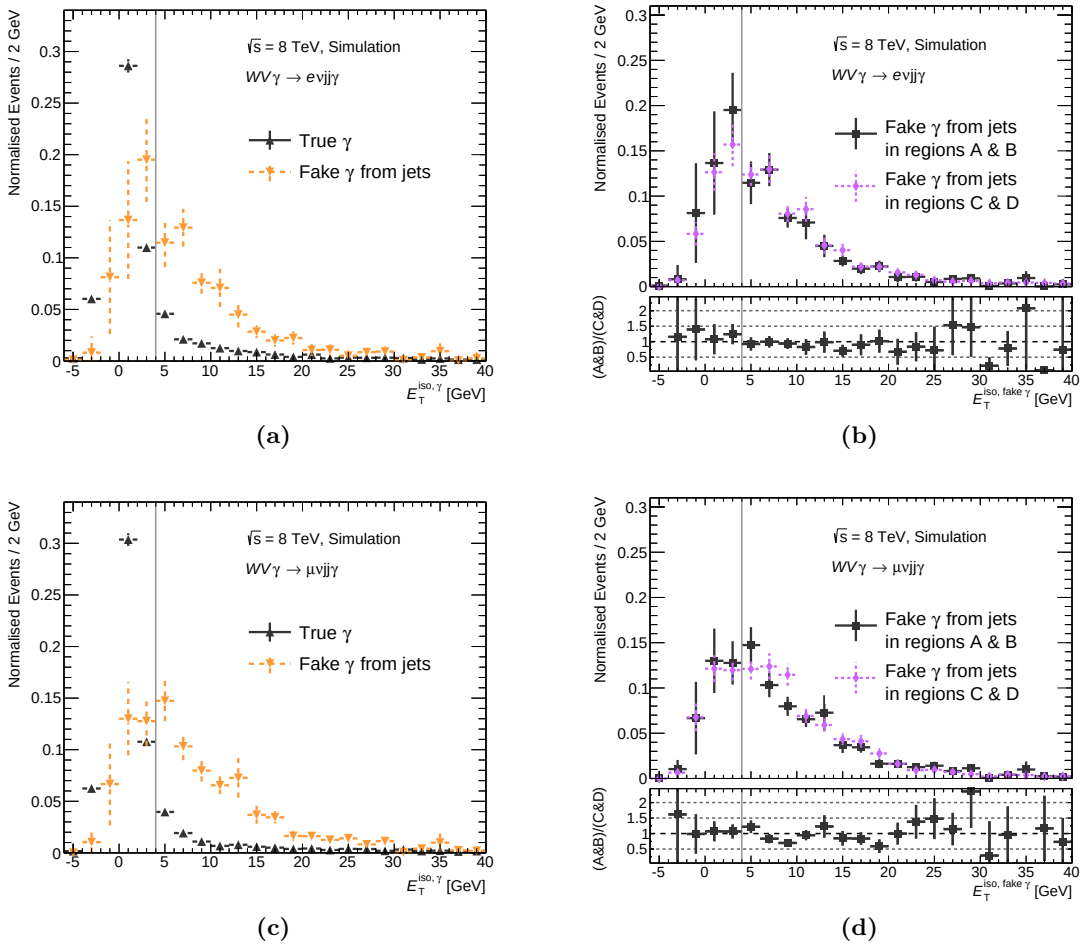

Figure 7.6.: Comparison of the isolation energy distribution for events containing correctly identified photons (labelled *true* γ) (yellow) and events containing misidentified photons (labelled *fake* γ *from jets*) (black) in (a) and (c) for the electron and muon channel, respectively. Also shown is the comparisons of the isolation energy distribution for fake photons in regions A & B (black) and regions C & D (violet) in (b) and (d) for the electron and muon channel, respectively. The grey line indicates the requirement on the isolation energy $E_{\mathrm{T}}^{\mathrm{iso}}$=4 GeV.

Writing this explicitly with τ and the correlation factor ρ as defined above, the following set of equations is obtained:

$$\begin{aligned} N_{\mathrm{A}}^{\mathrm{exp}} &= N_{\mathrm{A}}^{W\gamma} + N_{\mathrm{A}}^{\mathrm{fake}\ l} + N_{\mathrm{A}}^{\mathrm{other}} + N_{\mathrm{A}}^{\mathrm{fake}\ \gamma} \\ N^{\mathrm{exp}} &= N_{\mathrm{B}}^{W\gamma} + N_{\mathrm{B}}^{\mathrm{fake}\ l} + N_{\mathrm{B}}^{\mathrm{other}} + \tau \cdot N_{\mathrm{A}}^{\mathrm{fake}\ \gamma} \\ N_{\mathrm{C}}^{\mathrm{exp}} &= N_{\mathrm{C}}^{W\gamma} + N_{\mathrm{C}}^{\mathrm{fake}\ l} + N_{\mathrm{C}}^{\mathrm{other}} + N_{\mathrm{C}}^{\mathrm{fake}\ \gamma} \\ N_{\mathrm{D}}^{\mathrm{exp}} &= N_{\mathrm{D}}^{W\gamma} + N_{\mathrm{D}}^{\mathrm{fake}\ l} + N_{\mathrm{D}}^{\mathrm{other}} + \rho \cdot \tau \cdot N_{\mathrm{C}}^{\mathrm{fake}\ \gamma}. \end{aligned} \tag{7.25}$$

The free parameters are marked in blue in the equation. The number of $W\gamma$ + jets events in regions B, C and D are estimated from simulation ($N_{\mathrm{B}}^{W\gamma}$, $N_{\mathrm{C}}^{W\gamma}$ and $N_{\mathrm{D}}^{W\gamma}$) and are fixed in the simultaneous fit as the contribution in these regions is small. The number of events arising from other backgrounds in all four regions (N_i^{other}), such as $Z\gamma$ + jets, $t\bar{t}$, $WV\gamma$ (τ) and fake

photons from electrons backgrounds, are fixed in the fitting procedure to their predictions based on simulation. The number of events originating from the fake leptons from jets background is a free parameter in region A ($N_{\mathrm{A}}^{\mathrm{fake}\ l}$), but not in the other regions. To estimate the fake leptons from jets contribution in each of the remaining three regions, a data-driven method is developed and described in detail in Appendix A.6. In region A, the event yield is also obtained with this data driven method and is used as start value for the simultaneous fit, whereas the values obtained for regions B, C and D are fixed to the results of the data driven method. The correlation factor ρ is set to unity in the simultaneous fit. This is justified, as the correlation factor ρ is determined using Monte Carlo simulation and found to be 1.4 ± 0.4 (1.1 ± 0.2) in the electron (muon) channel, which is consistent with unity within uncertainties. This indicates low correlations between the four phase space regions. The deviation from unity of the correlation factor is considered as systematic uncertainty on the background estimation method and is discussed in Section 7.9.2.

The set of Equations 7.25 can either be solved analytically, or formulated as a likelihood function. Besides the general advantage that the likelihood formulation yields robust results in case statistics are low in one or more of the regions, it is also ideal for the combination with the two maximum likelihood fits to the m_{jj} and the $E_{\mathrm{T}}^{\mathrm{miss}}$ distribution. Therefore, in the implementation of the simultaneous fit, the likelihood formulation of the two-dimensional sideband method is employed. The likelihood function of the two-dimensional sideband method is given by:

$$\begin{aligned} L(N_{\mathrm{i}}^{\mathrm{obs.}}) &= \prod_{i=1}^{4} \frac{(N_i^{\mathrm{exp}})^{N_i^{\mathrm{obs.}}}}{N_i^{\mathrm{obs.}}!}\ e^{-N_i^{\mathrm{exp}}} \\ &= \prod_{i=1}^{4} Pois\left(N_i^{\mathrm{obs.}} | N_i^{\mathrm{exp}}\right) \end{aligned} \tag{7.26}$$

which is the product of four Poisson distributions, one for each region $i \in$ [A, B, C, D], to observe the event yield $N_i^{\mathrm{obs.}}$, when N_i^{exp} number of events are expected.

7.7. Other Backgrounds: Estimated from Simulation

Background events arising from $t\bar{t}\gamma$ and $Z\gamma$ + jets production are minor and estimated based on Monte Carlo simulation. These processes have been measured by the ATLAS collaboration as shown in Figure 7.7, where several Standard Model cross section results are shown[1]. The figure depicts the ratio of the cross section measured in data divided by the theory expectations in different colours depending on the used dataset along with the theoretical uncertainties, illustrated as grey bands around unity. The measurements of the $t\bar{t}\gamma$ and $Z\gamma$ + jets processes are coloured in green in the figure and good agreement between data and theory is observed for both processes. Backgrounds arising from $WV\gamma$ production containing tau leptons are also estimated from simulation, as the branching ratio of W bosons into τ leptons is well known. To avoid double counting, the backgrounds determined from Monte Carlo simulation have only correctly identified objects in the final state according to their truth information, as backgrounds containing misidentified objects are derived with data-driven methods.

[1]The $WW\gamma$ cross section given in the figure refers to the fully leptonic decay channel $e\nu\mu\nu\gamma$.

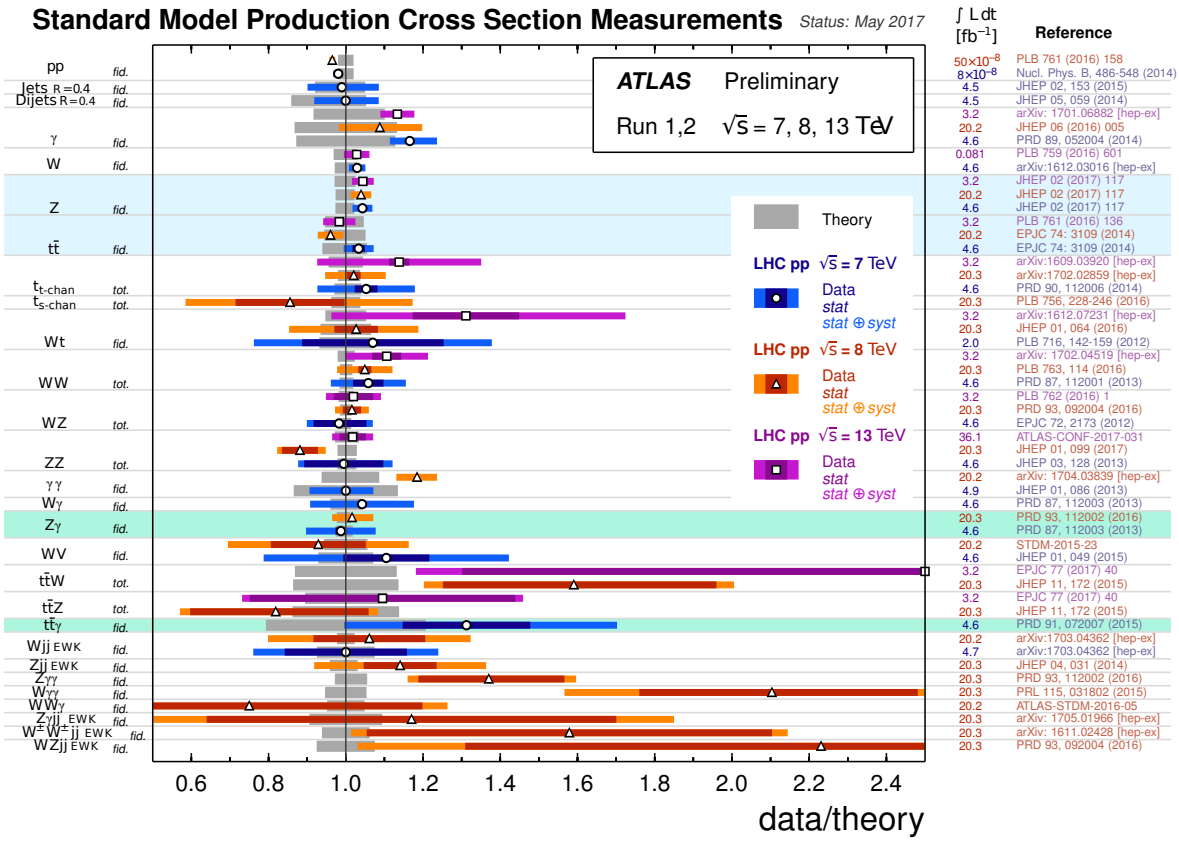

Figure 7.7.: The ratio of data and theory expectation is shown for several ATLAS Standard model cross section measurements corrected for the leptonic branching fractions at different centre-of-mass energies, indicated by the different colours. Statistical uncertainties are represented by the darker bands and the total uncertainties by the brighter bands. Theoretical uncertainties are shown as grey bands. The processes coloured in green are background processes of the $WV\gamma$ analysis and determined using Monte Carlo simulation. The processes coloured in blue are used to estimate the background contribution of electrons misidentified as photons, also relying on Monte Carlo simulation. The figure is modified from [40].

7.7.1. Electrons Misidentified as Photons

Processes such as $Z \to ee$ or $t\bar{t}$ mimic the signal signature, in case one of the electrons is misidentified as photon. This misidentification can happen, as the signatures of electrons and photons in the detector are very similar as described in detail in Section 5.2. The reconstruction algorithms are optimized to discriminate photons against electrons but nevertheless electrons can be misidentified as all three conversion types of photons (unconverted, single- and double-track converted). The misidentification of an electron as a photon in the ATLAS detector was studied using $Z \to e^+e^-$ events where the two electrons are identified correctly and where one of the electrons is misidentified as photon. The study is documented in Reference [129] and summarised in the following.

The expected number of events from $Z \to ee$ production, N_{ee}, is a function of the average electron reconstruction efficiency, ϵ, for a given electron identification criteria and the true number of $Z \to ee$ events, N_{ee}^{true}:

$$N_{ee} = \epsilon^2 \, N_{ee}^{\text{true}}. \tag{7.27}$$

The efficiency ϵ enters the equation squared, since two electrons with the same identification criteria are required in the final state. The expected number of events where one electron was misidentified as photon $N_{e\to\gamma}$, is given by:

$$N_{e\to\gamma} = 2\epsilon \, \rho \, N_{ee}^{\text{true}} \tag{7.28}$$

where ρ is the probability to misidentify an electron as a photon. Both electrons are allowed to be misidentified as photon, represented by the factor of 2 in the equation. Solving Equation 7.28 for ρ and inserting the information from Equation 7.27 gives:

$$\rho = \frac{N_{e\to\gamma}}{2\epsilon \, N_{ee}^{\text{true}}} \tag{7.29}$$

$$= \epsilon \, \frac{N_{e\to\gamma}}{2N_{ee}}. \tag{7.30}$$

The probability ρ to misidentify an electron as a photon, is corrected for the identification efficiency for electrons, since $N_{ee}^{\text{true}}(\epsilon)$ has a linear dependency on ϵ and $N_{ee}(\epsilon^2)$ a quadratic. However, the determined fake rate is dependent on the identification efficiencies of the photons.

For the estimation of the fake rate, the full 2012 dataset recorded with the ATLAS detector at a centre-of-mass energy of $\sqrt{s} = 8\,\text{TeV}$ is analysed, corresponding to an integrated luminosity of $L_{\text{int}} = 20.3\,\text{fb}^{-1}$. Either an electron-positron pair with opposite electric charge is selected or an electron-photon pair, independent of the electric charge. The object selection is very similar to the object selection used for the $WV\gamma$ analysis in this thesis. The study is performed on the Z boson mass resonance, requiring the invariant diobject mass to be close to it: $85\,\text{GeV} < |m_{ee/e\gamma}| < 95\,\text{GeV}$. The misidentification rates measured in data and in $Z \to ee$ Monte Carlo simulation exhibit a difference of a few percent. This difference originates from pixel modules, whose detection efficiency decreased with time. In the simulation, the response of these pixel modules is not well modelled as the efficiency loss is not taken into account. Additional studies showed that the misidentification rates are independent of the transverse energy of the photon and of pileup effects. In order to obtain a better description of the fake rate in simulation, correction factors are derived as a function of the pseudorapidity of the photon as well as of the conversion type of the photons. Theses correction factors are applied on an

event-by-event basis to the Monte Carlo simulation. Source of systematic uncertainties are due to a possible bias in the method, as both electrons can be misidentified as the photon, due to the choice of the Z boson mass window criteria, due to backgrounds arising from jets which are misidentified as either electron or photon and due to experimental uncertainties, arising from the reconstruction and identification inefficiencies. The total systematic uncertainty ranges from 3.0 % to 4.2 % and depends on the pseudorapidity of the photon.

The background contribution for the $WV\gamma$ analysis arising from electrons misidentified as photons is determined by applying the described correction factors to all Monte Carlo samples used in this thesis. This is done independently of the Monte Carlo generator, since the difference between the misidentification rate in data and in simulation is due to a mismodelling in the detector simulation, which is the same for all samples. The correction factors are only applied to events where the photon with the highest transverse momentum originates from an electron, identified by using the truth information of the simulated events. In the electron channel, events containing an electron which is misidentified as a photon arises mainly from Z + jets production and little from top pair production. In the muon channel, the Z + jets production is negligible, as described in Section 6.2 and the largest contribution arises from top pair production. The contribution originating from top pair production is of the same order of magnitude for both lepton channels. Since in the electron channel the additional contribution from $Z \to ee$ production is present, the fake photon from electron background is expected to be smaller in the muon channel. The production of Z + jets as well as the production of top pairs, has been measured by the ATLAS collaboration as shown in Figure 7.7 and marked in light blue. As can be seen in the figure, good agreement between the measured data and the simulation was found for both processes.

Since photons and electrons have similar signatures in the detector, the misidentification of a photon as an electron (fake electrons from photons background) are also possible. The rate of this misidentification is of the same order as the rate to misidentify an electron as photon and therefore it is a background component in the electron channel of the $WV\gamma$ analysis. It is evaluated together with the fake electrons from jets background. The processes dominating the two background components are very similar: γ + jets production for fake electrons from jets and $\gamma\gamma$ + jets production for fake electrons from photons. For the two processes, the m_{jj} and $E_{\mathrm{T}}^{\mathrm{miss}}$ distributions are very similar, as in both the jets originate from QCD processes and no genuine $E_{\mathrm{T}}^{\mathrm{miss}}$ is expected. The template shapes for the fake lepton from jets background is obtained from data using dedicated selection criteria, as described in Section 7.5. These dedicated criteria also select fake electrons from photons, as no criteria on the source of the misidentification are required. However, the event yield for the fake electrons from photons background is much smaller than the fake electrons from jets background, as is validated using Monte Carlo simulation. Thus, for the ease of terminology, the background is still referred to as fake electrons from jets.

	Electron Channel	Muon Channel
$W\gamma$ + jets	1.44 ± 0.04	1.42 ± 0.04
Fake γ from jets	1.58 ± 0.10	1.43 ± 0.08
Fake l from jets	3.62 ± 0.73	6.50 ± 5.84

Table 7.3.: Scale factors to relate the event yields in the $\mathrm{CR}_{m_{\mathrm{jj}}}$ with the event yields in region $\mathrm{CR}_{E_{\mathrm{T}}^{\mathrm{miss}}}$ for the three backgrounds estimated with the data driven methods: $W\gamma$ + jets, fake γ from jets and fake l from jets. The scale factors are given for the electron and muon channel.

7.8. Simultaneous Fit

The three data-driven methods used to estimate the event yields for the $W\gamma$ + jets, fake photons from jets and fake leptons from jets backgrounds are interdependent, as each of the methods relies on the results of the other two. The event yields of the background components, estimated with the maximum likelihood fit to the m_{jj} and $E_{\mathrm{T}}^{\mathrm{miss}}$ distributions in the two control regions $\mathrm{CR}_{m_{\mathrm{jj}}}$ and $\mathrm{CR}_{E_{\mathrm{T}}^{\mathrm{miss}}}$ are related via scale factors, defined as:

$$\widetilde{N}^B = s^B \cdot N^B \tag{7.31}$$

where $\widetilde{N}^B$ is the expected event yield of background B in the control region $\mathrm{CR}_{E_{\mathrm{T}}^{\mathrm{miss}}}$, N^B is the expected event yield of background B in the control region $\mathrm{CR}_{m_{\mathrm{jj}}}$ and s^B is the scale factor for background B. The scale factors are determined using the template shapes of the background for the likelihood fits. In Table 7.3, the scale factors are given for the three backgrounds, estimated with the simultaneous fit for both lepton channels. The scale factors for each background are in good agreement between the two lepton channels within the statistical uncertainties. The large uncertainty on the scale factor for the fake lepton from jets background in the muon channel arises from the low statistics in the template shapes. For all other backgrounds, the event yields in the two control regions $\mathrm{CR}_{m_{\mathrm{jj}}}$ and $\mathrm{CR}_{E_{\mathrm{T}}^{\mathrm{miss}}}$ are directly taken from Monte Carlo simulation and fixed to their theoretical predictions.

The expected event yields in region A of the two-dimensional sideband method are the same as the expected event yields in the control region $\mathrm{CR}_{m_{\mathrm{jj}}}$ and therefore: $N_{\mathrm{A}}^{W\gamma} = N^{W\gamma}$, $N_{\mathrm{A}}^{\text{fake }\gamma} = N^{\text{fake }\gamma}$, $N_{\mathrm{A}}^{\text{fake }l} = N^{\text{fake }l}$ and $N_{\mathrm{A}}^{\text{other}} = N^{\text{fixed}}$. The correlation factor ρ of the two-dimensional sideband method is set to unity, as no correlations are assumed.

The maximum likelihood fit of the invariant dijet mass distribution in the control region $\mathrm{CR}_{m_{\mathrm{jj}}}$, the maximum likelihood fit of the missing transverse energy distribution in the control region $\mathrm{CR}_{E_{\mathrm{T}}^{\mathrm{miss}}}$ and the two-dimensional sideband method, where region A coincides with the control region $\mathrm{CR}_{m_{\mathrm{jj}}}$, are performed simultaneously. This is done by minimising the three likelihoods, given in Equations 7.19, 7.20 and 7.26 simultaneously with respect to their respective datasets. The free parameters in the simultaneous fit are the event yields $N^{W\gamma}$, $N^{\text{fake }\gamma}$, $N_C^{\text{fake }\gamma}$, $N^{\text{fake }l}$ as well as the transfer factor τ, from the two-dimensional sideband method, while the backgrounds estimated from simulation are fixed in the procedure. The result from the simultaneous fit gives the expected event yields in the control region $\mathrm{CR}_{m_{\mathrm{jj}}}$. The simultaneous fit is performed separately for the electron and muon channel. It is implement using the statistical toolkits RooFit [130] and RooStat [131], both integrated in the ROOT [132] framework. For the minimisation the MINUIT [133] package is used, which is also integrated in ROOT.

Process	Electron Channel	Muon Channel	Estimation Method
$W\gamma$ + jets	$1\,120.2 \pm 37.8$ (stat.)	$1\,433.5 \pm 40.2$ (stat.)	Simultaneous fit
Fake γ from jets	286.9 ± 24.9 (stat.)	386.5 ± 29.0 (stat.)	Simultaneous fit
Fake l from jets	159.2 ± 16.0 (stat.)	31.9 ± 6.5 (stat.)	Simultaneous fit
$t\bar{t}\gamma$	46.2 ± 4.2	57.2 ± 4.8	MC simulation
Fake γ from e	42.3 ± 11.2	15.2 ± 3.5	Corrected simulation
$Z\gamma$ + jets	58.9 ± 2.9	64.2 ± 2.9	MC simulation
$WV\gamma$ ($\rightarrow \tau\nu$jjγ)	0.4 ± 0.0	0.5 ± 0.1	MC simulation
Total background	$1\,714.2 \pm 48.0$ (stat.)	$1\,988.9 \pm 49.9$ (stat.)	Sum of components
Data	1705	1989	Measurement

Table 7.4.: Observed and expected event yields in the control region $\mathrm{CR}_{m_{\mathrm{jj}}}$ together with the estimation method for the electron an the muon channel. The uncertainties on the backgrounds estimated with the simultaneous fit are due to the statistical uncertainties of the data. The uncertainties on the other backgrounds are the statistical uncertainties due to the Monte Carlo generation. The total number of events is the sum over all background components with the statistical uncertainty of the data only.

The result of the background estimation is given in Table 7.4 for both lepton channels. The expected event yields in the control region $\mathrm{CR}_{m_{\mathrm{jj}}}$ for the $W\gamma$ + jets, fake photons from jets and fake leptons from jets backgrounds are given with the statistical uncertainties of the data. The other backgrounds, estimated using simulation, are given with the statistical uncertainties of the Monte Carlo generation. The total number of expected background events is the sum over all individual background components given with the statistical uncertainties of the data. In both channels, the observed and expected event yields are in good agreement within the uncertainties.

Some of the free parameters in the simultaneous fit are strongly (anti-)correlated. The correlation matrix is obtained from RooFit after performing the simultaneous fit and given in Table 7.5. The first value in each column corresponds the correlation in the electron channel and the second value to the correlation in the muon channel. The anti-correlation arises from the constraint on the total number of events in the fit, which is the sum over the event yields of the individual background components. Therefore, if the event yield of one background component is increasing, the event yield of another background component has to decrease, in order to match the constraints of the total number of events. The event yield of the $W\gamma$ + jets background is 60 % (70 %) anti-correlated with the event yield of the fake photons from jets background in the electron (muon) channel. Both event yields of the fake photons from jets background in region A and region C are 80 % anti-correlated with the transfer factor τ in both lepton channels. The event yield of the fake photons from jets background in region A and region C are 70 % correlated with each other, as they are related via Equation 7.21.

	$N^{W\gamma}$	$N^{fakePho}$	$N^{fakeLep}$	$N_C^{fakePho}$	τ
	$(e \mid \mu)$	$(e \mid \mu)$	$(e \mid \mu)$	$(e \mid \mu)$	$(e \mid \mu)$
$N^{W\gamma}$	100 | 100	−60 | −70	−50 | −30	−40 | −50	50 | 60
$N^{fakePho}$	−60 | −70	100 | 100	−10 | 0	70 | 70	−80 | −80
$N^{fakeLep}$	−50 | −30	−10 | 0	100 | 100	−10 | 0	10 | 10
$N_{\mathrm{C}}^{fakePho}$	−40 | −50	−70 | −70	−10 | 0	100 | 100	−80 | −80
τ	50 | 60	−80 | −80	10 | 10	−80 | −80	100 | 100

Table 7.5.: Correlation matrix for the free parameters of the simultaneous fit, given in percent for the electron and the muon channel obtained from RooFit. Negative values represent anti-correlations.

7.9. Results

7.9.1. Extrapolation into the Signal Region

In order to obtain the event yields in the signal region, an extrapolation is necessary, as the results from the simultaneous fit give the event yields in the control region $\mathrm{CR}_{m_{\mathrm{jj}}}$. The extrapolation utilises the template shapes of the invariant dijet mass distribution. A scale factor is derived in the control region $\mathrm{CR}_{m_{\mathrm{jj}}}$ for each background component i, which is applied to the signal region m_{jj} distribution. Figure 7.8 compares the m_{jj} template shapes of the $W\gamma$ + jets, fake photon from jets and fake lepton from jets backgrounds in the electron and the muon muon channel. In Figure 7.8(a) the m_{jj} template shapes for the two lepton channels of the $W\gamma$ + jets background are shown and similar shapes are observed, as can be seen in the ratio in the lower panel. This is expected, due to lepton universality, which states that the electroweak interactions are independent of the lepton flavour. The event yields in the signal region of the $W\gamma$ + jets background are reduced by 72 % with respect to the event yields in the control region $\mathrm{CR}_{m_{\mathrm{jj}}}$. The m_{jj} template shapes for the fake photons from jets background are shown in Figure 7.8(b) for the electron and muon channel. Good agreement between the template shapes is observed within their statistical uncertainties. The event yields in the signal region are reduced by 70 % with respect to the control region $\mathrm{CR}_{m_{\mathrm{jj}}}$. Figure 7.8(c) shows the m_{jj} template shape for the fake leptons from jets background in the electron and muon channel. Large statistical uncertainties in the muon template make a comparison to the electron channel difficult, but no significant deviations are observed. In the template shape of the muon channel, a pronounced upward fluctuation is observed in the signal region. This fluctuation is the reason that the event yield in the signal region is quite large with respect to the event yield in the control region $\mathrm{CR}_{m_{\mathrm{jj}}}$: in the signal region, the event yield of the fake muons from jets background is only reduced by 15 % with respect to the event yield in the control region $\mathrm{CR}_{m_{\mathrm{jj}}}$, compared to a reduction of 65 % for the fake electrons from jets background.

The scale factors are defined as the ratio of the event yield after the simultaneous fit and the event yield before the fit $f_i = \frac{N_i^{\mathrm{after}}}{N_i^{\mathrm{before}}}$, where N_i^{before} is the number of events in the original distribution without any additional event yield adjustment. These scale factors are given in Table 7.6. The scale factor for the $W\gamma$ + jets background is given with respect to the event yield obtained from Monte Carlo simulation and is consistent with unity within uncertainty for both lepton channels. This is expected, as the measurement of the process by the ATLAS

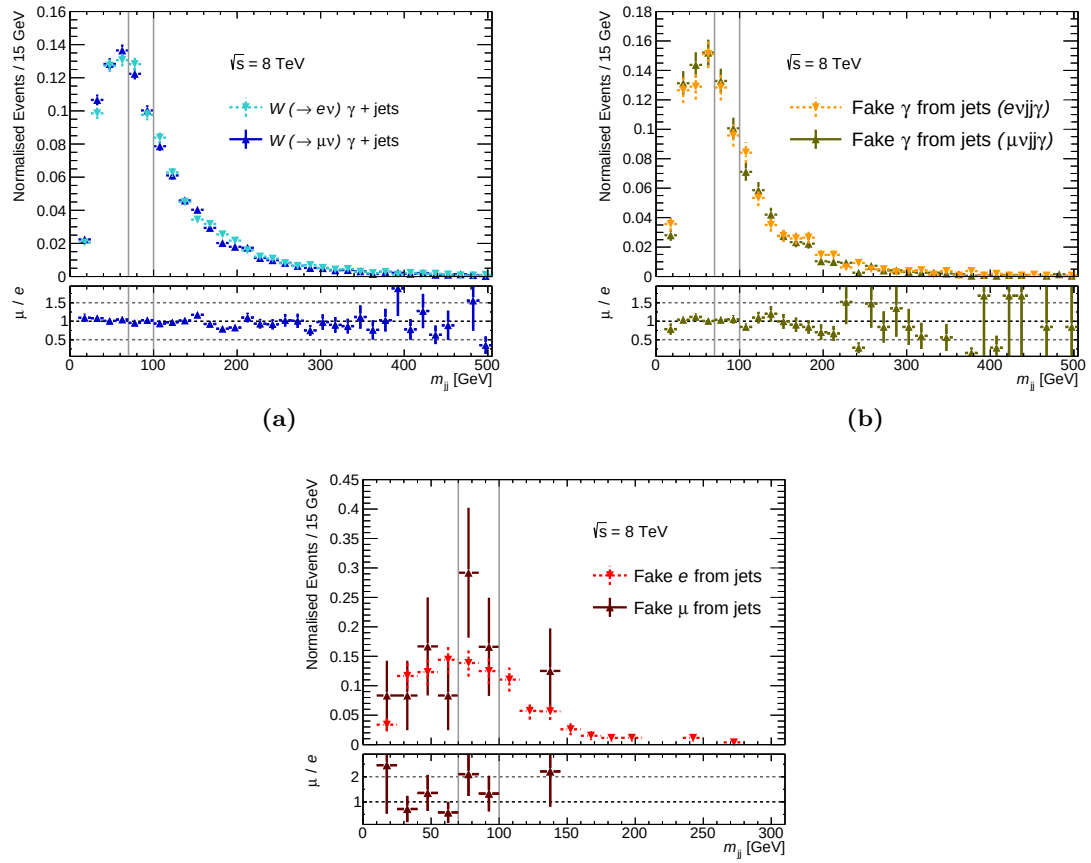

Figure 7.8.: Comparison of the invariant dijet mass template shapes of the electron and the muon channel used for the extrapolation of the fit result into the signal region. In (a) the $W\gamma$ + jets, in (b) the fake photons from jets and in (c) the fake leptons from jets backgrounds are shown. The signal region is indicated by the grey lines.

Process	Electron Channel	Muon Channel
$W\gamma$ + jets	0.97 ± 0.04	1.03 ± 0.03
Fake γ from jets	0.23 ± 0.02	0.26 ± 0.02
Fake l from jets	0.83 ± 0.10	2.45 ± 0.84

Table 7.6.: Scale factors to derive the event yields in the signal region from the simultaneous fit result, the event yield in the control region $\mathrm{CR}_{m_{\mathrm{jj}}}$ for the $W\gamma$ + jets, fake photons from jets and fake leptons from jets backgrounds. The scale factors are given for the electron and the muon channel individually.

collaboration has shown good agreement between data and simulation [119]. The scale factors for the fake photons and fake leptons from jets backgrounds are given relative to the original event yield in the respective data samples. For the fake photons from jets background, the scale factor in the two lepton channels is between 0.23 and 0.26 with a relative uncertainty of about 8 %, indicating good statistics in the data sample. For the fake leptons from jets background, the scale factor in the electron channel is 0.83 with a relative uncertainty of 12 % and significantly larger in the muon channel with around 2.45 and a relative uncertainty of 34 %. The large difference arises from the different processes leading to the misidentification of a jet as an electron or muon, described in Section 6.2, and from the low statistics in the data sample used to determine the template shapes for the fake muon from jet background.

The extrapolation yields for the total number of expected background events (551.7 ± 14.3) events and (620.7 ± 15.4) events in the electron and the muon channel, respectively. The quoted uncertainties are the uncertainty of the fit, considering only the statistical uncertainty of the data. It is evaluated as the same relative uncertainty as obtained in the control region $\mathrm{CR}_{m_{\mathrm{jj}}}$. The final results of the background estimation in the signal region are given in Section 7.9.3, after the discussion of the systematic uncertainties.

7.9.2. Systematic Uncertainties

Several effects influence the simultaneous fit and therefore need to be considered as systematic uncertainty on the background estimation. Sources of systematic uncertainty considered for the $WV\gamma$ analysis are uncertainties due to the fitting procedure itself, accounted for by varying the template shapes as well as the bin width of the distributions and the fit ranges. In addition, experimental uncertainties originating from identification and reconstruction inefficiencies on the objects are considered and propagated through the simultaneous fit. During the evaluation of the systematic uncertainties, the expected event yield for the separate background components can vary strongly with respect to the nominal expectation. However, due to the anti-correlations of the free parameters of the simultaneous fit, only small variations of the total number of expected background events are observed even when the individual components vary significantly. For setting the exclusion limits on the production cross section and on anomalous quartic gauge couplings, only the total expected event yield is used. Therefore, the systematic uncertainties are not evaluated for each background component separately, but jointly for the total number of expected events in the signal region. The impact of the template shape variations and the variations of the fit ranges and the bin widths are evaluated individually for the separate backgrounds and are given in Appendix A.8, but are not used in the following.

Systematic Uncertainties due to Statistical Uncertainties of the Templates

The influence of the statistical uncertainties of the template shapes on the event yield in the signal region is considered as one source of systematic uncertainty. In order to quantify the impact, new template shapes are generated using pseudo experiments. Each pseudo experiment consists of three parts, executed consecutively. First, a new template shape is generated by drawing pseudo data for each bin in the histogram. Then, the new template shape is used to perform the simultaneous fit. Finally the new event yield is extrapolated into the signal region. This is repeated ten-thousand times and a distribution of the new event yields in the signal region is obtained, shown in Figure 7.9 for both lepton channels. For each pseudo experiment,

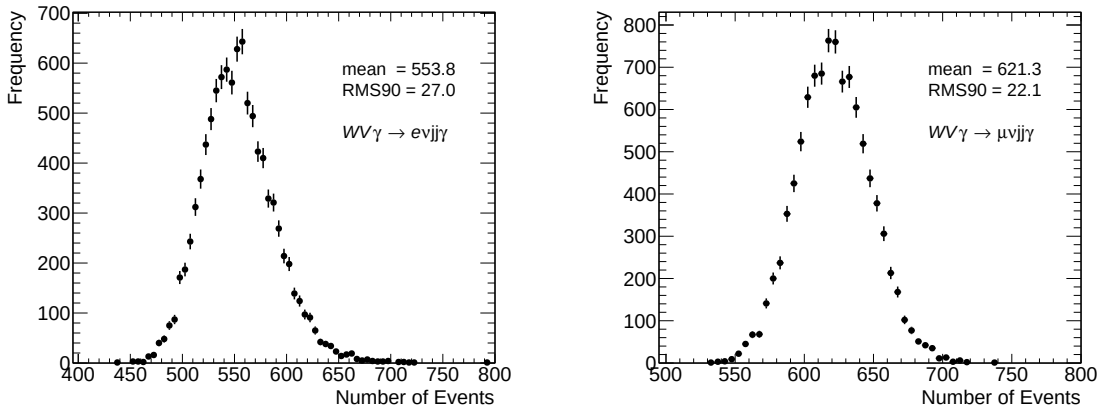

Figure 7.9.: Distribution of the total expected background event yield in the signal region for the 10000 pseudo experiments for the (a) electron and (b) muon channel. The RMS90 is taken as uncertainty to account for the statistical uncertainties of the templates.

the template shapes of all backgrounds are varied independent of each other. The systematic uncertainty is taken to be the interval which includes at least 90 % of the events around the mean value, referred to as *RMS90*.

The pseudo data for each bin in the histogram is drawn from a Gaussian distribution whose mean corresponds to the nominal value of the respective bin and whose width corresponds to the uncertainty of the respective bin. This allows the variation of the event yield in each bin as well as the total number of events of the histogram. For the template shapes obtained from data with dedicated selection requirements, the uncertainty in each bin corresponds to the statistical uncertainty of the data. Template shapes obtained from simulation have a bin uncertainty, which is the quadratic sum of the statistical uncertainty of the Monte Carlo simulation and the theoretical uncertainties. The theoretical uncertainties include uncertainties due to the renormalisation and factorisation scales, due the parton distribution functions as well as due to the value of strong coupling constant α_s. They are determined for each simulation sample separately, as discussed in Section 4.3.

The total systematic uncertainty originating from the statistical uncertainty of the template shapes on the total background expectation in the signal region is determined to be 4.9 % (3.6 %) in the electron (muon) channel. This is the dominant uncertainty on the background estimation in both lepton channels. The uncertainties for the separate background components are given in Appendix A.8.

Fit Related Systematic Uncertainties

Several fit related uncertainties also affect the background estimation. In order to estimate the influence on the final event yield originating from the bin widths of the m_{jj} and $E_{\mathrm{T}}^{\mathrm{miss}}$ distributions, the fit ranges as well as the correlation factor ρ, the nominal values are varied and the fit procedure is redone. All considered variations and their precise values are given in Table 7.7. The bin size of both distributions, m_{jj} and $E_{\mathrm{T}}^{\mathrm{miss}}$, is increased by a factor of two with respect to the nominal bin size, but decreased by only a factor of 1/3 for the $E_{\mathrm{T}}^{\mathrm{miss}}$ distribution

Variation	Nominal	Up (e | μ)	Down (e | μ)	Rel. Uncertainty [%] (e | μ)
$E_{\mathrm{T}}^{\mathrm{miss}}$ Fit Range Low	0 GeV	15 GeV	-	0.56 | 0.48
$E_{\mathrm{T}}^{\mathrm{miss}}$ Fit Range High	300 GeV	315 GeV	285 GeV	0.18 | 0.51
$E_{\mathrm{T}}^{\mathrm{miss}}$ Binning	15 GeV	30 GeV	10 GeV	0.04 | 0.02
m_{jj} Fit Range Low	10 GeV	25 GeV	-	0.05 | 0.04
m_{jj} Fit Range High	505 GeV	520 GeV	490 GeV	0.06 | 0.01
m_{jj} Binning	15 GeV	30 GeV	-	0.17 | 0.12
ρ (2-D sideband)	1.0	1.38 | 1.23	0.62 | 0.77	0.16 | 0.30
Total Uncertainty				0.64 | 0.77

Table 7.7.: The variations of the fit ranges and the bin widths of the m_{jj} and $E_{\mathrm{T}}^{\mathrm{miss}}$ distributions as well as the variations of the correlation factor ρ. The relative uncertainty for each variation is quoted for the electron and the muon channel.

and not decreased for the m_{jj} distribution. This is done as otherwise the statistical fluctuations in the distributions get too large. The upper and lower fit ranges are varied up and down by one bin size, unless the varied lower fit range is below 0 GeV. In addition, the correlation factor ρ of the two-dimensional sideband method is varied. The variation of ρ is chosen to be the larger value of either the statistical uncertainty or the deviation of the value obtained from simulation and unity. The variations are performed consecutively and independent of each other. For every variation the simultaneous fit is performed and the event yield in the signal region extracted. The maximal deviation between the nominal event yield in the signal region and the event yield obtained with either the up or the down variation is taken as uncertainty.

The total systematic uncertainty is obtained by adding the separate contributions in quadrature. The systematic uncertainty on the total number of expected background events in the signal region is estimated to be 0.64 % (0.77 %) for the electron (muon) channel. The total uncertainty is dominated by the variation of the fit ranges of the missing transverse energy distribution. The uncertainties on the individual backgrounds, are given in Appendix A.8.

Systematic Uncertainties due to Reconstruction and Identification Inefficiencies

Experimental uncertainties arising from reconstruction and identification inefficiencies, such as energy scales, resolutions or efficiencies of the objects are also considered as source of systematic uncertainty. In order to quantify the impact of the experimental uncertainties on the event yield in the signal region, each systematic uncertainty is varied by one standard deviation and the full event selection is rerun. This is important, as the variations often change the energy and the position of the object and therefore different events can be selected with respect to the nominal selection. These uncertainties only affect the backgrounds, which are determined using Monte Carlo simulation or whose template shapes are taken from Monte Carlo simulation. However, due to their varied template shapes and event yields, which are part of the simultaneous fit, the event yields of the backgrounds determined with the simultaneous fit are also altered and thus influenced indirectly.

In total about 35 different systematic uncertainties are considered and thus re-running the full background estimation with every variation requires a huge amount of computing resources. Therefore, the systematic uncertainty is determined with a *simplified background estimation* method, where only the two maximum likelihood fits are performed without the two-dimensional sideband method. This simplifies the background estimation, but the $W\gamma$ + jets and the fake photons from jets background cannot be distinguished any more and must be jointly evaluated. The event yields obtained with the nominal and with the simplified background estimation method are found to be in good agreement and therefore the simplified method is used to determine the systematic uncertainty due to experimental inefficiencies. More details on the simplified method are given in Appendix A.9.

The separate uncertainties related to the reconstruction and identification of the objects are discussed in Chapter 5. Therefore, the sources of systematic uncertainty that are accounted for in this thesis are briefly listed in the following:

- **Electron** Uncertainties due to the energy scale and resolution as well as identification, isolation and reconstruction efficiencies are considered.
- **Photon** Uncertainties due to the energy scale and resolution as well as identification efficiencies and uncertainties from the fake photons from electrons correction factors are considered.
- **Muon** Uncertainties due to the energy scale, resolutions of the inner detector and the muon spectrometer as well as reconstruction efficiencies are considered.
- **Jet** Uncertainties due to the energy scale and resolution as well as due to the jet vertex criteria are considered. In addition, the tagging efficiencies for b-jets, c-jets and light flavour jets are considered as well as the energy scale for b-jets.
- **Missing transverse energy** This uncertainty is partially evaluated with the above variations, as $E_{\mathrm{T}}^{\mathrm{miss}}$ is always recalculated during the varied object selection. However, uncertainties arising from the energy scale and the resolution of the soft terms are not included and therefore assessed separately.
- **Pileup** The distribution of the average number of interactions per bunch crossing $\langle\mu\rangle$ in the Monte Carlo is re-weighting to agree with the distribution measured in data. This re-weighting has an uncertainty of 4 % and the re-weighting factors are varied accordingly.

The event yield for each variation is determined with the simultaneous fit and the result is extrapolated into the signal region. The variations are preformed independently and the uncertainty in the signal region for each is taken as the maximal deviation between the event yield obtained from either the up or down variation and the nominal event yield using the simplified method. In Table 7.8 the individual systematic uncertainties are listed with their relative size on the total background event yield in the signal region for both lepton channels. The total uncertainty due to the reconstruction and identification inefficiencies of the objects is the quadratic sum of all contributions and is found to be 4.0 % (2.5 %) in the electron (muon) channel. In both lepton channels, the dominant uncertainty arises from the jet energy scale.

Systematic Component	Rel. Systematic Uncertainty on N^{bkd} [%] Electron Channel	Muon Channel
Electromagnetic Energy Scale	0.8	0.2
Electron Energy Resolution	0.4	0.0
Electron Identification	0.1	0.0
Electron Isolation	0.1	0.0
Electron Reconstruction Eff.	0.2	0.0
Photon Energy Resolution	0.4	0.2
Photon Identification	0.8	0.2
Photons from Electrons	0.9	0.2
Muon Energy Scale	0.1	0.1
Muon Reconstruction Eff.	0.1	0.0
Muon Resolution ID	0.1	0.0
Muon Resolution MS	0.1	0.1
Jet Energy Resolution	1.2	0.1
Jet Energy Scale	2.9	2.1
Jet Vertex Fraction	1.6	0.2
$E_{\text{T}}^{\text{miss}}$ Energy Scale Soft Terms	0.7	0.7
$E_{\text{T}}^{\text{miss}}$ Resolution Soft Terms	0.3	1.1
Pileup	0.7	0.1
Total Uncertainty	4.0	2.5

Table 7.8.: Relative systematic uncertainties due to reconstruction and identification inefficiencies of the objects on the total number of expected background events in the signal region, N^{bkd}, for the electron and the muon channel. The *Jet Energy Scale* entry includes the flavour specific uncertainties.

Total Uncertainty

The combined systematic uncertainty on the total number of expected background events in the signal region, N^{bkd}, is given by the quadratic sum of all systematic uncertainties discussed above. The expected event yield in the signal region, estimated with the full background estimation method, is found to be:

$$\begin{aligned} N_{e\nu\text{jj}\gamma}^{\text{bkd}} &= 551.7 \pm 14.4\ (\text{stat.}) \pm 35.2\ (\text{syst.}) \\ N_{\mu\nu\text{jj}\gamma}^{\text{bkd}} &= 620.7 \pm 15.4\ (\text{stat.}) \pm 27.1\ (\text{syst.}) \end{aligned} \tag{7.32}$$

for the electron and muon channel, respectively. In the following, the expected event yield is used with the total uncertainty, which is the sum of the statistic and the systematic uncertainty:

$$N_{e\nu\text{jj}\gamma}^{\text{bkd}} = 551.7 \pm 38.0 \qquad N_{\mu\nu\text{jj}\gamma}^{\text{bkd}} = 620.7 \pm 31.2 \tag{7.33}$$

corresponding to a relative uncertainty of 7.6 % (7.2 %) in the electron (muon) channel. In both lepton channels the dominant uncertainty arises from the statistical uncertainties of the template shapes followed by the experimental uncertainties originating from reconstruction and identification inefficiencies.

Process	Electron Channel	Muon Channel	Estimation Method
$W\gamma$ + jets	324.0 ± 11.0 (stat.)	406.9 ± 11.4 (stat.)	Simultaneous fit
Fake γ from jets	82.5 ± 7.2 (stat.)	117.3 ± 8.8 (stat.)	Simultaneous fit
Fake l from jets	56.9 ± 5.7 (stat.)	26.9 ± 5.5 (stat.)	Simultaneous fit
$t\bar{t}\gamma$	35.4 ± 5.8	46.3 ± 7.3	MC simulation
Fake γ from e	33.2 ± 12.3	2.9 ± 0.8	Corrected simulation
$Z\gamma$ + jets	19.4 ± 3.7	19.9 ± 2.9	MC simulation
$WV\gamma$ ($\rightarrow \tau\nu$jjγ)	0.5 ± 0.1	0.4 ± 0.1	MC simulation
Total background	551.7 ± 38.0 (total)	620.7 ± 31.2 (total)	Sum of components
Expected signal	13.7 ± 2.0	17.5 ± 1.6	Corrected VBFNLO
Data	490	599	Measurement

Table 7.9.: Observed and expected event yields in the signal region along with the estimation method. The uncertainties on the backgrounds estimated with the simultaneous fit originate from the statistical uncertainty on the data. The uncertainties on the other background components comprise the statistical uncertainties due to the Monte Carlo generation as well as theoretical uncertainties. The total number of background events is the sum over all background components an the total uncertainty includes the statistical and systematic components.

7.9.3. Results in the Signal Region

The scale factors for the extrapolation from the control region $\mathrm{CR}_{m_{\mathrm{jj}}}$ into the signal region, determined in Section 7.8, are applied to the respective invariant dijet mass distribution in the signal region to obtain the event yield in the signal region. The expected number of events after the extrapolation are listed in Table 7.9 for both lepton channels. The given uncertainties are the statistical uncertainty of the data for the backgrounds estimated with the simultaneous fit. The uncertainties on all other backgrounds are the uncertainties obtained from the pseudo experiments and therefore comprise the statistical uncertainties of the Monte Carlo simulation as well as theoretical uncertainties. The total expected background event yield is given with the total uncertainty, including statistical and systematic components. In both lepton channels, less events are observed than expected from the background estimation in the signal region. Nevertheless, good agreement between the observed data and the background expectation is found within $1.6\,\sigma$. The signal expectations are calculated using the VBFNLO generator and corrected for acceptance and efficiency effects.

The results of the simultaneous fit are illustrated in Figure 7.10. The fit results in the missing transverse energy distributions in the control region $\mathrm{CR}_{E_{\mathrm{T}}^{\mathrm{miss}}}$ are shown in Figures 7.10(a) and 7.10(c) for the electron and muon channel, respectively. Good agreement between the data and the background estimation is found as the ratio is consistent with unity within the uncertainties for both lepton channels. The fit results in the invariant dijet mass distribution are depicted in Figures 7.10(b) and 7.10(d) also for the electron and the muon channel, respectively. The results from the simultaneous fit in the control region $\mathrm{CR}_{m_{\mathrm{jj}}}$, indicated by the grey arrows, are illustrated as well as the expected event yields in the signal region. The lower panel depicts the ratio of the data and the sum of the signal and background expectations. Good agreement between data and the expectations is observed within the uncertainties. At low m_{jj} values a

trend is visible; the data is above the background expectations, but still within the quoted uncertainties. This trend is studied further by repeating the background estimation with an alternative $W\gamma$ + jets template shape simulated with SHERPA. A slight improvement is observed in the low m_{jj} region with the alternative template shape. However, the expected event yields in the signal region are found to be in good agreement with the nominal expectations within the quoted uncertainties. Therefore, no additional uncertainty is assigned and any potential shift is assumed to be covered by the uncertainties. Details about the study using the alternative $W\gamma$ + jets template shape are given in Appendix A.10.

In summary, the presented background estimation for the $WV\gamma$ analysis yields the expected number of events in the signal region separately for the two lepton channels. At the heart of the background estimation method is the simultaneous fit, used to determine the $W\gamma$ + jets, fake photons from jets and fake leptons from jets backgrounds, comprising three different data-driven methods. This allows to account for the interdependencies of the data-driven methods and minimises the dependence on theory for the most dominant backgrounds. The uncertainties on the expected event yields in the signal region are about 7 % in the electron channel and about 5 % in the muon channel. In both lepton channels, the statistical uncertainties due to the template shapes are the dominant uncertainty on the event yield. The observed and expected event yields in the signal region agree within 1.6 standard deviations. No deviations from the Standard Model are observed.

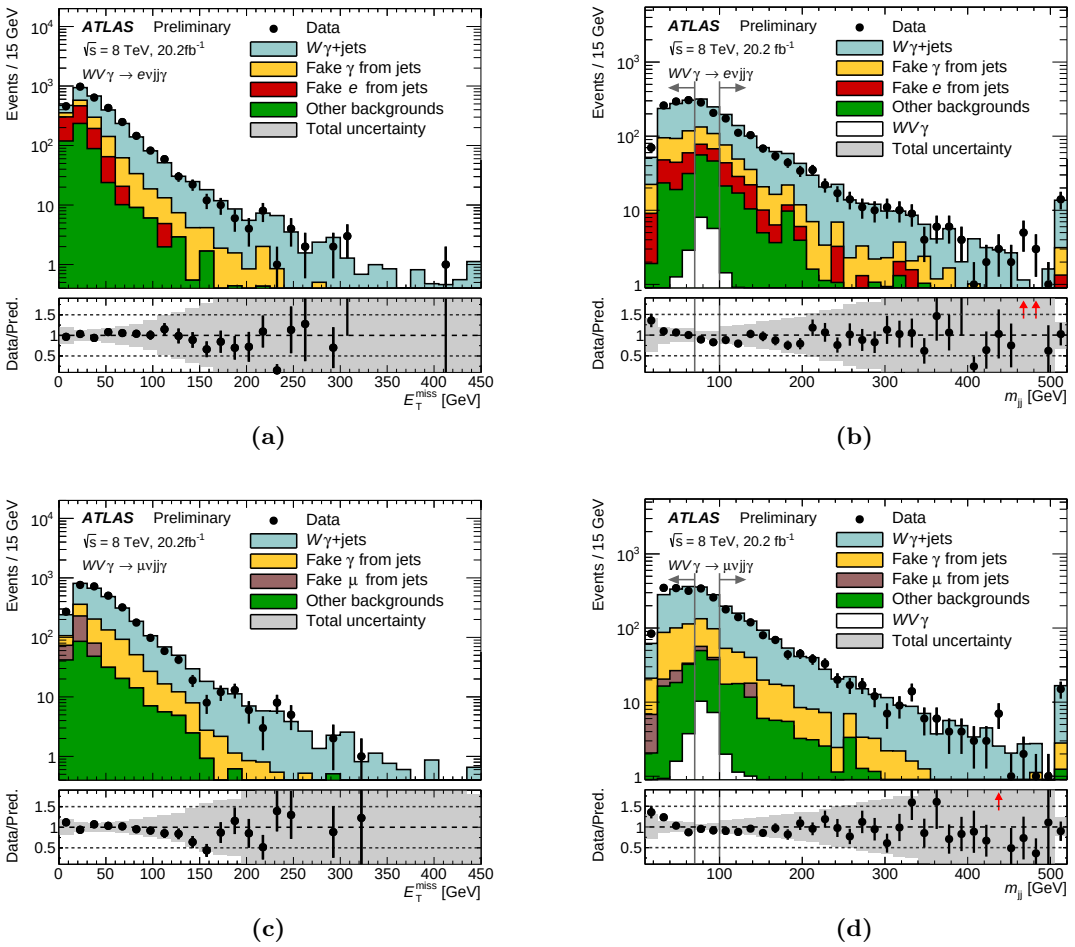

Figure 7.10.: Comparison of the data and the background expectation after the simultaneous fit to the (a) and (c), missing transverse energy distribution and the (b) and (d) invariant dijet mass distribution, in the electron (top) and the muon channel (bottom). The missing transverse energy distribution is shown in the control region $\mathrm{CR}_{E_{\mathrm{T}}^{\mathrm{miss}}}$. The maximum likelihood fit in the invariant dijet mass is performed in the control region $\mathrm{CR}_{m_{\mathrm{jj}}}$, indicated by the grey arrows. The $WV\gamma$ signal expectation in white, is included in the invariant dijet mass distributions. [10]

8. Limits on the $WV\gamma$ Production Cross Section

The production cross section of the $WV\gamma$ process is predicted by the gauge structure of the SU(2) symmetry group, making the measurement of the cross section a sensitive test of the Standard Model. In general, the cross section of the process is determined by:

$$\sigma = \frac{N^{\text{obs}} - N^{\text{exp}}}{C \cdot L_{\text{int}}} \tag{8.1}$$

where N^{obs} is the observed number of events, N^{exp} is the expected number of background events, L_{int} is the integrated luminosity and C the correction factor, correcting for detector acceptance and efficiency effects. In this thesis, upper limits on the $WV\gamma$ process are determined.

The limits on the production cross section are set in a *fiducial phase space*, defined on particle level and with similar selection criteria as for the signal region on reconstruction level. In the following chapter, *signal region* is used to refer to the selection at reconstruction level. To derive limits on the total cross section, large theoretical extrapolations would be necessary, introducing strong dependencies on the theoretical model used. These dependencies are avoided by setting the limits on the cross section in the fiducial phase space. The results are presented at particle level, where the results are independent of detector effects, allowing for easier comparisons to theoretical models.

The chapter starts with the definition of the fiducial region in Section 8.1. The correction factors used to correct the measurement for detector effects are discussed in Section 8.2. In Section 8.3 the determination of the cross section expectations for the $WV\gamma$ process at particle level are explained, followed by the statistical methods of the CL_S limit setting and the cross section limits, which are presented in Section 8.4.

8.1. Fiducial Region Definition

The analysis of $l\nu\text{jj}\gamma$ final states is performed in the signal region, as discussed in Chapter 6. The fiducial region of this analysis is defined at particle level and based on the same event selection criteria as the signal region. An overview of the selection criteria of the fiducial region are given in Table 8.1. A few modifications are introduced to obtain a theoretically well motivated phase space region that is independent of detector specific selection criteria. The geometrical acceptance of the electrons and photons is extended into the transition region of the electromagnetic barrel and end-cap, $1.37 < |\eta| < 1.53$. In addition, the pseudorapidity range of the leptons is extended slightly to $|\eta| < 2.5$ in order to have the same geometrical acceptance for electrons and muons. In the electron channel, the criterion on the invariant mass of the electron-photon pair $m_{e\gamma}$ is removed, to define the same phase space for the two lepton channels.

Object	Selection Criteria
Photon	≥ 1 photon
	$E_{\mathrm{T}} > 15\,\mathrm{GeV}$
	$\epsilon_h < 0.5$
	$\lvert\eta\rvert < 2.37$
	$\Delta R(l,\gamma) > 0.5$
W boson	1 electron or 1 muon
	$p_{\mathrm{T}} > 25\,\mathrm{GeV}$
	no 2^{nd} lepton ($p_{\mathrm{T}} > 7\,\mathrm{GeV}$)
	$\lvert\eta\rvert < 2.5$
	$E_{\mathrm{T}}^{\mathrm{miss}} > 30\,\mathrm{GeV}$
	$m_{\mathrm{T}}^{l\nu} > 30\,\mathrm{GeV}$
V boson	≥ 2 and $N_{b\text{-jets}} = 0$
	$p_{\mathrm{T}} > 25\,\mathrm{GeV}$
	$\lvert\eta\rvert < 2.5$
	$\lvert\Delta\eta_{\mathrm{jj}}\rvert < 1.2$
	$\Delta R_{\mathrm{jj}} < 3.0$
	$70\,\mathrm{GeV} < m_{\mathrm{jj}} < 100\,\mathrm{GeV}$
	$\Delta R(\mathrm{jet},\gamma) > 0.5$
	$\Delta R(\mathrm{jet},l) > 0.3$

Table 8.1.: The event selection criteria of the fiducial region, defined at particle level, for the $e\nu\mathrm{jj}\gamma$ and $\mu\nu\mathrm{jj}\gamma$ final states. The sequence of the overlap removal between jets and leptons, $\Delta R(\mathrm{jet},l)$, is different for electrons and muons, as described in Section 5.5.1.

For photons, a relative isolation, ϵ_h, defined at particle level, is used:

$$\epsilon_h = \frac{E_{\mathrm{T}}^{\mathrm{iso}}}{E_{\mathrm{T}}^{\gamma}} \tag{8.2}$$

where E_{T}^{γ} is the transverse energy of the photon and $E_{\mathrm{T}}^{\mathrm{iso}}$ is the transverse energy of other particles within a cone of radius $R = 0.4$ around the photon candidate. The relative isolation ϵ_h is required to be below 0.5.

8.2. Correction Factor

The correction factor, C, quantifies the difference of the event selection between the signal and the fiducial region. It is defined as the ratio of the event yield in the signal region, N^{reco}, at reconstruction level and the event yield in the fiducial phase space, N^{fid}, at particle level:

$$C = \frac{N^{\mathrm{reco}}}{N^{\mathrm{fid}}}. \tag{8.3}$$

The correction factors for the $WW\gamma$ and $WZ\gamma$ processes are derived separately using the Sherpa signal Monte Carlo samples and are combined into one correction factor for the $WV\gamma$

process via:

$$C_{WV\gamma} = f_{WW\gamma} \cdot C_{WW\gamma} \; + \; \Big(1 - f_{WW\gamma}\Big) \cdot C_{WZ\gamma} \tag{8.4}$$

where $f_{WW\gamma}$ is defined as:

$$f_{WW\gamma} = \frac{\sigma^{\text{fid}}_{WW\gamma}}{\sigma^{\text{fid}}_{WW\gamma} + \sigma^{\text{fid}}_{WZ\gamma}}. \tag{8.5}$$

Using the VBFNLO generator, $f_{WW\gamma}$ is evaluated to be 0.86.

The correction factors for the $WV\gamma$ process in the two lepton channels are:

$$C_{e\nu\text{jj}\gamma} = 0.280 \pm 0.006\,(\text{stat.}) \pm 0.022\,(\text{syst.})$$
$$C_{\mu\nu\text{jj}\gamma} = 0.395 \pm 0.008\,(\text{stat.}) \pm 0.034\,(\text{syst.})$$

indicating that about 28 % (40 %) of the events generated at particle level in the fiducial region are eventually reconstructed in the signal region of the electron (muon) channel. The largest impact on the correction factor C arises from the reconstruction inefficiencies of the photon candidate. The difference between the two lepton channels originates from the different reconstruction efficiencies for electrons and muons as well as from the additional selection requirement on the invariant mass of the electron-photon pair in the electron channel. Minor differences arise from the different geometrical extrapolations in the two lepton channels.

To study the origin of the differences in more detail, the correction factor is split into two components:

$$C = \epsilon \cdot A \tag{8.6}$$

where ϵ is the identification and reconstruction efficiencies and A is the acceptance correction arising from different geometrical requirements in the signal region and the fiducial region. This allows to study the impact of these two effects separately and to understand the difference between the correction factors in the electron and muon channel.

Acceptance Correction

The acceptance correction, A, quantifies the extrapolation into the larger phase space from the relaxed requirements on the pseudorapidity. It is defined at particle level as:

$$A = \frac{N^{\text{red. fid}}}{N^{\text{fid}}} \tag{8.7}$$

where $N^{\text{red. fid}}$ is the number of selected events in the geometrically reduced phase space at particle level. It is defined as the fiducial region, but requires the geometrical acceptances from the signal region: photons must be within $|\eta| < 2.37$ excluding the transition region from the calorimeter barrel to the end-caps $1.37 < |\eta| < 1.52$, electrons must be within $|\eta| < 2.47$ also excluding the transition region and muons must be within $|\eta| < 2.4$. It is evaluated using the $WV\gamma$ signal simulation samples generated with SHERPA and is determined to:

$$A_{e\nu\text{jj}\gamma} = 0.888 \pm 0.004\,(\text{stat.})$$
$$A_{\mu\nu\text{jj}\gamma} = 0.935 \pm 0.003\,(\text{stat.})$$

for the electron and muon channel respectively. This indicates that only 11 % (7 %) of the events fall in the region of the geometrical extension. The pseudorapidity extrapolation is slightly larger for electrons than for muons and this effect is one reason for the lower correction factor C in the electron channel.

Efficiency Correction

The efficiency correction, ϵ, corrects for limited detector resolution and inefficiencies in the object reconstruction. It is defined as the ratio of the event yield at reconstruction level N^{reco} and the event yield at particle level in the reduced phase space $N^{\text{red. fid}}$:

$$\epsilon = \frac{N^{\text{reco}}}{N^{\text{red. fid}}} \tag{8.8}$$

and thus corrects the measurement from reconstruction level to particle level. It is also evaluated using the $WV\gamma$ signal Monte Carlo samples simulated with SHERPA and is found to be:

$$\epsilon_{e\nu\text{jj}\gamma} = 0.316 \pm 0.007 \text{ (stat.)}$$
$$\epsilon_{\mu\nu\text{jj}\gamma} = 0.423 \pm 0.008 \text{ (stat.)}$$

for the electron and muon channel respectively. This implies that 32 % (42 %) of the events selected in the reduced fiducial region in the electron (muon) channel, are also selected in the signal region. The values for ϵ are quite low, as they are determined by the product of the identification and reconstruction inefficiencies for the multiple objects present in the final state. The identification efficiency for the photons ranges from 45 % to above 95 % depending on the energy, the detector region as well as the conversion type of the photon (Figure 5.4 in Section 5.2). The efficiency for the reconstruction and identification of electrons ranges from 50 % to about 95 % depending on the energy, (Figure 5.5 in Section 5.2), in contrast to the reconstruction efficiency for muons, which is about 99 % in most regions of the pseudorapidity, (Figure 5.6 in Section 5.3). This leads to a larger reconstruction efficiency in the muon channel with respect to the electron channel. In addition, the efficiency correction accounts for the removed requirement on the invariant mass of the electron-photon pair, which further decreases the value in the electron channel.

8.2.1. Statistical Uncertainties

To determine the statistical uncertainty on the correction factor C, the *bootstrap method* [134] is employed, which accounts for correlations between the event yield in the signal region (numerator) and the event yield in the fiducial region (denominator). The nominal distributions of the numerator and denominator are used to derive a set of replicas that reflect the statistical features of the nominal ones. The replicas are determined by drawing random weights for each event from a Poisson distribution with mean of 1.0. By weighting the common events in the numerator and denominator with the same random weight, the statistical correlation is incorporated, while treating different events independently of each other. The mean of the Poisson distribution is at unity by construction, since one is the expected event yield per event. For each event passing either selection category, ten thousands replicas are generated and treated as independent measurements of the event yields. Using these replicas, the correction factor C is re-computed. In Figure 8.1 the distributions of the correction factors for the $WW\gamma$ and $WZ\gamma$ processes are

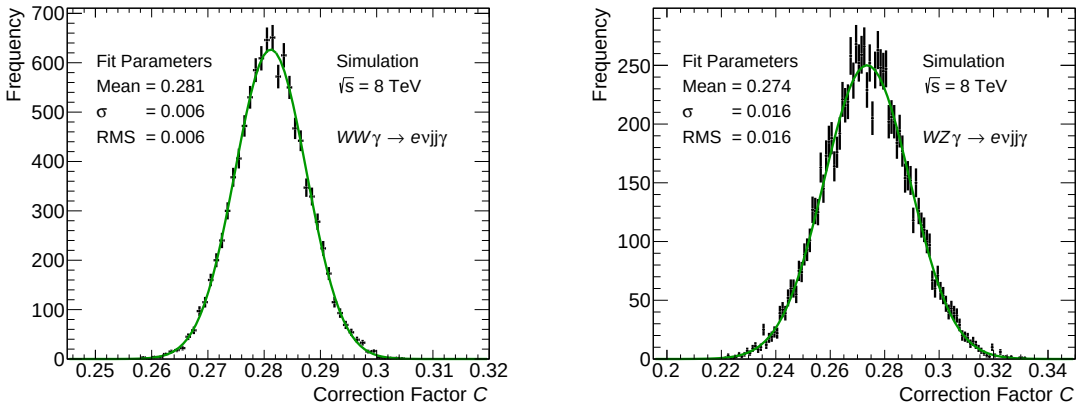

Figure 8.1.: Distributions of the correction factor C after re-sampling the original input event yields ten thousand times with the bootstrap method (a) for the $WW\gamma$ and (b) for the $WZ\gamma$ process. Both distributions exhibit Gaussian behaviour as indicated by the fit in green. The mean value of the distribution corresponds of the nominal correction factor and the RMS is taken as statistical uncertainty. Only the electron channel is shown.

shown for the electron channel. The mean of the distribution is the nominal correction factor and the width, derived as the root mean square (RMS), is taken as statistical uncertainty. The nominal values of the correction factors derived for the $WW\gamma$ and $WZ\gamma$ processes are found to be in good agreement within their statistical uncertainties. A similar behaviour is found in the muon channel. The relative statistical uncertainty on the correction factor C for the $WV\gamma$ process is found to be 2.1 % (2.0 %) in the electron (muon) channel.

8.2.2. Systematic Uncertainties

Systematic uncertainties on the correction factor arise due to inefficiencies in the reconstruction and identification of the objects. These include uncertainties arising from energy calibrations, reconstruction inefficiencies of the objects and corrections of the pileup simulations in the Monte Carlo generation. These effects and their uncertainties are discussed in detail in Chapter 5. By varying each systematic up and down by one standard deviation, the influence on the correction factor is evaluated, following the same approach as in Section 7.9.2. For each systematic variation the correction factor is recomputed. For the systematic, i, the uncertainty ΔC_i, is taken as the maximum deviation of the correction factor determined with the up or down variation to the nominal value. The systematic uncertainties are derived separately for the $WW\gamma$ and $WZ\gamma$ processes and combined to yield the uncertainties for the $WV\gamma$ process, according to Equation 8.4 using standard Gaussian error propagation. This is done separately for each lepton channel. In Table 8.2 the systematic uncertainties on the correction factor C are shown with their relative sizes for both lepton channels.

In addition, the choice of the Monte Carlo generator is also taken as source of systematic uncertainty. This includes uncertainties due to the computation of the hard scattering matrix as well as uncertainties arising from hadronisation and showering models. The nominal correction factor is derived with the SHERPA signal samples using the CT10 [66] parton distribution functions. In order to estimate the influence on the correction factor due to the generator

Systematic Component	Electron Channel Relative Uncertainty [%]	Muon Channel
Electromagnetic Energy Scale	0.86	0.65
Electron Energy Resolution	0.16	0.00
Electron Identification	0.73	0.00
Electron Isolation	0.17	0.00
Electron Reconstruction Eff.	0.26	0.00
Photon Energy Resolution	0.32	0.13
Photon Identification	1.03	1.02
Photons from Electrons	0.00	0.00
Muon Energy Scale	0.00	0.17
Muon Reconstruction Eff.	0.00	0.22
Muon Resolution ID	0.00	0.10
Muon Resolution MS	0.00	0.20
Jet Energy Resolution	2.52	2.96
Jet Energy Scale	4.17	5.33
Jet Vertex Fraction	1.67	1.82
$E_{\mathrm{T}}^{\mathrm{miss}}$ Energy Scale Soft Terms	0.60	0.68
$E_{\mathrm{T}}^{\mathrm{miss}}$ Resolution Soft Terms	0.65	0.54
Pileup	0.61	0.44
Generator Dependence	6.17	6.17
Total Systematic Uncertainty	7.69	8.48

Table 8.2.: Relative systematic uncertainties on the correction factor C for the electron (left) and the muon channel (right).

choice, the correction factor is determined using the alternative $WV\gamma$ signal simulation samples, generated with MadGraph. The alternative samples use MadGraph to simulate the hard scattering process with the CTEQ6L1 parton distribution functions, interfaced to Pythia for the hadronisation and showering. As the two simulation samples are generated with different parton distribution functions, the simulated events generated with MadGraph are re-weighed, based on the momentum fractions of the incoming partons, to match the CT10 parton distribution functions. This is done as the uncertainty due to the choice of the parton distribution function is considered as theoretical uncertainty, as discussed in Section 4.2. To avoid double counting, it is not considered as an uncertainty component on the correction factor C. The difference of the correction factors evaluated with the nominal simulation sample and with the alternative sample is taken as additional uncertainty. Good agreement is observed for the generator difference between the $WW\gamma$ and the $WZ\gamma$ processes as well as between the two lepton channels. Therefore, the four values for the generator difference are averaged according to their relative cross sections, to obtain one value for the generator difference, independent of the lepton flavour or the process. The resulting uncertainty due to the choice of the generator dependence, is evaluated to 6.17 %, also listed in Table 8.2.

The total systematic uncertainty on the correction factor C is derived by adding the separate systematic components, given in Table 8.2, in quadrature and is evaluated to 7.69 % (8.48 %) in the electron (muon) channel. The dominant uncertainty arises from the generator dependence followed by the uncertainties due to the jet energy scale and resolution.

8.3. Standard Model Predictions

The theoretical expectation for the $WV\gamma$ production cross section is derived using the VBFNLO generator, as discussed in detail in Section 4.2. In the fiducial region the parton level cross section is $\sigma_{\text{theory}}^{\text{parton}} = (3.78 \pm 0.11)$ fb per lepton flavour. The measurement, in contrast, is corrected to particle level and cannot be compared directly to the theoretical predications on parton level. Therefore, a correction is applied to the parton level cross section, in order to obtain predictions at particle level, called the *parton-to-particle correction*.

Parton-to-Particle Correction

The parton-to-particle correction factor, C^{p2p}, is the ratio of the event yield in the fiducial phase space at particle level and the event yield in the same phase space defined at parton level:

$$C^{\text{p2p}} = \frac{N^{\text{fid}}}{N^{\text{parton}}}. \tag{8.9}$$

The selection requirements at parton level are the same as defined in Table 8.1, however the object definitions are different. The different object definitions have the most significant impact on jets, as the constituents of the parton level jets are quarks and gluons in contrast to the particles after the parton shower and hadronisation at particle level. This has an effect on the energies and the directions of the jets. In addition, the relative photon isolation ϵ_h, defined in Equation 8.2, is influenced. Since the relative photon isolation is based on the energy of the objects close to the photon, any differences in the energy and direction of the jets, influences its magnitude. The different lepton definitions also lead to small differences, but are minimised by the definition of the lepton at particle level. Leptons, defined at particle level, can radiate a photon during the showering process in contrast to leptons at parton level, which are defined before this radiation. Therefore, when at particle level, photons are close to a lepton, the four momenta of the photons and the lepton are added. In this way, the lepton at particle level is corrected for photon radiation and its properties are comparable to the properties of the lepton at parton level.

The parton-to-particle correction factors are evaluated with the $WV\gamma$ signal samples generated with SHERPA and are found to be:

$$C_{e\nu\text{jj}\gamma}^{\text{p2p}} = 0.639 \pm 0.006\,(\text{stat.}) \pm 0.010\,(\text{syst.})$$
$$C_{\mu\nu\text{jj}\gamma}^{\text{p2p}} = 0.571 \pm 0.006\,(\text{stat.}) \pm 0.019\,(\text{syst.})$$

for the electron and muon channel respectively. This indicates that only 64 % (57 %) of the events selected at parton level are also selected at particle level. The difference between the electron and the muon channel arises solely from the different overlap removal criteria between the jet and either the electron or the muon, as described in Section 5.5.1; when an electron candidate is close to a jet, the jet is discarded, whereas when a jet is close to a muon candidate, the muon candidate is discarded. The large parton-to-particle corrections arise from the hadronisation and showering of the jets. Figure 8.2 compares the invariant dijet mass distribution at parton and particle level for the $WW\gamma$ and $WZ\gamma$ processes in the electron channel. At parton level, most of the events are generated on the mass resonance of the hadronically decaying heavy gauge boson. At particle level, less events are selected and the distributions are broadened and

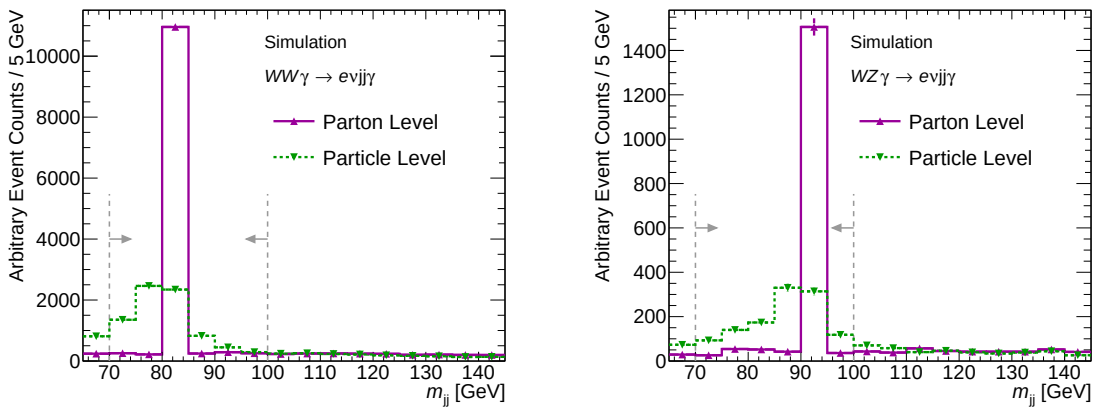

(a) **(b)**

Figure 8.2.: Comparison of the invariant dijet mass distribution at parton level (solid magenta line) and at particle level (dashed green line) in (a) for the $WW\gamma$ process and in (b) for the $WZ\gamma$ process. The grey arrows indicate the signal region. Only the electron channel is shown.

shifted towards lower values. This leads to a parton-to-particle correction factor significantly lower than unity. In the muon channel, a similar behaviour is observed.

Since the hadronisation and showering process is causing a large difference between the parton and particle level, a systematic uncertainty due to the different showering and hadronisation models is considered on the parton-to-particle correction factor. Therefore, C^{p2p} is determined with the alternative signal Monte Carlo generated with MadGraph for the hard scattering and interfaced to Pythia for the hadronisation and showering. The difference between the values of the parton-to-particle correction factors determined with the nominal and the alternative sample is used as uncertainty and evaluated to 1.5 % (3.3 %) in the electron (muon) channel. This strategy is chosen, as none of the two generators is intrinsically favoured over the other.

Cross Section Expectation on Particle Level

The theoretical cross section expectation at particle level is obtained by multiplying the cross section at parton level with the correction factor C^{p2p}:

$$\sigma^{\mathrm{theory}} = C^{\mathrm{p2p}} \cdot \sigma^{\mathrm{theory}}_{\mathrm{parton}}. \tag{8.10}$$

The theory expectations of the $WV\gamma$ cross section at particle level is then:

$$\sigma^{\mathrm{theory}}_{e\nu\mathrm{jj}\gamma} = (2.42 \pm 0.08)\ \mathrm{fb}$$
$$\sigma^{\mathrm{theory}}_{\mu\nu\mathrm{jj}\gamma} = (2.16 \pm 0.10)\ \mathrm{fb}$$

where the difference between the electron and muon channel arises solely from the different parton-to-particle correction factors, as discussed.

8.4. Determination of the Production Cross Section Limit

The limits on the production cross section are derived by determining the maximal event yield for a given cross section value, which is still in agreement with the observed event yield considering all uncertainties. The expected signal event yield is parametrised via:

$$N^{\text{sig}}(\sigma_{\text{fid}}) = C \cdot L_{\text{int}} \cdot \sigma_{\text{fid}} \tag{8.11}$$

where C is the correction factor, L_{int} is the integrated luminosity and σ_{fid} is the cross section at particle level in the fiducial region and the parameter of interest in the following. The expected event yield, N^{exp}, is the sum of the number of expected signal events N^{sig} and the number of expected background events, N^{bkg}:

$$N^{\text{exp}}(\sigma_{\text{fid}}) = N^{\text{sig}}(\sigma_{\text{fid}}) + N^{\text{bkg}}. \tag{8.12}$$

where N^{bkg} is determined with the background estimation method discussed in Chapter 7. The probability, or likelihood L, to observe N^{obs} events when N^{exp} are expected, is given by the Poisson distribution:

$$L(N^{\text{obs}}|\sigma_{\text{fid}}) = Pois(N^{\text{obs}}|N^{\text{exp}}(\sigma_{\text{fid}})) \tag{8.13}$$

$$= \frac{(N^{\text{exp}})^{N^{\text{obs}}}}{N^{\text{obs}}!}\, e^{-N^{\text{exp}}}. \tag{8.14}$$

The different sources of uncertainties on the signal and background estimation are incorporated into the likelihood function as nuisance parameters $\theta = [\theta^{\text{sig}}, \theta^{\text{bkg}}]$. The uncertainties on the integrated luminosity ΔL_{int} and on the correction factor ΔC are considered for the signal estimation and the total uncertainty on the total background event yield ΔN^{bkd}, as described in Chapter 7, is considered for the background estimation. Each nuisance parameter i is constrained by a Gaussian distribution, $Gauss(\theta_i, \sigma_{\theta_i})$, with the mean at the central value, θ_i, and the width, σ_{θ_i}, corresponding to the uncertainty. The likelihood for a single lepton channel is therefore:

$$\begin{aligned} L(N^{\text{obs}}|\sigma_{\text{fid}}, \theta) = {} & Pois(N^{\text{obs}}|N^{\text{sig}}(\sigma_{\text{fid}}, \theta^{\text{sig}}) + N^{\text{bkg}}(\theta^{\text{bkd}})) \\ & \cdot Gauss(L_{\text{int}}, \Delta L_{\text{int}}) \cdot Gauss(C, \Delta C) \cdot Gauss(N^{\text{bkd}}, \Delta N^{\text{bkd}}). \end{aligned} \tag{8.15}$$

In order to increase the sensitivity, the electron and muon channel are combined by multiplying the respective likelihood functions:

$$\begin{aligned} L_{l\nu\text{jj}\gamma}(N^{\text{obs}}|\sigma_{\text{fid}}, \theta) = {} & Pois(N^{\text{obs}}_{e\nu\text{jj}\gamma}|N^{\text{exp}}_{e\nu\text{jj}\gamma}(\sigma_{\text{fid}}, \theta_{e\nu\text{jj}\gamma})) \\ & \cdot Gauss(C_{e\nu\text{jj}\gamma}, \Delta C_{e\nu\text{jj}\gamma}) \cdot Gauss(N^{\text{bkd}}_{e\nu\text{jj}\gamma}, \Delta N^{\text{bkd}}_{e\nu\text{jj}\gamma}) \\ & \cdot Pois(N^{\text{obs}}_{\mu\nu\text{jj}\gamma}|N^{\text{exp}}_{\mu\nu\text{jj}\gamma}(\sigma_{\text{fid}}, \theta_{\mu\nu\text{jj}\gamma})) \\ & \cdot Gauss(C_{\mu\nu\text{jj}\gamma}, \Delta C_{\mu\nu\text{jj}\gamma}) \cdot Gauss(N^{\text{bkd}}_{\mu\nu\text{jj}\gamma}, \Delta N^{\text{bkd}}_{\mu\nu\text{jj}\gamma}) \\ & \cdot Gauss(L_{\text{int}}, \sigma_{L_{\text{int}}}). \end{aligned} \tag{8.16}$$

It should be noted that the Gaussian constraint for in the integrated luminosity appears only once in the combined likelihood, as it is the same for the two lepton channels.

Upper limits on the production cross section σ_{fid} of the $WV\gamma$ process in the fiducial region are set using the CL_S method [135] at 95 % confidence level. The CL_S method is chosen, as it does not exclude models to which the measurement has only low sensitivity.

8.4.1. CL_S Limit Setting

The statistical concepts of the CL_S method are summarised following the description in [136, 137]. The CL_S method uses a so-called *test statistic* to discriminate the hypothesis that the observed data consists of signal and background events $(S + B)$ from the hypothesis that the observed data consists only of background events (B). For the $WV\gamma$ analysis, the test statistic is based on the profile likelihood ratio λ:

$$\lambda(\mu) = \frac{L(\mu, \hat{\hat{\theta}})}{L(\hat{\mu}, \hat{\theta})} \tag{8.17}$$

where μ is the parameter of interest, corresponding to the particle level cross section of the $WV\gamma$ process σ_{fid}, and θ the nuisance parameters, corresponding to the uncertainties of the measurement. The denominator is the *unconditional likelihood* with the maximum likelihood estimators $\hat{\mu}$ and $\hat{\theta}$, maximising the likelihood for the observed data. The numerator is the *conditional likelihood*, which is maximal for the parameter values $\hat{\hat{\theta}}$, given a specific value of μ. The profile likelihood ratio λ is defined between $0 < \lambda \leq 1$ and is maximal for $\hat{\mu} = \mu$ by construction. Using this definition, the test statistic, q_μ, is constructed as:

$$q_\mu = \begin{cases} -2 \ln \lambda(\mu) & , \text{ for } \mu \geq \hat{\mu} \geq 0 \\ 0 & , \text{ else .} \end{cases} \tag{8.18}$$

The negative logarithm of the likelihood ratio is used for the definition of the test statistic, as it is computationally favourable, since products in the likelihood function are transformed into sums. The factor of two is convention. As the parameter of interest is the $WV\gamma$ production cross section, the test statistic is required to be positive; negative values are excluded, since they are unphysical. The value of the test statistic for the observed data is q_{obs}. The probability density function $f(q_\mu|S + B) = f(q_\mu|N^{\text{sig}}(\mu, \theta^{\text{sig}}) + N^{\text{bkg}}(\theta^{\text{bkd}}))$ under the tested signal hypothesis μ is typically derived by drawing pseudo experiments, where the nuisance parameters are allowed to float within their constraints. Similarly, the probability density function $f(q_\mu|B) = f(q_\mu|N^{\text{bkg}}(\theta^{\text{bkd}}))$ under the background-only hypothesis is also determined by drawing pseudo experiments, where the nuisance parameters are allowed to float within their constraints. The probability, p_{S+B}, to obtain a value of the test statistic q_μ under the signal and background hypothesis that is equal or less likely than the observed one q_{obs}, is given by:

$$p_{S+B} = \int_{q_{\text{obs}}}^{\infty} f(q_\mu|N^{\text{sig}}(\mu) + N^{\text{bkg}})dq. \tag{8.19}$$

This is used for the so-called CL_{S+B} method, an alternative way to derive limits, where the signal hypothesis for the value μ is rejected if $p_{S+B} < \alpha$, with $\alpha = 0.05$ conventionally. The confidence level is given by $1 - \alpha$, leading to a 95 % confidence level for $\alpha = 0.05$. Upper limits at a 95 % confidence level indicate that the true value of the parameter of interest is below the quoted upper limit with a probability of at least 95 %. When the sensitivity of a measurement to a specific signal model is low, the number of expected signal events is low with respect to the expected background events. The resulting distributions of the test statistic

for the two hypotheses are close to each other and have a large overlap. If the data also have a sufficiently large downward fluctuation, the limits derived with the p_{S+B} method might exclude signal models, even when the measurement has no or only low sensitivity to it. To avoid this behaviour, the probability, p_B, to obtain a value of the test statistic q_μ under the background-only hypothesis that is equal or less likely than the observed one q_{obs}:

$$p_B = \int_{-\infty}^{q_{\text{obs}}} f(q_\mu|B)dq. \tag{8.20}$$

The p_{S+B} and p_B are commonly referred to as *p-values*. Using the p_{S+B} and p_B probabilities, the CL_S probability is defined as:

$$CL_S \equiv \frac{p_{S+B}}{1-p_B}. \tag{8.21}$$

The tested hypothesis is rejected when $CL_S < \alpha$, where $\alpha = 0.05$ is chosen conventionally, corresponding to a 95 % confidence level. When the distributions of the test statistic for the two hypotheses are well separated, the $1 - p_B$ term is close to unity and the obtained limits are the same as derived with the p_{S+B} method. However, in case the two distributions are close to each other, the denominator gets small and penalises the p_{S+B} probability. The resulting limit is less stringent, which accounts for the low sensitivity of the measurement to the signal model. Hence, limits derived with the CL_S methods are always equal or weaker than the limits derived with the p_{S+B} method and therefore the former is more conservative.

In this thesis, the CL_S method is implemented using the ROOT framework, with the integrated RooStat and RooFit extensions, providing useful statistical tools. Theorems by Wilks and Wald [138, 139] state that for large event yields the likelihood ratio follows a χ^2- distribution, also referred to as *asymptotic formula*. Based on the asymptotic formula, one representative dataset can be constructed for the test statistic, which replaces the large number of pseudo datasets and thus decreases the computational effort significantly. This representative dataset is called *Asimov datasets* [137] and is derived by setting the values of the observed quantities equal to the expected values. The upper limit is determined numerically, using the cumulative distribution function of the χ^2- distribution [137]. See Appendix A.11 for more information about the asymptotic formula. The asymptotic formula and the Asimov dataset are implemented using the AsymptoticCalculator class, provided by RooStat [140]. To justify the usage of the asymptotic formula, the exclusion limits have also been derived using a full Frequentist procedure and the results are found to be in good agreement with the nominal results. More details about the full Frequentist procedure are given in Appendix A.12.

	N^{obs}	N^{bkg}	C	L_{int} [fb^{-1}]
$e\nu\text{jj}\gamma$	490	551.7 ± 38.0	0.28 ± 0.02	20.24 ± 0.38
$\mu\nu\text{jj}\gamma$	599	620.7 ± 31.2	0.40 ± 0.03	20.24 ± 0.38

Table 8.3.: Overview of the inputs for the CL_S limit setting for both lepton channels. N^{obs} is the observed event yield, N^{bkg} is the expected background event yield, both in the signal region, along with the correction factor C and the integrated luminosity L_{int}.

	Observed Limit [fb]	Expected Limit [fb]	Theory Prediction [fb]
$e\nu\text{jj}\gamma$	9.9	$15.6^{+6.4}_{-4.4}$	2.42 ± 0.08
$\mu\nu\text{jj}\gamma$	8.3	$10.0^{+4.1}_{-2.8}$	2.16 ± 0.10
$l\nu\text{jj}\gamma$	5.7	$8.4^{+3.4}_{-2.4}$	2.29 ± 0.06

Table 8.4.: Observed and expected upper limits on the $WV\gamma$ production cross section at the 95 % confidence level using the CL_s method for the $e\nu\text{jj}\gamma$ and $\mu\nu\text{jj}\gamma$ final states as well as averaged over the lepton flavour, $l\nu\text{jj}\gamma$. The expected exclusion limits are determined under the background only hypothesis. The theoretical predictions for the expected cross sections are computed with the VBFNLO generator and corrected to particle level.

8.4.2. Results

The inputs to derive the CL_S limits are listed in Table 8.3. Exclusion limits at 95 % confidence level on the production cross section are derived for the $e\nu\text{jj}\gamma$ and $\mu\nu\text{jj}\gamma$ final states as well as averaged over the lepton flavours, $l\nu\text{jj}\gamma$. Table 8.4 gives the observed and the expected exclusion limits, as well as the theoretical cross section expectations for the $WV\gamma$ signal in the Standard Model. The expected limits are determined under the assumption of the background only hypothesis.

In the electron channel, the observed upper limit on the production cross section is 9.9 fb and the expected limit is 15.6 fb. In the muon channel, the observed upper limit is 8.3 fb and the expected limit is 10.0 fb. The observed exclusion limits are more stringent than the expected limits in both lepton channels, as in both less events are observed than expected. The muon channel is slightly more sensitive, due to the lower uncertainty on the background estimation. Combining both channels, yields the most stringent exclusion limits on the production cross section, with an observed upper limit of 5.7 fb and an expected limit of 8.4 fb. This corresponds to an observed exclusion limit which is about 2.5 times larger than the Standard Model cross section expectation. In Figure 8.3, the CL_S probability is illustrated as a function of the fiducial cross section, for the $l\nu\text{jj}\gamma$ combination, averaged over the lepton flavours. By definition, cross section values with a corresponding CL_S value of lower than 0.05 are excluded.

The search for $WV\gamma$ production performed by the CMS collaboration, using a dataset with the same centre-of-mass energy and comparable integrated luminosity, also sets upper limits on the production cross section combining the electron and muon channel, but in a different phase space region. The expected exclusion limits are about a factor of 4.4 larger than the Standard Model expectation and the observed limits are about 3.4 times larger than the Standard Model prediction. More details about the CMS analysis can be found in Reference [11]. The exclusion

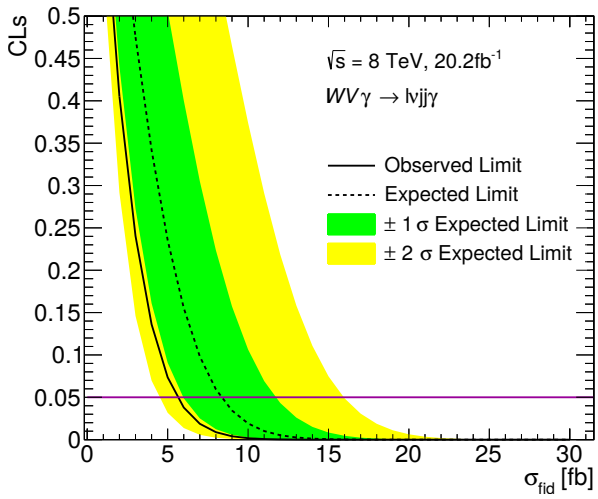

Figure 8.3.: Distribution of the CL_S probability as a function of the fiducial cross section σ_{fid}, averaged over the lepton flavours, $l\nu\text{jj}\gamma$. The magenta line illustrates the 0.05 threshold, corresponding to the 95 % confidence level. Production cross sections with lower CL_S values are excluded. The solid line represents the observed exclusion limits and the dotted line the expected upper limit under the assumption no signal is present. The green and yellow bands represent the one and two sigma bands of the expected upper limit, respectively.

limit presented in this thesis improves the limit determined by the CMS Collaboration by 25 % and thus yield the best upper limits on the $WV\gamma$ production cross section to date. As no deviations from the Standard Model are observed, the measurement is used to constrain new physics beyond the Standard Model, discussed in the following chapter.

9. Search for New Physics Beyond the Standard Model

The results of the cross section limit showed no deviation from the Standard Model and therefore the measurement of $WV\gamma$ production is used to constrain new physics beyond the Standard Model. In this analysis, effects arising from new physics are formulated in the framework of an effective field theory, as discussed in Section 2.3. The anomalous quartic gauge couplings (aQGC) are parametrised as operators with mass dimension eight and are constrained by deriving Frequentist exclusion limits at 95 % confidence level on the individual coupling parameter.

In Section 9.1 the statistical method to derive the Frequentist limits is discussed and followed by a detailed description of the phase space optimisation in Section 9.2. Besides the limits on anomalous quartic gauge couplings, also CL_S exclusion limits on the production cross section of the $WV\gamma$ process are determined in the new phase space. The results of the CL_S limits and the limits on the aQGCs are presented in Section 9.3.

Anomalous quartic gauge couplings can be parametrised in different ways and for the $WV\gamma$ analysis, the parametrisation of VBFNLO in used. Several analyses that also set limits on anomalous quartic gauge couplings use a different parametrisation and therefore, the exclusion limits given in other publications, which are discussed in this chapter, might be defined on a different basis. However, the coupling parameters can be converted from one notation into the other as described in Reference [141]. For convenience, all limits discussed in this thesis are converted into the same notation.

9.1. Limit Setting Procedure

In order to constrain anomalous quartic gauge couplings, exclusion limits are derived on the coupling parameter $\frac{f_i}{\Lambda^4}$ of the operator i, where f_i denotes the coupling strength and Λ, the energy scale where new physics occurs. The $WV\gamma$ process is sensitive to fourteen different dimension eight operators, listed in Appendix A.2. New physics phenomena might only modify some of the operators and not all fourteen at the same time. As it is not known which of theses operators are modified by potential new physics and to maximise the sensitivity to each coupling, the operators are treated independent of each other. Thus, the exclusion limits are derived for one coupling parameter at a time, while the others are set to zero.

The exclusion limits are derived by estimating the maximal event yield expected for the tested parameter, which is still in agreement with the observed number of events under the consideration off all experimental uncertainties. The expected cross section in the presence of anomalous quartic gauge couplings with coupling parameter $\frac{f_i}{\Lambda^4}$, defined as the signal cross section in the following, is proportional to the square of the matrix element determined from the effective

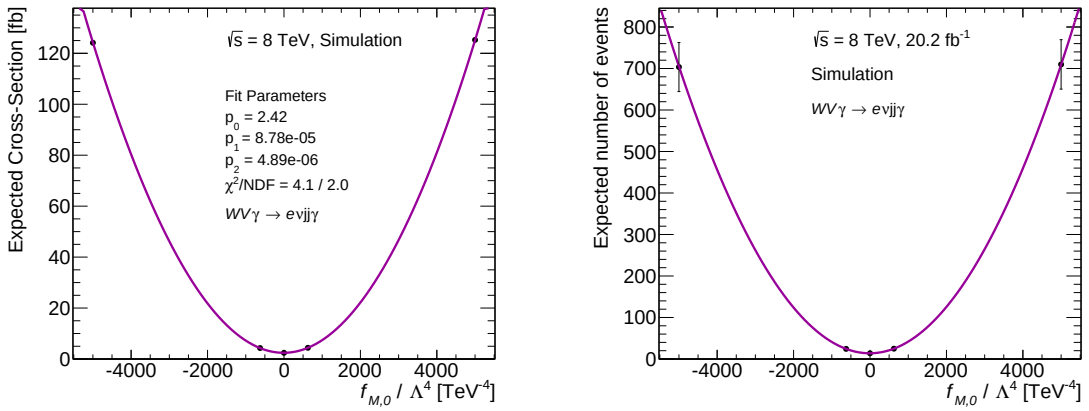

(a) **(b)**

Figure 9.1.: Parabolic parametrization of the (a) cross section prediction including anomalous quartic gauge couplings and of (b) the expected event yield, both defined on particle level. The cross section is evaluated for five different values of the coupling strength (black dots) with VBFNLO and fitted using a parabolic function (magenta line). The results are shown for the $\frac{f_{M,0}}{\Lambda^4}$ parameter in the electron channel.

Lagrangian, as given in Equation 2.13:

$$\begin{aligned}\sigma^{\text{sig}} \sim \left|\mathcal{M}_{if}^{\text{EFT}}\right|^2 &= \left|\mathcal{M}_{if}^{\text{SM}} + \mathcal{M}_{if}^{\text{aQGC}}\right|^2 \\ &= \left|\mathcal{M}_{if}^{\text{SM}}\right|^2 + \underbrace{2\left|\mathcal{M}_{if}^{\text{SM}}\,\mathcal{M}_{if}^{\text{aQGC}}\right|}_{\sim \frac{f_i}{\Lambda^4}} + \underbrace{\left|\mathcal{M}_{if}^{\text{aQGC}}\right|^2}_{\sim \left(\frac{f_i}{\Lambda^4}\right)^2}. \end{aligned} \tag{9.1}$$

It consists of the Standard Model contribution, a contribution arising solely from the anomalous coupling, which is proportional to $\left(\frac{f_i}{\Lambda^4}\right)^2$ and the interference of the two, proportional to $\frac{f_i}{\Lambda^4}$. Therefore, the cross section is parametrised by a parabolic function with three free parameters:

$$\sigma^{\text{sig}} = p_0 + p_1 \cdot \frac{f_i}{\Lambda^4} + p_2 \cdot \left(\frac{f_i}{\Lambda^4}\right)^2 \tag{9.2}$$

where p_0 corresponds to the Standard Model cross section of the semi-leptonic $WV\gamma$ process. This is referred to as the signal cross section in the following, comprising the Standard Model expectation and the anomalous quartic gauge boson prediction. The expected cross section is evaluated for five different coupling values $\frac{f_i}{\Lambda^4}$ for each operator in the fiducial phase space using the VBFNLO generator. By fitting the parabolic function from Equation 9.2 to the five points, the cross section can be determined for any value of the coupling parameter $\frac{f_i}{\Lambda^4}$. This is depicted in Figure 9.1(a), where the expected cross section as a function of the coupling parameter $f_{M,0}$ is shown. Good agreement between the parabolic fit and the simulated points are observed. The expected number of signal events, N^{sig}, is determined using the signal cross section expectation σ^{sig} and Equations 8.1 and 8.10:

$$N^{\text{sig}}\left(\frac{f_i}{\Lambda^4}\right) = L_{\text{int}} \cdot C \cdot C^{\text{p2p}} \cdot \sigma^{\text{sig}} \tag{9.3}$$

$$= L_{\text{int}} \cdot C \cdot C^{\text{p2p}} \cdot \left(p_0 + p_1 \cdot \frac{f_i}{\Lambda^4} + p_2 \cdot \left(\frac{f_i}{\Lambda^4}\right)^2\right) \tag{9.4}$$

where L_{int} is the integrated luminosity, C is the correction factor, and C^{p2p} is the parton-to-particle correction factor. The event yield for the new physics scenario is shown in Figure 9.1(b) for the $f_{M,0}$ parameter, which follows the same parabolic behaviour as the cross section.

The exclusion limits are derived using Frequentist intervals at 95 % confidence level, based on a likelihood formulation. The likelihood to obtain the observed event yield N^{obs} in an experiment where N^{exp} events are expected is given by the Poisson distribution:

$$L(N^{\text{obs}}) = Pois(N^{\text{obs}}|N^{\text{exp}}) \tag{9.5}$$

as in Equations 8.13 and 8.14. The expected number of events N^{exp} is the sum over the expected event yields arising from background and signal processes:

$$N^{\text{exp}}(\frac{f_i}{\Lambda^4}) = N^{\text{bkg}} + N^{\text{sig}}(\frac{f_i}{\Lambda^4}) \tag{9.6}$$

and is dependent on the strength of the anomalous quartic gauge coupling $\frac{f_i}{\Lambda^4}$.

The limit setting is similar to the method described in Section 8.4, but the uncertainties on the signal and the background event yields are incorporated slightly differently. Here, the total uncertainty on the signal yield, ΔN^{sig}, and the total uncertainty on the background event yield, ΔN^{bkg}, are introduced via nuisance parameters $\boldsymbol{\theta} = [\theta^{\text{sig}}, \theta^{\text{bkg}}]$, respectively. Nominally, the nuisance parameters θ^{sig} and θ^{bkg} are set to zero, but during the maximisation of the likelihood, they are allowed to float within a normal Gaussian distribution with mean zero and unit width. The expected event yields for the signal and the background can be expressed as a function of their nuisance parameters:

$$N^{\text{sig}}(\theta^{\text{sig}}) = N^{\text{sig}}\Big(1 + \theta^{\text{sig}}\Big) \tag{9.7}$$

$$N^{\text{bkg}}(\theta^{\text{bkg}}) = N^{\text{bkg}}\Big(1 + \theta^{\text{bkg}}\Big). \tag{9.8}$$

The total uncertainty usually comprises several different sources of uncertainties, which are added in quadrature. By introducing the covariance matrix C_{ij}, correlations between the individual sources, such as for example the luminosity, can be accounted for. For one lepton channel the covariance matrix is a 2×2 matrix given by:

$$C_{ij} = \sum_k \sigma_{ik}\sigma_{jk} \tag{9.9}$$

where σ are the k individual sources of uncertainties and $i, j \in [1, 2]$, represent the signal and background categories. With this definition, only two nuisance parameters are introduced to the likelihood, instead of $2k$. In the $WV\gamma$ analysis, the considered sources of uncertainties are the uncertainty on the background estimation, the uncertainties on the correction factors C and C^{p2p} and the integrated luminosity L_{int}. Incorporating the correlation matrix in the likelihood function yields:

$$L(N^{\text{obs}}|\frac{f_i}{\Lambda^4}, \boldsymbol{\theta}) = Pois\Big(N^{\text{obs}}|N^{\text{sig}}(\frac{f_i}{\Lambda^4}, \theta^{\text{sig}}) + N^{\text{bkg}}(\theta^{\text{bkg}})\Big) \cdot \frac{1}{2\pi} e^{-\frac{1}{2}(\boldsymbol{\theta} C^{-1} \boldsymbol{\theta})}. \tag{9.10}$$

This is the likelihood function for one lepton channel. As the $WV\gamma$ analysis comprises two lepton channels, four nuisance parameters are considered in total, leading to a 4×4 correlation matrix. The likelihood function for each channel is multiplied in order to obtain the combined

likelihood:

$$L(N^{\text{obs}}|\frac{f_i}{\Lambda^4},\boldsymbol{\theta}) = \prod_{\ell=1}^{2} Pois\Big(N_\ell^{\text{obs}}|N_\ell^{\text{sig}}(\frac{f_i}{\Lambda^4},\theta_\ell^{\text{sig}}) + N_\ell^{\text{bkg}}(\theta_\ell^{\text{bkg}})\Big) \cdot \frac{1}{(2\pi)^2} e^{-\frac{1}{2}(\boldsymbol{\theta}C^{-1}\boldsymbol{\theta})} \tag{9.11}$$

where $\ell \in [1,\ 2]$ represents the electron and muon channel.

As in Section 8.4, the exclusion limits are derived using p-values, which give the probability to obtain a measurement which is equal or less likely than what is observed in data under the tested hypothesis. In this case, the test hypothesis is the presence of anomalous quartic gauge couplings with coupling strength $\frac{f_i}{\Lambda^4}$. In order to test how likely the observed number of events are under the hypothesis, the profile likelihood ratio is used, as defined in Equation 8.17:

$$\lambda\big(\tfrac{f_i}{\Lambda^4}\big) = \frac{L\Big(\frac{f_i}{\Lambda^4},\hat{\hat{\boldsymbol{\theta}}}\Big)}{L\Big(\frac{\hat{f}_i}{\Lambda^4},\hat{\boldsymbol{\theta}}\Big)} \tag{9.12}$$

where $\frac{f_i}{\Lambda^4}$ is the anomalous coupling and the parameter of interest. Anomalous quartic gauge couplings $\frac{f_i}{\Lambda^4}$, can be positive and negative; therefore, two-sided limits are derived. This is a difference to the CL_S method, which sets only upper limits on the parameter of interest.

The p-value, under the hypothesis of a given anomalous quartic gauge coupling $\frac{f_i^{\text{test}}}{\Lambda^4}$, can be determined by drawing a large number of pseudo experiments. In each pseudo experiment, the number of observed events in data is replaced by drawing a value from a Poisson with mean $N^{\text{sig}}(\frac{f_i^{\text{test}}}{\Lambda^4}) + N^{\text{bkd}}$. In addition, $N^{\text{sig}}(\frac{f_i^{\text{test}}}{\Lambda^4})$ and N^{bkd} are allowed to float within their uncertainties. The p-value is then determined via:

$$p\Big(\frac{f_i^{\text{test}}}{\Lambda^4}\Big) = \frac{N_{\ell\ell}^{\text{ps}}(\frac{f_i^{\text{test}}}{\Lambda^4})}{N_{\text{ps}}(\frac{f_i^{\text{test}}}{\Lambda^4})} \tag{9.13}$$

where $N^{\text{ps}}(\frac{f_i^{\text{test}}}{\Lambda^4})$ is the total number of pseudo experiments and $N_{\ell\ell}^{\text{ps}}(\frac{f_i^{\text{test}}}{\Lambda^4})$ is the number of pseudo experiments, where the result is less likely than the result actually observed in data, defined as $\lambda(N^{\text{ps}}, \frac{f_i^{\text{test}}}{\Lambda^4}) < \lambda(N^{\text{obs}}, \frac{f_i^{\text{test}}}{\Lambda^4})$. When the p-value is below 0.05, the anomalous quartic gauge coupling $\frac{f_i^{\text{test}}}{\Lambda^4}$ is excluded at 95 % confidence level. The expected limits are determined by drawing pseudo data under the Standard Model hypothesis, $\frac{f_i^{\text{test}}}{\Lambda^4} = 0$, and then deriving the limits on the tested anomalous quartic gauge coupling for this pseudo experiment. With this procedure, two distributions are obtained, one for the upper bounds and the other one for the lower bounds. The mean of these distributions is used as the upper and lower limits, respectively and the standard deviation as σ [142].

Instead of drawing a large number of pseudo datasets, one representative dataset can be constructed, the Asimov dataset [137]. For the expected limits, the Asimov dataset is generated by maximising the likelihood, given in Equation 9.11, on the observed data under the Standard Model hypothesis [142]. Using the obtained parameters $\boldsymbol{\theta'}$, the Asimov dataset is determined via:

$$N^{\text{AD}} = N^{\text{sig}}_{|\frac{f_i^{\text{test}}}{\Lambda^4}=0}(1+\theta'^{\,\text{sig}}) + N^{\text{bkg}}(1+\theta'^{\,\text{bkg}}). \tag{9.14}$$

The upper and lower limits derived with the Asimov dataset coincide with the mean of the

upper and lower limit distribution obtained with the pseudo experiments. The uncertainties on the limits, derived with the Asimov dataset are calculated using [142]:

$$\sigma^2_{\mathrm{AD}} = \frac{(\frac{f_i^{\mathrm{test}}}{\Lambda^4})^2}{-2\ln\lambda(\frac{f_i^{\mathrm{test}}}{\Lambda^4})} \tag{9.15}$$

This thesis uses the implementation of the statistical method by the ATLAS collaboration, which is documented in an ATLAS internal report [142]. The expected limits for the $WV\gamma$ analysis are derived employing Asimov datasets.

9.2. Optimization of the Phase Space

The nominal phase space, defined in Section 8.1, is optimised to have the best signal significance to the Standard Model production of the $WV\gamma$ process. However, it is not ensured that this phase space is also optimal for the search of new physics. Therefore, the phase space is re-optimised with respect to the best expected exclusion limits. The exclusion limits on anomalous quartic gauge couplings are derived using a dipole form factor $\mathcal{F}(\hat{s}) = (1 + \hat{s}/\Lambda^2_{FF})^{-2}$, previously defined in Equation 2.16, where $\hat{s}$ is the energy scale of the hard interaction squared and Λ_{FF} is the form factor scale. Three different values are chosen for the form factor scale: 0.5 TeV, 1.0 TeV and ∞, where the latter one corresponds to the non-unitarised case. The phase space optimisation is designed to find the best phase space region for all three values of the form factor scale and all fourteen anomalous quartic gauge coupling parameters, the analysis is sensitive to. Also, the same definition of the new phase space is desired for the electron and the muon channel in order to determine the $WV\gamma$ production cross section limits for the individual lepton channels as well as for the average of the two. In the following, the optimisation of the phase space is presented for the electron channel using the $f_{M,0}$ parameter, but similar results are obtained for the muon channel as well as for other anomalous quartic gauge coupling parameters.

In the presence of anomalous quartic gauge couplings, the cross section is enhanced in case a photon with high transverse energy is present in the event, as shown in Figure 9.2(a). The figure depicts the differential cross section expectation of the semi-leptonic $WV\gamma$ process as a function of the leading photon E_{T} and shows the distributions of the Standard Model prediction as well as the distributions when anomalous couplings with $\frac{f_{M,0}}{\Lambda^4} = 625\,\mathrm{TeV}^{-4}$ and $\frac{f_{M,0}}{\Lambda^4} = 5\,000\,\mathrm{TeV}^{-4}$ are present. For higher values of the coupling strengths, the cross section expectations become larger at high photon energies. The explicit values of the anomalous quartic gauge coupling shown in the figure are only of illustrative nature, as they are already excluded by more than an order of magnitude [21]. In Figure 9.2(b), the impact of unitarisation on the cross section expectations is depicted. The Standard Model prediction is shown as well as the predictions for the anomalous coupling $\frac{f_{M,0}}{\Lambda^4} = 5\,000\,\mathrm{TeV}^{-4}$ with the three different form factor scales of the dipole form factor, considered in this thesis. The lower the form factor scale, the stronger the damping, leading to lower separation power between the Standard Model predictions and the unitarised coupling parameter. The cross section parabolas, illustrated in Figure 9.1, become broader due to the unitarisation.

At high transverse energies of the photon, two effects occur: the cross section expectation increases for the anomalous quartic gauge couplings while the cross section expectation for the Standard Model $WV\gamma$ and the background processes decreases. This is shown in Figure 9.3(a),

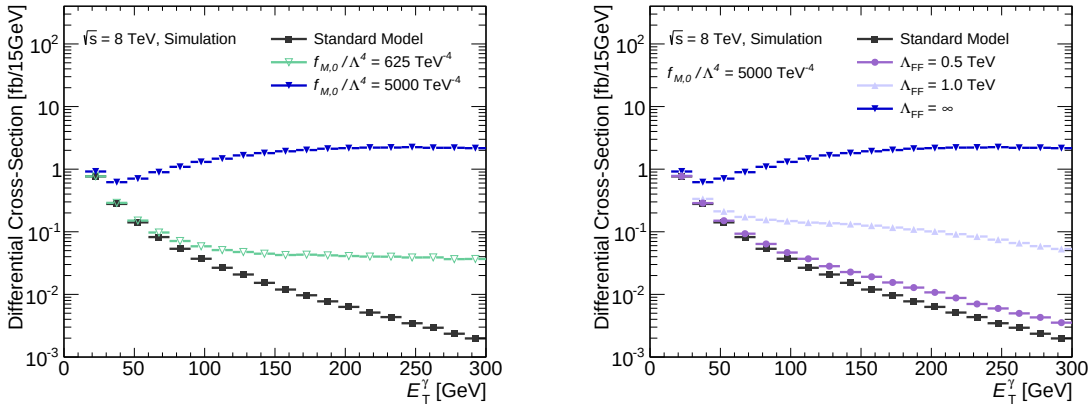

Figure 9.2.: Differential $WV\gamma$ production cross section as a function of the transverse energy of the photon E_{T}^{γ}. In (a) the Standard Model predictions are shown in black and compared to two different values of the non-unitarised coupling parameter $\frac{f_{M,0}}{\Lambda^4} = 5\,000\,\mathrm{TeV}^{-4}$ in blue and $\frac{f_{M,0}}{\Lambda^4} = 625\,\mathrm{TeV}^{-4}$ in light green. In (b) the Standard Model prediction is compared to the coupling parameter $\frac{f_{M,0}}{\Lambda^4} = 5\,000\,\mathrm{TeV}^{-4}$ for three different values of the form factor scale $\Lambda_{FF} = \infty$ in blue, $\Lambda_{FF} = 1.0\,\mathrm{TeV}$ in light blue and $\Lambda_{FF} = 0.5\,\mathrm{TeV}$ in light purple.

where the E_{T} distribution of the photon is shown in the signal region. For the data, the $WV\gamma$ Standard Model contribution and the background expectations the event yields are decreasing with higher transverse energies of the photons, in contrast to the expectation for an aQGC reference model with $f_{T,0}/\Lambda^4 = 1\,374\,\mathrm{TeV}^{-4}$, where the event yield increases. Thus, by increasing the threshold of the selection criteria on the transverse energy of the photon, a significant amount of background events are discarded while most events arising from anomalous couplings are kept. This increases the sensitivity to anomalous quartic gauge couplings. The optimal threshold criteria is obtained by determining the expected exclusion limits on each aQGC parameter as a function of the E_{T}^{γ} threshold. The new E_{T}^{γ} threshold is chosen to correspond to the best expected exclusion limits. For the estimation of the expected exclusion limits, the expected number of background events for each threshold point needs to be evaluated. Ideally, the entire background estimation method, discussed in Chapter 7, is redone for each tested value of the E_{T}^{γ} threshold. However, as the event yield for the background processes is steeply falling with rising photon energies, the full method cannot be repeated, due to low statistics in the control regions. Therefore, the background expectation is estimated with the nominal photon criteria of $E_{\mathrm{T}}^{\gamma} > 15\,\mathrm{GeV}$ and the distribution of the photon transverse energy in the signal region is obtained. The E_{T}^{γ} distribution for the total background expectation is fitted with a function, in order to extrapolate the expected event yield into the high photon E_{T}^{γ} region. The function that best describes the E_{T}^{γ} spectrum is found the be the sum of two exponential functions:

$$f(x) = p_0\,\mathrm{e}^{-p_1 \cdot x} + p_2\,\mathrm{e}^{-p_3 \cdot x} \tag{9.16}$$

where p_i are the free parameters and $i \in [0, ..., 3]$. The fit range extends from 15 GeV to 500 GeV and the extrapolation is shown in Figure 9.3 for both lepton channels. The expected event yield for one specific test value of the photon transverse energy threshold, $E_{\mathrm{T}}^{\gamma,\mathrm{test}}$, is derived as the integral over the extrapolation function $f(x)$, from the test point to infinity. Statistical uncertainties of the bins are accounted for by varying the parameters of the fit

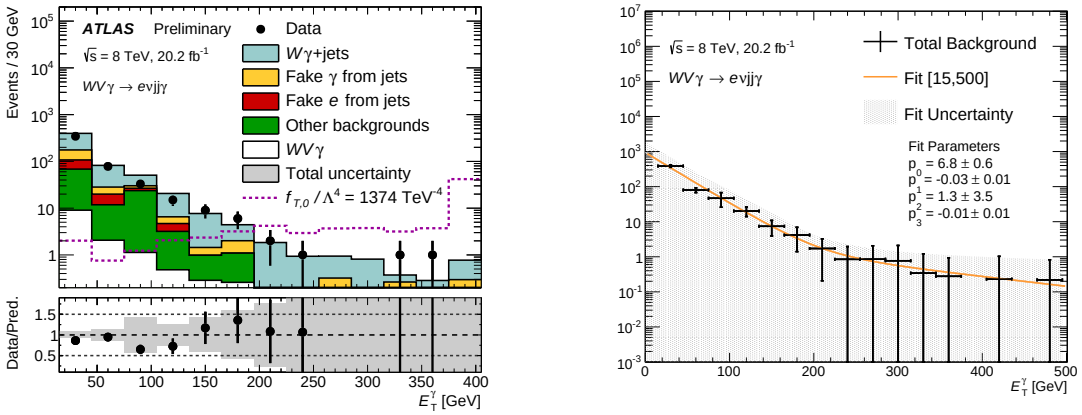

(a) **(b)**

Figure 9.3.: In (a) the distributions of the transverse energy of the photon are shown, for the data, the expected backgrounds and the Standard Model $WV\gamma$ expectations as well as the prediction for aQGCs in a reference model with $f_{T,0}/\Lambda^4 = 1\,374\,\text{TeV}^{-4}$ [10]. In (b) the distribution of the transverse energy of the photon is shown, for the total expected backgrounds as well as the fit used to extrapolate the expected event yield into the high E_T^γ region (orange). In both figures the electron channel is shown.

function within their uncertainties, excluding non-physical variations. The difference between the expected event yield obtained with the varied and the nominal parameters is determined and the maximal deviation is taken as uncertainty. In addition, systematic uncertainties due to the fitting procedure are accounted for by increasing and decreasing the upper and lower fit ranges independently by 15 GeV. The expected number of background events is evaluated and the maximal difference to the event yield with nominal fit conditions is taken as uncertainty. In order to obtain the total uncertainty on the extrapolation, the two components are added in quadrature.

The scan of the expected limits on the anomalous quartic gauge couplings over the E_T^γ phase space is performed in steps of 15 GeV starting with $E_\text{T}^\gamma = 15\,\text{GeV}$. For each tested E_T^γ threshold, the cross section parabolas, shown in Figure 9.1, need to be evaluated. Therefore, five cross section expectations at different anomalous quartic gauge couplings are derived for each E_T^γ threshold using the VBFNLO generator and fit with a parabolic function. The expected event yield for every value of the anomalous coupling strength can thus be calculated by using the parabolic parametrisation, given in Equation 9.4. The E_T^γ scan in the electron channel is shown in Figure 9.4 for the $\frac{f_{M,0}}{\Lambda^4}$ coupling and for the three values of the form factor scale. The expected limits on the anomalous quartic gauge coupling parameter are weakest at low values of the photon transverse energies, indicating that the nominal phase space with $E_\text{T}^\gamma > 15\,\text{GeV}$ is not favoured to derive the limits an anomalous quartic gauge couplings. With increasing E_T^γ threshold, the limits improve as more background events are discarded while maintaining high signal expectations. The maximal sensitivity is approximately reached at an E_T^γ threshold of 200 GeV, indicated by the dashed line in the figure. The sensitivity decreases for unitarised couplings when the minimum transverse energy of the photon is raised even more. This is due to the dipole form factor, which dampens the cross section and thus less signal events are expected for the very high E_T^γ region.

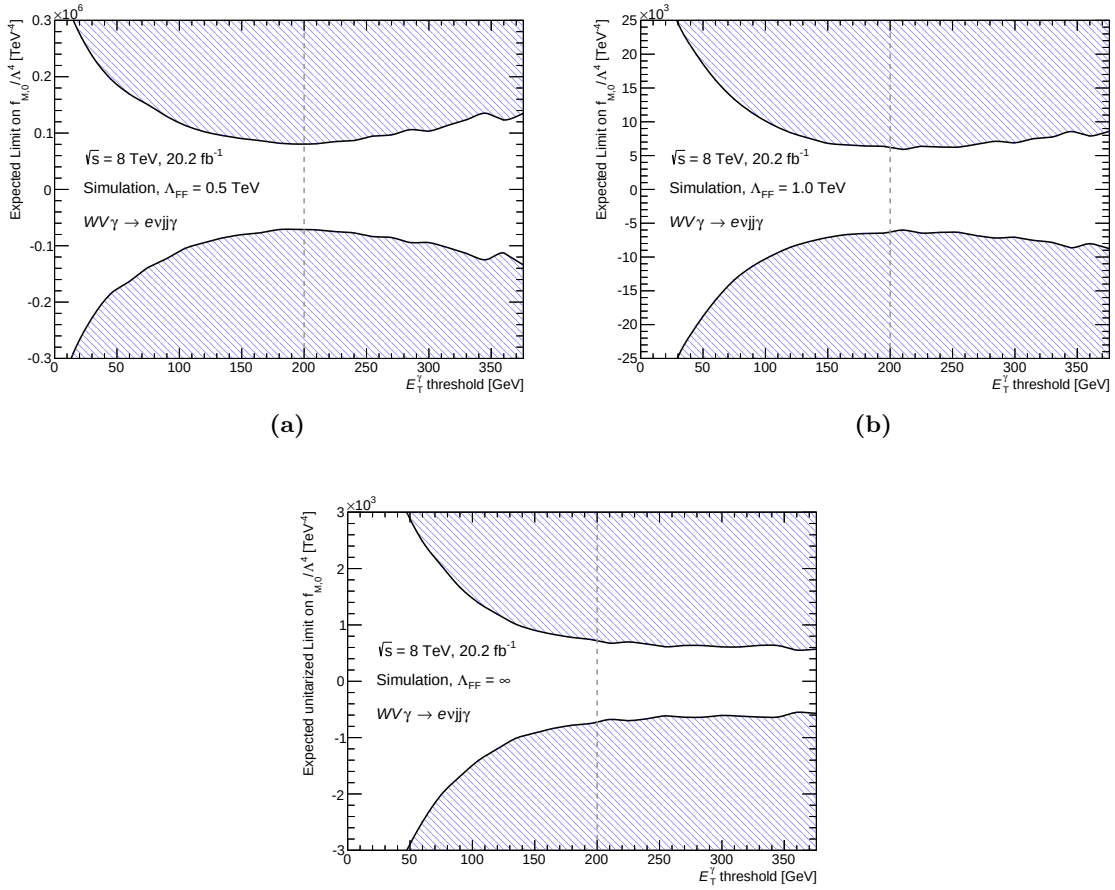

Figure 9.4.: Expected limits on the $\frac{f_{M,0}}{\Lambda^4}$ parameter as a function of the E_{T}^{γ} threshold. The coupling values in the hashed areas are excluded. Three different values for the form factor scale of the dipole form factor are shown in (a) for $\Lambda_{FF} = 0.5\,\mathrm{TeV}$, in (b) for $\Lambda_{FF} = 1.0\,\mathrm{TeV}$ and in (c) for $\Lambda_{FF} = \infty$. The highest sensitivity is approximately achieved for a selection criteria of $E_{\mathrm{T}}^{\gamma} = 200\,\mathrm{GeV}$, indicated by the dashed line. Only the electron channel is shown.

A similar behaviour of the sensitivity is observed for all anomalous quartic gauge couplings and for both lepton channels. Therefore, the new phase space is defined as in Section 8.1 with the more stringent requirement of $E_{\mathrm{T}}^{\gamma} > 200\,\mathrm{GeV}$ to ensure optimal sensitivity to anomalous quartic gauge couplings.

	Generator	$E_{\mathrm{T}}^{\gamma} > 15\,\mathrm{GeV}$	$E_{\mathrm{T}}^{\gamma} > 200\,\mathrm{GeV}$	rel. Change
$C_{e\nu\mathrm{jj}\gamma}$	Sherpa	0.28 ± 0.01	0.37 ± 0.05	+ 32 %
	MadGraph	0.30 ± 0.01	0.34 ± 0.04	+ 14 %
$C_{\mu\nu\mathrm{jj}\gamma}$	Sherpa	0.40 ± 0.01	0.39 ± 0.05	− 2 %
	MadGraph	0.37 ± 0.01	0.42 ± 0.04	+ 14 %

Table 9.1.: Comparison of the correction factors, evaluated in the nominal phase space with $E_{\mathrm{T}}^{\gamma} > 15\,\mathrm{GeV}$ and in the new phase space with $E_{\mathrm{T}}^{\gamma} > 200\,\mathrm{GeV}$ and with the Sherpa and the MadGraph $WV\gamma$ signal Monte Carlo samples. The numbers are given for the electron and the muon channel.

9.3. Determination of the Exclusion Limits

For the results in the previous section, the correction factor C and the parton-to-particle correction factor C^{p2p} were assumed to be constant for each test value of the $E_{\mathrm{T}}^{\mathrm{iso},\gamma}$ threshold. Since the correction factors directly influence the expected event yield, the parabolic parametrisation of the cross section expectation in the presence of anomalous gauge couplings only holds when the correction factors are independent of the coupling strength. Therefore, the correction factor C is re-evaluated in the new fiducial phase space with the requirement on the transverse energy of the photon $E_{\mathrm{T}}^{\gamma} > 200\,\mathrm{GeV}$. It is determined using the Sherpa Standard Model signal simulation samples and evaluated to:

$$C_{e\nu\mathrm{jj}\gamma} = 0.37 \pm 0.05\,(\mathrm{stat.}) \pm 0.05\,(\mathrm{syst.})$$
$$C_{\mu\nu\mathrm{jj}\gamma} = 0.39 \pm 0.05\,(\mathrm{stat.}) \pm 0.05\,(\mathrm{syst.}).$$

The correction factors have large statistical uncertainties, due to the low statistics in the high photon region. In the electron channel, the correction factor is about 32 % higher than in the nominal phase space, arising from the increased photon identification efficiencies with higher photon energies. However, in the muon channel, the correction factor is about the same as in the nominal phase space, which is not expected, as the photon identification efficiencies should be independent of the lepton flavour. This behaviour is studied using the alternative signal Monte Carlo samples generated with MadGraph and is found to arise from statistical fluctuations. In Table 9.1, the correction factors are given, evaluated with Sherpa and MadGraph, in the nominal phase space, $E_{\mathrm{T}}^{\gamma} > 15\,\mathrm{GeV}$, and for the new phase space, $E_{\mathrm{T}}^{\gamma} > 200\,\mathrm{GeV}$. In the new phase space, good agreement between Sherpa and MadGraph is observed within their statistical uncertainties. The correction factors, determined with MadGraph in the new phase space, show a raise by 14 % with respect to the nominal values determined with MadGraph in both lepton channels. The difference in the relative increase between the electron and the muon channel observed in the new phase space, is not visible in the MadGraph samples. Therefore, the observed behaviour in the Sherpa samples is interpreted as statistical fluctuation and covered by the statistical uncertainty. The systematic uncertainty on the correction factor in the new phase space is evaluated as described in Section 8.2. It is dominated by the generator difference and the jet energy scale uncertainty.

	N^{obs}	N^{bkg}	C	C^{p2p}	L_{int} [fb^{-1}]
$e\nu\text{jj}\gamma$	4	6.3 ± 6.1	0.37 ± 0.07	0.64 ± 0.16	20.24 ± 0.38
$\mu\nu\text{jj}\gamma$	3	4.4 ± 12.0	0.39 ± 0.07	0.57 ± 0.12	20.24 ± 0.38

Table 9.2.: Observed and expected event yields in the phase space with $E_{\text{T}}^{\gamma} > 200\,\text{GeV}$, along with the correction factor C, the parton-to-particle correction factor C^{p2p} and the integrated luminosity, for both lepton channels.

In order to study the dependence of the correction factor C on anomalous quartic gauge couplings, C is evaluated for five different parameters, namely $\frac{f_{M,0}}{\Lambda^4} = -1\,876\,\text{TeV}^{-4}$, $\frac{f_{M,1}}{\Lambda^4} = -30\,482\,\text{TeV}^{-4}$, $\frac{f_{M,2}}{\Lambda^4} = -13\,099\,\text{TeV}^{-4}$, $\frac{f_{M,3}}{\Lambda^4} = -21\,285\,\text{TeV}^{-4}$ and $\frac{f_{T,0}}{\Lambda^4} = 1\,374\,\text{TeV}^{-4}$. The samples are simulated with MadGraph and the values for the anomalous quartic gauge coupling parameters are chosen to be about a factor of ten higher than the best limits. All samples simulated with MadGraph are produced with the CTEQ6L1 parton distribution functions and re-weighted to match the CT10 parton distribution functions, used for the samples simulated with Sherpa. The correction factors derived with the aQGC samples are in agreement with the correction factor derived in the new phase space, within one standard deviation of its total uncertainty. This indicates that the correction factor C is independent on anomalous quartic gauge couplings and thus no additional uncertainty is considered.

The parton-to-particle correction factor C^{p2p} is also re-evaluated in the new phase space using the Sherpa signal Monte Carlo samples and found to be:

$$C^{\text{p2p}}_{e\nu\text{jj}\gamma} = 0.64 \pm 0.01\,(\text{stat.}) \pm 0.16\,(\text{syst.})$$
$$C^{\text{p2p}}_{\mu\nu\text{jj}\gamma} = 0.57 \pm 0.01\,(\text{stat.}) \pm 0.12\,(\text{syst.})$$

for the electron and the muon channel respectively. Since good agreement between the values of C^{p2p} are observed between the nominal and the new phase space, the values derived in the nominal phase space are taken as central values, as their statistical uncertainties are much smaller. This is justified, as the parton-to-particle correction factor is expected to be approximately independent of the transverse energy of the photon energy threshold, as the showering and hadronisation process, which has the largest impact on C^{p2p}, is not altered. The parton-to-particle correction is also determined using the Standard Model samples as well as the samples including anomalous quartic gauge couplings generated with MadGraph. In order to cover for any potential systematic uncertainty arising from the choice of the Monte Carlo generator, the maximal deviation between the C^{p2p} value obtained in the new phase space with the nominal Sherpa samples and the value obtained in the new phase space with any of the MadGraph samples is taken as systematic uncertainty.

Table 9.2 lists the inputs, which are used for the limit setting procedure in the new phase space, optimised to the best sensitivity of anomalous quartic gauge couplings. In the data 4 (3) events are observed in the electron (muon) channel while 6.3 (4.4) events are expected from the background extrapolation.

	Observed Limit [ab]	Expected Limit [ab]	SM Theory Prediction [ab]
$e\nu$jjγ	1266	1340^{+540}_{-309}	57 ± 13
$\mu\nu$jjγ	1118	1129^{+546}_{-276}	51 ± 11
$l\nu$jjγ	878	917^{+293}_{-180}	54 ± 9

Table 9.3.: Observed and expected exclusion limits in the phase space with $E_{\mathrm{T}}^{\gamma} > 200\,\mathrm{GeV}$ along with the Standard Model cross section expectation. The limits are set using the CL_S method at 95 % confidence level for the electron and muon channel, as well as averaged over the lepton flavour.

9.3.1. CL_S Limits on the Production Cross Section

Upper limits on the production cross section of the $WV\gamma$ process are derived in the new phase space, using the CL_S method at a 95 % confidence level, as described in Section 8.4.1. These limits have the advantage, that they do not depend on a model for new physics beyond the Standard Model, as only the observed and expected event yields are used to derive the limits. The inputs are given in Table 9.2 and the limits are derived for the separate lepton channels as well as averaged over the lepton flavour. The exclusion limits are given in Table 9.3 and the best limit in this phase space is about a factor of sixteen higher than the Standard Model cross section expectation. In comparison to the exclusion limits derived in the nominal phase space, given in Table 8.4, the limits are less stringent, as the new phase space it optimised for the observation of anomalous quartic gauge couplings and not for the Standard Model production.

9.3.2. Limits on anomalous Quartic Gauge Couplings

The exclusion limits on the anomalous quartic gauge coupling parameters are derived using the statistical method described in Section 9.1 and the input values given in Table 9.2. The implementation of the method by the ATLAS Collaboration is employed, documented internally in Reference [142]. In order to obtain the highest sensitivity, the two lepton channels are combined in the limit setting. The observed and expected limits on non-unitarised couplings, corresponding to $\Lambda_{FF} = \infty$, are given in Table 9.4 along with the current best limit on each parameter and the analysis it is derived with. The limits on the anomalous quartic gauge couplings are also illustrated in Figure 9.5. For all parameters, the observed limits are more stringent than the expected limits as in both lepton channels less events are observed than expected. The exclusion limits on the anomalous quartic gauge couplings determined with the $WV\gamma$ analysis confirm previous measurements. Current best limits are obtained with processes based on *vector boson scattering* (VBS) and *vector boson fusion* (VBF) topologies. In this topologies, two electroweak gauge bosons are radiated off two quarks and scatter with each other or produce new particles. In addition, two jets are produced from the initial quarks with special characteristics, such as a large separation in the pseudorapidity. This allows for an effective background suppression and increases the sensitivity to anomalous quartic gauge couplings. However, studying triboson final states provides an independent and complementary approach in the search for anomalous quartic gauge couplings. The analyses quoted in Table 9.4 are briefly discussed in the following.

Coupling	Observed [10^3 TeV^{-4}]	Expected [10^3 TeV^{-4}]	Current Best [10^1 TeV^{-4}]	Analysis
$f_{M,0}/\Lambda^4$	[-0.6, 0.6]	[-0.7, 0.7]	[-0.4, 0.4]	$\gamma\gamma \to WW$
$f_{M,1}/\Lambda^4$	[-0.9, 1.0]	[-1.1, 1.1]	[-1.6, 1.6]	$\gamma\gamma \to WW$
$f_{M,2}/\Lambda^4$	[-3.4, 3.4]	[-4.0, 4.0]	[-2.6, 2.6]	VBS $W\gamma$
$f_{M,3}/\Lambda^4$	[-5.1, 5.2]	[-6.1, 6.2]	[-4.3, 4.4]	VBS $W\gamma$
$f_{M,4}/\Lambda^4$	[-1.6, 1.6]	[-2.0, 1.9]	[-4.0, 4.0]	VBS $W\gamma$
$f_{M,5}/\Lambda^4$	[-2.2, 2.2]	[-2.6, 2.6]	[-6.5, 6.5]	VBS $W\gamma$
$f_{M,6}/\Lambda^4$	[-1.2, 1.2]	[-1.4, 1.5]	[-6.5, 6.3]	ss WW
$f_{M,7}/\Lambda^4$	[-1.7, 1.7]	[-1.9, 2.0]	[-7.0, 6.6]	ss WW
$f_{T,0}/\Lambda^4$	[-0.2, 0.2]	[-0.2, 0.2]	[-0.4, 0.3]	VBS $Z\gamma$
$f_{T,1}/\Lambda^4$	[-0.2, 0.2]	[-0.3, 0.3]	[-0.2, 0.2]	ss WW
$f_{T,2}/\Lambda^4$	[-0.5, 0.5]	[-0.6, 0.6]	[-0.6, 0.7]	ss WW
$f_{T,5}/\Lambda^4$	[-2.4, 2.4]	[-2.8, 2.8]	[-0.4, 0.4]	VBS $W\gamma$
$f_{T,6}/\Lambda^4$	[-2.7, 2.7]	[-3.2, 3.2]	[-0.3, 0.3]	VBS $W\gamma$
$f_{T,7}/\Lambda^4$	[-5.9, 6.0]	[-6.9, 6.9]	[-0.7, 0.8]	VBS $W\gamma$

Table 9.4.: Observed and expected limits on the fourteen different anomalous quartic gauge coupling parameters without unitarisation. The current best limit on each parameter is given (please note the different exponent) as well as the analysed process used to derive it. The current best limits are taken from References [17, 18, 20, 21].

$\gamma\gamma \to WW$ This analysis studies the (quasi) exclusive production of a W boson pair, originating from two photons. The selection requires an electron-muon pair with opposite charge arising from a vertex which has no additional charged particles associated to it. The analysis is performed by the CMS Collaboration and in order to increase the sensitivity, combines the results from the analyses using data collected at centre-of-mass energies of 7 TeV and 8 TeV, corresponding to integrated luminosities of 5.05 fb^{-1} and 19.7 fb^{-1}, respectively. The obtained limits are the current best limits on the $\frac{f_{M,0}}{\Lambda^4}$ and $\frac{f_{M,1}}{\Lambda^4}$ parameters. Details about this analysis can be found in Reference [21].

VBS $W\gamma$ This denotes the electroweak production of $W\gamma$ events in association with two jets. The selection requires exactly one electron or muon, missing transverse energy, one photon and two jets with a large rapidity separation to account for the vector boson scattering topology. The analysed data are recorded with the CMS detector at a centre-of-mass energy of 8 TeV and correspond to an integrated luminosity of 19.7 fb^{-1}. This analysis is the first to publish limits on all fourteen coupling parameters. In addition it sets the most stringent limits on the $\frac{f_{M,2}}{\Lambda^4}$, $\frac{f_{M,3}}{\Lambda^4}$, $\frac{f_{M,4}}{\Lambda^4}$, $\frac{f_{M,5}}{\Lambda^4}$, $\frac{f_{T,5}}{\Lambda^4}$, $\frac{f_{T,6}}{\Lambda^4}$ and $\frac{f_{T,7}}{\Lambda^4}$ parameters. The analysis is presented in Reference [18].

ss WW This is the abbreviation for the *same sign* WW analysis, which searches for the electroweak production of two W bosons with the same electric charge and two jets. It selects events with exactly two leptons of the same charge, missing transverse energy as well as two jets

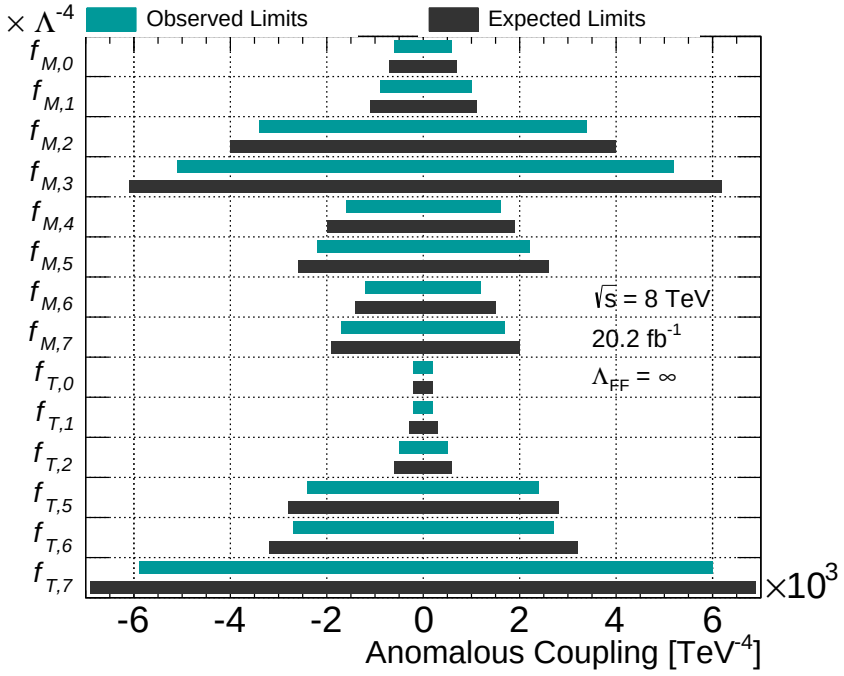

Figure 9.5.: Observed and expected limits on the fourteen different anomalous quartic gauge coupling parameters without unitarisation.

with a large rapidity separation and high invariant dijet mass values. The study is presented by the CMS Collaboration in Reference [20], analysing the data collected at a centre-of-mass energy of 8 TeV with an integrated luminosity of 19.7 fb^{-1}. It sets the best constraints on the $\frac{f_{M,6}}{\Lambda^4}$, $\frac{f_{M,7}}{\Lambda^4}$, $\frac{f_{T,1}}{\Lambda^4}$ and $\frac{f_{T,2}}{\Lambda^4}$ parameters.

VBS $Z\gamma$ This analysis searches for the electroweak production of $Z\gamma$ events by selecting a pair of electrons or muons with opposite charge in association with one photon and two jets. This study also analyses the data collected at a centre-of-mass energy of 8 TeV corresponding to an integrated luminosity of 19.7 fb^{-1} with the CMS detector. It sets the tightest constraints on the $\frac{f_{T,0}}{\Lambda^4}$ parameter and is discussed in detail in Reference [17].

The observed and expected limits on anomalous quartic gauge couplings, unitarised with a dipole form factor and the form factor scales $\Lambda_{FF} = 0.5$ TeV and $\Lambda_{FF} = 1.0$ TeV are given in Table 9.5 and illustrated in Figure 9.6. As before, the observed limits are more stringent than the expected limits, as less events are observed in data than expected. The limits on the coupling parameters are weakest for the form factor scale $\Lambda_{FF} = 0.5$ TeV, as it enforces the largest damping of the cross section. Not all analyses constraining anomalous quartic gauge couplings also constrain unitarised couplings and if unitarised limits are published, often different values for the form factor scale than in this thesis are chosen. No other exclusion limits with a form factor scale of $\Lambda_{FF} = 1.0$ TeV are published and thus, it is not possible to compare the exclusion limits to other results. Unitarised limits on four anomalous quartic gauge couplings $\frac{f_{M,0-3}}{\Lambda^4}$ are set by the CMS Collaboration studying $\gamma\gamma \to WW$ production [21] with a form factor scale of $\Lambda_{FF} = 0.5$ TeV. The derived limits are also given in Table 9.5 and are the most stringent limits on these parameters. No published exclusion limits are available for the other coupling parameters with a form factor scale of $\Lambda_{FF} = 0.5$ TeV.

Coupling	$\Lambda_{FF} = 1\,\text{TeV}$ Observed [10^4 TeV^{-4}]	$\Lambda_{FF} = 1\,\text{TeV}$ Expected [10^4 TeV^{-4}]	$\Lambda_{FF} = 0.5\,\text{TeV}$ Observed [10^4 TeV^{-4}]	$\Lambda_{FF} = 0.5\,\text{TeV}$ Expected [10^4 TeV^{-4}]	$\Lambda_{FF} = 0.5\,\text{TeV}$ Current Best [10^3 TeV^{-4}]
$f_{M,0}/\Lambda^4$	[-0.5, 0.5]	[-0.6, 0.6]	[-3.5, 3.4]	[-4.1, 4.0]	[-0.8, 0.8]
$f_{M,1}/\Lambda^4$	[-0.7, 0.8]	[-0.9, 0.9]	[-5.6, 5.9]	[-6.6, 6.9]	[-2.8, 3.3]
$f_{M,2}/\Lambda^4$	[-3.0, 3.0]	[-3.5, 3.4]	[-27.9, 28.3]	[-31.6, 32.1]	[-6.2, 6.2]
$f_{M,3}/\Lambda^4$	[-4.2, 4.3]	[-5.0, 5.0]	[-27.8, 27.9]	[-32.3, 32.0]	[-18.7, 22.3]
$f_{M,4}/\Lambda^4$	[-1.4, 1.4]	[-1.6, 1.6]	[-89.7, 73.9]	[-102.2, 87.3]	-
$f_{M,5}/\Lambda^4$	[-1.8, 1.8]	[-2.2, 2.1]	[-21.8, 22.5]	[-23.9, 24.7]	-
$f_{M,6}/\Lambda^4$	[-1.0, 1.0]	[-1.2, 1.2]	[-14.1, 13.6]	[-16.4, 15.8]	-
$f_{M,7}/\Lambda^4$	[-1.3, 1.3]	[-1.6, 1.5]	[-37.2, 33.4]	[-43.4, 39.1]	-
$f_{T,0}/\Lambda^4$	[-0.2, 0.2]	[-0.2, 0.2]	[-1.1, 1.1]	[-1.3, 1.3]	-
$f_{T,1}/\Lambda^4$	[-0.2, 0.2]	[-0.3, 0.3]	[-1.3, 1.3]	[-1.6, 1.6]	-
$f_{T,2}/\Lambda^4$	[-0.5, 0.5]	[-0.6, 0.6]	[-3.2, 3.0]	[-3.7, 3.5]	-
$f_{T,5}/\Lambda^4$	[-2.2, 2.2]	[-2.6, 2.6]	[-20.4, 21.3]	[-22.4, 23.8]	-
$f_{T,6}/\Lambda^4$	[-2.6, 2.6]	[-3.0, 3.0]	[-26.4, 27.5]	[-28.8, 30.8]	-
$f_{T,7}/\Lambda^4$	[-5.9, 6.0]	[-7.0, 7.1]	[-117.6, 122.9]	[-129.0, 134.6]	-

Table 9.5.: Observed and expected limits on the fourteen anomalous quartic gauge coupling parameters unitarised with a dipole form factor and form factor scales $\Lambda_{FF} = 1.0\,\text{TeV}$ and $\Lambda_{FF} = 0.5\,\text{TeV}$. Only for some of the coupling parameters, unitarised limits with the form factor scale of $\Lambda_{FF} = 0.5\,\text{TeV}$ are comparable to other analyses. The best limits are taken from References [21]. For the other coupling parameters and the other form factor scales no limits are published.

In summary, the study of $l\nu$jjγ final states showed no deviations from the Standard Model cross section expectations and therefore the analysis is also used to constrains new physics effects. The anomalous quartic gauge couplings are parametrised as an effective field theory and limits on fourteen anomalous quartic gauge coupling parameters are set. To ensure the quoted limits are determined in a region where unitarity is conserved, the limits on the couplings parameters have been derived with and without unitarisation. Using triboson final states to constrain anomalous quartic gauge couplings, is a complementary approach to the study of diboson final states and the presented limits on aQGCs, derived in this thesis with the $l\nu$jjγ final states, confirm the current best limits.

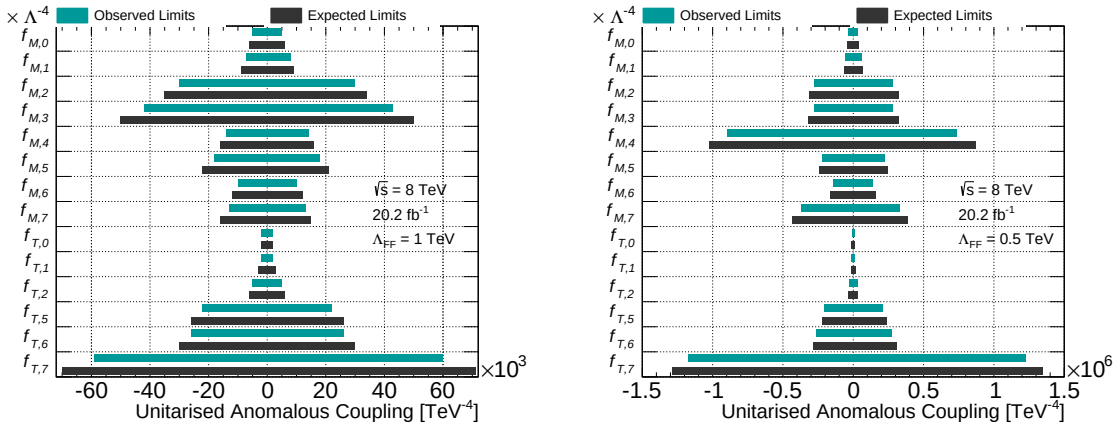

Figure 9.6.: Observed and expected limits on the fourteen anomalous quartic gauge coupling parameters unitarised with a dipole form factor scale of (a) $\Lambda_{\mathrm{FF}} = 1.0\,\mathrm{TeV}$ and of (b) $\Lambda_{\mathrm{FF}} = 0.5\,\mathrm{TeV}$.

10. Summary

The study of three gauge bosons in proton−proton interactions is a precise test of the Standard Model and its non-abelian structure of the SU(2) symmetry group. In the Standard Model, triple and quartic vertices involving weak gauge bosons are predicted with specific coupling strengths and any measurement that deviates from the Standard Model would hint to new physics.

In this thesis, the production of $WW\gamma$ and $WZ\gamma$ is studied in two separate lepton channels: the electron channel with $e\nu\mathrm{jj}\gamma$ final states and the muon channel with $\mu\nu\mathrm{jj}\gamma$ final states. Due to the detector resolution, the hadronically decaying W and Z bosons cannot be separated and are thus commonly referred to as V boson. The analysed proton−proton data are recorded with the ATLAS detector at a centre-of-mass energy of $\sqrt{s} = 8\,\mathrm{TeV}$, corresponding to an integrated luminosity of $20.2\,\mathrm{fb}^{-1}$. Backgrounds arising from $W\gamma$ + jets, fake leptons from jets and fake photons from jets are estimated using a simultaneous fit, which consists of three data-driven methods: a maximum likelihood fit to the m_{jj} distribution, a maximum likelihood fit to the $E_{\mathrm{T}}^{\mathrm{miss}}$ distribution and a two-dimensional sideband method. Other backgrounds are estimated using Monte Carlo simulation. The largest uncertainty on the background estimation arises from the statistical uncertainties on the template shapes used in the simultaneous fit.

In both lepton channels no excess over the background expectation is observed. Exclusion limits on the production cross section are derived using the CL_S method at a 95 % confidence level (CL), in two different phase space regions; the nominal phase space region is optimised to the Standard Model $WV\gamma$ production and the second one to the search of new physics. Both phase space regions are defined at particle level and are correct for detector effects and efficiencies. The best observed upper limit on the Standard Model $WV\gamma$ production cross section is 5.7 fb, which is about a factor of 2.5 larger than the expected Standard Model cross section. This is the most stringent limit on the $WV\gamma$ production cross section to date. In addition, the measurement is used to constrain anomalous quartic gauge couplings, which is parametrised with an effective field theory and uses a dipole form factor to avoid unitarity violation. Frequentist exclusion limits at 95 % CL are derived on fourteen different anomalous quartic gauge couplings in the second phase space region, applying three different form factor scales Λ_{FF} of 0.5 TeV, 1.0 TeV and ∞, where the latter one corresponds to the non-unitarised case. The obtained limits confirm the limits from other analyses and provide a complementary test to the study of quartic gauge couplings. The most stringent limits on anomalous quartic gauge couplings are set with analyses studying vector boson scattering or vector boson fusion topologies, which were found to allow for better background rejection.

In conclusion, the measurement of $WW\gamma$ and $WZ\gamma$ production with the subsequent semi-leptonic decay of the heavy gauge bosons, sets exclusion limits on the production cross section in two different phase space regions as well as on fourteen different anomalous quartic gauge boson couplings. The presented results confirm and extend the current knowledge on triboson production in the Standard Model and on anomalous quartic gauge couplings.

A. Auxiliary Material

A.1. Muon Channel Candidate Event Display

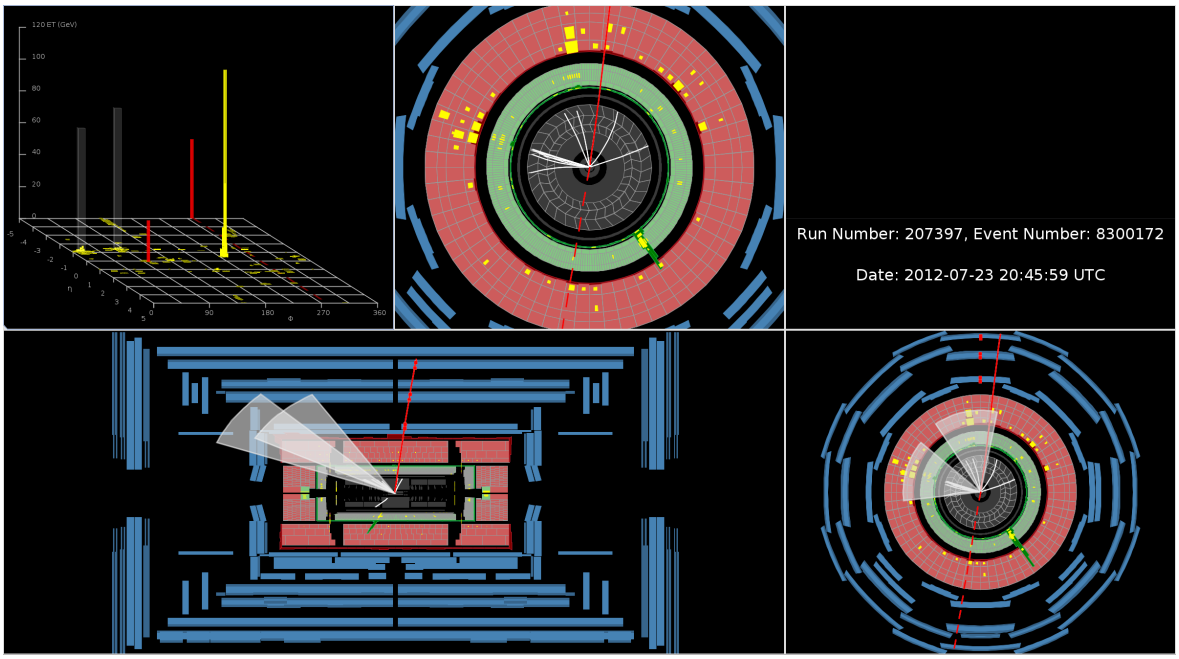

Figure A.1.: Event display of a candidate event of $WV\gamma$ production with the decay into $\mu\nu$jjγ final states, recorded with ATLAS detector at a centre-of-mass energy of $\sqrt{s} = 8\,\text{TeV}$ on July, 23^{rd} 2012. [143]

A.2. Effective Field Theory Operators

The $WV\gamma$ analysis is sensitive to fourteen different dimension eight operators. The operators are adapted from Reference [41]. The dimension eight operators are constructed from the field strength tensors $\hat{W}_{\mu\nu} \equiv \sum_a W^a_{\mu\nu} \frac{\sigma^a}{2}$, with $a \in [1,2,3]$, of the SU(2) and $B_{\mu\nu}$ of the U(1) as well as the covariant derivative of the Higgs field $D_\mu\Phi$. In the equations Tr represents the trace of a matrix, defined as the sum of the elements on the main diagonal. Depending on the composition of the operators, two different categories are defined.

1. Operators containing $D_\mu\Phi$ and two of the field strength tensors

$$\mathcal{O}_{M,0} = \mathrm{Tr}\left[\hat{W}_{\mu\nu}\hat{W}^{\mu\nu}\right] \times \left[(D_\beta\Phi)^\dagger\, D^\beta\Phi\right] \tag{A.1}$$

$$\mathcal{O}_{M,1} = \mathrm{Tr}\left[\hat{W}_{\mu\nu}\hat{W}^{\nu\beta}\right] \times \left[(D_\beta\Phi)^\dagger\, D^\mu\Phi\right] \tag{A.2}$$

$$\mathcal{O}_{M,2} = \mathrm{Tr}\left[B_{\mu\nu}B^{\mu\nu}\right] \times \left[(D_\beta\Phi)^\dagger\, D^\beta\Phi\right] \tag{A.3}$$

$$\mathcal{O}_{M,3} = \mathrm{Tr}\left[B_{\mu\nu}B^{\nu\beta}\right] \times \left[(D_\beta\Phi)^\dagger\, D^\mu\Phi\right] \tag{A.4}$$

$$\mathcal{O}_{M,4} = \mathrm{Tr}\left[(D_\mu\Phi)^\dagger\, \hat{W}_{\beta\nu}\, D^\mu\Phi\right] \times B^{\beta\nu} \tag{A.5}$$

$$\mathcal{O}_{M,5} = \mathrm{Tr}\left[(D_\mu\Phi)^\dagger\, \hat{W}_{\beta\nu}\, D^\nu\Phi\right] \times B^{\beta\mu} \tag{A.6}$$

$$\mathcal{O}_{M,6} = \mathrm{Tr}\left[(D_\mu\Phi)^\dagger\, \hat{W}_{\beta\nu}\hat{W}^{\beta\nu}\, D^\mu\Phi\right] \tag{A.7}$$

$$\mathcal{O}_{M,7} = \mathrm{Tr}\left[(D_\mu\Phi)^\dagger\, \hat{W}_{\beta\nu}\hat{W}^{\beta\mu}\, D^\nu\Phi\right] \tag{A.8}$$

$$\tag{A.9}$$

2. Operators containing solely field strength tensors

$$\mathcal{O}_{T,0} = \mathrm{Tr}\left[\hat{W}_{\mu\nu}\hat{W}^{\mu\nu}\right] \times \mathrm{Tr}\left[\hat{W}_{\alpha\beta}\hat{W}^{\alpha\beta}\right] \tag{A.10}$$

$$\mathcal{O}_{T,1} = \mathrm{Tr}\left[\hat{W}_{\alpha\nu}\hat{W}^{\mu\beta}\right] \times \mathrm{Tr}\left[\hat{W}_{\mu\beta}\hat{W}^{\alpha\nu}\right] \tag{A.11}$$

$$\mathcal{O}_{T,2} = \mathrm{Tr}\left[\hat{W}_{\alpha\mu}\hat{W}^{\mu\beta}\right] \times \mathrm{Tr}\left[\hat{W}_{\beta\nu}\hat{W}^{\nu\alpha}\right] \tag{A.12}$$

$$\mathcal{O}_{T,5} = \mathrm{Tr}\left[\hat{W}_{\mu\nu}\hat{W}^{\mu\nu}\right] \times B_{\alpha\beta}B^{\alpha\beta} \tag{A.13}$$

$$\mathcal{O}_{T,6} = \mathrm{Tr}\left[\hat{W}_{\alpha\nu}\hat{W}^{\mu\beta}\right] \times B_{\mu\beta}B^{\alpha\nu} \tag{A.14}$$

$$\mathcal{O}_{T,7} = \mathrm{Tr}\left[\hat{W}_{\alpha\mu}\hat{W}^{\mu\beta}\right] \times B_{\beta\nu}B^{\nu\alpha} \tag{A.15}$$

$$\tag{A.16}$$

The operators of the first category are denoted by the index M and have contributions from longitudinal and transverse polarisation modes. In contrast, the operators of the second category are denoted by the index T and have contributions only from the transverse modes.

A.3. Input Files for the VbfNlo Generator

The VbfNlo generator, used to derive the theoretical cross section expectations for the $WW\gamma$ and $WZ\gamma$ processes, is mainly steered by two input files. The `vbfnlo.dat` file specifies the process, the final state objects as well as the choices for the scales and the parton density functions. The `cuts.dat` file defines the required selection criteria for the objects. Some of the selection criteria, such as the $m_{\mathrm{T}}^{l\nu}$, $|\Delta\eta_{\mathrm{jj}}|$ or ΔR_{jj} requirements, are implemented by the author in a local version the VbfNlo generator. One example for each file is given.

Example of `vbfnlo.dat` file:

```
!   Main input file for vbfnlo

!   General parameters of the calculation
!-----------------------------------------
PROCESS              = 461                ! Identifier for process
LOPROCESS_PLUS_JET   = false              ! switch: LO process with 1 additional jet
LEPTONS              = 98                 ! final state leptons
DECAY_QUARKS         = 93                 ! final state quarks (u,d,s,c)

! lepton numbering according to MC particle numbering scheme
! particles are given positive numbers, antiparticles negative numbers
! e-   ve   mu-  vm   ta-  vt
! 11   12   13   14   15   16
! 98 : leptons are either generation 1 or generation 2
! 99 : any lepton

LO_ITERATIONS        = 5         ! number of iterations for LO calculation
NLO_ITERATIONS       = 5         ! number of iterations for real-emissions calc.
LO_POINTS            = 25        ! number of points for LO calculation (= 2^..)
NLO_POINTS           = 25        ! number of points for real-emissions calc. (= 2^..)
LO_GRID              = "grid2_1" "grid2_2" "grid2_3" "grid2_4" ! names of LO files
NLO_GRID             = "grid3_1" "grid3_2" "grid3_3" "grid3_4" ! names of real emissions files
PHTN_GRID            = "grid4_1" "grid4_2" "grid4_3" "grid4_4" ! names of photon emission files
FLOOP_GRID           = "grid5_1" "grid5_2" "grid5_3" "grid5_4" ! names of fermion loop files
NLO_SWITCH           = true      ! switch: nlo/lo calculation
EWCOR_SWITCH         = false     ! Whether electoweak corrections are included
FERMIONLOOP          = 3         ! Contribution of gluon-induced fermionic loops for dibosons
                                 ! 0: none
                                 ! 1: only box diagrams
                                 ! 2: only Higgs resonance
                                 ! 3: both contributions (default)
NLO_SEMILEP_DECAY    = 1         ! 0: had decay V->qq at LO QCD (default)
                                 ! 1: had decay V->qq is including approx NLO order QCD effects

ECM                  = 8000d0    ! collider center-of-mass energy
BEAM1                = 1         ! type of beam 1 (1=proton, -1 = antiproton)
BEAM2                = 1         ! type of beam 2 (1=proton, -1 = antiproton)

ID_MUF               = 4         ! ID for factorization scale
ID_MUR               = 4         ! ID for renormalization scale
MUF_USER             = 100d0     ! user defined factorization scale, if MUF is set to 0
MUR_USER             = 100d0     ! user defined renormalization scale, if MUR is set to 0
XIF                  = 1.0d0     ! scale factor xi for mu_F (not mu^2!!)
XIR                  = 1.0d0     ! scale factor xi for mu_R
```

```
!   Physics parameters
!------------------------
HMASS       = 126.0d0         ! Higgs mass
HTYPE       = 0               ! Type of Higgs produced:
                              !      0     SM Higgs with mass HMASS
                              !      1     light cp-even type higgs h0
                              !      2     heavy cp-even type higgs HH
                              !      3     lightest cp-odd type higgs A0
                              !   SUSY parameters for 1-3 are set in susy.dat.
                              !   For these options, if input 'MODEL' is set
                              !   to 1 (SM), calculation will run in the SM
                              !   for a Higgs with equivalent mass to that
                              !   chosen in the MSSM.
MODEL       = 1               ! model: 1 for SM, 2 for MSSM
HWIDTH      = -999d0          ! Higgs width (set to -999d0 for internal calculation)
TOPMASS     = 172.4d0         ! Top mass
BOTTOMMASS  = 4.855d0         ! Bottom Pole mass
CHARMMASS   = 1.65d0          ! Charm Pole mass
TAU_MASS    = 1.77684D0       ! Tau mass
ALFA_S      = 0.1176d0        ! Strong coupling constant
EWSCHEME    = 3               ! Choose scheme for electroweak parameters (1,2,3,4)
EW_APPROX   = 0               ! Approximation used when calculating electroweak
FERMI_CONST = 1.16637d-5      ! Fermi Constant
ALFA        = 7.2973525376d-3 ! Fine-structure constant
SIN2W       = 0.23119d0       ! Weak mixing angle
WMASS       = 80.398d0        ! W mass
ZMASS       = 91.1876d0       ! Z mass
ANOM_CPL    = false           ! Anomalous couplings
KK_MOD      = false           ! Warped Higgsless Model
SPIN2       = false           ! Spin-2 model


!   Parameters for the LHA event output
!----------------------------------------
LHA_SWITCH            = false    ! Les Houches interface only for LO calculation
LHA_FILE              = event.lhe  ! Name of Les Houches output file
HEPMC_SWITCH          = false      ! HepMC interface only for LO calculation
HEPMC_FILE            = event.hepmc ! Name of HepMC output file
UNWEIGHTING_SWITCH    = true     ! unweighted/weighted (T/F) events for LHA
PRENEVUNW             = 1000     ! number of events to calculate pre-maximal weight
TAUMASS               = false    ! Include mass of the tau lepton(s) in the LHA file for VBF


!   PDF set parameters
!------------------------
PDF_SWITCH    = 1      ! which pdfs to use: 1 = lhapdf, 0 = hard-wired cteq
LO_PDFNAME    = CT14nlo
NLO_PDFNAME   = CT14nlo
LO_PDFMEMBER  = 0
NLO_PDFMEMBER = 0


!   Parameters for histogram creation
!---------------------------------------
XSECFILE = xsection_nominal ! name of output-file (+ .out)
ROOT     = true             ! create root-file?
TOP      = false            ! create top-drawer file?
GNU      = false            ! create gnu-plot script file?
```

```
DATA     = false            ! create data file?
REPLACE  = true             ! replace output files?
ROOTFILE = histograms       ! name of root-file ( + '.root')
TOPFILE  = histograms       ! name of top-drawer file ( + '.top')
GNUFILE  = histograms       ! name of gnuplot file ( + '.gp')
DATAFILE = histograms       ! name of data directory ( + '.dir')
```

Example of `cuts.dat` file:

```
! input file for the cut parameters

!   Jet cuts
!-------------
RJJ_MIN    = 0.4d0      ! min jet-jet R separation
Y_P_MAX    = 2.5d0      ! max pseudorapidity for partons
PGENKTJET  = -1.0d0     ! exponent of generalised k_T algorithm
PT_JET_MIN = 25.0d0     ! min jet pT
Y_JET_MAX  = 2.5d0      ! max jet rapidity

!   Lepton cuts (only applied to charged leptons)
!-------------------------------------------------
Y_L_MAX    = 2.5d0      ! max lepton rapidity
PT_L_MIN   = 25.0d0     ! min lepton pT
MLL_MIN    = 0.0d0      ! min. m_l+l- for any comb. of opposite charged leptons
MLL_MAX    = 70000d0    ! max. m_l+l- for any comb. of opposite charged leptons
RLL_MIN    = 0.1d0      ! min lepton-lepton R separation
RLL_MAX    = 500.0d0    ! max lepton-lepton R separation
MTW_MIN    = 30.0d0     ! Aless MTW cut

!   Photon cuts
!----------------
Y_G_MAX    = 2.37d0
PT_G_MIN   = 15.0d0
RGG_MIN    = 0.0d0      ! min photon-photon R separation
RGG_MAX    = 500.0d0    ! max photon-photon R separation
PHISOLCUT  = 0.4        ! photon isolation cut
EFISOLCUT  = 0.5        ! efficiency of photon isolation cut

!   Additional R-separation cuts
!---------------------------------
RJL_MIN    = 0.3d0      ! min jet-lepton R separation
RJG_MIN    = 0.5d0      ! min jet-photon R separation
RLG_MIN    = 0.5d0      ! min lepton-photon R separation
MLG_MIN    = 0.0d0      ! min. m_lg for any comb. of charged leptons and photons
MLG_MAX    = 1.d20      ! max. m_lg for any comb. of charged leptons and photons
PTMISS_MIN = 30.0d0     ! min. missing transverse momentum


JVETO      = false      ! veto jet cuts
DELY_JVETO = 0.0d0      ! min veto-tag y-dist
YMAX_VETO  = 4.4d0      ! max |y| for veto jet
PTMIN_VETO = 25.0d0     ! min pT for veto jet

!   Vector boson fusion cuts (only applied to tagging jets in VBF processes)
!-----------------------------------------------------------------------------
ETAJJ_MIN  = 0d0        ! jet-jet rapidity separation
YSIGN      = false      ! jets #1 and #2 must have opposite sign rapidity
```

```
LRAPIDGAP  = false      ! leptons fall inside rapidity gap
DELY_JL    = 0.0d0      ! min y-dist of leptons from tagging jets
GRAPIDGAP  = false      ! photons fall inside rapidity gap
DELY_JG    = 0.0d0      ! min y-dist of photons from tagging jets
RJJ_MAX    = 3.0d0      ! Aless DRjj cut
ETAJJ_MAX  = 1.2d0      ! Aless Detajj cut
MDIJ_MIN   = 70.0d0     ! dijet min mass cut on tag jet
MDIJ_MAX   = 100.0d0    ! dijet max mass cut on tag jet

!  Cuts for semileptonic decays
!---------------------------------
DEF_TAGJET      = 1         ! switch for different tagging jet definitions
                            ! 1=two jets with largest pT
PTMIN_TAG_1     = 25.0d0    ! min transverse momentum for the harder tagging jet
PTMIN_TAG_2     = 25.0d0    ! min transverse momentum for the softer tagging jet
HARD_CENTRAL    = false     ! if true, additional jets in central region
PTMIN_CENTRAL   = 25.0d0    ! min pT for the additional hard jet
VBFCUTS_ALWAYS  = true      ! usually VBF cuts are only applied fro VBS,
                            ! BUT those cuts also supplement the s-channel part for
                            ! semileptonic di- and triboson production
RECONST_HAD_V   = 0         ! cut on reconstructed inv mass of had. decaying V bosons
                            ! 0= no cuts are taken into account
                            ! 1= use two jets
V_MASS_RANGE    = 70000.0d0 ! invariant V boson mass |m_V-m_reconst| < V_MASS_RANGE
SINGLE_DECAYJET = 0         ! 0= two jets required from the hadronic decay
QSQAMIN_ZDEC    = 0.0d0     ! minimal photon virtuallity of had. decaying Z/y*
```

A.4. Variables used for Electron and Photon Identification

Type	Variable	Description
Strip layer of EM Calorimeter	w_{s3}	Shower width for three strips around strip with maximum energy
	w_{stot}	Total lateral shower width
	F_{side}	Energy outside the three central strips but within seven strips divided by energy of three central strips
	ΔE	Difference between energy associated with second maximum in strip layer and the energy reconstructed in the strip with the minimal value found between the first and the second maxima
	E_{ratio}	Ratio of the energy difference between the largest and second largest energy deposits to the sum over these energies
Middle layer of EM Calorimeter	$w_{\eta 2}$	Lateral shower width
	R_{ϕ}	Ratio of cell energies in 3×3 and 3×7 cells (in $\eta \times \phi$)
	R_{η}	Ratio of cell energies in 3×7 and 7×7 cells (in $\eta \times \phi$)
Back layer of EM Calorimeter	f_3	Ratio of energy in back layer and total energy in EM accordion calorimeter
Hadronic leakage	R_{Had1}	Ratio of E_T in first HAD calorimeter layer and E_T of EM cluster (for $\lvert\eta\rvert < 0.8$ or $\lvert\eta\rvert > 1.37$)
	R_{Had}	Ratio of E_T in full HAD calorimeter layer and E_T of EM cluster (for $0.8 < \lvert\eta\rvert < 1.37$)
Track Quality	n_{Blayer}	Total number of hits in b-layer (first pixel layer)
	n_{Pixel}	Total number of hits in pixel detector
	n_{Si}	Total number of hits in silicon detectors
	d_0	Transverse impact parameter
TRT	n_{TRT}	Total number of TRT hits
	F_{HT}	Ratio of number of high-threshold hits and the total number of TRT hits
Cluster-track matching	$\Delta\eta$	$\Delta\eta$ between cluster position in middle layer and extrapolated track
	$\Delta\phi$	$\Delta\phi$ between cluster position in middle layer and extrapolated track
	E/p	Ratio of cluster energy and track momentum
Conversions	isConv	Identify electron candidates matched to reconstructed photon conversion

Table A.1.: Definitions of the variables used for the photon and electron identification. From References [110] and [51].

Type	Variable	Electron		Photon	
		`medium`	`tight`	`loose`	`tight`
Strip layer of EM calorimeter	w_{s3}				✓
	w_{stot}	✓	✓		✓
	F_{side}				✓
	ΔE				✓
	E_{ratio}	✓	✓		✓
Middle layer of EM calorimeter	$w_{\eta 2}$	✓	✓	✓	✓
	R_{ϕ}				✓
	R_{η}	✓	✓	✓	✓
Back layer of EM calorimeter	f_3	✓	✓		
Hadronic leakage	$R_{\mathrm{Had}(1)}$	✓	✓	✓	✓
Track quality	n_{Blayer}	✓	✓		
	n_{Pixel}	✓	✓		
	n_{Si}	✓	✓		
	d_0	✓	✓		
TRT	n_{TRT}	✓	✓		
	F_{HT}	✓	✓		
Cluster-track matching	$\Delta\eta$	✓	✓		
	$\Delta\phi$		✓		
	E/p		✓		
Conversions	isConv		✓		

Table A.2.: Variables used in the different cut based identification criteria for electron [110] and photon candidates [51].

A.5. Selection Criteria on Reconstruction Level

Object	Selection Criteria
Photon	≥ 1 `tight` photon
	$p_{\mathrm{T}} > 15\,\mathrm{GeV}$
	$\lvert\eta\rvert < 2.37$ && $1.37 < \lvert\eta\rvert < 1.52$
	$E_{\mathrm{T}}^{cone40} < 4\,\mathrm{GeV}$
	$\Delta R(\ell, \gamma) > 0.5$
Electron	`tight`
	Author = 1 OR 3
	`(el_OQ & 1446)= 0`
	$E_{\mathrm{T}}^{cone30}/E_{\mathrm{T}} < 0.14$
	$p_{\mathrm{T}}^{cone30}/E_{\mathrm{T}} < 0.07$
	$\lvert z_0 \cdot sin\theta\rvert < 0.5\,\mathrm{mm}$
	$\lvert\frac{d_0}{\sigma(d_0)}\rvert < 5.0$
	$p_{\mathrm{T}} > 25\,\mathrm{GeV}$
	$\lvert\eta\rvert < 2.47$ && $1.37 < \lvert\eta\rvert < 1.52$
Muon	`medium`
	not Standalone
	p_{T}^{cone20} / $p_T < 0.1$
	$\lvert\frac{d_0}{\sigma(d_0)}\rvert < 3.0$
	$p_{\mathrm{T}} > 25\,\mathrm{GeV}$
	$\lvert\eta\rvert < 2.4$
W boson	$E_{\mathrm{T}}^{\mathrm{miss}} > 30\,\mathrm{GeV}$
	$m_{\mathrm{T}}^{l\nu} > 30\,\mathrm{GeV}$
Jets	$N_{\mathrm{jets}} >= 2$
	not `isBadLooseMinus`
	JVF > 0.5
	$p_{\mathrm{T}} > 25\,\mathrm{GeV}$
	$\lvert\eta\rvert < 2.5$
	$\Delta R(\mathrm{jet}, \gamma) > 0.5$
	$\Delta R(\mathrm{jet}, l) > 0.3$
V boson	$70\,\mathrm{GeV} < m_{\mathrm{jj}} < 100\,\mathrm{GeV}$
	$\lvert\Delta\eta_{\mathrm{jj}}\rvert < 1.2$
	$\Delta R_{\mathrm{jj}} < 3.0$
Veto events:	with b-jets
	with additional leptons with $p_{\mathrm{T}} > 7\,\mathrm{GeV}$
	(`medium` electrons or `medium` muons)

Table A.3.: Selection criteria for the $WV\gamma$ analysis for objects defined at reconstruction level.

A.6. Fake Leptons from Jets Background for the Two-Dimensional Sideband Method

The event yield in each of the four regions of the two-dimensional sideband method is expressed via:

$$N_i^{\text{exp}} = N_i^{W\gamma} + N_i^{\text{fake } l} + N_i^{\text{other}} + N_i^{\text{fake } \gamma} \tag{A.17}$$

where $i \in$ [A, B, C, D]. The $N_i^{\text{fake } l}$ cannot be determined using the γ + jets Monte Carlo simulation sample, as it has not enough statistics to determine the event yields reliably. Therefore, a data driven method is developed to estimate the fake lepton from jets contribution in the four regions of the two-dimensional sideband method.

A binned extended maximum likelihood fit to the $E_{\text{T}}^{\text{miss}}$ distribution is performed in all four regions. The are criteria, defining the four A, B, C and D regions are based on the isolation energy of the photon $E_{\text{T}}^{\text{iso},\gamma}$ and the `tight`/`non-tigh` photon identification, as defined in Section 7.6. The fit is performed in each of the four regions with the additional requirements of inverting the criteria on the invariant dijet mass, $m_{\text{jj}} < 70\,\text{GeV}$ or $m_{\text{jj}} > 100\,\text{GeV}$ and dropping the $E_{\text{T}}^{\text{miss}}$ criteria (control region $\text{CR}_{E_{\text{T}}^{\text{miss}}}$). In each region, three templates are defined: one combined template, comprising the $W\gamma$ + jets and the fake photons from jets backgrounds, one template for the fake lepton from jets background, and one template for all other backgrounds. The template shape for the $W\gamma$ + fake γ from jets component is determined from the two separate distributions; the $W\gamma$ + jets distribution is obtained from simulation and the fake γ from jets distribution is obtained from the control region C+D, normalised to the expectation from simulation. The combined template shape is obtained by adding the two distributions and normalising it to unity.

The template shape for the fake lepton from jets contribution in each region is obtained from data, using the dedicated selection criteria, defined in Section 7.5 and in addition the criteria defining the respective region A, B, C and D. This defines four different fake lepton from jets template shapes, one for each region, while ensuring that in region A, the template shape is the same as in the simultaneous fit.

Other contributions are determined from simulation in the respective regions and added into one template. As in the simultaneous fit, this component is fixed in the fit and not allowed to float.

The fit range extends from 0 GeV $E_{\text{T}}^{\text{miss}}$ 300 GeV and is performed independently in each of the four regions and the event yields for the fake leptons from jets and the $W\gamma$ + fake γ from jets components are the free parameters in the fit. The post-fit $E_{\text{T}}^{\text{miss}}$ distributions for the four regions are shown in Figure A.2 for the electron channel and in Figure A.3 for the muon channel. In Table A.4, the expected event yields for the fake lepton from jets component in all four regions are given. The event yields of the fake leptons from jets in regions B, C and D derived with this data-driven method, are used for the two-dimensional sideband method. In region A, the obtained event yield for the fake lepton from jets $N_{\text{A}}^{\text{fake } l}$ is only used as start value in the simultaneous fit.

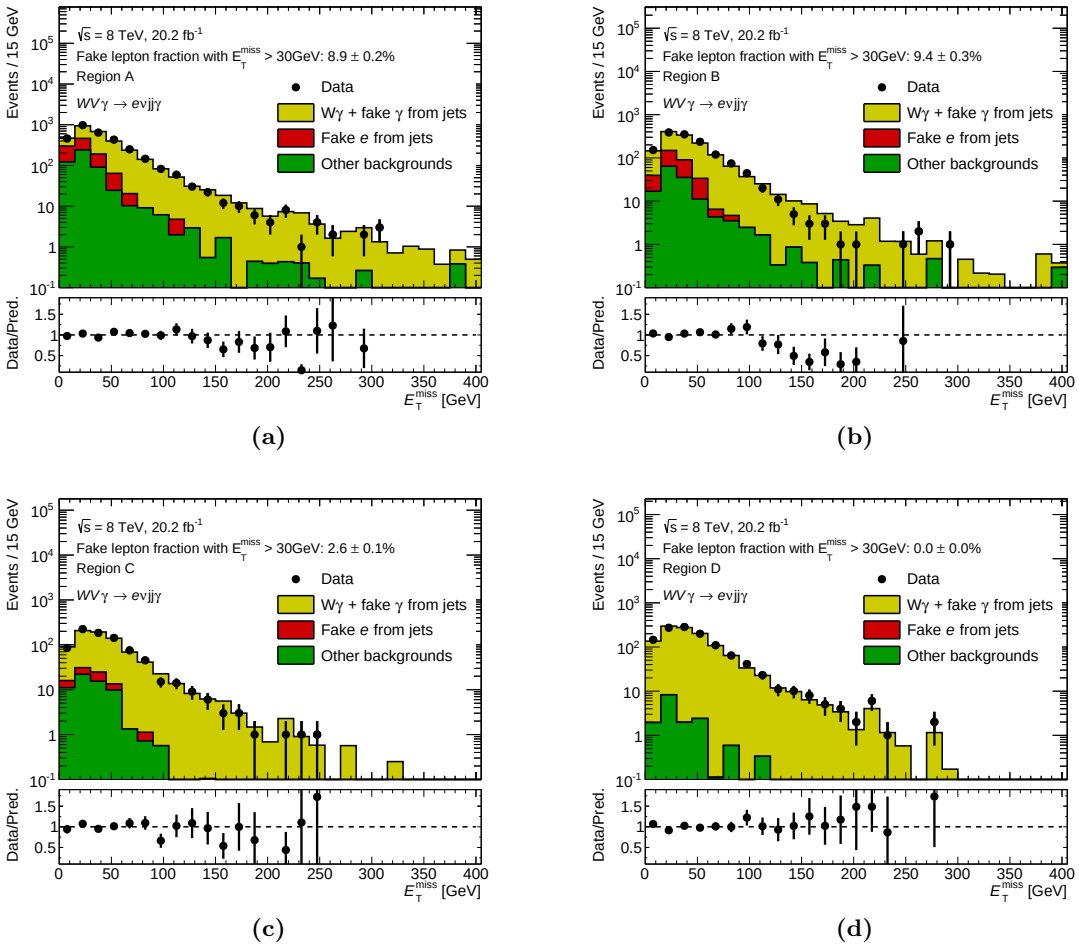

Figure A.2.: Comparison of the data and the background expectation from the fit to the $E_{\mathrm{T}}^{\mathrm{miss}}$ distribution for (a) region A, (b) region B, (c) region C and (d) region D, the four two-dimensional sideband regions in the electron channel.

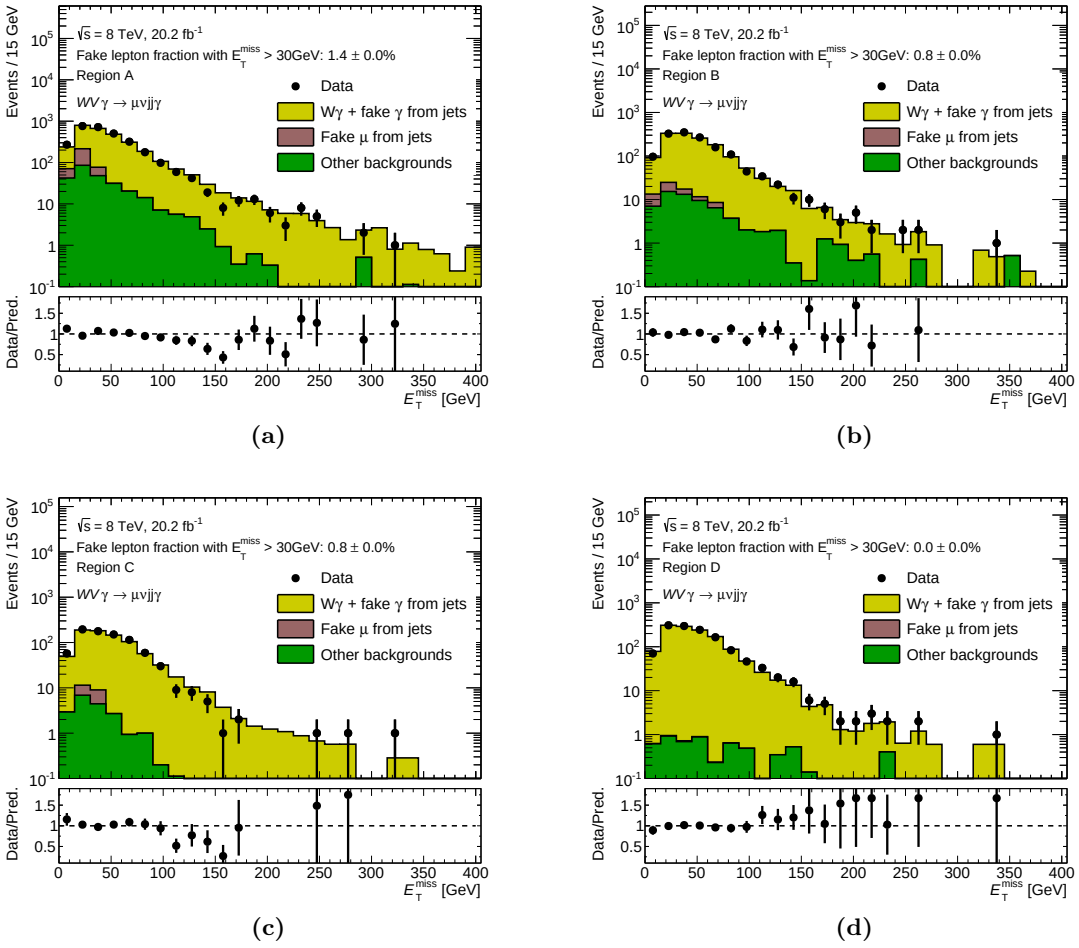

Figure A.3.: Comparison of the data and the background expectation from the fit to the $E_{\mathrm{T}}^{\mathrm{miss}}$ distribution for (a) region A, (b) region B, (c) region C and (d) region D, the four two-dimensional sideband regions in the muon channel.

	Electron Channel	Muon Channel
Region A	136.7 ± 19.0	28.7 ± 20.3
Region B	78.3 ± 9.8	8.1 ± 2.9
Region C	8.2 ± 1.4	4.5 ± 2.6
Region D	0.0 ± 0.0	0.1 ± 1.1

Table A.4.: The event yields for the fake leptons from jets, used as start value in region A and as input values for the two-dimensional sideband method of the simultaneous fit in regions B,C and D. The numbers are given for the electron and muon channel.

A.7. $WV\gamma$ Contribution in the Control Regions

Inverting the criterion on the invariant dijet mass $m_{\mathrm{jj}} < 70\,\mathrm{GeV}$ or $m_{\mathrm{jj}} > 100\,\mathrm{GeV}$ in the control region $\mathrm{CR}_{m_{\mathrm{jj}}}$, leads to a $WV\gamma$ signal contamination of about 0.7 % (0.8 %) in the electron (muon) channel. In comparison, the $WV\gamma$ signal contribution in the signal region is about 3 % for both lepton channels and thus, the signal contribution in the control region is not particularly small. As a cross check, the $WV\gamma$ signal contribution is included in the simultaneous fit for the background estimation.

Ideally, the event yield of the $WV\gamma$ signal contribution would be included as a free parameter in the simultaneous fit. However, due to its low contribution to the total composition and the similarities between the $E_{\mathrm{T}}^{\mathrm{miss}}$ template shapes for the $WV\gamma$ signal and the $W\gamma$ + jets processes, the fit has not enough power to estimate the $WV\gamma$ signal contribution. Thus, the same approach as for the backgrounds using Monte Carlo simulation is chosen: the $WV\gamma$ template shapes are estimated from the Sherpa Monte Carlo simulation, and the event yields are normalised to next-to-leading order using VbfNlo. The $WV\gamma$ signal contribution is fixed in the simultaneous fit. Including the $WV\gamma$ signal in the simultaneous fit with this approach has the disadvantage that the background estimation depends on the signal prediction.

The results of the simultaneous fit, including the $WV\gamma$ signal contribution, in the control region $\mathrm{CR}_{m_{\mathrm{jj}}}$ are given in Table A.5 and the results extrapolated into the signal region are given in Table A.6. Comparing the event yields to the event yields obtained when the $WV\gamma$ signal is neglected in the simultaneous fit (see Table 7.4 and Table 7.9, respectively), excellent agreement within the statistical uncertainties of the data is observed. When the $WV\gamma$ signal is included in the simultaneous fit, the main impact is visible on the event yield of the $W\gamma$ + jets background. The event yields of the two other backgrounds estimated with the simultaneous fit (fake γ from jets and fake l from jets) are only minimal influenced. Furthermore, when the $WV\gamma$ signal is neglected in the simultaneous fit, the total event yield of all backgrounds are slightly higher, in comparison to the total event yield of all backgrounds when the $WV\gamma$ signal is included in the simultaneous fit. This is observed in both lepton channels. Therefore, the expected limits on the production cross section are more conservative when the $WV\gamma$ signal is neglected in the simultaneous fit.

The cross check has shown that the background estimation is only minimal influenced when the $WV\gamma$ signal contribution is considered in the simultaneous fit. In order to be less dependent on the theory prediction production, the $WV\gamma$ signal contribution is neglected in the control regions, defined with the inverted m_{jj} criterion. This approach also provides more conservative cross section limits on the $WV\gamma$ production. No additional uncertainty is considered, as the expected event yields for the total backgrounds, estimated with the $WV\gamma$ signal contribution included and excluded in the simultaneous fit, are in excellent agreement within the statistical uncertainties of the data.

Process	Electron Channel	Muon Channel	Estimation Method
$W\gamma$ + jets	$1\,107.6 \pm 37.8$ (stat.)	$1\,416.1 \pm 39.8$ (stat.)	Simultaneous fit
Fake γ from jets	287.0 ± 24.9 (stat.)	387.0 ± 28.9 (stat.)	Simultaneous fit
Fake l from jets	159.8 ± 16.0 (stat.)	32.2 ± 6.5 (stat.)	Simultaneous fit
$t\bar{t}\gamma$	46.2 ± 4.2	57.2 ± 4.8	MC simulation
Fake γ from e	42.3 ± 11.2	15.2 ± 3.5	Corrected simulation
$Z\gamma$ + jets	58.9 ± 2.9	64.2 ± 2.9	MC simulation
$WV\gamma$ (signal)	12.0 ± 1.7	16.7 ± 1.5	Corrected VBFNLO
$WV\gamma$ ($\rightarrow \tau\nu$jjγ)	0.4 ± 0.0	0.5 ± 0.1	MC simulation
Total expectation	$1\,714.2 \pm 48.0$ (stat.)	$1\,989.0 \pm 49.6$ (stat.)	Sum of components
Data	1705	1989	Measurement

Table A.5.: Observed and expected event yields in the control region $\mathrm{CR}_{m_{\mathrm{jj}}}$ including the $WV\gamma$ signal prediction in the background estimation method, together with the estimation method for the electron an the muon channel. The uncertainties on the backgrounds estimated with the simultaneous fit are due to the statistical uncertainties of the data. The uncertainties on the other backgrounds are the statistical uncertainties due to the Monte Carlo generation. The total number of events is the sum over all background components with the statistical uncertainty of the data only.

Process	Electron Channel	Muon Channel	Estimation Method
$W\gamma$ + jets	320.3 ± 11.0 (stat.)	402.0 ± 11.4 (stat.)	Simultaneous fit
Fake γ from jets	82.5 ± 7.2 (stat.)	117.4 ± 8.8 (stat.)	Simultaneous fit
Fake l from jets	57.2 ± 5.7 (stat.)	27.2 ± 5.5 (stat.)	Simultaneous fit
$t\bar{t}\gamma$	35.4 ± 3.6	46.3 ± 4.3	MC simulation
Fake γ from e	33.2 ± 11.7	2.9 ± 0.5	Corrected simulation
$Z\gamma$ + jets	19.4 ± 1.7	19.9 ± 1.5	MC simulation
$WV\gamma$ ($\rightarrow \tau\nu$jjγ)	0.5 ± 0.0	0.4 ± 0.0	MC simulation
Total background	548.3 ± 14.2 (stat.)	616.2 ± 15.4 (stat.)	Sum of components
Expected signal	13.7 ± 2.0	17.5 ± 1.6	Corrected VBFNLO
Data	490	599	Measurement

Table A.6.: Observed and expected event yields (including the $WV\gamma$ signal prediction in the background estimation method) in the signal region along with the estimation method. The uncertainties on the backgrounds estimated with the simultaneous fit originate from the statistical uncertainty on the data. The uncertainties on the other background components are the statistical uncertainties due to the Monte Carlo generation. The total number of events is the sum over all background components with the statistical uncertainty of the data only.

A.8. Systematic Uncertainties for Separate Background Components

Systematic Uncertainties due to Statistical Uncertainties of the Templates

The uncertainties arising from the statistical uncertainties of the templates are evaluated as described in Section 7.9.2 for the individual background components and given in Table A.7. The central values for the background estimation vary slightly from the nominal values, given in Table 7.9, since the central values listed here are obtained as the mean value of the distribution of the signal region event yields from the 10000 pseudo experiments. Good agreement is found between the nominal values and the mean values of the distributions. The uncertainties on the individual backgrounds range between 2.4 % and 35.3 %. The uncertainty on the total expected backgrounds is evaluated separately for each pseudo experiment and does not correspond to the quadratic sum of the individual uncertainties, due to large anti-correlations of the background components in the simultaneous fit. Only the total background and its corresponding uncertainty is used to determine the exclusion limits on the cross section and on aQGCs.

	Electron channel			Muon channel		
Process	Value	abs. Uncert.	rel. Uncert.	Value	abs. Uncert.	rel. Uncert.
$W\gamma$ + jets	326.7	± 10.2	3.1 %	408.7	± 10.0	2.4 %
Fake γ from jets	80.7	± 10.2	12.7 %	116.1	± 8.0	6.9 %
Fake l from jets	55.9	± 10.2	18.3 %	27.1	± 7.9	29.1 %
Fake γ from e	34.5	± 12.3	35.5 %	3.0	± 0.8	26.1 %
$Z\gamma$	20.2	± 3.7	18.4 %	19.9	± 2.9	14.4 %
$t\bar{t}\gamma$	35.3	± 5.8	16.4 %	46.2	± 7.3	15.7 %
$WV\gamma$ (τ)	0.5	± 0.1	15.7 %	0.4	± 0.1	15.3 %
Total Backgrounds	553.8	± 27.0	4.9 %	621.3	± 22.1	3.6 %

Table A.7.: Systematic uncertainty due to the statistical uncertainties of the templates split into the individual background components as well as the total expected background yield.

Fit Related Systematic Uncertainties

Fit related systematic uncertainties are evaluated as described in Section 7.9.2 for the three background components, determined with the simultaneous fit, and given in Table A.8. The uncertainties on the individual backgrounds range between 7.9 % and 57.4 %. The uncertainty on the total expected backgrounds does not correspond to the quadratic sum of the individual uncertainties, due to the large correlations of the background components in the simultaneous fit. Only the total background and its corresponding uncertainty is used to determine the cross section and aQGC exclusion limits.

	Electron Channel			Muon Channel		
Process	Value	abs. Uncert.	rel. Uncert.	Value	abs. Uncert.	rel. Uncert.
$W\gamma$ + jets	324.0	± 43.4	13.4 %	406.9	± 32.0	7.9 %
Fake γ from jets	82.5	± 47.3	57.4 %	117.3	± 34.6	29.5 %
Fake l from jets	56.9	± 9.9	17.5 %	26.9	± 6.2	23.1 %
Total Backgrounds	551.7	± 3.5	0.6 %	620.7	± 4.8	0.8 %

Table A.8.: Fit related systematic uncertainties split into the individual background components as well as the total expected background yield.

A.9. Simplified Background Estimation Method

A simplified method for the background estimation is developed to cross check the results obtained with the simultaneous fit and to estimate the uncertainties originating from reconstruction and identification inefficiencies on the expected background event yield. The simplified method performs simultaneously two maximum likelihood fits to the m_{jj} and the $E_{\mathrm{T}}^{\mathrm{miss}}$ distributions, but does not include the two-dimensional sideband method. This simplifies the background estimation method and reduces the computational effort significantly. Since no additional constrains on the fake photons from jets backgrounds are incorporated in the background estimation method, the two backgrounds cannot be distinguished and are evaluated together. Therefore, the template shapes for the $W\gamma$ + jets background and the fake photons from jets background are studied further. Figure A.4 shows the m_{jj} distributions in the $\mathrm{CR}_{m_{\mathrm{jj}}}$ and the $E_{\mathrm{T}}^{\mathrm{miss}}$ distributions in the $\mathrm{CR}_{E_{\mathrm{T}}^{\mathrm{miss}}}$ for the $W\gamma$ + jets template, obtained using Monte Carlo simulation and the fake photon from jets template, obtain using the control region C+D, as defined in Section 7.6. For both lepton channels and both distributions, m_{jj} and $E_{\mathrm{T}}^{\mathrm{miss}}$, the

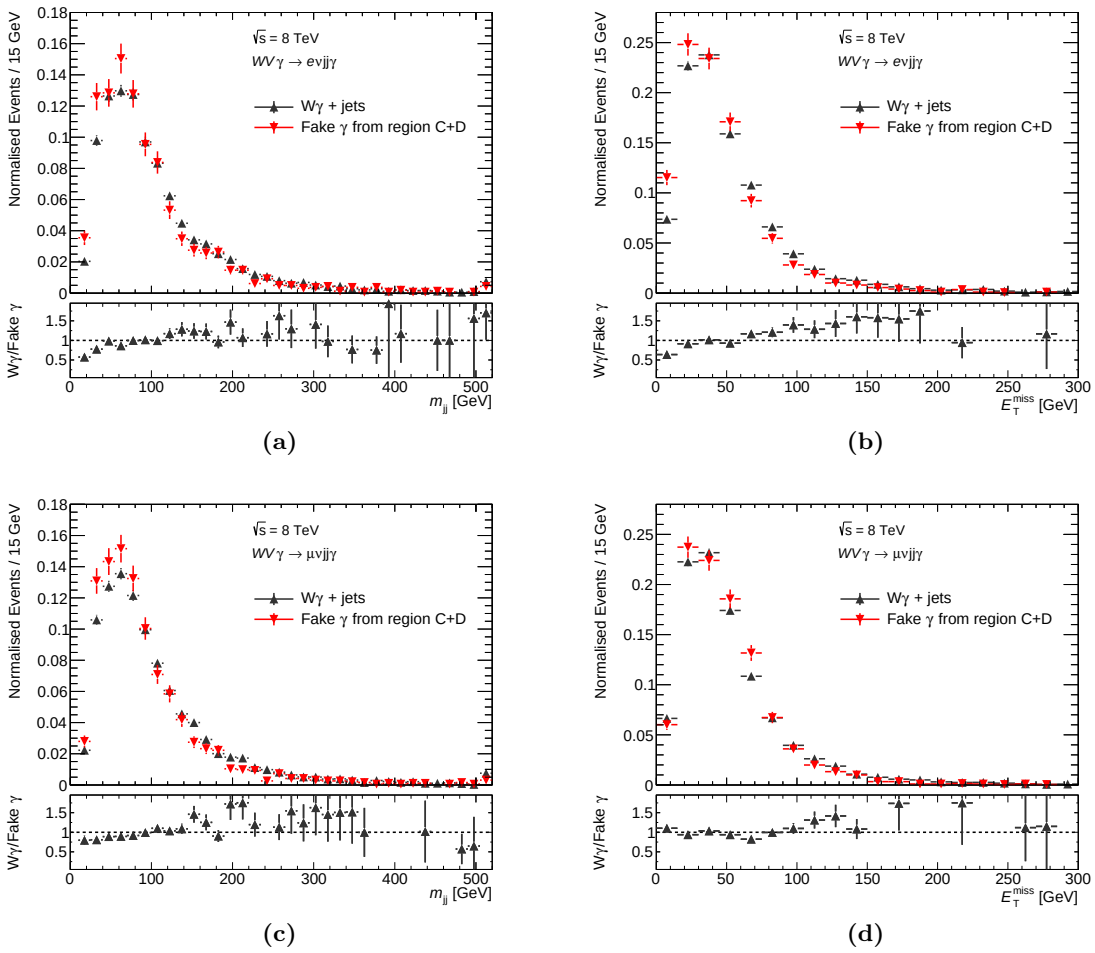

Figure A.4.: Comparison of the $W\gamma$ +jets and fake photons from jets templates shapes of the m_{jj} distribution in the (a) electron and (c) muon channel and of the the $E_{\mathrm{T}}^{\mathrm{miss}}$ distribution ($\mathrm{CR}_{E_{\mathrm{T}}^{\mathrm{miss}}}$), also in the (b) electron and (d) muon channel.

templates shapes for the $W\gamma$ + jets and the fake photon from jets background show reasonable agreement within the uncertainties.

As further cross check, the shapes of the truth p_{T} distribution of the leptonically decaying W boson at particle level are studied. The dominant process contributing to the fake photon from jets background arises from W + jets production. Therefore, the p_{T} distribution of the leptonically decaying W boson is compared for $W\gamma$ + jets production and the W + jets production. To have comparable phase spaces, the $W\gamma$ + jets selection requires at least one photon with E_{T} above 15 GeV and the W + jets selection requires a third jet with p_{T} above 15 GeV. In Figure A.5 the truth p_{T} shapes of the W boson of the $W\gamma$ + jets and W + jets samples are shown for the region 70 GeV $< m_{\mathrm{jj}} <$ 100 GeV as well as for the full m_{jj} region. In both lepton channels and both phase spaces, good agreement is found for the truth p_{T} distribution of the W boson, giving confidence in using one common template shape for the two backgrounds.

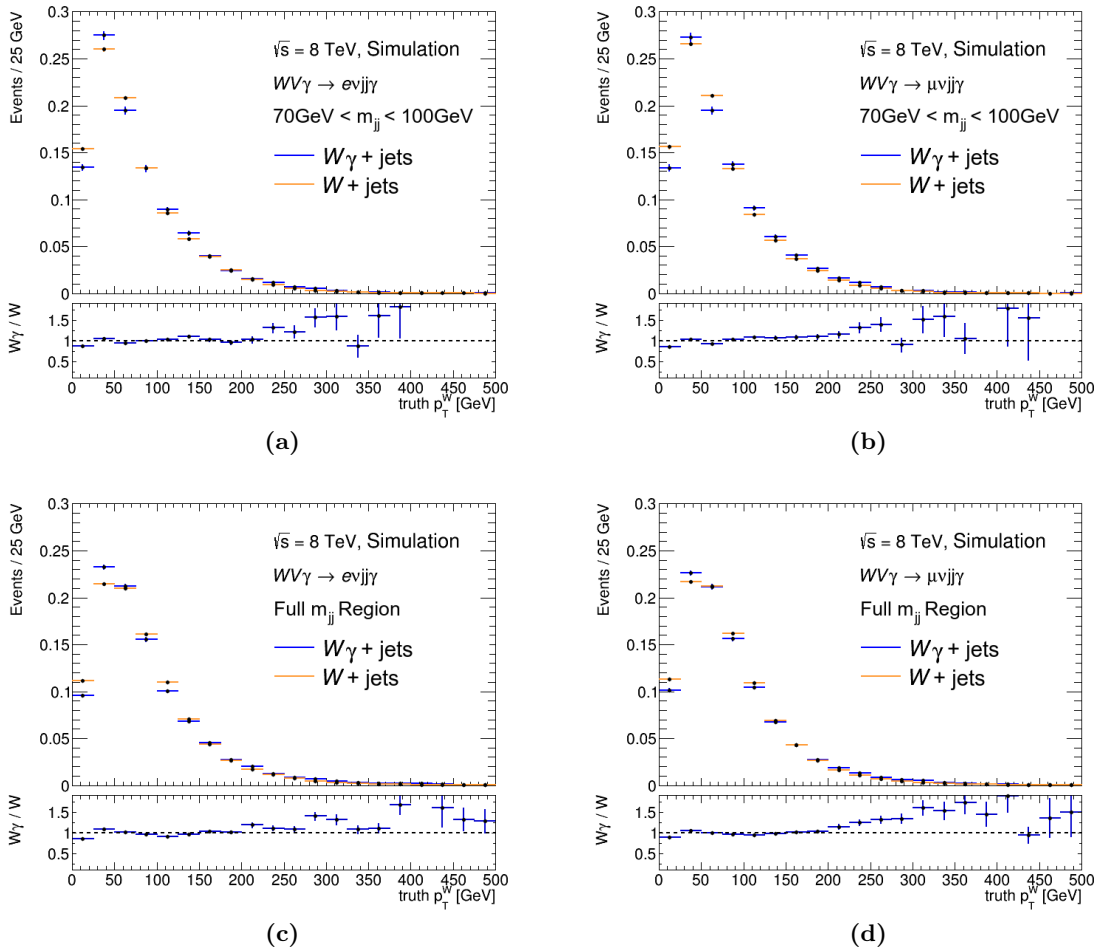

Figure A.5.: Comparison of the $W\gamma$ +jets and W + jets shapes of the truth p_{T} distribution of the leptonically decaying W boson in the region 70 GeV $< m_{\mathrm{jj}} <$ 100 GeV, in the (a) electron and (b) muon channel and in the full m_{jj} region in the (c) electron and (d) muon channel.

The simplified method comprises a binned extended maximum likelihood to the m_{jj} distribution in the $\mathrm{CR}_{m_{\mathrm{jj}}}$ and a maximum likelihood to the $E_{\mathrm{T}}^{\mathrm{miss}}$ distribution in the $\mathrm{CR}_{E_{\mathrm{T}}^{\mathrm{miss}}}$, performed

simultaneously. The likelihood functions are the same as given in Equations 7.19 and 7.20 with the difference that no individual term for the fake photon from jets background is introduced and this background is determined together with the $W\gamma$ + jets background. As template for the $W\gamma$ + fake photon from jets template, the $W\gamma$ + jets template shape from simulation is taken, since it has the smaller statistical uncertainties. The result obtained from the simplified method is extrapolated into the signal region in the same way as in the nominal method, described in Section 7.9. In Table A.9, the expected event yields are given, estimated with the simplified method and extrapolated into the signal region. The uncertainties for the $W\gamma$ +

Process	Electron Channel	Muon Channel
$W\gamma$ + fake γ from jets	401.0 ± 10.4	516.0 ± 9.7
fake l from jets	61.2 ± 5.8	28.5 ± 5.6
$t\bar{t}\gamma$	35.3 ± 3.6	46.5 ± 4.3
fake γ from e	33.3 ± 11.8	2.9 ± 0.5
$Z\gamma$ + jets	20.7 ± 1.6	20.0 ± 1.5
$WV\gamma$ ($\rightarrow \tau\nu$jjγ)	0.5 ± 0.1	0.4 ± 0.0
Total background	551.9 ± 17.2	614.2 ± 12.1
Expected signal	13.7 ± 2.0	17.5 ± 1.6

Table A.9.: Expected event yields in the signal region estimated with the simplified method. The uncertainties on the backgrounds estimated with the simplified method originate from the statistical uncertainty of the data. The uncertainties on the other background components are the statistical uncertainties due to the Monte Carlo generation. The total number of events is the sum over all background components an the uncertainty corresponds to the statistical uncertainty of the data.

fake photon from jets, the fake leptons from jets and the total backgrounds are the statistical uncertainties of the data. The other backgrounds, estimated using simulation, are given with the statistical uncertainties of the Monte Carlo generation. Good agreement within the uncertainties is observed between the expected event yields obtained with the simplified method and the nominal background estimation method, given in Table 7.9.

In addition, the fit related systematic uncertainties and the systematic uncertainties due to the statistical uncertainties of the templates, described in Section 7.9.2, are also evaluated for the simplified method and found the be in excellent agreement between the two methods. Therefore, it is justified to use the simplified method for the evaluation of the systematic uncertainties due to the reconstruction and identification inefficiencies of the objects.

A.10. Alternative $W\gamma$ + jets Template Shape

In Figure 7.10, a trend at low values of m_{jj} is visible in both lepton channels: the data is underestimated by the background expectation, but still within the estimated uncertainties. This trend was studied further by using an alternative $W\gamma$ + jets template shape, generated with SHERPA. The simultaneous fit, described in Chapter 7, is repeated with the alternative template shape. The obtained event yields in the signal region and the $\mathrm{CR}_{m_{\mathrm{jj}}}$ are given in Table A.10 and can be directly compared to the event yields obtained with the nominal $W\gamma$ + jets template shapes in Tables 7.9 and 7.4. The post-fit m_{jj} distribution for both lepton channels using the alternative $W\gamma$ +jets template shapes are shown in Figure A.6. In both lepton channels, the trend is less pronounced when using the SHERPA samples. Good agreement within one standard deviation is observed between the total event yields obtained with the two different $W\gamma$ + jets template shapes and therefore, no additional uncertainty is assigned.

	Electron Channel		Muon Channel	
Process	Signal Region	$\mathrm{CR}_{m_{\mathrm{jj}}}$	Signal Region	$\mathrm{CR}_{m_{\mathrm{jj}}}$
$W\gamma$ + jets	290.2	1 119.0	424.7	1 443.9
Fake γ from jets	89.3	310.6	117.6	387.7
Fake l from jets	44.7	124.2	19.7	23.4
$t\bar{t}\gamma$	35.4	46.2	46.3	57.2
Fake γ from e	33.2	50.1	2.9	15.2
$Z\gamma$ + jets	19.4	58.9	19.9	64.2
$WV\gamma$ (τ)	0.5	0.4	0.4	0.5
Total Backgrounds	512.4	1 709.4	631.6	1 992.0
Data	490	1 705	599.0	1 989

Table A.10.: Observed and expected event yields in the signal region and the control region $\mathrm{CR}_{m_{\mathrm{jj}}}$ determined using the alternative $W\gamma$ + jets template shape.

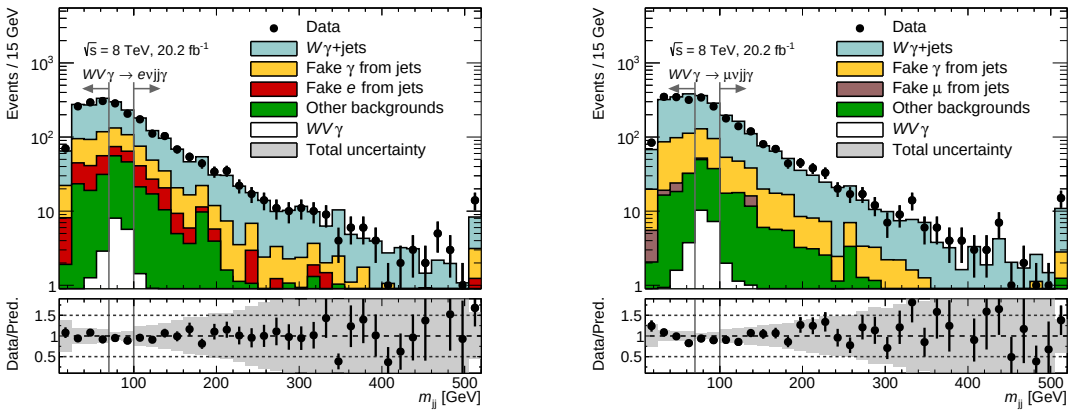

Figure A.6.: Comparison of the data and the background expectation of the invariant dijet mass distribution m_{jj} in the (a) electron and (b) muon channel. The background expectation is determined using the alternative $W\gamma$ + jets simulation sample generated with Sherpa. The total uncertainty is not re-evaluated. For illustrative purposes only, the uncertainty as derived with the nominal $W\gamma$ + jets sample are shown.

A.11. Asymptotic Formula for q_μ

The determination of the p-value and the the upper limit, using the asymptotic formula for the test statistic q_μ is described in detail in Reference [137], Section 3.6, and summarised in the following. Using Wald's theorem [139], it can be shown, that the test statistic q_μ can be written as:

$$q_\mu = \begin{cases} \frac{(\mu-\hat{\mu})^2}{\sigma^2} & , \text{ for } \mu > \hat{\mu} \\ 0 & , \text{ for } \mu < \hat{\mu}. \end{cases} \tag{A.18}$$

where the parameter of interest, μ, is distributed according to a Gauss distribution with mean μ' and the standard deviation σ. The probability density function, $f(q_\mu|\mu)$, for the special case when $\mu = \mu'$ is given by:

$$f(q_\mu|\mu) = \frac{1}{2}\delta(q_\mu) + \frac{1}{2}\frac{1}{\sqrt{2\pi}\,\sqrt{q_\mu}}\, e^{-q_\mu/2} \tag{A.19}$$

which is a mixture of a delta function $\delta(q_\mu)$ at q_μ and a χ^2- distribution with one degree of freedom. The corresponding cumulative distribution is given by:

$$F(q_\mu|\mu) = \Phi(\sqrt{q_\mu}) \tag{A.20}$$

where Φ is the cumulative distribution of the standard Gauss with mean at zero and unit width. For the tested parameter μ, the p-value is determined via:

$$p_\mu = 1 - F(q_\mu|\mu). \tag{A.21}$$

The p-value which corresponds to 95 % confidence level is obtained for $p_\mu \leq 0.05$. Using Equations A.18 and A.21, the upper limit μ_{up} is obtained from:

$$\mu_{up} = \hat{\mu} + \sigma\Phi^{-1}(1 - 0.05) \tag{A.22}$$

where $\Phi^{-1}(1 - 0.05) = 1.64$. In general, σ depends on μ and therefore the upper limit is often obtained numerically, by solving Equation A.21 for the value of μ which yields $p_\mu = 0.05$ [137].

A.12. Cross Section Limit with Frequentist Calculator

The expected limits in this thesis are determined based on the asymptotic formula and use Asimov datasets. However, these assumptions are only valid in case of large event counts. In order to study, if the $WV\gamma$ analysis fulfils these requirements, the exclusion limits are also derived with a full Frequentist approach. In this procedure, the test statistic is sampled by drawing 5000 pseudo data events for the background only and the signal plus background hypothesis. It is implemented using the Frequentist calculator of the RooStat package. The CL_S limits are listed in Table A.11 and are in good agreement with the limits obtained using the Asimov datasets in Table 8.4.

	Observed Limit [fb]	Expected Limit [fb]	Theory Prediction [fb]
$e\nu$jjγ	10.0	$15.6^{+6.3}_{-4.3}$	2.42 ± 0.08
$\mu\nu$jjγ	8.4	$9.7^{+4.2}_{-2.0}$	2.16 ± 0.10
$l\nu$jjγ	5.6	$8.6^{+3.3}_{-2.8}$	2.29 ± 0.06

Table A.11.: Observed and expected upper limits on the $WV\gamma$ production cross section at the 95 % confidence level using the CL_s method for the $e\nu$jjγ and $\mu\nu$jjγ final states as well as averaged per lepton flavour $l\nu$jjγ. The expected exclusion limits are determined under the background only hypothesis and using a full Frequentist approach. The theoretical predictions for the expected cross sections are computed with the VBFNLO generator and corrected to particle level.

Bibliography

[1] F. Englert and R. Brout, *Broken Symmetry and the Mass of Gauge Vector Mesons*, Phys. Rev. Lett. 13 (9 1964) p. 321.

[2] P. Higgs, *Broken symmetries, massless particles and gauge fields*, Phys. Lett. 12 (1964) p. 132 , ISSN: 0031-9163.

[3] P. W. Higgs, *Broken Symmetries and the Masses of Gauge Bosons*, Phys. Rev. Lett. 13 (16 1964) p. 508.

[4] P. W. Higgs, *Spontaneous Symmetry Breakdown without Massless Bosons*, Phys. Rev. 145 (4 1966) p. 1156.

[5] G. S. Guralnik, C. R. Hagen and T. W. B. Kibble, *Global Conservation Laws and Massless Particles*, Phys. Rev. Lett. 13 (20 1964) p. 585.

[6] T. W. B. Kibble, *Symmetry Breaking in Non-Abelian Gauge Theories*, Phys. Rev. 155 (5 1967) p. 1554.

[7] ATLAS Collaboration, *Observation of a new particle in the search for the Standard Model Higgs boson with the ATLAS detector at the LHC*, Phys. Lett. B716 (2012) p. 1, arXiv: 1207.7214 [hep-ex].

[8] CMS Collaboration, *Observation of a new boson at a mass of 125 GeV with the CMS experiment at the LHC*, Phys. Lett. B716 (2012) p. 30, arXiv: 1207.7235 [hep-ex].

[9] P. A. R. Ade et al., *Planck 2015 results. XIII. Cosmological parameters*, Astron. Astrophys. 594 (2016) A13, arXiv: 1502.01589 [astro-ph.CO].

[10] ATLAS Collaboration, *Studies of $WV\gamma$ Production in pp Collisions at $\sqrt{s} = 8$ TeV and Limits on Anomalous Quartic Gauge Couplings with the ATLAS Experiment*, 2017, URL: https://atlas.web.cern.ch/Atlas/GROUPS/PHYSICS/PAPERS/STDM-2016-05/.

[11] CMS Collaboration, *Search for $WW\gamma$ and $WZ\gamma$ production and constraints on anomalous quartic gauge couplings in pp collisions at $\sqrt{s} = 8$ TeV*, Phys. Rev. D 90 (2014) p. 032008, arXiv: 1404.4619 [hep-ex].

[12] The ALEPH, DELPHI, L3 and OPAL Collaborations; the LEP Electroweak Working Group, *Electroweak Measurements in Electron-Positron Collisions at W-Boson-Pair Energies at LEP*, Phys. Rept. 532 (2013) p. 119, arXiv: 1302.3415 [hep-ex].

[13] ATLAS Collaboration, *Evidence of $W\gamma\gamma$ Production in pp Collisions at $\sqrt{s} = 8$ TeV and Limits on Anomalous Quartic Gauge Couplings with the ATLAS Detector*, Phys. Rev. Lett. 115 (2015) p. 031802, arXiv: 1503.03243 [hep-ex].

[14] ATLAS Collaboration, *Measurements of $Z\gamma$ and $Z\gamma\gamma$ production in pp collisions at $\sqrt{s} = 8$ TeV with the ATLAS detector*, Phys. Rev. D 93 (2016) p. 112002, arXiv: 1604.05232 [hep-ex].

[15] ATLAS Collaboration, *Search for triboson $W^{\pm}W^{\pm}W^{\mp}$ production in pp collisions at $\sqrt{s} = 8$ TeV with the ATLAS detector*, Eur. Phys. J. C 77 (2016) p. 141, arXiv: 1610.05088 [hep-ex].

[16] CMS Collaboration, *Measurements of the $pp \to W\gamma\gamma$ and $pp \to Z\gamma\gamma$ cross sections and limits on anomalous quartic gauge couplings at $\sqrt{s} = 8$ TeV*, submitted to JHEP (2017), arXiv: 1704.00366 [hep-ex].

[17] CMS Collaboration, *Measurement of the cross section for electroweak production of $Z\gamma$ in association with two jets and constraints on anomalous quartic gauge couplings in proton-proton collisions at $\sqrt{s} = 8$ TeV*, 2017, arXiv: 1702.03025 [hep-ex].

[18] CMS Collaboration, *Measurement of electroweak-induced production of $W\gamma$ with two jets in pp collisions at $\sqrt{s} = 8$ TeV and constraints on anomalous quartic gauge couplings*, 2016, arXiv: 1612.09256 [hep-ex].

[19] ATLAS Collaboration, *Studies of $Z\gamma$ production in association with a high-mass dijet system in pp collisions at $\sqrt{s} = 8$ TeV with the ATLAS detector*, (2017), arXiv: 1705.01966 [hep-ex].

[20] CMS Collaboration, *Study of vector boson scattering and search for new physics in events with two same-sign leptons and two jets*, Phys. Rev. Lett. 114 (2015) p. 051801, arXiv: 1410.6315 [hep-ex].

[21] CMS Collaboration, *Evidence for exclusive $\gamma\gamma \to W^+W^-$ production and constraints on anomalous quartic gauge couplings in pp collisions at $\sqrt{s} = 7$ and 8 TeV*, JHEP 08 (2016) p. 119, arXiv: 1604.04464 [hep-ex].

[22] ATLAS Collaboration, *Measurement of $W^{\pm}W^{\pm}$ vector-boson scattering and limits on anomalous quartic gauge couplings with the ATLAS detector*, submitted to PRD (2016), arXiv: 1611.02428 [hep-ex].

[23] ATLAS Collaboration, *Evidence for Electroweak Production of $W^{\pm}W^{\pm}jj$ in pp Collisions at $\sqrt{s} = 8$ TeV with the ATLAS Detector*, Phys. Rev. Lett. 113 (2014) p. 141803, arXiv: 1405.6241 [hep-ex].

[24] ATLAS Collaboration, *Search for anomalous electroweak production of WW/WZ in association with a high-mass dijet system in pp collisions at $\sqrt{s} = 8$ TeV with the ATLAS detector*, Phys. Rev. D 95 (2017) p. 032001, arXiv: 1609.05122 [hep-ex].

[25] A. E. Baas et al., *In-situ jet pseudorapidity intercalibration of the ATLAS detector using the Trigger Combination Method*, ATL-COM-PHYS-2013-1219, 2013, URL: https://cds.cern.ch/record/1595578.

[26] A. Djouadi, *The Anatomy of electro-weak symmetry breaking. I: The Higgs boson in the standard model*, Phys. Rept. 457 (2008) p. 1, arXiv: 0503172 [hep-ph].

[27] M. Thomson, *Modern Particle Physics*, Cambridge University Press, 2013, ISBN: 9781107034266.

[28] A. Pich, *The Standard Model of Electroweak Interactions*, Proceedings, 18th European School (ESHEP 2010): Raseborg, Finland, June 20 - July 3 in 2010, 2012 p. 1, arXiv: 1201.0537 [hep-ph].

[29] S. L. Glashow, *Partial Symmetries of Weak Interactions*, Nucl. Phys. 22 (1961) p. 579.

[30] A. Salam, *Weak and Electromagnetic Interactions*, Conf. Proc. C680519 (1968) p. 367.

[31] S. Weinberg, *A Model of Leptons*, Phys. Rev. Lett. 19 (21 1967) p. 1264.

[32] H. D. Politzer, *Reliable Perturbative Results for Strong Interactions?*, Phys. Rev. Lett. 30 (26 1973) p. 1346.

[33] D. J. Gross and F. Wilczek, *Ultraviolet Behavior of Non-Abelian Gauge Theories*, Phys. Rev. Lett. 30 (26 1973) p. 1343.

[34] M. Drewes, *The Phenomenology of Right Handed Neutrinos*, Int. J. Mod. Phys. E22 (2013) p. 1330019, arXiv: 1303.6912 [hep-ph].

[35] C. Patrignani et al., *Review of Particle Physics*, Chin. Phys. C40 (2016) p. 100001.

[36] J. Baglio et al., *Release Note - VBFNLO 2.7.0*, (2014), arXiv: 1404.3940 [hep-ph].

[37] J. Baglio et al., *VBFNLO: A Parton Level Monte Carlo for Processes with Electroweak Bosons – Manual for Version 2.5.0*, (2011), arXiv: 1107.4038 [hep-ph].

[38] K. Arnold et al., *VBFNLO: A Parton level Monte Carlo for processes with electroweak bosons*, Comput. Phys. Commun. 180 (2009) p. 1661, arXiv: 0811.4559 [hep-ph].

[39] B. Feigl, *Electroweak Processes in the Standard Model and Beyond: Backgrounds to Higgs Physics and Semileptonic Decay Modes*, 2013, Karlsruhe Institut für Technologie, URL: https://publikationen.bibliothek.kit.edu/1000037298.

[40] ATLAS Collaboration, *Summary plots from the ATLAS Standard Model physics group*, 2016, URL: https://atlas.web.cern.ch/Atlas/GROUPS/PHYSICS/CombinedSummaryPlots/SM/.

[41] O. J. P. Éboli, M. C. Gonzalez-Garcia and S. M. Lietti, *Bosonic quartic couplings at CERN LHC*, Phys. Rev. D 69 (9 2004) p. 095005.

[42] C. Degrande et al., *Effective field theory: A modern approach to anomalous couplings*, Ann. Phys. 335 (2013) p. 21 , ISSN: 0003-4916.

[43] C. Degrande et al., *Monte Carlo tools for studies of non-standard electroweak gauge boson interactions in multi-boson processes: A Snowmass White Paper*, Proceedings, Community Summer Study 2013: Snowmass on the Mississippi (CSS2013): Minneapolis, MN, USA, July 29-August 6, 2013, arXiv: 1309.7890 [hep-ph].

[44] E. Fermi, *Versuch einer Theorie der β-Strahlen.*, Zeitschrift für Physik 88 (1934) p. 161, ISSN: 0044-3328.

[45] V. D. Barger et al., *Strong W^+W^+ scattering signals at pp supercolliders*, Phys. Rev. D 42 (1990) p. 3052.

[46] L. Evans and P. Bryant, *LHC Machine*, JINST 3 (2008) S08001.

[47] F. Müller, *Jet production measurement at the ATLAS experiment*, Heidelberg University, 2014, URL: https://www.kip.uni-heidelberg.de/Veroeffentlichungen/details.php?id=2966.

[48] ATLAS Collaboration, *The ATLAS Experiment at the CERN Large Hadron Collider*, JINST 3 (2008) S08003.

[49] ATLAS Collaboration, *The ATLAS Inner Detector commissioning and calibration*, Eur. Phys. J. C 70 (2010) p. 787, arXiv: 1004.5293 [physics.ins-det].

[50] M. Aharrouche et al., *Energy linearity and resolution of the ATLAS electromagnetic barrel calorimeter in an electron test-beam*, Nucl. Instrum. Meth. 568 (2006) p. 601 , ISSN: 0168-9002.

[51] ATLAS Collaboration, *Measurement of the photon identification efficiencies with the ATLAS detector using LHC Run-1 data*, Eur. Phys. J. C 76 (2016) p. 666, ISSN: 1434-6052.

[52] T. Davidek et al., *ATLAS Tile Calorimeter performance for single particles in beam tests*, Journal of Physics: Conference Series 160 (2009) p. 012057, URL: http://stacks.iop.org/1742-6596/160/i=1/a=012057.

[53] B. Dowler, et al., *Performance of the ATLAS hadronic end-cap calorimeter in beam tests*, Nucl. Instrum. Meth. A 482 (2002) p. 94.

[54] J. P. Archambault et al., *Energy calibration of the ATLAS liquid argon forward calorimeter*, JINST 3 (2008) P02002.

[55] R. Achenbach et al., *The ATLAS level-1 calorimeter trigger*, JINST 3 (2008) P03001.

[56] V. Cindro et al., *The ATLAS beam conditions monitor*, JINST 3 (2008) P02004.

[57] S. van der Meer, *Calibration of the effective beam height in the ISR*, CERN-ISR-PO-68-31. ISR-PO-68-31, 1968, URL: http://cds.cern.ch/record/296752.

[58] ATLAS Collaboration, *Luminosity determination in pp collisions at $\sqrt{s} = 8\,TeV$ using the ATLAS detector at the LHC*, Eur. Phys. J. C 76 (2016) p. 653, ISSN: 1434-6052.

[59] T. Sjostrand, *Monte Carlo Generators*, High-energy physics. Proceedings, European School, Aronsborg, Sweden, June 18-July 1, 2006 p. 51, arXiv: 0611247 [hep-ph].

[60] J. M. Campbell, J. W. Huston and W. J. Stirling, *Hard Interactions of Quarks and Gluons: A Primer for LHC Physics*, Rept. Prog. Phys. 70 (2007) p. 89, arXiv: 0611148 [hep-ph].

[61] J. C. Collins and D. E. Soper, *The Theorems of Perturbative QCD*, Ann. Rev. Nucl. Part. Sci. 37 (1987) p. 383.

[62] G. Altarelli and G. Parisi, *Asymptotic Freedom in Parton Language*, Nucl. Phys. B 126 (1977) p. 298.

[63] V. N. Gribov and L. N. Lipatov, *Deep inelastic e p scattering in perturbation theory*, Sov. J. Nucl. Phys. 15 (1972) p. 438, [Yad. Fiz.15,781(1972)].

[64] L. N. Lipatov, *The parton model and perturbation theory*, Sov. J. Nucl. Phys. 20 (1975) p. 94, [Yad. Fiz.20,181(1974)].

[65] Y. L. Dokshitzer, *Calculation of the Structure Functions for Deep Inelastic Scattering and e+ e- Annihilation by Perturbation Theory in Quantum Chromodynamics.*, Sov. Phys. JETP 46 (1977) p. 641, [Zh. Eksp. Teor. Fiz.73,1216(1977)].

[66] H.-L. Lai et al., *New parton distributions for collider physics*, Phys. Rev. D 82 (2010) p. 074024, arXiv: 1007.2241 [hep-ph].

[67] S. Dulat et al.,
New parton distribution functions from a global analysis of quantum chromodynamics,
Phys. Rev. D 93 (2016) p. 033006, arXiv: 1506.07443 [hep-ph].

[68] J. Pumplin et al.,
New generation of parton distributions with uncertainties from global QCD analysis,
JHEP 07 (2002) p. 012, arXiv: 0201195 [hep-ph].

[69] V. V. Sudakov, *Vertex Parts at Very High Energies in Quantum Electrodynamics*,
Zh.E.T.F. 30 (1956, (*Sov. Phys. J.E.T.P.*, vol. 30, p. 65, 1956)) p. 87.

[70] T. Sjostrand, *A Model for Initial State Parton Showers*, Phys. Lett. B157 (1985) p. 321.

[71] S. Frixione, *Isolated photons in perturbative QCD*, Phys. Lett. B429 (1998) p. 369,
arXiv: 9801442 [hep-ph].

[72] B. Andersson et al., *Parton fragmentation and string dynamics*,
Phys. Rept. 97 (1983) p. 31 , ISSN: 0370-1573.

[73] B. Webber, *A QCD model for jet fragmentation including soft gluon interference*,
Nucl. Phys. B 238 (1984) p. 492 , ISSN: 0550-3213.

[74] S. Agostinelli et al., *GEANT4: A simulation toolkit*,
Nucl. Instrum. Meth. A 506 (2003) p. 250.

[75] S. Catani et al., *QCD matrix elements + parton showers*, JHEP 11 (2001) p. 063,
arXiv: 0109231 [hep-ph].

[76] A. De Roeck and H. Jung, eds., *HERA and the LHC: A Workshop on the implications of HERA for LHC physics: Proceedings Part A*, CERN, 2005 pp.1,
arXiv: 0601012 [hep-ph].

[77] T. Gleisberg et al., *Event generation with SHERPA 1.1*, JHEP 02 (2009) p. 007,
arXiv: 0811.4622 [hep-ph].

[78] S. Höche et al., *QCD matrix elements and truncated showers*, JHEP 05 (2009) p. 053,
arXiv: 0903.1219 [hep-ph].

[79] T. Gleisberg and S. Höche, *Comix, a new matrix element generator*,
JHEP 12 (2008) p. 039, arXiv: 0808.3674 [hep-ph].

[80] S. Schumann and F. Krauss,
A Parton shower algorithm based on Catani-Seymour dipole factorisation,
JHEP 03 (2008) p. 038, arXiv: 0709.1027 [hep-ph].

[81] T. Sjöstrand, S. Mrenna and P. Z. Skands, *PYTHIA 6.4 Physics and Manual*,
JHEP 05 (2006) p. 026, arXiv: 0603175.

[82] T. Sjöstrand, S. Mrenna and P. Z. Skands, *A Brief Introduction to PYTHIA 8.1*,
Comput. Phys. Commun. 178 (2008) p. 852, arXiv: 0710.3820 [hep-ph].

[83] J. Alwall et al., *The automated computation of tree-level and next-to-leading order differential cross sections, and their matching to parton shower simulations*,
JHEP 07 (2014) p. 079, arXiv: 1405.0301 [hep-ph].

[84] J. Alwall et al., *MadGraph 5 : Going Beyond*, JHEP 1106 (2011) p. 128,
arXiv: 1106.0522 [hep-ph].

[85] P. Nason, *A New method for combining NLO QCD with shower Monte Carlo algorithms*,
JHEP 11 (2004) p. 040, arXiv: 0409146 [hep-ph].

[86] S. Frixione, P. Nason and C. Oleari, *Matching NLO QCD computations with Parton Shower simulations: the POWHEG method*, JHEP 11 (2007) p. 070, arXiv: 0709.2092 [hep-ph].

[87] M. L. Mangano et al., *ALPGEN, a generator for hard multiparton processes in hadronic collisions*, JHEP 07 (2003) p. 001, arXiv: 0206293 [hep-ph].

[88] G. Corcella et al., *HERWIG 6: An Event generator for hadron emission reactions with interfering gluons (including supersymmetric processes)*, JHEP 01 (2001) p. 010, arXiv: 0011363 [hep-ph].

[89] J. M. Butterworth, J. R. Forshaw and M. H. Seymour, *Multiparton interactions in photoproduction at HERA*, Z. Phys. C72 (1996) p. 637, arXiv: 9601371 [hep-ph].

[90] ATLAS Collaboration, *The ATLAS Simulation Infrastructure*, Eur. Phys. J. C 70 (2010) p. 823, arXiv: 1005.4568 [physics.ins-det].

[91] ATLAS Collaboration, *ATLAS detector and physics performance: Technical Design Report, 1*, Technical Design Report ATLAS, CERN, 1999, URL: https://cds.cern.ch/record/391176.

[92] MadGraph Collaboration, *What are the default dynamic factorization and renormalization scales in MadEvent?*, URL: https://cp3.irmp.ucl.ac.be/projects/madgraph/wiki/FAQ-General-13.

[93] A. D. Martin et al., *Parton distributions for the LHC*, Eur. Phys. J. C 63 (2009) p. 189, arXiv: 0901.0002 [hep-ph].

[94] J. Butterworth et al., *PDF4LHC recommendations for LHC Run II*, J. Phys. G43 (2016) p. 023001, arXiv: 1510.03865 [hep-ph].

[95] M. Kirill, S. Markus and S. Andreas, *QCD corrections to top quark pair production in association with a photon at hadron colliders*, Phys. Rev. D 83 (7 2011) p. 074013.

[96] ATLAS Collaboration, *Observation of top-quark pair production in association with a photon and measurement of the $t\bar{t}\gamma$ production cross section in pp collisions at $\sqrt{s} = 7$ TeV using the ATLAS detector*, Phys. Rev. D 91 (7 2015) p. 072007.

[97] M. Cacciari, G. P. Salam and G. Soyez, *The Anti-k_t jet clustering algorithm*, JHEP 04 (2008) p. 063, arXiv: 0802.1189 [hep-ph].

[98] M. Cacciari and G. P. Salam, *Dispelling the myth for the jet-finder*, Physics Letters B 641 (2006) p. 57 , ISSN: 0370-2693.

[99] M. Cacciari, G. P. Salam and G. Soyez, *FastJet User Manual*, Eur. Phys. J. C 72 (2012) p. 1896, arXiv: 1111.6097 [hep-ph].

[100] ATLAS Collaboration, *Topological cell clustering in the ATLAS calorimeters and its performance in LHC Run 1*, (2016), arXiv: 1603.02934 [hep-ex].

[101] ATLAS Collaboration, *Jet energy measurement and its systematic uncertainty in proton–proton collisions at $\sqrt{s} = 7$ TeV with the ATLAS detector*, Eur. Phys. J. C 75 (2015) p. 17, ISSN: 1434-6052.

[102] ATLAS Collaboration, *Monte Carlo Calibration and Combination of In-situ Measurements of Jet Energy Scale, Jet Energy Resolution and Jet Mass in ATLAS*, ATLAS-CONF-2015-037, 2015, URL: http://cds.cern.ch/record/2044941.

[103] ATLAS Collaboration, *Data-driven determination of the energy scale and resolution of jets reconstructed in the ATLAS calorimeters using dijet and multijet events at $\sqrt{s} = 8\ TeV$*, ATLAS-CONF-2015-017, 2015, URL: http://cds.cern.ch/record/2008678.

[104] ATLAS Collaboration, *Determination of the jet energy scale and resolution at ATLAS using Z/γ–jet events in data at $\sqrt{s} = 8\ TeV$*, ATLAS-CONF-2015-057, 2015, URL: http://cds.cern.ch/record/2059846.

[105] ATLAS Collaboration, *Jet global sequential corrections with the ATLAS detector in proton-proton collisions at sqrt(s) = 8 TeV*, ATLAS-CONF-2015-002, 2015, URL: http://cds.cern.ch/record/2001682.

[106] ATLAS Collaboration, *Performance of pile-up mitigation techniques for jets in pp collisions at $\sqrt{s} = 8\ TeV$ using the ATLAS detector*, Eur. Phys. J. C 76 (2016) p. 581, arXiv: 1510.03823 [hep-ex].

[107] ATLAS Collaboration, *Performance of b-Jet Identification in the ATLAS Experiment*, JINST 11 (2016) P04008, arXiv: 1512.01094 [hep-ex].

[108] *Calibration of b-tagging using dileptonic top pair events in a combinatorial likelihood approach with the ATLAS experiment*, ATLAS-CONF-2014-004, 2014, URL: http://cds.cern.ch/record/1664335.

[109] *Calibration of the performance of b-tagging for c and light-flavour jets in the 2012 ATLAS data*, ATLAS-CONF-2014-046, 2014, URL: http://cds.cern.ch/record/1741020.

[110] ATLAS Collaboration, *Electron efficiency measurements with the ATLAS detector using 2012 LHC proton–proton collision data*, Eur. Phys. J. C 77 (2017) p. 195, ISSN: 1434-6052.

[111] ATLAS Collaboration, *Electron and photon energy calibration with the ATLAS detector using LHC Run 1 data*, Eur. Phys. J. C 74 (2014) p. 3071, arXiv: 1407.5063 [hep-ex].

[112] W. Lampl et al., *Calorimeter Clustering Algorithms: Description and Performance*, URL: https://cds.cern.ch/record/1099735.

[113] ATLAS Collaboration, *Expected photon performance in the ATLAS experiment*, ATL-PHYS-PUB-2011-007, 2011, URL: https://cds.cern.ch/record/1345329.

[114] ATLAS Collaboration, *Electron reconstruction and identification efficiency measurements with the ATLAS detector using the 2011 LHC proton-proton collision data*, Eur. Phys. J. C 74 (2014) p. 2941, arXiv: 1404.2240 [hep-ex].

[115] ATLAS Collaboration, *Measurement of the inclusive isolated prompt photon cross section in pp collisions at $\sqrt{s} = 7$ TeV with the ATLAS detector*, Phys. Rev. D 83 (5 2011) p. 052005.

[116] ATLAS Collaboration, *Measurement of the muon reconstruction performance of the ATLAS detector using 2011 and 2012 LHC proton–proton collision data*, Eur. Phys. J. C 74 (2014) p. 3130, arXiv: 1407.3935 [hep-ex].

[117] ATLAS Collaboration, *Performance of algorithms that reconstruct missing transverse momentum in $\sqrt{s} = 8$ TeV proton–proton collisions in the ATLAS detector*, Eur. Phys. J. C 77 (2017) p. 241, ISSN: 1434-6052.

[118] ATLAS Collaboration, *Performance of Missing Transverse Momentum Reconstruction in Proton-Proton Collisions at 7 TeV with ATLAS*, Eur. Phys. J. C 72 (2012) p. 1844, arXiv: 1108.5602 [hep-ex].

[119] ATLAS Collaboration, *Measurements of $W\gamma$ and $Z\gamma$ production in pp collisions at $\sqrt{s}$=7 TeV with the ATLAS detector at the LHC*, Phys. Rev. D 87 (11 2013) p. 112003.

[120] ATLAS Collaboration, *Observation of top-quark pair production in association with a photon and measurement of the $t\bar{t}\gamma$ production cross section in pp collisions at $\sqrt{s} = 7$ TeV using the ATLAS detector*, Phys. Rev. D 91 (7 2015) p. 072007.

[121] ATLAS Collaboration, *Total Integrated Luminosity and Data Quality in 2012*, 3.3.2016, URL: https://twiki.cern.ch/twiki/bin/view/AtlasPublic/LuminosityPublicResults.

[122] ATLAS Collaboration, *Performance of primary vertex reconstruction in proton–proton collisions at $\sqrt{s} = 7$ TeV in the ATLAS experiment*, ATLAS-CONF-2010-069, 2010, URL: https://cds.cern.ch/record/1281344.

[123] ATLAS Collaboration, *Performance of the ATLAS Inner Detector Track and Vertex Reconstruction in High Pile-Up LHC Environment*, ATLAS-CONF-2012-042, 2012, URL: https://cds.cern.ch/record/1435196.

[124] ATLAS Collaboration, *Electron trigger performance in 2012 ATLAS data*, 2015, URL: https://twiki.cern.ch/twiki/bin/view/AtlasPublic/EgammaTriggerPublicResults#2012_Data_8_TeV.

[125] ATLAS Collaboration, *Muon trigger performances in 2012 (approved plots for ICHEP 2013)*, 2013, URL: https://twiki.cern.ch/twiki/bin/view/AtlasPublic/MuonTriggerPublicResults#Plots_for_2012_data_8_TeV.

[126] G. Cowan, *Statistical Data Analysis*, Clarendon (Oxford), 1998 (ISBN: 0-19-850156-0 or 0-19-850155-2 in paperback).

[127] V. S. Lang, *Measurement of the W boson production in association with jets using sqrts = 8 TeV proton-proton collisions at the ATLAS detector*, Heidelberg University, 2016, URL: https://www.kip.uni-heidelberg.de/Veroeffentlichungen/details.php?id=3338.

[128] ATLAS Collaboration, *iLumiCalc Tool*, URL: https://atlas-lumicalc.cern.ch.

[129] A. Bocci, L. Shi and Z. Liang, *Measurements of the $e \to \gamma$ fake rate*, ATL-COM-PHYS-2014-026, 2014, URL: https://cds.cern.ch/record/1643300.

[130] W. Verkerke and D. P. Kirkby, *The RooFit toolkit for data modeling*, eConf C0303241 (2003), 186(2003), arXiv: physics/0306116 [physics].

[131] L. Moneta et al., *The RooStats project*, (2011), arXiv: 1009.1003 [physics].

[132] R. Brun and F. Rademakers, *ROOT: An object oriented data analysis framework*, Nucl. Instrum. Meth. A 389 (1997) p. 81.

[133] F. James and M. Roos, *Minuit - a system for function minimization and analysis of the parameter errors and correlations*, Comput. Phys. Commun. 10 (1975) p. 343 , ISSN: 0010-4655.

[134] B. Efron, *Bootstrap Methods: Another Look at the Jackknife*, Ann. Statist. 7 (1979) p. 1.

[135] A. L. Read, *Presentation of search results: The CL(s) technique*, J. Phys. G28 (2002) p. 2693.

[136] ATLAS Statistics Forum, *CLsInfo*, 2017, URL: https://twiki.cern.ch/twiki/pub/AtlasProtected/StatisticsTools/CLsInfo.pdf.

[137] G. Cowan et al., *Asymptotic formulae for likelihood-based tests of new physics*, Eur. Phys. J. C 71 (2011) p. 1554, [Erratum: Eur. Phys. J. C 73,2501(2013)], arXiv: 1007.1727 [physics.data-an].

[138] S. S. Wilks, *The Large-Sample Distribution of the Likelihood Ratio for Testing Composite Hypotheses*, Ann. Math. Stat. 9 (1938) p. 60.

[139] A. Wald, *An Extension of Wilks' Method for Setting Tolerance Limits*, Ann. Math. Statist. 14 (1943) p. 45.

[140] RooStats, *RooStats::AsymptoticCalculator Class Reference*, 2017, URL: https://root.cern.ch/doc/v608/classRooStats_1_1AsymptoticCalculator.html.

[141] VBFNLO Collaboration, *Conventions in VBFNLO for Anomalous Quartic Gauge Boson Couplings*, 3.04.2017, URL: https://www.itp.kit.edu/vbfnlo/wiki/doku.php?id=documentation:details:aqgc.

[142] RooStats, *TGClim Manual*, 2017, URL: https://svnweb.cern.ch/trac/atlasphys-sm/browser/Physics/StandardModel/ElectroWeak/Common/Software/TGC/TGClim/trunk/docs/TGClimManual.pdf.

[143] ATLAS Collaboration, *Event display for ATLAS*, 2017, URL: http://atlantis.web.cern.ch/atlantis/.

Acknowledgements

At the very end of my thesis, I would like to thank all the great and inspiring people, without whom this thesis would not have been possible.

First of all, I would like to thank my supervisor Prof. Dr. Hans-Christian Schultz-Coulon for the opportunity to pursue my doctoral studies within the ATLAS group of the Kirchhoff-Institute for Physics. I am grateful for his guidance and valuable input throughout this research project as well as his support and encouragement, whenever it was needed.

I would also like to thank Prof. Dr. Stephanie Hansmann-Menzemer, who kindly agreed to be the co-referee of this thesis.

At CERN, I would like to thank the ATLAS Standard Model group, and especially the Electroweak subgroup, giving valuable feedback and supporting the analysis during the publication process.

In addition, I am an also very grateful for all the support from the Heidelberg group. Special thanks go to Monica Dunford, for her supervision as well as her invaluable advices and discussions about my research, physics and non-physics topics. In addition I would like to thank Monica Dunford, Pavel Starovoitov, Rainer Stamen, Julia Djuvsland, Patrick Eckert, Johann Brehmer and Claire Antel for their time proofreading and discussing my thesis. Furthermore, I would like to express my gratitude to the ATLAS and ILC group, for the friendly and inspiring atmosphere. I especially would like to mention my sister analyser Julia, who is the best colleague I could wish for and I am happy to find a close friend in her. I benefited from her experience in triboson measurements and from her valuable input and ideas in many discussions - not only about physics. Out of all my great colleagues, I would like to particularly thank Patrick, Julia, Tobias, Konrad, Jan, Merve, Felix, Hanno and Manuel, for the fantastic time in and outside the institute. Furthermore, I would also like to thank Veit Scharf, for his supervision especially during the beginning of my PhD and Johann Brehmer for his support from the theory perspective.

Last but not least, I would like to thank the people who are closest to me. My parents and my sister Bernadette, for their never-ending support and encouragement to find my own way. But most of all, I would like to thank Patrick. Thank you for your patience, for making me smile every day and for constantly reminding me, that there is a life outside of physics.